

University of Windsor

## Scholarship at UWindor

---

Electronic Theses and Dissertations

Theses, Dissertations, and Major Papers

---

2005

### On the understanding of metallocene structure and dynamics via solid-state NMR.

Ivan Hung  
*University of Windsor*

Follow this and additional works at: <https://scholar.uwindsor.ca/etd>

---

#### Recommended Citation

Hung, Ivan, "On the understanding of metallocene structure and dynamics via solid-state NMR." (2005). *Electronic Theses and Dissertations*. 2927.  
<https://scholar.uwindsor.ca/etd/2927>

This online database contains the full-text of PhD dissertations and Masters' theses of University of Windsor students from 1954 forward. These documents are made available for personal study and research purposes only, in accordance with the Canadian Copyright Act and the Creative Commons license—CC BY-NC-ND (Attribution, Non-Commercial, No Derivative Works). Under this license, works must always be attributed to the copyright holder (original author), cannot be used for any commercial purposes, and may not be altered. Any other use would require the permission of the copyright holder. Students may inquire about withdrawing their dissertation and/or thesis from this database. For additional inquiries, please contact the repository administrator via email ([scholarship@uwindsor.ca](mailto:scholarship@uwindsor.ca)) or by telephone at 519-253-3000ext. 3208.

## INFORMATION TO USERS

This manuscript has been reproduced from the microfilm master. UMI films the text directly from the original or copy submitted. Thus, some thesis and dissertation copies are in typewriter face, while others may be from any type of computer printer.

**The quality of this reproduction is dependent upon the quality of the copy submitted.** Broken or indistinct print, colored or poor quality illustrations and photographs, print bleedthrough, substandard margins, and improper alignment can adversely affect reproduction.

In the unlikely event that the author did not send UMI a complete manuscript and there are missing pages, these will be noted. Also, if unauthorized copyright material had to be removed, a note will indicate the deletion.

Oversize materials (e.g., maps, drawings, charts) are reproduced by sectioning the original, beginning at the upper left-hand corner and continuing from left to right in equal sections with small overlaps.

ProQuest Information and Learning  
300 North Zeeb Road, Ann Arbor, MI 48106-1346 USA  
800-521-0600

UMI<sup>®</sup>



On the Understanding of Metallocene Structure and  
Dynamics via Solid-State NMR

By

Ivan Hung

A Dissertation

Submitted to the Faculty of Graduate Studies and Research  
through the Department of Chemistry and Biochemistry  
in Partial Fulfillment of the Requirements for the  
Degree of Doctor of Philosophy at the  
University of Windsor

Windsor, Ontario, Canada

2005

© 2005 Ivan Hung



Library and  
Archives Canada

Bibliothèque et  
Archives Canada

0-494-09712-4

Published Heritage  
Branch

Direction du  
Patrimoine de l'édition

395 Wellington Street  
Ottawa ON K1A 0N4  
Canada

395, rue Wellington  
Ottawa ON K1A 0N4  
Canada

*Your file* *Votre référence*

*ISBN:*

*Our file* *Notre référence*

*ISBN:*

**NOTICE:**

The author has granted a non-exclusive license allowing Library and Archives Canada to reproduce, publish, archive, preserve, conserve, communicate to the public by telecommunication or on the Internet, loan, distribute and sell these worldwide, for commercial or non-commercial purposes, in microform, paper, electronic and/or any other formats.

The author retains copyright ownership and moral rights in this thesis. Neither the thesis nor substantial extracts from it may be printed or otherwise reproduced without the author's permission.

**AVIS:**

L'auteur a accordé une licence non exclusive permettant à la Bibliothèque et Archives Canada de reproduire, publier, archiver, sauvegarder, conserver, transmettre au public par télécommunication ou par l'Internet, prêter, distribuer et vendre des thèses partout dans le monde, à des fins commerciales ou autres, sur support microforme, papier, électronique et/ou autres formats.

L'auteur conserve la propriété du droit d'auteur et des droits moraux qui protège cette thèse. Ni la thèse ni des extraits substantiels de celle-ci ne doivent être imprimés ou autrement reproduits sans son autorisation.

---

In compliance with the Canadian Privacy Act some supporting forms may have been removed from this thesis.

Conformément à la loi canadienne sur la protection de la vie privée, quelques formulaires secondaires ont été enlevés de cette thèse.

While these forms may be included in the document page count, their removal does not represent any loss of content from the thesis.

Bien que ces formulaires aient inclus dans la pagination, il n'y aura aucun contenu manquant.

  
**Canada**

**Abstract**

This thesis focuses on the use of solid-state NMR spectroscopy to study the metal nuclei in various metallocenes and metallocenium cations, including,  $\text{Cp}^*_2\text{Al}^+$ ,  $\text{Cp}^*_2\text{B}^+$ ,  $\text{Cp}^*_2\text{BMe}$ ,  $\text{Cp}_2\text{Be}$ ,  $\text{Cp}^*_2\text{Be}$ ,  $(\text{C}_5\text{Me}_4\text{H})_2\text{Be}$ ,  $\text{Cp}_2\text{Mg}$ ,  $\text{Cp}_2\text{ZrCl}_2$ ,  $\text{Cp}^*_2\text{ZrCl}_2$ ,  $\text{Cp}_2\text{ZrBr}_2$ ,  $(\text{C}_5\text{Me}_3\text{H}_2)_2\text{ZrBr}_2$ ,  $(\text{Me}_3\text{Si}-\text{C}_5\text{H}_4)_2\text{ZrBr}_2$ ,  $\text{O}(\text{Me}_2\text{SiC}_5\text{H}_4)_2\text{ZrBr}_2$ ,  $(\text{O}(\text{Me}_2\text{Si})_2\text{C}_5\text{H}_3)_2\text{ZrBr}_2$ ,  $(\text{Me}_2\text{ClSi}-\text{C}_5\text{H}_4)\text{ZrCl}_3$ , and  $\text{Cp}_2\text{ZrMe}_2$ . Since few studies of this nature have been reported, much of the initial material involves examining the correlation between anisotropic quadrupolar and chemical shielding interaction tensors with structural and/or dynamic features of the metallocenes. Detailed quantum mechanical calculations are also employed in order to strengthen our understanding of these correlations and the origins of anisotropic NMR interactions. Notable properties which are specific to each metallocene are investigated in detail, examples include, the very small electric field gradient (EFG) and large chemical shielding anisotropy in  $\text{Cp}^*_2\text{Al}^+$ , sigmatropic rearrangement of the  $\eta^1$ - $\text{Cp}^*$  ring in  $\text{Cp}^*_2\text{B}^+$ , and the dynamic ‘slip’ structure of  $\text{Cp}_2\text{Be}$ . In particular, strong correlations are observed between the spherical symmetry around the metal nuclei and the magnitude of the quadrupolar interaction, as well as between  $\text{Cp}'$  ring hapticity and the average nuclear magnetic shielding.

Part of the reason why many metallocenes have not been studied by solid-state metal NMR is the inherently low sensitivity of the nuclei of interest, which arises from low natural abundance, low magnetogyric ratios and/or large anisotropic interactions. An attempt is made to overcome these obstacles by combining preparatory pulse sequences (double frequency sweeps (DFS), rotor-assisted population transfer (RAPT) and cross

polarization (CP)) with a multiple-pulse method called the “Carr-Purcell Meiboom-Gill” (QCPMG) pulse sequence. These combined pulse sequences are tested on a variety of standard samples and result in signal enhancements of an order of magnitude or more depending on nuclear relaxation properties. These signal enhancement techniques make possible the solid-state NMR characterization of  $\text{Cp}_2\text{Mg}$  and  $\text{Cp}_2\text{ZrCl}_2$ , which are important compounds in the fields of metalorganic chemical vapor deposition and olefin polymerization catalysis, respectively.

The solid-state  $^{91}\text{Zr}$  NMR study of a series of zirconocenes is also presented, wherein an attempt is made at understanding the correlation between structure and measured EFG parameters. In particular, brominated zirconocenes which mimic the conformation of species before ( $\text{Cp}_2\text{ZrBr}_2$ ,  $(\text{C}_5\text{Me}_3\text{H}_2)_2\text{ZrBr}_2$ ,  $(\text{Me}_3\text{Si}-\text{C}_5\text{H}_4)_2\text{ZrBr}_2$ ) and after adsorption ( $\text{O}(\text{Me}_2\text{SiC}_5\text{H}_4)_2\text{ZrBr}_2$ ,  $\text{O}(\text{Me}_2\text{Si})_2\text{C}_5\text{H}_3)_2\text{ZrBr}_2$ ) to surface materials show promise in the characterization of industrially relevant systems. The  $^{91}\text{Zr}$  quadrupole coupling constant is shown to be very sensitive to geometrical changes and serves as an invaluable probe for the characterization of zirconocenes.

The fear of the LORD is the beginning of wisdom...  
— Proverbs 9:10, NIV

Therefore do not worry about tomorrow, for tomorrow will worry about itself.  
Each day has enough trouble of its own.  
— Matthew 6:34, NIV

*This work is dedicated to my family, friends and AKIRA.*



## Acknowledgements

Due to my typically asocial manner, there is not many for me to acknowledge except those who I have had the opportunity to share my working space with throughout all these years, well, *all these* almost five years.

No doubt, I must thank Rob (Dr. Schurko) for helping me begin the long journey of learning about solid-state NMR. I especially admire his patience and willingness to teach about things that I should probably know by now. While at the same time, I find it humorous how some trivial things irritate him beyond belief. It is quite non-coincidental, I think, that Rob had been hired and looking for grad students just as I had finished my undergrad and was looking for a supervisor. Most people might attribute this coincidence to luck, though I prefer to marvel at God's perfect plans. I also express my deepest gratitude to Rob for taking a gamble on me (I must admit that my transcript was by no means spotless), and for his willingness to take the group and I to many NMR conferences; they were quite enlightening.

I thank professors Douglas W. Stephan, Charles L. B. Macdonald, Randy J. Bowers, and Dr. Zhehong Gan for serving on my advisory committee.

I also thank Dr. Stephan for his support and allowing us to use his gloveboxes and other facilities before we had any lab space.

I thank Mr. Mike Fuerth for all his help with the Bruker solution NMR spectrometers and the initial setup of the Varian/Chemagnetics solid-state NMR spectrometer (it was quite a painful and lengthy process).

I also thank Chuck (Dr. Macdonald) for his help in the preparation of the

beryllocenes and determining their crystal structures, as well as all the help and suggestions he has provided pertaining to all related aspects of synthetic chemistry. At this point, I would also like to especially mention Aaron Rossini for his help in packing some of the beryllium samples into rotors, on which occasion he staked his life for the advancement of science, i.e., he accidentally poked himself through the gloves while working in the glovebox, and also because I forgot to acknowledge him in the beryllocene article.

Throughout my years of graduate study, I have had the opportunity to “live” (live = spending countless hours with; any graduate student can attest to the amount of time spent in the office/lab) with a mix of people: Andy Y. H. Lo, Joel A. Tang, Cory M. Widdifield, Aaron J. Rossini, Hiyam Hamaed, Mathew Willans, Siri Schauff, Iga Stasiak, Vivian Chow and Josh Mutus. Though experiences were not always pleasant, there was always something to be learned, e.g., patience, optimism, bad humor, attention to detail, [homestarrunner.com](http://homestarrunner.com), and how to pretend you are working and yet get nothing done.

I would also like to thank Cory Widdifield for his quirky presence and humor, as well as his habit of trying to get to the root of things when faced with problems/concepts we did not understand.

Most importantly, I express the utmost gratitude to my family. Acknowledgement of my parents goes without saying, especially because they have never questioned me as to why I am still in school rather than earning money to take care of them. Their unconditional support (to quote MasterCard): priceless.

Finally, I thank AKIRA for all and everything.

# Statement of Originality

I certify that this thesis, and the research to which it refers, are the product of my own work, and that any ideas or quotations from the work of other people, published or otherwise, are fully acknowledged in accordance with the standard referencing practices of the discipline. I acknowledge the helpful guidance and support of my supervisor, Professor Robert W. Schurko.

**This thesis is based on the following publications:**

## Chapter 2

R.W. Schurko, I. Hung, C.L.B. Macdonald, A.H. Cowley. Anisotropic NMR Interaction Tensors in the Decamethylaluminumocenium Cation. *J. Am. Chem. Soc.*, **2002**, *124*, 13204-13214; DOI: 10.1021/ja020394p.

R.W. Schurko, I. Hung, S. Schauff, C.L.B. Macdonald, A.H. Cowley. Anisotropic  $^{11}\text{B}$  and  $^{13}\text{C}$  NMR Interaction Tensors in Decamethylcyclopentadienyl Boron Complexes. *J. Phys. Chem. A*, **2002**, *106*, 10096-10115; DOI: 10.1021/jp020800r.

## Chapter 3

I. Hung, C.L.B. Macdonald, R.W. Schurko. Structure and Dynamics of Homoleptic Beryllocenes: A Solid-State  $^9\text{Be}$  and  $^{13}\text{C}$  NMR Study. *Chem.-Eur. J.*, **2004**, *10*, 5923-5935; DOI: 10.1002/chem.200400404.

## Chapter 4:

I. Hung, A.J. Rossini, R.W. Schurko. Application of the Carr-Purcell Meiboom-Gill Pulse Sequence for the Acquisition of Solid-State NMR Spectra of Spin-1/2 Nuclei. *J. Phys. Chem. A*, **2004**, *108*, 7112-7120; DOI: 10.1021/jp0401123.

## Chapter 5

R.W. Schurko, I. Hung, C.M. Widdifield. Signal Enhancement in NMR Spectra of Half-Integer Quadrupolar Nuclei via DFS-QCPMG and RAPT-QCPMG Pulse Sequences. *Chem. Phys. Lett.*, **2003**, *379*, 1-10; DOI: 10.1016/S0009-2614(03)01345-9.

## Chapter 6

I. Hung, R.W. Schurko. Solid-state  $^{25}\text{Mg}$  QCPMG NMR of bis(cyclopentadienyl)magnesium. *Solid State Nucl. Magn. Reson.*, **2003**, *24*, 78-93; DOI: 10.1016/S0926-2040(03)00050-X. (*Invited Article*)

## Chapter 7

I. Hung, R.W. Schurko. Solid-State  $^{91}\text{Zr}$  NMR of Bis(cyclopentadienyl)dichlorozirconium(IV). *J. Phys. Chem. B*, **2004**, *108*, 9060-9069; DOI: 10.1021/jp040270u.

# Contents

Abstract .....	iii
Dedication .....	v
Acknowledgements .....	vi
Statement of Originality .....	viii
List of Tables .....	xiii
List of Figures .....	xvi
List of Abbreviations .....	xxiv
List of Symbols .....	xxvi
<b>1 Introduction .....</b>	<b>1</b>
1.1 Metallocenes .....	1
1.2 Nuclear Magnetic Resonance .....	3
1.2.1 Chemical Shielding .....	4
1.2.2 Quadrupolar Interaction .....	7
1.2.3 Relative Orientation of CS and EFG Tensors .....	8
1.3 Context of Research .....	9
Bibliography .....	12
<b>2 Correlation of Anisotropic NMR Interaction Tensors with the Structure and Dynamics of Cp*<sub>2</sub>Al<sup>+</sup>, Cp*<sub>2</sub>B<sup>+</sup> and Cp*<sub>2</sub>BMe .....</b>	<b>18</b>
2.1 Introduction .....	18
2.2 Experimental .....	21
2.2.1 Samples .....	21
2.2.2 Solid-State NMR Spectroscopy .....	21
2.2.2.1 <sup>27</sup> Al NMR Experiments .....	21
2.2.2.2 <sup>11</sup> B NMR Experiments .....	22
2.2.2.3 <sup>13</sup> C NMR Experiments .....	23
2.2.3 Spectral Simulations .....	23
2.2.4 Theoretical Calculations .....	24
2.3 Results and Discussion .....	26
2.3.1 Solid-State <sup>27</sup> Al and <sup>11</sup> B NMR .....	26
2.3.1.1 Variable-Temperature <sup>11</sup> B MAS NMR .....	37
2.3.2 Solid-State <sup>13</sup> C NMR .....	38
2.3.2.1 <sup>13</sup> C/ <sup>11</sup> B/ <sup>1</sup> H TRAPDOR NMR of Cp* <sub>2</sub> B <sup>+</sup> .....	40
2.3.3 Theoretical Study of <sup>27</sup> Al and <sup>11</sup> B EFG and Chemical Shielding Tensors .....	43
2.3.4 Theoretical Study of Carbon Shielding Tensors and Cp* Ring Dynamics .....	61
2.4 Conclusion .....	67
Bibliography .....	70

<b>3</b>	<b>Correlation of Anisotropic NMR Interaction Tensors With the Structure and Dynamics of Homoleptic Beryllocenes</b>	75
3.1	Introduction	75
3.2	Experimental	80
3.2.1	Sample Preparation and Handling	80
3.2.2	Solid-State NMR Spectroscopy	80
3.2.3	Spectral Simulations	82
3.2.4	Theoretical Methods	83
3.3	Results and Discussion	84
3.3.1	Solid-State $^9\text{Be}$ NMR	84
3.3.2	Solid-State $^{13}\text{C}$ NMR	90
3.3.3	Theoretical Calculations	99
3.4	Conclusion	106
	Bibliography	108
<b>4</b>	<b>Signal Enhancement in the NMR Spectra of Half-Integer Quadrupolar Nuclei Through the Combination of DFS and RAPT with QCPMG</b>	115
4.1	Introduction	115
4.2	Experimental	119
4.2.1	Sample Preparation and Handling	119
4.2.2	Solid-State NMR Spectroscopy	119
4.3	Results and Discussion	121
4.3.1	$^{87}\text{Rb}$ NMR Experiments	121
4.3.2	$^{39}\text{K}$ NMR Experiments	126
4.3.3	$^{85}\text{Rb}$ NMR Experiments	129
4.4	Conclusion	132
	Bibliography	134
<b>5</b>	<b>Application of the Carr-Purcell Meiboom-Gill Pulse Sequence for the Acquisition of Solid-State NMR Spectra of Spin-1/2 Nuclei</b>	136
5.1	Introduction	136
5.2	Experimental	141
5.2.1	Sample Preparation and Handling	141
5.2.2	Solid-State NMR Spectroscopy	142
5.2.3	Spectral Simulations	145
5.3	Results and Discussion	145
5.3.1	$^{113}\text{Cd}$ NMR	146
5.3.2	$^{199}\text{Hg}$ NMR	151
5.3.3	$^{207}\text{Pb}$ NMR	157
5.3.4	$^{15}\text{N}$ NMR	159
5.3.5	$^{109}\text{Ag}$ NMR	162
5.4	Conclusion	164
	Bibliography	166

<b>6</b>	<b>Solid-State <math>^{25}\text{Mg}</math> and <math>^{13}\text{C}</math> NMR of Bis(cyclopentadienyl)magnesium</b>	171
6.1	Introduction	171
6.2	Experimental	174
6.2.1	Sample Preparation and Handling	174
6.2.2	Solid-State NMR Spectroscopy	174
6.2.3	Spectral Simulations	175
6.2.4	Theoretical calculations	176
6.3	Results and Discussion	177
6.3.1	Solid-State $^{25}\text{Mg}$ NMR	177
6.3.2	Solid-State $^{13}\text{C}$ NMR	181
6.3.3	Theoretical Calculations	182
6.4	Conclusion	189
	Bibliography	191
<b>7</b>	<b>Solid-State <math>^{91}\text{Zr}</math> NMR of Bis(cyclopentadienyl)dichloro Zirconium(IV)</b>	195
7.1	Introduction	195
7.2	Experimental	198
7.2.1	Solid-State NMR Spectroscopy	198
7.2.2	Spectral Simulations	201
7.2.3	Theoretical calculations	202
7.3	Results and Discussion	203
7.3.1	Solid-State $^{91}\text{Zr}$ NMR	203
7.3.2	Comparing Signal Enhancement Pulse Techniques	211
7.3.3	Theoretical Calculations	214
7.4	Conclusion	220
	Bibliography	222
<b>8</b>	<b>Ongoing Research: Towards the Study of Zirconocenes Immobilized on Solid Support Materials via Solid-State <math>^{91}\text{Zr}</math> NMR</b>	227
8.1	Introduction	227
8.2	Experimental	231
8.2.1	Samples	231
8.2.2	Solid-State NMR Spectroscopy	231
8.2.3	Spectral Simulations	232
8.2.4	Theoretical Calculations	232
8.3	Results and Discussion	233
8.3.1	Solid-State NMR	233
8.3.2	Theoretical Calculations	241
8.4	Conclusion	246
	Bibliography	250
<b>9</b>	<b>Future Work: Solid-State NMR Study of Surface-Adsorbed Metallocenes</b>	253

## Appendices

<b>A</b>	<b>Synthesis and X-ray Crystallography</b>	256
A.1.1	Preparation of $[\text{Cp}^*_2\text{Al}][\text{AlCl}_4]$	256
A.1.2	Preparation of $\text{Cp}^*_2\text{BMe}$	257
A.2.1	X-ray Crystallography Procedures for $[\text{Cp}^*_2\text{Al}][\text{AlCl}_4]$ and $\text{Cp}^*_2\text{BMe}$	258
A.2.2	X-ray Crystallography Procedures for $\text{Cp}_2\text{Be}$ , $\text{Cp}^*_2\text{Be}$ and $(\text{C}_5\text{Me}_4\text{H})_2\text{Be}$	259
A.3.1	X-ray crystal structure of $[\text{Cp}^*_2\text{Al}][\text{AlCl}_4]$	262
A.3.2	X-ray Crystallography of $\text{Cp}_2\text{Be}$ , $\text{Cp}^*_2\text{Be}$ and $(\text{C}_5\text{Me}_4\text{H})_2\text{Be}$	264
<b>B</b>	<b>Additional Figures</b>	268
B.1	Supplementary Figures for Chapter 3	268
B.2	Supplementary Figures for Chapter 5	270
B.3	Supplementary Figures for Chapter 7	272
B.4	Supplementary Figures for Chapter 8	273
<b>C</b>	<b>Supplementary Calculations and SCF Energies</b>	276
C.1	SCF Energies from Calculations for $\text{Cp}_2\text{Mg}$ Presented in Chapter 6	276
C.2	Supplementary Calculations for $\text{Cp}_2\text{Mg}$	277
C.3	SCF Energies from Calculations for $\text{Cp}_2\text{ZrCl}_2$ Presented in Chapter 7	278
C.4	Calculations Comparing the Two Inequivalent Crystallographic Sites of $\text{Cp}_2\text{ZrCl}_2$	279
C.5	Calculations for a Geometry Optimized Molecule of $\text{Cp}_2\text{ZrCl}_2$	280
	<b>Vita Auctoris</b>	281

# List of Tables

2.1	Experimental Chemical Shielding and Quadrupolar Parameters Derived from Simulation of NMR Spectra .....	29
2.2	Experimental $^{13}\text{C}$ Chemical Shielding Tensors in $\text{Cp}^*_2\text{B}^+$ .....	40
2.3	Experimental and Theoretical Quadrupolar Parameters .....	44
2.4	Experimental and Theoretical Aluminum Chemical Shielding Tensors in $\text{Cp}^*_2\text{Al}^+$ .....	46
2.5	Experimental and Theoretical Boron Chemical Shielding Tensors in $\text{Cp}^*_2\text{B}^+$ and $\text{Cp}^*_2\text{BMe}$ .....	47
2.6	Theoretical Diamagnetic and Paramagnetic Contributions to Shielding at the Aluminum in $\text{Cp}^*_2\text{Al}^+$ and $\text{Al}(\text{H}_2\text{O})_6^{3+}$ .....	53
2.7	Theoretical Diamagnetic and Paramagnetic Contributions to Shielding at the Boron in $\text{Cp}^*_2\text{B}^+$ , $\text{Cp}^*_2\text{BMe}$ and $\text{BH}_4^-$ .....	54
2.8	ADF Numerical Calculations of Contributions to Aluminum Chemical Shielding from Orbital Mixing .....	56
2.9	Major Paramagnetic Shielding Contributions in $\text{Cp}^*_2\text{Al}^+$ from Molecular Orbital Mixing .....	57
2.10	List of Molecular Orbitals and Most Significant Symmetrized Fragment Orbitals .....	58
2.11	Experimental and Theoretical $^{13}\text{C}$ Chemical Shielding Tensors in $\text{Cp}^*_2\text{Al}^+$ ..	61
2.12	Theoretical $^{13}\text{C}$ Chemical Shielding Tensors in $\text{Cp}^*_2\text{B}^+$ .....	62
3.1	Experimental $^9\text{Be}$ and $^{13}\text{C}$ NMR Parameters .....	86
3.2	Experimental and Theoretical $^{13}\text{C}$ NMR CS Parameters of $(\text{C}_5\text{Me}_4\text{H})_2\text{Be}$ ....	93
3.3	Experimental and Theoretical Beryllium Chemical Shielding Tensors .....	99
3.4	Experimental and Theoretical $^9\text{Be}$ EFG Parameters .....	100



3.5	Theoretical (B3LYP/6-311G**) <sup>9</sup> Be EFG and CS Parameters at Different Beryllium Stationary Points Along the Reaction Coordinates of the ‘Inversion’ Process .....	105
5.1	Nuclear Properties of Studied Nuclei .....	140
5.2	Anisotropic Chemical Shielding Parameters of Investigated Compounds ...	148
6.1	Experimental and Theoretical <sup>25</sup> Mg Quadrupolar Parameters for Cp <sub>2</sub> Mg ...	183
6.2	Theoretical Magnesium Chemical Shielding Tensors for Cp <sub>2</sub> Mg .....	186
6.3	Experimental and Theoretical Carbon Shielding Tensors in Cp <sub>2</sub> Mg .....	187
7.1	Experimental <sup>91</sup> Zr Chemical Shielding and Quadrupolar Parameters .....	211
7.2	Calculated Zirconium Chemical Shielding Tensors for Cp <sub>2</sub> ZrCl <sub>2</sub> .....	215
7.3	Theoretical Zirconium Quadrupolar Parameters in Cp <sub>2</sub> ZrCl <sub>2</sub> .....	216
8.1	Experimental <sup>91</sup> Zr EFG Parameters .....	233
8.2	Experimental and Theoretical <sup>91</sup> Zr EFG Parameters .....	242
A.1	Crystal data and structure refinement for [Cp* <sub>2</sub> Al][AlCl <sub>4</sub> ] and Cp* <sub>2</sub> BMe ...	258
A.2	Summary of X-ray crystallographic data for <b>1</b> , <b>2</b> , and <b>3</b> .....	261
C.1	SCF energies of calculations performed on the X-ray crystal structure (optimized hydrogen positions) of Cp <sub>2</sub> Mg .....	276
C.2	SCF energies of calculations performed on the optimized gas-phase structure of Cp <sub>2</sub> Mg .....	276
C.3	Theoretical <sup>25</sup> Mg Quadrupolar Parameters in Cp <sub>2</sub> Mg .....	277
C.4	Calculated Magnesium Chemical Shielding Tensors in Cp <sub>2</sub> Mg .....	277
C.5	SCF Energies for Calculations on the Isolated Solid-State Geometry of Cp <sub>2</sub> ZrCl <sub>2</sub> .....	278
C.6	Ab Initio SCF Energies for Calculations on Both Crystallographic Sites of Cp <sub>2</sub> ZrCl <sub>2</sub> .....	279

<b>C.7</b>	Theoretical $^{91}\text{Zr}$ Quadrupolar Parameters for Both Crystal Sites of $\text{Cp}_2\text{ZrCl}_2$ .....	279
<b>C.8</b>	Ab Initio Zirconium Chemical Shielding Tensors for Both Crystal Sites of $\text{Cp}_2\text{ZrCl}_2$ .....	279
<b>C.9</b>	SCF Energies for Calculations on Geometry Optimized Isolated Gas-Phase Molecule of $\text{Cp}_2\text{ZrCl}_2$ .....	280
<b>C.10</b>	Theoretical $^{91}\text{Zr}$ Quadrupolar Parameters in Geometry Optimized $\text{Cp}_2\text{ZrCl}_2$ .....	280
<b>C.11</b>	Zirconium Chemical Shielding Tensors in Geometry Optimized $\text{Cp}_2\text{ZrCl}_2$ ..	280

# List of Figures

- 1.1** Sketch of a selection of metallocene structures where M is an arbitrary metal, L denotes arbitrary ligands and Cp' rings are represented by generic pentagons . 1
- 1.2** Schematic representation of the three principal components of the chemical shift tensor and other parameters used to describe powder patterns arising solely from the chemical shielding interaction ..... 5
- 1.3** Illustration of rotational operations performed on an arbitrary axis system ( $x, y, z$ ) by the angles  $\alpha, \beta$  and  $\gamma$  resulting in coincidence with the axes ( $X, Y, Z$ ). In this thesis, the ( $x, y, z$ ) and ( $X, Y, Z$ ) coordinate systems are taken to be the EFG and CS PASSs, respectively ..... 8
- 2.1**  $^{27}\text{Al}$  MAS NMR spectra of  $[\text{Cp}^*_2\text{Al}][\text{AlCl}_4]$ . (b) Expansion of the  $\text{Cp}^*_2\text{Al}^+$  region. Asterisks denote the isotropic resonances of  $\text{Cp}^*_2\text{Al}^+$  ..... 27
- 2.2** (a)  $^{27}\text{Al}$  SATRAS NMR spectrum of  $[\text{Cp}^*_2\text{Al}][\text{AlCl}_4]$  with (b) numerical simulation of one  $\text{Cp}^*_2\text{Al}^+$  site. Inset shows the full satellite transition pattern and accompanying simulation ..... 28
- 2.3** Experimental and simulated  $^{11}\text{B}$  MAS NMR spectra at 8.46 T of (a)  $[\text{Cp}^*_2\text{B}][\text{AlCl}_4]$  at  $\nu_{\text{rot}} = 6000$  Hz and (b)  $\text{Cp}^*_2\text{BMe}$  at  $\nu_{\text{rot}} = 20000$  Hz ..... 29
- 2.4** (a) Top view and (b) side view of the superposition of  $\text{Cp}^*_2\text{Al}^+$  onto a centrosymmetric dodecahedron with Al at the center and carbons atoms located on 10 of the 20 vertices ..... 30
- 2.5** (a) Static  $^{27}\text{Al}$  NMR spectrum of  $[\text{Cp}^*_2\text{Al}][\text{AlCl}_4]$ . (b) Expansion of the  $\text{Cp}^*_2\text{Al}^+$  CSA pattern with accompanying simulation ..... 33
- 2.6** Experimental and simulated static  $^{11}\text{B}$  NMR spectra at 8.46 T of (a)  $\text{Cp}^*_2\text{B}^+$  and (b)  $\text{Cp}^*_2\text{BMe}$ . Simulations with and without the effects of boron chemical shielding anisotropy are included for comparison ..... 35
- 2.7** Experimental and numerical simulations of  $^{11}\text{B}$  MAS NMR spectra of (a)  $\text{Cp}^*_2\text{B}^+$  and (b)  $\text{Cp}^*_2\text{BMe}$  ..... 36
- 2.8**  $^{11}\text{B}$  VT MAS NMR spectra of  $\text{Cp}^*_2\text{B}^+$  at 8.46 T. (a) Full spectral width. (b) Expanded isotropic resonances with corresponding simulations shown as the lower traces for each temperature ..... 37

2.9	<sup>13</sup> C CP/MAS NMR spectra of (a) [Cp* <sub>2</sub> Al][AlCl <sub>4</sub> ] at 9.4 T and (b) [Cp* <sub>2</sub> B][AlCl <sub>4</sub> ] at 8.46 T at varying spinning frequencies. Asterisk denotes the isotropic signal for the Cp* ring carbons in Cp* <sub>2</sub> Al <sup>+</sup> . . . . .	38
2.10	<sup>13</sup> C/ <sup>11</sup> B/ <sup>1</sup> H CP/MAS TRAPDOR and control CP/MAS NMR spectra of [Cp* <sub>2</sub> B][AlCl <sub>4</sub> ] at +25 °C and -150 °C. Inset of spectrum acquired at -150 °C shows detail of individual methyl carbon sites on the η <sup>1</sup> -Cp* ring . . . . .	41
2.11	Orientation of the (a) electric field gradient and (b) chemical shielding tensors in Cp* <sub>2</sub> Al <sup>+</sup> , as determined by RHF calculations with the 6-31G** basis set. Hydrogen atoms are omitted for clarity . . . . .	48
2.12	Theoretical <sup>11</sup> B (a) EFG tensor and (b) CS tensor orientations in Cp* <sub>2</sub> B <sup>+</sup> and Cp* <sub>2</sub> BMe . . . . .	49
2.13	Rotational barrier: SCF energy versus relative dihedral angle between Cp* rings with D <sub>5h</sub> being 0° from Gaussian 98 (▲) B3LYP/6-311G** geometry optimization, and (●) B3LYP/6-31G** and (■) B3LYP/ 6-311G** NMR calculations . . . . .	50
2.14	Occupied (2E <sub>1u</sub> (1, 2), 3A <sub>2u</sub> , 5A <sub>2u</sub> and 5E <sub>1u</sub> (1, 2)) and virtual (6A <sub>2u</sub> , 8A <sub>2u</sub> and 10A <sub>2u</sub> ) molecular orbitals in Cp* <sub>2</sub> Al <sup>+</sup> , which mix to make the largest aluminum paramagnetic shielding contributions . . . . .	60
2.15	Orientation of theoretical carbon CS tensors of aromatic carbons in Cp* <sub>2</sub> B <sup>+</sup> . Arrows signify direction of σ <sub>33</sub> at all carbons with σ <sub>11</sub> and σ <sub>22</sub> components omitted for clarity. The full CS tensor orientation is shown for the <i>ipso</i> -carbon in the η <sup>1</sup> -Cp* ring . . . . .	65
2.16	Simulations of <sup>13</sup> C static NMR powder patterns undergoing five-fold chemical exchange. Inset: Picture of five-fold ring and orientations of CS tensors determined from B3LYP/6-311G** calculations . . . . .	66
3.1	Schematic of proposed Cp <sub>2</sub> Be structures with different point symmetries. . . . .	76
3.2	Molecules of (1) Cp <sub>2</sub> Be, (2) Cp* <sub>2</sub> Be and (3) (C <sub>5</sub> Me <sub>4</sub> H) <sub>2</sub> Be from their respective crystal structures . . . . .	80
3.3	<sup>9</sup> Be MAS NMR spectra of (a) 1, (b) 2 and (c) 3. Simulations of 1 and 2 were performed with SIMPSON and that of 3 with WSOLIDS . . . . .	85
3.4	Static <sup>9</sup> Be NMR spectra of (a)1, (b) 2 and (c) 3. Traces: bottom – experimental; middle – simulation including CSA; top – simulation excluding CSA. Asterisk	

	(*) points out resonance at the isotropic position .....	87
<b>3.5</b>	Static $^9\text{Be}$ VT NMR spectra of <b>1</b> .....	89
<b>3.6</b>	$^{13}\text{C}$ CP/MAS NMR spectra of (a) <b>1</b> , (b) <b>2</b> and (c) <b>3</b> at different spinning frequencies. Inset in (c) shows the labelling scheme of the carbon sites in <b>3</b> .	91
<b>3.7</b>	$^{13}\text{C}$ VT CP/MAS spectra employed for calculation of the activation energy ( $E_a = 36.9 \text{ kJ mol}^{-1}$ ) for Cp ring 'inversion' in <b>1</b> . Expansion of the isotropic resonances for each of the spectra are shown on the right .....	95
<b>3.8</b>	$^{13}\text{C}/^9\text{Be}/^1\text{H}$ CP/TRAPDOR spectra of <b>3</b> ; asterisk (*) marks the $\eta^1\text{-C}_5\text{Me}_4\text{H}$ carbon resonance .....	97
<b>3.9</b>	$^{13}\text{C}/^9\text{Be}/^1\text{H}$ VT CP/TRAPDOR spectra of <b>2</b> . Variable contact time experiments display no difference compared to the spectra shown .....	98
<b>3.10</b>	Theoretical $^9\text{Be}$ EFG and CS tensors of (a) <b>1</b> (top and side view of molecule) (b) <b>2</b> (top and side view of molecule) and (c) <b>3</b> . Methyl hydrogen atoms have been omitted in <b>2</b> and <b>3</b> for clarity .....	102
<b>4.1</b>	The (a) QCPMG, (b) DFS/QCPMG, and (c) RAPT/QCPMG pulse sequences .....	116
<b>4.2</b>	(a) Static $^{87}\text{Rb}$ Hahn echo and DFS/Hahn echo NMR spectra of $\text{RbClO}_4$ along with corresponding QCPMG experiments. The vertical scales of both echo spectra are augmented by a factor of 4. (b) $^{87}\text{Rb}$ MAS Hahn echo, RAPT/Hahn echo, DFS/Hahn echo, QCPMG, RAPT/QCPMG and DFS/QCPMG NMR spectra of $\text{RbClO}_4$ . All spectra were acquired with 128 scans. Integrated intensities with respect to the static and MAS $^{87}\text{Rb}$ Hahn echo experiments are located to the right of each spectrum .....	122
<b>4.3</b>	(a) Time-domain representation of a converging DFS pulse and corresponding schematic representation of the DFS in the frequency domain. (b) Fourier transformed frequency-domain representation of the DFS pulse used in $^{87}\text{Rb}$ NMR experiments (—) along with simulation of the $\text{RbClO}_4$ powder pattern including the $\pm 1/2 - \pm 3/2$ satellite transitions (- - -) .....	124
<b>4.4</b>	(a) Static $^{39}\text{K}$ Hahn echo and DFS/Hahn echo NMR spectra of $\text{KHCO}_3$ and corresponding QCPMG experiments. (b) $^{39}\text{K}$ MAS Hahn echo, RAPT/Hahn echo, DFS/Hahn echo and corresponding QCPMG NMR spectra of $\text{KHCO}_3$ . Integrated intensities with respect to the static and MAS Hahn echo experiments are located to the right of each spectrum. QCPMG experiments were acquired	

	with ca. 10 times fewer scans than corresponding echo experiments . . . . .	128
<b>4.5</b>	(a) Static $^{85}\text{Rb}$ Hahn echo and DFS/Hahn echo NMR spectra of $\text{RbClO}_4$ and corresponding QCPMG experiments. The vertical scale of both echo spectra is augmented by a factor of 2. (b) $^{85}\text{Rb}$ MAS Hahn echo, RAPT/Hahn echo, DFS/Hahn echo and corresponding QCPMG NMR spectra of $\text{RbClO}_4$ . Integrated intensities with respect to the static and MAS $^{85}\text{Rb}$ Hahn echo experiments are located to the right of each spectrum. QCPMG experiments were acquired with 10 times fewer scans than corresponding echo experiments . . . . .	131
<b>5.1</b>	Schematics of the (a) (Q)CPMG and (b) CP/CPMG with TPPM decoupling pulse sequences. The phases for each of the pulses in the CP/CPMG sequence are: $\varphi_1 = 2, 0, 0, 2$ ; $\varphi_2 = 1$ ; $\varphi_3 = 3, 2$ ; $\varphi_4 = 1, 0, 1, 0, 3, 2, 3, 2$ ; $\varphi_5 = 1, 0, 1, 0, 3, 2, 3, 2, 3, 2, 3, 2, 1, 0, 1, 0$ ; with receiver phase list $\varphi_r = (2, 3, 0, 1) \times 4$ , where $\{n\pi/2 \mid n = 0, 1, 2, 3\}$ . . . . .	137
<b>5.2</b>	$^{113}\text{Cd}$ CP/MAS at (a) $\nu_{\text{rot}} = 7000$ Hz and (b) $\nu_{\text{rot}} = 2000$ Hz, (c) static CP/Hahn echo and (d) static CP/CPMG ( $1/\tau_a = 2000$ Hz) NMR spectra of $\text{Cd}(\text{NO}_3)_2 \cdot 4\text{H}_2\text{O}$ ; all recorded with a total of 16 transients. Scaling factors used in modifying the vertical scale of spectra are shown in parentheses, otherwise, all spectra are shown on the same scale. The relevant S/N ratios are shown at the left of each spectrum . . . . .	147
<b>5.3</b>	$^{113}\text{Cd}$ (a) MAS at $\nu_{\text{rot}} = 2000$ Hz, (b) Hahn echo and (c) CPMG ( $1/\tau_a = 2000$ Hz) NMR spectra of $\text{Cd}(\text{NO}_3)_2 \cdot 4\text{H}_2\text{O}$ ; 164 transients were averaged for all three spectra . . . . .	150
<b>5.4</b>	$^{199}\text{Hg}$ (a) CP/MAS at $\nu_{\text{rot}} = 3000$ Hz, (b) CP/Hahn echo, (c) CP/CPMG ( $1/\tau_a = 4000$ Hz) and (d) piecewise wideline CP/CPMG ( $1/\tau_a = 4000$ Hz) NMR spectra of $(\text{CH}_3\text{COO})_2\text{Hg}$ . 16 transients were recorded for the CP/MAS spectrum and CP/CPMG sub-spectra, while 160 transients were acquired for the CP/Hahn echo spectrum . . . . .	153
<b>5.5</b>	$^{199}\text{Hg}$ wideline CP/CPMG ( $1/\tau_a = 4000$ Hz) spectra of $(\text{CH}_3\text{COO})_2\text{Hg}$ along with (a) analytical simulation of the spectral envelope. Sub-spectra (top of figure) were acquired by varying the transmitter frequency in 28 kHz steps, where 16 transients were acquired for each sub-spectrum. The $^{199}\text{Hg}$ wideline CP/CPMG spectra were obtained by (b) addition, and (c) taking the skyline-projection of the individual segments in the frequency domain . . . . .	154
<b>5.6</b>	Comparison of the $^{199}\text{Hg}$ (a) MAS at $\nu_{\text{rot}} = 3000$ Hz and (b) wideline CPMG ( $1/\tau_a = 3000$ Hz) spectra of $(\text{CH}_3\text{COO})_2\text{Hg}$ ; 16 transients were acquired for the	

	MAS spectrum and each of the three CPMG sub-spectra. The CPMG spectrum results from taking the skyline projection of the sub-spectra . . . . .	156
5.7	<sup>207</sup> Pb (a) MAS ( $\nu_{\text{rot}} = 7000$ Hz), (b) CP/MAS ( $\nu_{\text{rot}} = 4000$ Hz), (c) wideline CPMG and (d) wideline CP/CPMG ( $1/\tau_a = 4000$ Hz) NMR spectra of (CH <sub>3</sub> COO) <sub>2</sub> Pb·3H <sub>2</sub> O; analytical simulations are shown above corresponding wideline spectra. 64 and 144 transients were acquired for each of the CPMG and CP/CPMG sub-spectra, respectively . . . . .	158
5.8	<sup>15</sup> N CP/MAS at (a) $\nu_{\text{rot}} = 5300$ Hz and (b) $\nu_{\text{rot}} = 500$ Hz, (c) CP/Hahn echo and (d) CP/CPMG ( $1/\tau_a = 500$ Hz) NMR spectra of the NO <sub>3</sub> site in doubly 98% <sup>15</sup> N-enriched NH <sub>4</sub> NO <sub>3</sub> recorded with a total of 16 transients in each case . . .	161
5.9	<sup>109</sup> Ag CP/MAS at (a) $\nu_{\text{rot}} = 500$ Hz, (b) CP/Hahn echo and CP/CPMG with (c) $1/\tau_a = 500$ Hz and (d) $1/\tau_a = 200$ Hz NMR spectra of AgSO <sub>3</sub> CH <sub>3</sub> ; 480 transients were acquired for all spectra . . . . .	163
6.1	(a) Experimental <sup>25</sup> Mg MAS QCPMG NMR spectrum of Cp <sub>2</sub> Mg and corresponding (b) SIMPSON numerical and (c) WSOLIDS analytical simulations . . . . .	178
6.2	Superposition of (a) Cp* <sub>2</sub> Al <sup>+</sup> and (b) Cp <sub>2</sub> Mg on centro-symmetric dodecahedra having edge lengths corresponding to their C-C bond lengths . . . . .	179
6.3	(a) Experimental static <sup>25</sup> Mg QCPMG NMR spectrum of Cp <sub>2</sub> Mg along with numerical (SIMPSON) simulations (b) including and (c) excluding the effects of CSA . . . . .	180
6.4	Experimental <sup>13</sup> C CP/MAS NMR spectra of Cp <sub>2</sub> Mg at 9.4 T with spinning frequencies of 2000 and 3500 Hz . . . . .	182
6.5	Magnesium (a) EFG and (b) CS tensor orientation within the molecular frame from calculation (RHF/6-311+G**) yielding best agreement with experimental <sup>25</sup> Mg EFG values. Asterisk marks the carbon closest to the magnesium nucleus . . . . .	185
6.6	Simulation of the <sup>13</sup> C NMR powder pattern from a system undergoing 5-site chemical exchange (at different exchange rates). Dashed (---) spectrum is derived from experimentally obtained values. Inset: <sup>13</sup> C chemical shielding tensors from theoretical calculations . . . . .	188
7.1	<sup>91</sup> Zr static NMR spectra of Cp <sub>2</sub> ZrCl <sub>2</sub> at 9.4 T: (a) DFS/Hahn echo spectrum (1925 minute acquisition time), (b) DFS/QCPMG spectrum, from Fourier	

transformation of co-added spin echoes and (c) DFS/QCPMG spectrum, from Fourier transformation of complete echo train (197 minute acquisition time) .....	204
<b>7.2</b> Piecewise acquisition of the static $^{91}\text{Zr}$ QCPMG NMR spectrum of $\text{Cp}_2\text{ZrCl}_2$ packed inside a 5 mm o.d. $\text{ZrO}_2$ rotor. Irradiation frequencies are offset by 50 kHz steps in order to acquire the complete powder pattern .....	206
<b>7.3</b> Static $^{91}\text{Zr}$ QCPMG NMR spectra of $\text{Cp}_2\text{ZrCl}_2$ packed inside (a) a 5 mm o.d. Teflon tube and (b) a 5 mm o.d. $\text{ZrO}_2$ rotor, and (c) $^{91}\text{Zr}$ QCPMG spectrum of a $\text{ZrO}_2$ rotor filled with adamantane and KBr (this latter sample is to get a measurement of the $^{91}\text{Zr}$ NMR spectrum arising solely from the rotor). Simulated static $^{91}\text{Zr}$ NMR powder patterns for (d) a 7:10 mixture of tetragonal and orthorhombic phases of zirconia, along with the sub-spectra for (e) the tetragonal phase ( $C_Q = 19.4$ MHz, $\eta_Q = 0.0$ , $\delta_{\text{iso}} = 200$ ppm) and (f) the orthorhombic phase of zirconia ( $C_Q = 16.5$ MHz, $\eta_Q = 0.85$ , $\delta_{\text{iso}} = 300$ ppm) .....	207
<b>7.4</b> (a) Experimental $^{91}\text{Zr}$ MAS RAPT/QCPMG NMR spectrum of $\text{Cp}_2\text{ZrCl}_2$ along with (b) numerical and (c) analytical simulations at 9.4 T .....	209
<b>7.5</b> Experimental (bottom trace) $^{91}\text{Zr}$ static NMR spectra of $\text{Cp}_2\text{ZrCl}_2$ along with simulations including (middle trace) and excluding (top trace) the effects of CSA at magnetic fields (a) $B_0 = 9.4$ T and (b) $B_0 = 11.74$ T .....	210
<b>7.6</b> (a) Static $^{91}\text{Zr}$ Hahn echo and DFS/Hahn echo NMR spectra of $\text{Cp}_2\text{ZrCl}_2$ and corresponding QCPMG experiments (same number of transients recorded in each case). The vertical scales of echo spectra are augmented by a factor of 10. (b) $^{91}\text{Zr}$ MAS Hahn echo, RAPT/Hahn echo, DFS/Hahn echo and corresponding QCPMG NMR spectra of $\text{Cp}_2\text{ZrCl}_2$ . MAS QCPMG experiments were acquired with 10 times less scans than their spin-echo counterparts. Integrated intensities with respect to the static and MAS $^{91}\text{Zr}$ Hahn echo experiments are located to the right of each spectrum .....	213
<b>7.7</b> (a) Relative orientation of the zirconium CS tensor with respect to the theoretical $^{91}\text{Zr}$ EFG tensor obtained using experimentally measured Euler angles. (b) $^{91}\text{Zr}$ EFG tensor orientation within the molecular frame from calculations yielding best agreement with experimental values .....	218
<b>8.1</b> Schematic representation of compounds <b>1 – 8</b> .....	230
<b>8.2</b> $^{91}\text{Zr}$ MAS NMR spectra of (a) <b>1</b> at $\nu_{\text{rot}} = 10000$ Hz, (b) <b>2</b> at $\nu_{\text{rot}} = 10000$ Hz, (c) <b>3</b> at $\nu_{\text{rot}} = 15500$ Hz, (d) <b>4</b> at $\nu_{\text{rot}} = 11000$ Hz, (e) <b>5</b> at $\nu_{\text{rot}} = 10000$ Hz, and (f) <b>6</b> at	



$\nu_{\text{rot}} = 10000$ Hz. Corresponding analytical simulations are drawn as dashed lines (---) .....	234
<b>8.3</b> (a) Experimental and (b) calculated static $^{91}\text{Zr}$ wideline QCPMG NMR spectra of <b>7</b> .....	238
<b>8.4</b> (a) Static $^{91}\text{Zr}$ wideline QCPMG NMR spectrum of <b>8</b> . (b) Numerical and (c) analytical simulations of (a) .....	239
<b>8.5</b> $^{13}\text{C}$ CP/MAS NMR spectrum of $(\text{Me}_2\text{BrSi}-\text{C}_3\text{H}_4)_2\text{ZrBr}_2/\text{SiO}_2$ at $\nu_{\text{rot}} = 6000$ Hz .....	240
<b>8.6</b> Theoretical $^{91}\text{Zr}$ EFG orientations viewed from the top and sides of (a) <b>8</b> and (b) $\text{Cp}_2\text{ZrCl}_2$ .....	244
<b>8.7</b> Side and top views of the electrostatic potential mapped onto the total electron density of (a) $\text{Cp}_2\text{ZrCl}_2$ and (b) $\text{Cp}_2\text{ZrMe}_2$ . Regions of highest positive and negative charge are denoted by the blue and red colored areas, respectively. ....	246
<b>9.1</b> Solid-state $^{47/49}\text{Ti}$ MAS NMR spectra of $\text{CpTiCl}_3$ , at a spectrometer frequency of 22.5 MHz and $\nu_{\text{rot}} = 10000$ Hz, acquired using the (a) DFS/Hahn echo and (b) DFS/QCPMG pulse sequences. The spectrum in (b) is the result of Fourier transformation of the sum of all echoes in the time domain QCPMG fid. The vertical scale of (a) has been expanded by a factor of 20. Simulation of the $^{47}\text{Ti}$ and $^{49}\text{Ti}$ patterns in spectra (a) and (b) are shown as dashed lines (---), and are characterized by the quadrupolar parameters [ $^{47}\text{Ti}$ : $\delta_{\text{iso}} = -600$ ppm, $C_Q = 1.90$ MHz, $\eta_Q = 1.0$ ; $^{49}\text{Ti}$ : $\delta_{\text{iso}} = -340$ ppm, $C_Q = 1.65$ MHz, $\eta_Q = 1.0$ ]. ....	255
<b>A.1</b> The unit cell for $[\text{Cp}^*_2\text{Al}][\text{AlCl}_4]$ .....	262
<b>A.2</b> Structure of the $[\text{Cp}^*_2\text{Al}]^+$ cation with $D_{3d}$ symmetry. Hydrogen atoms are omitted for clarity .....	263
<b>A.3</b> (a) Molecules of <b>1</b> – <b>3</b> from their respective crystal structures; (b) molecular structure of <b>1</b> at $-100$ °C and $20$ °C .....	264
<b>B.1</b> Inset shows an expansion of the central transition, which demonstrates a change in the isotropic shift from $-23.1$ ppm to $-25.7$ ppm as the temperature is decreased through the temperature range shown. It is also interesting to note that the $C_Q(^9\text{Be})$ appears to increase with decrease in temperature, as shown by the increase in area covered by spinning sidebands .....	268
<b>B.2</b> Analysis of $^{13}\text{C}$ VT CP/MAS NMR spectra of $\text{Cp}_2\text{Be}$ . The activation energy	

	was calculated to be $36.9 \text{ kJ mol}^{-1}$ for the chemical exchange process giving rise to the observed spectra .....	269
<b>B.3</b>	Trajectories of the largest principal components, $V_{33}$ and $\sigma_{33}$ , of the theoretical $^9\text{Be}$ (c) EFG and (d) CS tensors of <b>1</b> at different positions along the ‘inversion.’ Accompanying are plots of (a) $C_Q$ (■) and $\eta_Q$ (▼), and (b) $\Omega$ (■) and $\kappa$ (▼), at each of the positions where $^9\text{Be}$ $V_{33}$ and $\sigma_{33}$ vectors are shown .....	269
<b>B.4</b>	$^{207}\text{Pb}$ (a) MAS, (b) CP/MAS, (c) wideline CPMG and (d) wideline CP/CPMG NMR spectra of a $(\text{CH}_3\text{COO})_2\text{Pb}\cdot 3\text{H}_2\text{O}$ sample before recrystallization; sample is believed to have undergone dehydration and phase transformation. Notably, the optimal CP conditions for the hydrated and dehydrated compounds were markedly different. 64 and 16 transients were acquired for each of the CPMG and CP/CPMG sub-spectra, respectively .....	270
<b>B.5</b>	Comparison of the $^{15}\text{N}$ CP/Hahn echo and CP/CPMG NMR spectra of $^*\text{NH}_4^*\text{NO}_3$ (98% enriched in $^{15}\text{N}$ ). The co-added CP/CPMG spectrum results from adding up the train of echoes in the time-domain and subsequent Fourier transformation. For comparison, the vertical scale of the CP/Hahn echo spectrum has been scaled up by a factor of 25 times .....	271
<b>B.6</b>	$^{91}\text{Zr}$ wideline QCPMG spectrum of $\text{Cp}_2\text{ZrCl}_2$ in a $\text{ZrO}_2$ NMR rotor. Comparison of taking the skyline projection (bottom trace) and adding (top trace) of the individually acquired spectral pieces .....	272
<b>B.7</b>	$^{91}\text{Zr}$ triple-quantum multiple-quantum MAS NMR spectrum of $\text{Cp}_2\text{ZrBr}_2$ at $\nu_{\text{rot}} = 10000 \text{ Hz}$ . The isotropic projection is shown on the left and the anisotropic projection on top .....	273
<b>B.8</b>	Static $^{91}\text{Zr}$ wideline QCPMG NMR spectrum of $\text{CpZrCl}_3$ . The pattern seems to result from the overlap of more than one zirconium site .....	274
<b>B.9</b>	Side and top views of molecular orbitals taking part in $\pi$ -donation between the Zr and Cl atoms obtained from the calculation using the B3LYP method and basis sets mentioned in chapter 8. The molecular orbital energies are given in the left-most column, while simplified sketches are presented on the right for easier visualization of the orbitals involved. ....	275

# List of Abbreviations

ADF	Amsterdam Density Functional
B3LYP	Becke's three parameter exchange functional and the correlation functional of Lee, Yang and Parr
$C_5$	five-fold rotation axis
Cp	cyclopentadienyl ligand, $C_5H_5$
Cp*	pentamethylcyclopentadienyl ligand, $C_5(CH_3)_5$
CP	cross polarization
CS	chemical shielding
CSA	chemical shielding anisotropy
DFT	density functional theory
EFG	electric field gradient
Et	ethyl, $CH_3CH_2-$
fid, FID	free induction decay
FT	Fourier transformation
GIAO	gauge including atomic orbital
MAS	magic angle spinning
Me	methyl, $CH_3-$
MO	molecular orbital
MQMAS	multiple quantum magic angle spinning
n.a.	natural abundance
NMR	nuclear magnetic resonance

o.d.	outer diameter
occ	occupied molecular orbital
PAS	principal axis system
ppm	parts per million
rf	radio frequency
RHF	restricted Hartree-Fock calculation method
S/N	signal-to-noise ratio
SATRAS	satellite transition spectroscopy
SCF	self consistent field
TMS	tetramethyl silane
TRAPDOR	transfer of population in double resonance
VACP	variable amplitude cross polarization
vir	virtual (or unoccupied) molecular orbital
VT	variable temperature

# List of Symbols

$\alpha, \beta, \gamma$	Euler angles relating the principal axis systems of the electric field gradient and chemical shielding tensors
$\gamma$	gyromagnetic ratio
$\Delta\nu_{1/2}$	line width at half height
$\delta_{11}, \delta_{22}, \delta_{33}$	principal components of the chemical shift tensor
$\delta_{\text{iso}}$	isotropic chemical shift
$\eta^x$	hapticity of carbocycle coordination
$\eta_Q$	asymmetry of the electric field gradient tensor
$\kappa$	skew of the chemical shielding tensor
$\nu_0$	Larmor frequency
$\nu_1$	pulse radiofrequency
$\nu_{\text{rot}}$	rotor magic angle spinning frequency
$\sigma_{11}, \sigma_{22}, \sigma_{33}$	principal components of the chemical shielding tensor
$\sigma_{ii}^d, \sigma_{ii}^p$	diamagnetic and paramagnetic contributions, respectively, to the principal chemical shielding component $\sigma_{ii}$ according to Ramsey's formulation of chemical shielding
$\sigma_{\text{iso}}$	isotropic chemical shielding
$\sigma_{\text{iso}}^d, \sigma_{\text{iso}}^p$	diamagnetic and paramagnetic contributions, respectively, to the isotropic chemical shielding according to Ramsey's formulation of chemical shielding
$\Omega$	span of the chemical shielding tensor
$B_0$	strength of the external static magnetic field
$B_1$	strength of the radiofrequency field during a pulse

$C_Q$	nuclear quadrupole coupling constant
$e$	elementary electron charge ( $1.602 \times 10^{-19}$ C)
$h$	Planck constant ( $6.626 \times 10^{-34}$ J s)
$I$	nuclear spin quantum number
$Q$	nuclear quadrupole moment
$R_{DD}$	direct dipolar coupling constant
$T_1$	longitudinal (or spin-lattice) relaxation time
$T_2$	transverse (or spin-spin) relaxation time
$T_2^*$	transverse (or spin-spin) relaxation time including the effects of magnetic field inhomogeneity
$V_{11}, V_{22}, V_{33}$	principal components of the electric field gradient tensor

# Chapter 1

## Introduction

### 1.1 Metallocenes

Metallocenes, in their original form, are compounds comprised of a metal “sandwiched” by two aromatic, five-member, carbon rings. The premier example is ferrocene, which features iron coordinated to the delocalized  $\pi$ -electron clouds of two parallel cyclopentadienyl (Cp) rings; ferrocene was first prepared in 1951.<sup>[1,2]</sup> Discovery and explanation of the ferrocene structure and bonding<sup>[3-6]</sup> largely initiated the study of direct metal–carbon bonds, which gave rise to the field of *organometallic* chemistry. Since then, the preparation of metallocenes,  $\text{Cp}'_n\text{ML}_{m-n}$  ( $\text{Cp}' = \text{C}_5\text{R}_5^-$ ,  $\text{R} = \text{H}, \text{Me}, \text{Ph}, \text{Bz}$ ;  $\text{M} = \text{metal}$ ;  $m$  is usually 2 or 4 for main group and transition metallocenes,

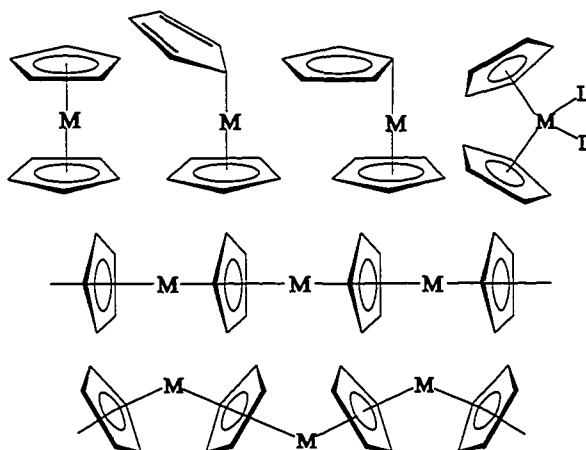


**Figure 1.1** Sketch of a selection of metallocene structures where M is an arbitrary metal, L denotes arbitrary ligands and Cp' rings are represented by generic pentagons.

respectively;  $n = 1$  to  $m$ ; L = other ligands), containing alkali, main group, transition, and lanthanide metals have been reported (Figure 1.1).<sup>[7,8]</sup> Today, the word ‘metallocene’ commonly refers to any compound where a metal atom is  $\pi$ -coordinated to at least one Cp ring.

The vast interest in metallocenes is derived from their versatile applications, which range from the fundamentally scientific to the pragmatically industrial. Indeed, the uniqueness, diversity and control of metallocene structure and bonding provides for researchers an immense arena to explore otherwise little seen electronic phenomena; while the importance of metallocenes as industrial materials can be seen from its many present and potential applications in processes, such as, olefin polymerization,<sup>[9]</sup> molecular recognition,<sup>[10-12]</sup> and as constituents of magnetic materials,<sup>[13-15]</sup> anti-tumor agents,<sup>[16-19]</sup> metallocene-containing polymers,<sup>[20-23]</sup> and non-linear optical materials.<sup>[24, 25]</sup>

Metallocenes have found greatest interest and application in the field of olefin polymerization. Metallocenes emerged as an invaluable innovation in catalysis, owing to the uniform molecular structure of active species taking part in polymerization. In contrast to the active sites of classical Ziegler-Natta catalysts which display variations in their environments depending on their position on the catalyst surface,<sup>[26, 27]</sup> the active site of metallocene species have well defined coordination environments, which result in polymers with much smaller molecular mass distributions. Metallocene catalysts are not only able to provide much greater control over the resulting polymers, but they display the ability to polymerize many more types of monomers than classical Ziegler-Natta systems, largely expanding the area of olefin polymerization.<sup>[28]</sup>



Much work has gone into the modification of metallocene catalysts in order to tailor the resulting polymers in terms of their tacticity, molecular mass, and molecular mass distribution. The enormous success of metallocene catalysts arises from the ability to rationally (on the basis of electron donation and/or steric bulk effects) modify the Cp ligands in order to control the resulting polymer properties.<sup>[29-31]</sup>

Although the nature of the active metallocene species, the role and mechanism of co-catalyst (e.g., MAO) participation, as well as polymer initiation, growth and termination mechanisms have been studied extensively leading to very insightful observations, definitive evidence remains to be found for many of the aspects of olefin polymerization. Seeing that many of the processes involving metallocenes are not fully understood, it is the goal of this thesis to improve the understanding of metallocene structure and dynamics via solid-state NMR, in order to set the basis for investigation of their role in the aforementioned applications. Furthermore, various attempts are made to examine metallocene species immobilized on heterogeneous support materials, as these are the forms in which many metallocene catalysts are employed in an industrial setting.

## **1.2 Nuclear Magnetic Resonance**

In recent decades, nuclear magnetic resonance (NMR) spectroscopy has grown to be an indispensable tool for structural characterization, easily evidenced by the immense yearly growth in the number of NMR publications,<sup>[32]</sup> and the routine use of solution NMR in conjunction with X-ray diffraction techniques for the verification of structure in synthetic chemistry.

The success of NMR can largely be attributed to its ability to provide structural information at the atomic and/or molecular level. The most prominent application of NMR is undoubtedly derived from the powerful correlation observed in solution  $^1\text{H}$  and  $^{13}\text{C}$  NMR between atomic environment and chemical shift and  $J$ -coupling.

NMR interactions are anisotropic (i.e., orientation dependent), however, due to the rapid tumbling of molecules in solution, the orientation dependence of these interactions are averaged out, diminishing the amount of information that can be observed. In condensed matter, most types of molecular motion are restricted; therefore, it is theoretically possible to examine NMR interactions in their entirety (i.e., including their anisotropy). As a result, the NMR lineshape becomes broadened and complicated, leading generally to loss in resolution and signal intensity. Fortunately, the theoretical basis behind anisotropic NMR interactions is well developed<sup>[33, 34]</sup> and adequate analysis of recorded spectra can yield information which can be directly related to molecular structure and symmetry. The present study of metallocenes mainly revolves around two NMR interactions, namely, the quadrupolar and chemical shielding interactions. Detailed discussions of these and other interactions, and how NMR spectra exhibit their effects can be found elsewhere.<sup>[34, 35]</sup> A brief explanation will suffice for the intents and purposes of this thesis.

### 1.2.1 Chemical Shielding

Under the influence of an external magnetic field, electrons tend to circulate in a manner which modifies the strength of the external field at the nucleus. Due to the slight

perturbation in the local field, this interaction has been termed nuclear magnetic shielding, chemical shielding, or just shielding. Magnetic shielding is anisotropic, i.e., the effective magnetic field experienced at the nucleus varies along different directions. The chemical shielding (CS) interaction can be described in its own axis system by a second-rank spherical tensor ( $3 \times 3$  matrix) with three principal components from greatest to least,  $\sigma_{33} \geq \sigma_{22} \geq \sigma_{11}$ , which are defined with respect to the nucleus without electrons and with shielding of  $\sigma = 0$ . The isotropic chemical shielding is the average of these three components,  $\sigma_{\text{iso}} = (\sigma_{11} + \sigma_{22} + \sigma_{33})/3$ , and is the sole property of the CS interaction which can be observed in cases where rapid isotropic motion averages the chemical shielding anisotropy. Within the convention of Herzfeld and Berger, the magnitude of the CS interaction is given by the span ( $\Omega = \sigma_{33} - \sigma_{11}$ ), while the skew ( $\kappa = 3(\sigma_{\text{iso}} - \sigma_{22})/\Omega$ ) denotes the asymmetry (or the degree of axial symmetry) of the CS tensor.<sup>[36]</sup> Chemical

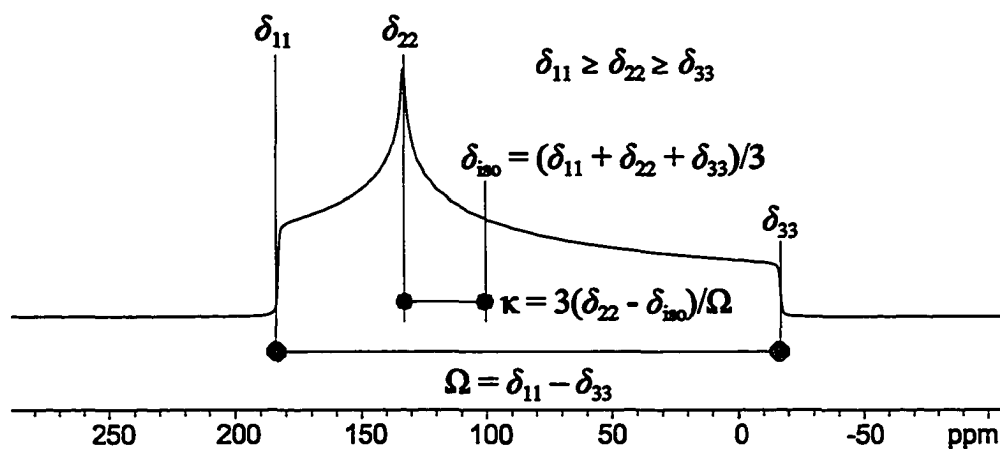


**Figure 1.2** Schematic representation of the three principal components of the chemical shift tensor and other parameters used to describe powder patterns arising solely from the chemical shielding interaction.

shielding is usually described with respect to a reference compound, which is arbitrarily assigned a chemical shift value. The chemical shift can be related to chemical shielding by the equation:  $\delta_{\text{sample}} = (\sigma_{\text{ref}} - \sigma_{\text{sample}})/(1 - \sigma_{\text{ref}}) \times 10^6 \approx \sigma_{\text{ref}} - \sigma_{\text{sample}}$ , where  $\sigma_{\text{ref}}$  is the absolute chemical shielding of the reference compound.<sup>[37, 38]</sup> Thus, the chemical shift tensor has principal components  $\delta_{11} \geq \delta_{22} \geq \delta_{33}$ , and the isotropic shift, span and skew can equivalently be redefined as  $\delta_{\text{iso}} = (\delta_{11} + \delta_{22} + \delta_{33})/3$ ,  $\Omega = \delta_{11} - \delta_{33}$  and  $\kappa = 3(\delta_{22} - \delta_{\text{iso}})/\Omega$ ;  $-1 \leq \kappa \leq +1$ , respectively.<sup>[39]</sup> The chemical shielding and chemical shift tensors are distinguished primarily by their referencing systems, therefore, the designation of their principal components and other parameters are often times used interchangeably.

Ramsey was the first to develop a theory to explain nuclear magnetic shielding, within which diamagnetic and paramagnetic shielding contributions were identified.<sup>[40-43]</sup> Diamagnetic shielding, which is responsible for magnetically shielding the nucleus from the applied magnetic field, arises from induced circulation of electrons in ground state molecular orbitals. Paramagnetic shielding, which is usually associated with magnetic deshielding of the nucleus, arises primarily from magnetic-dipole allowed mixing of ground and excited state molecular orbitals (MOs). Since excited states must be taken into account, calculation of the paramagnetic terms is much more difficult than the diamagnetic terms. The diamagnetic and paramagnetic contributions cannot be distinguished experimentally by NMR spectroscopy; however, careful analysis of orientation-dependent diamagnetic and paramagnetic shielding contributions often help to elucidate the origin of chemical shielding and its relation to molecular orbitals and structure.

## 1.2.2 Quadrupolar Interaction

Nuclei with spin greater than 1/2 possess a quadrupole moment ( $Q$ ) due to the non-spherical distribution of positive charge within the nucleus. The quadrupolar interaction is the interaction between the nuclear quadrupole moment and the electric field gradient (EFG) around the nucleus. The electric field gradient can be described by a second-rank tensor, which is traceless, symmetric and can be expressed in its own principal axis system (PAS) by three components such that  $|V_{33}| \geq |V_{22}| \geq |V_{11}|$ . These can be reduced to two commonly reported parameters (since  $V_{11} + V_{22} + V_{33} = 0$ ): the nuclear quadrupole coupling constant,  $C_Q = eQV_{33}/h$  (in Hz), which represents the strength of the interaction, and the quadrupolar asymmetry parameter  $\eta_Q = (V_{11} - V_{22})/V_{33}$  ( $0 \leq \eta_Q \leq 1$ ), which gives an indication of the axial symmetry of the EFG around the nucleus.

The electric field gradient tensor is a ground-state property of the molecule, which is dependent upon the distribution of electronic charge near the nucleus. In the past, calculations of the EFG tensor involved the use of a simple point charge model, where atoms surrounding the nucleus were assigned arbitrary charges, which were then summed to calculate the EFG tensor. Such point charge calculations rarely correspond closely with experimental data, as they do not account for polarization of electron density and rely on empirically assigned charges. Presently, Hartree-Fock and DFT calculations are the most common methods for calculation of the EFG tensor in isolated molecules and small clusters of atoms. In fact, there are many instances where calculation of nuclear quadrupole coupling constants and asymmetry parameters closely match experimental

solid-state data. In solids, the EFG tensor at a nucleus is mainly dependent upon the local chemical environment, though it can be influenced by long range electrostatic interactions with distant electric monopoles, dipoles and quadrupoles.<sup>[44]</sup> Embedded cluster molecular orbital (ECMO) calculations, which involve RHF or DFT calculations on a cluster embedded within a lattice of point charges, are also often employed to improve the accuracy of theoretical calculations of EFG tensors by taking into account electrostatic interactions from sources distant to the nucleus.<sup>[45-47]</sup>

### 1.2.3 Relative Orientation of CS and EFG Tensors

The relative orientation of the CS and EFG tensors plays a role in determining the shape of NMR powder patterns for non-spinning samples.<sup>[48, 49]</sup> The relative orientation of these tensors are usually described by the rotational operation  $\mathbf{R}(\alpha, \beta, \gamma) = \mathbf{R}_z(\gamma)\mathbf{R}_y(\beta)\mathbf{R}_x(\alpha)$  with Euler angles  $\alpha$ ,  $\beta$  and  $\gamma$ ,<sup>[50]</sup> where  $\mathbf{R}_i(\theta)$  performs a positive (counter-clockwise) rotation about the positive  $i$ -axis by angle  $\theta$ , producing a new

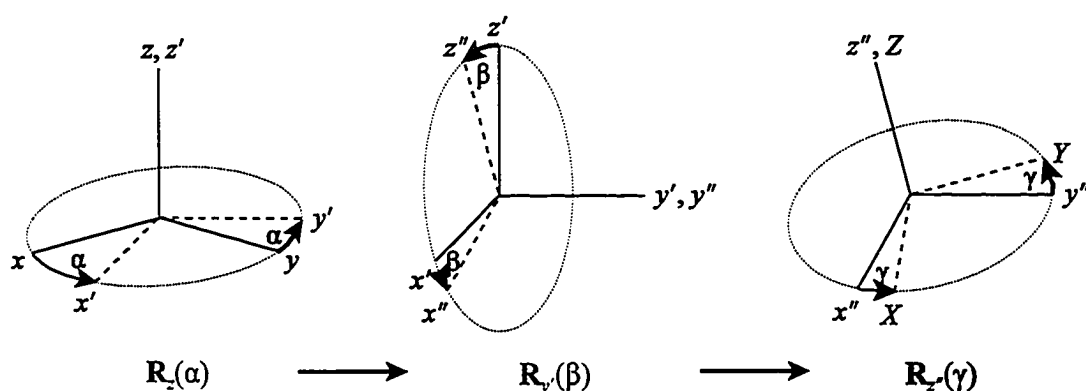


**Figure 1.3** Illustration of rotational operations performed on an arbitrary axis system  $(x, y, z)$  by the angles  $\alpha$ ,  $\beta$  and  $\gamma$  resulting in coincidence with the axes  $(X, Y, Z)$ . In this thesis, the  $(x, y, z)$  and  $(X, Y, Z)$  coordinate systems are taken to be the EFG and CS PASs, respectively.

rotation axis  $i'$ , such that a coordinate system initially coincident with the EFG PAS ends up coincident with the chemical shielding PAS (Figure 1.3). By examining the quadrupolar and chemical shielding interactions and their relative orientations, we are potentially afforded with a powerful probe of the structure, dynamics and bonding about the nucleus of concern.

### 1.3 Context of Research

Solid-state  $^{13}\text{C}$  NMR studies have been conducted on a variety of metallocenes in order to study ring motion, carbon chemical shielding tensors and  $J$ -coupling.<sup>[51-61]</sup> Solid-state deuterium NMR has also been used to examine the motion of oriented cobaltocene molecules in several instances.<sup>[62, 63]</sup> Despite the numerous solution NMR studies on metallocenes and related organometallic complexes,<sup>[64-66]</sup> relatively few solid-state NMR experiments have been reported on the metallocene metal nuclei. Notably, prior to our research in this area, solid-state NMR studies had only been reported on the metal nuclei of lithocenes,<sup>[67]</sup>  $\text{CpNa-TMEDA}$ ,<sup>[68]</sup>  $[\text{Cp}_2\text{Co}]\text{NO}_3\cdot\text{H}_2\text{O}$ ,<sup>[69]</sup>  $\text{Cp}'_2\text{Yb(II)}$  complexes,<sup>[70]</sup> stannocenes and plumbocenes.<sup>[71-73]</sup> Of note is the fact that many of the metal nuclei studied have nuclear spin quantum number of  $I = 1/2$ , and more importantly, little work has gone into investigating molecular properties which direct the observed NMR parameters of the metal.

Solid-state NMR of quadrupolar nuclei provides a powerful means of studying structure and dynamics in metallocenes, since anisotropic NMR tensors are very sensitive to changes in the electronic environment around the nuclei. The work included herein

seeks to improve the overall understanding of metallocene complexes by establishing fundamental relationships between NMR observables and molecular properties, thus allowing future characterization of systems wherein nuclei of interest might be very dilute, in molecular environments that have not been encountered, or cannot be characterized with X-ray techniques. In particular, it is important to correlate NMR interaction tensors with the chemistry metallocenes, as this presents great potential for identifying precursors and by-products of catalysis in disordered systems, studying catalyst initiation and termination, metallocene reactivity and transition states, as well as probing inter- and intra-molecular dynamics and chemical exchange mechanisms in metallocenes.

Chapter 2 encompasses our first venture into understanding the correlation between anisotropic NMR interactions and molecular properties. The effects of the general symmetry about the metal nuclei in  $\text{Cp}^*_2\text{Al}^+$ ,  $\text{Cp}^*_2\text{B}^+$  and  $\text{Cp}^*_2\text{BMe}$  on the quadrupolar and chemical shielding interactions are explored. It is generally seen that: (i) as the spherical symmetry around the metal nuclei decreases, the magnitude of the quadrupolar interaction increases, and (ii) as the hapticity of the  $\text{Cp}^*$  rings increases, the metal nuclei become more shielded. The origin of large chemical shielding anisotropy in these main-group metallocenes is also studied by density functional theory calculations. In chapter 3, the correlation between anisotropic NMR interactions and molecular structure and dynamics, is applied to a series of homoleptic beryllocenes ( $\text{Cp}_2\text{Be}$ ,  $\text{Cp}^*_2\text{Be}$  and  $(\text{C}_5\text{Me}_4\text{H})_2\text{Be}$ ). The trends observed in chapter 3 in terms of molecular geometry and the magnitude of anisotropic NMR interactions are in agreement with observations from



chapter 2. Special focus is given to the unusual ‘slip’ sandwich structure of  $\text{Cp}_2\text{Be}$ , for which an attempt is made to elucidate the transit of the beryllium atom between its two half-occupied crystallographic sites.  $^{13}\text{C}$  variable-temperature NMR experiments provide evidence for chemical exchange of the beryllium positions and permits measurement of its activation barrier. Chapter 4 details the combination of sensitivity enhancement techniques (DFS + QCPMG and RAPT + QCPMG) for application on half-integer quadrupolar nuclei, while chapter 5 explains the combination of CP with CPMG for the enhancement of spin-1/2 static NMR spectra. In both cases, a signal enhancement of approximately an order of magnitude is attained, greatly facilitating the solid-state NMR study of nuclei and complexes which would have been much more difficult to study previously. Initial application of the QCPMG pulse sequence to the study of  $\text{Cp}_2\text{Mg}$ , an important component for Mg doping of group 13 nitrides, is discussed in chapter 6. In contrast to the case of  $\text{Cp}^*_2\text{Al}^+$ ,  $\text{Cp}_2\text{Mg}$  exhibits a large quadrupolar interaction and negligible chemical shielding anisotropy. Chapter 7 describes the solid-state  $^{91}\text{Zr}$  NMR investigation of  $\text{Cp}_2\text{ZrCl}_2$ , an important catalytic precursor and starting material for the preparation of zirconocene catalysts. In chapter 8, a comprehensive study of various zirconocenes is presented, which shows the strong potential of solid-state  $^{91}\text{Zr}$  NMR for the characterization of surface-bound zirconocenes as found for many heterogeneous catalysts.

# Bibliography

- [1] T. J. Kealy, P. L. Paulson, *Nature (London, United Kingdom)* **1951**, 168, 1039.
- [2] S. A. Miller, J. A. Tebboth, J. F. Tremaine, *Journal of the Chemical Society (London)* **1952**, 632.
- [3] G. Wilkinson, M. Rosenblum, M. C. Whiting, R. B. Woodward, *Journal of the American Chemical Society* **1952**, 74, 2125.
- [4] R. B. Woodward, M. Rosenblum, M. C. Whiting, *Journal of the American Chemical Society* **1952**, 74, 3458.
- [5] J. D. Dunitz, L. E. Orgel, *Nature (London, United Kingdom)* **1953**, 171, 121.
- [6] E. O. Fischer, H. P. Fritz, *Advances Inorganic Chem. and Radiochem. (H. J. Emelius and A. G. Sharpe, editors. Academic Press Inc.)* **1959**, 1, 55.
- [7] A. Togni, R. L. Halterman (Eds.), *Metallocenes: Synthesis, Reactivity, Applications, Vol. 1*, Wiley-VCH, Weinheim, **1998**.
- [8] A. Togni, R. L. Halterman (Eds.), *Metallocenes: Synthesis, Reactivity, Applications, Vol. 2*, Wiley-VCH, Weinheim, **1998**.
- [9] J. A. Ewen, in *Metallocene-based Polyolefins: Preparation, Properties and Technology, Vol. 1* (Eds.: J. Scheirs, W. Kaminsky), John Wiley and Sons, Ltd., New York, **2000**.
- [10] E. C. Constable, *Angewandte Chemie-International Edition in English* **1991**, 30, 407.
- [11] P. D. Beer, *Advances in Inorganic Chemistry* **1992**, 39, 79.

- [12] C. D. Hall, in *Ferrocenes: Homogeneous Catalysis, Organic Synthesis, Materials Science* (Eds.: A. Togni, T. Hayashi), VCH, Weinheim, **1995**.
- [13] J. S. Miller, A. J. Epstein, *Angewandte Chemie-International Edition in English* **1994**, 33, 385.
- [14] J. S. Miller, A. J. Epstein, in *Materials Chemistry: An Emerging Discipline, Vol. 245* (Eds.: L. V. Interrante, L. A. Casper, A. B. Ellis), Oxford University Press, Oxford, **1995**, pp. 161.
- [15] A. Togni, T. Hayashi (Eds.), *Ferrocenes: homogeneous catalysis, organic synthesis, materials science*, VCH, Weinheim, **1995**.
- [16] F. Caruso, M. Rossi, *Metal Ions in Biological Systems* **2004**, 42, 353.
- [17] M. Guo, P. Yang, B. Yang, *Huaxue Tongbao* **1995**, 1.
- [18] M. M. Harding, G. Mokdsi, *Current Medicinal Chemistry* **2000**, 7, 1289.
- [19] E. Melendez, *Critical Reviews in Oncology Hematology* **2002**, 42, 309.
- [20] E. W. Neuse, Rosenber.H, *Journal of Macromolecular Science-Reviews in Macromolecular Chemistry* **1970**, C 4, 1.
- [21] Z. Lin, X. Ni, H. Hu, *Progress in Natural Science* **1996**, 6, 120.
- [22] P. Nguyen, P. Gomez-Elipe, I. Manners, *Chemical Reviews* **1999**, 99, 1515.
- [23] R. D. A. Hudson, *Journal of Organometallic Chemistry* **2001**, 637, 47.
- [24] D. M. Roundhill, J. P. Fackler, Jr. (Eds.), *Optoelectronic Properties of Inorganic Compounds*, Plenum Press, New York, **1999**.
- [25] N. J. Long, *Angewandte Chemie-International Edition in English* **1995**, 34, 21.
- [26] J. Boor, Jr., *Ziegler-Natta Catalysts and Polymerizations*, Academic Press, New

York, **1979**.

[27] H. Sinn, W. Kaminsky, *Advances in Organometallic Chemistry* **1980**, *18*, 99.

[28] H. J. Adler, P. Fischer, A. Heller, I. Jansen, D. Kuckling, H. Komber, D. Lehmann, J. Piontek, D. Pleul, F. Simon, *Acta Polymerica* **1999**, *50*, 232.

[29] Y. Imanishi, N. Naga, *Progress in Polymer Science* **2001**, *26*, 1147.

[30] G. Muller, B. Rieger, *Progress in Polymer Science* **2002**, *27*, 815.

[31] R. Mulhaupt, *Macromolecular Chemistry and Physics* **2003**, *204*, 289.

[32] D. L. Bryce, G. M. Bernard, M. Gee, M. D. Lumsden, K. Eichele, R. E.

Wasylishen, *Canadian Journal of Analytical Sciences and Spectroscopy* **2001**, *46*, 46.

[33] A. Abragam, *The Principles of Nuclear Magnetism*, Clarendon Press, Oxford, **1961**.

[34] M. Mehring, *Principles of High Resolution NMR in Solids*, 2nd ed., Springer-Verlag, New York, **1983**.

[35] U. Haeberlen, *High Resolution NMR in Solids*, Academic Press, New York, **1976**.

[36] J. Herzfeld, A. E. Berger, *Journal of Chemical Physics* **1980**, *73*, 6021.

[37] C. J. Jameson, J. Mason, in *Multinuclear NMR* (Ed.: J. Mason), Plenum Press, New York, **1987**, pp. 51.

[38] C. J. Jameson, in *Encyclopedia of Nuclear Magnetic Resonance* (Eds.: D. M. Grant, R. K. Harris), John Wiley & Sons, Chichester, U. K., **1996**, pp. 1273.

[39] J. Mason, *Solid State Nuclear Magnetic Resonance* **1993**, *2*, 285.

[40] N. F. Ramsey, *Physical Review* **1950**, *77*, 567.

[41] N. F. Ramsey, *Physical Review* **1950**, *78*, 699.

- [42] N. F. Ramsey, *Physical Review* **1951**, *83*, 540.
- [43] N. F. Ramsey, *Physical Review* **1952**, *86*, 243.
- [44] E. A. C. Lucken, *Nuclear Quadrupole Coupling Constants*, Academic Press, New York, **1969**.
- [45] D. W. Mitchell, T. P. Das, W. Potzel, W. Schiessl, H. Karzel, M. Steiner, M. Kofferlein, U. Hiller, G. M. Kalvius, A. Martin, W. Schafer, G. Will, I. Halevy, J. Gal, *Physical Review B* **1996**, *53*, 7684.
- [46] L. Hemmingsen, U. Ryde, *Journal of Physical Chemistry* **1996**, *100*, 4803.
- [47] P. L. Bryant, C. R. Harwell, K. Wu, F. R. Fronczek, R. W. Hall, L. G. Butler, *Journal of Physical Chemistry A* **1999**, *103*, 5246.
- [48] W. P. Power, R. E. Wasylshen, S. Mooibroek, B. A. Pettitt, W. Danchura, *Journal of Physical Chemistry* **1990**, *94*, 591.
- [49] K. Eichele, R. E. Wasylshen, J. H. Nelson, *Journal of Physical Chemistry A* **1997**, *101*, 5463.
- [50] R. N. Zare, *Angular Momentum - Understanding Spatial Aspects in Chemistry and Physics*, John Wiley and Sons, New York, **1988**.
- [51] H. Heise, F. H. Kohler, E. B. Brouwer, R. K. Harris, S. Steuernagel, *Magnetic Resonance in Chemistry* **1999**, *37*, 573.
- [52] H. Heise, F. H. Kohler, X. L. Xie, *Journal of Magnetic Resonance* **2001**, *150*, 198.
- [53] F. H. Kohler, X. L. Xie, *Magnetic Resonance in Chemistry* **1997**, *35*, 487.
- [54] J. Blumel, M. Herker, W. Hiller, F. H. Kohler, *Organometallics* **1996**, *15*, 3474.
- [55] A. M. Orendt, J. C. Facelli, Y. J. Jiang, D. M. Grant, *Journal of Physical Chemistry*

*A* **1998**, *102*, 7692.

[56] D. E. Wemmer, A. Pines, *Journal of the American Chemical Society* **1981**, *103*, 34.

[57] D. E. Wemmer, D. J. Ruben, A. Pines, *Journal of the American Chemical Society* **1981**, *103*, 28.

[58] S. J. Heyes, C. M. Dobson, *Journal of the American Chemical Society* **1991**, *113*, 463.

[59] E. J. Munson, M. C. Douskey, S. M. De Paul, M. Ziegeweid, L. Phillips, F. Separovic, M. S. Davies, M. J. Aroney, *Journal of Organometallic Chemistry* **1999**, *577*, 19.

[60] A. J. Campbell, C. A. Fyfe, *Journal of the American Chemical Society* **1972**, *94*, 8387.

[61] A. P. M. Kentgens, H. Karrenbeld, E. De Boer, H. Schumann, *Journal of Organometallic Chemistry* **1992**, *429*, 99.

[62] J. S. O. Evans, D. Ohare, R. Clement, *Journal of the American Chemical Society* **1995**, *117*, 4595.

[63] S. J. Mason, S. J. Heyes, D. O'Hare, *Journal of the Chemical Society-Chemical Communications* **1995**, 1657.

[64] W. von Philipsborn, *Chemical Society Reviews* **1999**, *28*, 95.

[65] D. Rehder, *Coordination Chemistry Reviews* **1991**, *110*, 161.

[66] R. Benn, A. Rufinska, *Angewandte Chemie-International Edition in English* **1986**, *25*, 861.

[67] D. Johnels, A. Boman, U. Edlund, *Magnetic Resonance in Chemistry* **1998**, *36*,

S151.

[68] T. Pietrass, P. K. Burkert, *Inorganica Chimica Acta* **1993**, *207*, 253.

[69] H. W. Spiess, H. Haas, H. Hartmann, *Journal of Chemical Physics* **1969**, *50*, 3057.

[70] J. M. Keates, G. A. Lawless, *Organometallics* **1997**, *16*, 2842.

[71] C. Janiak, H. Schumann, C. Stader, B. Wrackmeyer, J. J. Zuckerman, *Chem. Ber.* **1988**, *121*, 1745.

[72] B. Wrackmeyer, E. Kupce, G. Kehr, A. Sebald, *Magnetic Resonance in Chemistry* **1992**, *30*, 964.

[73] D. R. Armstrong, M. J. Duer, M. G. Davidson, D. Moncrieff, C. A. Russell, C. Stourton, A. Steiner, D. Stalke, D. S. Wright, *Organometallics* **1997**, *16*, 3440.

# Chapter 2

## Correlation of Anisotropic NMR Interaction Tensors with the Structure and Dynamics of $\text{Cp}^*_2\text{Al}^+$ , $\text{Cp}^*_2\text{B}^+$ and $\text{Cp}^*_2\text{BMe}$

### 2.1 Introduction

From the perspective of solid-state nuclear magnetic resonance, metallocenes represent a great opportunity to study the central metal nuclei in an array of structurally and chemically tuneable molecular structures. Main group metallocenes can be synthesized that possess non-bridged or bridged  $\text{Cp}'$  rings of variable hapticity, diverse ring substituents, variable ring dynamics, and linear or bent geometries about the central nucleus depending on the steric and electronic characteristics of the substituents. Many of the main group metallocenes investigated possess quadrupolar nuclei (i.e., spin  $I > 1/2$ ) that are amenable to solid-state NMR analysis by virtue of their small nuclear quadrupole moments, high natural abundances and large magnetogyric ratios. The manifestation of the second-order quadrupolar interaction in MAS spectra of half-integer quadrupolar nuclei should provide much insight into the electronic environment and symmetry at the metal center of metallocenes. Moreover, variable-temperature (VT) double- and triple-resonance solid-state NMR experiments are useful for providing an enhanced understanding of ring dynamics in such systems.

The decamethylaluminocenium cation,  $\text{Cp}^*_2\text{Al}^+$ , has a highly symmetric, ferrocene-like  $D_{5d}$  structure with a staggered conformation of the  $\text{Cp}^*$  rings (without



considering the methyl protons). On the other hand, the decamethylborocenium cation,  $\text{Cp}^*_2\text{B}^+$ ,<sup>[1,2]</sup> is a “tightly-squeezed” metallocene where one of the Cp\* rings has  $\eta^5$ -coordination to the boron, while the other is  $\eta^1$ -coordinated. The  $(\text{C}_5\text{R}_5)_2\text{B}^+$  (R = H, Me) cations have been the subject of a recent computational investigation, from which it was concluded that there may be fluxional degrees of hapticity between the two rings.<sup>[3]</sup> For example, a ring may initially be  $\eta^1$ -coordinated, progress through an  $\eta^2$ -arrangement, and end up  $\eta^5$ -coordinated. Addition of a third ligand to the boron center generates a tri-coordinate borane, in which both of the Cp\* rings are  $\eta^1$ -coordinated.

$^{27}\text{Al}$  is a quadrupolar nucleus (nuclear spin  $I = 5/2$ ) with a moderately sized nuclear quadrupole moment ( $Q(^{27}\text{Al}) = 1.403 \times 10^{-29} \text{ m}^2$ ),<sup>[4,5]</sup> and is well suited for solid-state NMR experiments due to its 100% natural abundance and magnetogyric ratio ( $\gamma = 6.9762 \times 10^7 \text{ rad T}^{-1} \text{ s}^{-1}$ )<sup>[6]</sup> comparable to that of  $^{13}\text{C}$ . Similarly,  $^{11}\text{B}$  is an excellent NMR nucleus, with  $I = 3/2$ , a high natural abundance of 80.42%, a relatively small nuclear quadrupole moment  $Q(^{11}\text{B}) = 4.100 \times 10^{-30} \text{ m}^2$ ,<sup>[5]</sup> and high magnetogyric ratio  $\gamma = 8.5847 \times 10^7 \text{ rad T}^{-1} \text{ s}^{-1}$ .

Many isotropic aluminum chemical shifts have been reported in the literature, spanning a chemical shift range of about 300 ppm.<sup>[7,8]</sup> It has also been shown that solid-state  $^{27}\text{Al}$  NMR spectra may be influenced by anisotropic chemical shielding interactions. However, only a few instances of aluminum CSA have been reported, namely, from  $^{27}\text{Al}$  NMR studies on single crystals of  $\alpha\text{-Al}_2\text{O}_3$ ,<sup>[9]</sup> and powder samples of four-coordinate  $\text{AlCl}_3\text{OPCl}_3$ <sup>[10]</sup> and hexacoordinate tridentate aluminum complexes.<sup>[11]</sup> Although there is an abundance of  $^{11}\text{B}$  quadrupolar data in the literature for three- and four-coordinate

boron complexes, very few definitive cases of boron anisotropic chemical shielding have been reported.<sup>[12, 13]</sup> The standard boron chemical shift range spans approximately 230 ppm,<sup>[14]</sup> including inorganic and organometallic boron complexes and boranes. Given the foregoing lack of information, there is a clear need for additional experimental studies of anisotropic shielding tensors for these and other group 13 elements.

The results of solid-state  $^{27}\text{Al}$  NMR experiments on  $[\text{Cp}^*_2\text{Al}][\text{AlCl}_4]$ , and  $^{11}\text{B}$  NMR experiments on  $[\text{Cp}^*_2\text{B}][\text{AlCl}_4]$  and  $\text{Cp}^*_2\text{BMe}$  are presented herein. From a combination of MAS and non-spinning NMR experiments, the quadrupolar parameters and chemical shielding tensors in these complexes have been determined.  $^{13}\text{C}$  CP/MAS NMR spectra are also presented, along with CS tensors for the aromatic  $\text{Cp}^*$  carbons. In addition, the  $\text{Cp}^*_2\text{B}^+$  cation has been examined using variable temperature (VT)  $^{11}\text{B}$  MAS NMR,  $^{13}\text{C}$  CP/MAS NMR and  $^{13}\text{C}/^{11}\text{B}/^1\text{H}$  CP/TRAPDOR (TRANSfer of Populations in DOuble Resonance)<sup>[15, 16]</sup> NMR experiments. The quadrupolar powder pattern, the effectiveness of cross polarization and efficiency of the TRAPDOR effect all indicate the existence of rapid  $\eta^5$ - $\text{Cp}^*$  ring rotation, and as yet undescribed motions of the  $\eta^1$ - $\text{Cp}^*$  ring in the solid state.

Experimental spectra are accompanied by a series of detailed quantum mechanical calculations of EFG and CS tensors. Pure DFT calculations are employed as well to provide an analysis of which molecular orbitals contribute the most to magnetic shielding of the aluminum nucleus in  $\text{Cp}^*_2\text{Al}^+$ . A simple chemical exchange model is presented which explains the discrepancies between experimental and theoretical carbon CS tensors. The overall objective is to provide insight into the relationship between NMR

interaction tensors and molecular symmetry, dynamics and electronic structure in the series of main group metallocenes,  $[\text{Cp}^*_2\text{Al}][\text{AlCl}_4]$ ,  $[\text{Cp}^*_2\text{B}][\text{AlCl}_4]$  and  $\text{Cp}^*_2\text{BMe}$ , where the symmetry about the central metal varies.

## 2.2 Experimental

### 2.2.1 Samples

Samples of  $[\text{Cp}^*_2\text{Al}][\text{AlCl}_4]$ ,  $[\text{Cp}^*_2\text{B}][\text{AlCl}_4]$  and  $\text{Cp}^*_2\text{BMe}$  were kindly provided by C. L. B. Macdonald and A. H. Cowley (University of Texas at Austin), who determined the crystal structures of  $[\text{Cp}^*_2\text{Al}][\text{AlCl}_4]$  and  $\text{Cp}^*_2\text{BMe}$  (Appendix A). The X-ray crystal structure of  $[\text{Cp}^*_2\text{B}][\text{AlCl}_4]$  has been published elsewhere.<sup>[1]</sup>

### 2.2.2 Solid-State NMR Spectroscopy

#### 2.2.2.1 $^{27}\text{Al}$ NMR Experiments

Samples were carefully powdered under an inert atmosphere and packed tightly into 4 mm o.d. rotors. Solid-state MAS and static NMR spectra were obtained on a 9.4 T ( $^1\text{H} = 400$  MHz) wide bore Bruker AMX-400 NMR spectrometer at Dalhousie University, operating at  $\nu_0(^{27}\text{Al}) = 104.26$  MHz. A Bruker 4 mm triple-resonance MAS NMR probe was used for the acquisition of both static and MAS spectra, with typical MAS spinning speeds of  $\nu_{\text{rot}} = 6260$  and 8000 Hz. Bloch decay experiments were performed with high power proton-decoupling ( $\nu_2 = 62.5$  kHz). Pulse widths of 1.8 and 5.0  $\mu\text{s}$  were applied in the static and MAS  $^{27}\text{Al}$  experiments, respectively, both with

$\nu_1 = 50$  kHz. For MAS experiments, 1000 – 2000 transients were collected, and for static experiments, ca. 45000 scans were acquired. The  $^{27}\text{Al}$  satellite transition (SATRAS) NMR spectrum was acquired at spinning frequency of  $\nu_{\text{rot}} = 6000$  Hz using a pulse width of  $0.6 \mu\text{s}$  and rf field  $\nu_1 = 86$  kHz. A total of 12916 transients were collected using a 3.0 s pulse delay and high-power proton decoupling. The MAS speed was chosen very carefully in order to prevent overlap of peaks from different aluminum sites. Processed spectra were baseline corrected using NUTS NMR processing software.

Additional  $^{27}\text{Al}$  NMR spectra were acquired on a Varian Infinity+ NMR spectrometer and Oxford 9.4 T magnet at the University of Windsor, at similar operating frequencies. Aluminum-27 chemical shifts were referenced to a 1.0 M solution of  $\text{Al}(\text{NO}_3)_3$  ( $\delta_{\text{iso}} = 0$  ppm).

#### 2.2.2.2 $^{11}\text{B}$ NMR Experiments

Samples were prepared under an  $\text{N}_2$  environment and packed into 3.2 mm o.d. rotors. Spectra were acquired on an 8.46 T ( $\nu_0(^{1}\text{H}) = 360$  MHz) Chemagnetics CMX-360 NMR spectrometer at the State University of New York at Stony Brook (courtesy of C. P. Grey), with  $\nu_0(^{11}\text{B}) = 115.52$  MHz. A Chemagnetics 3.2 mm triple-resonance HXY probe was applied for all experiments. For  $^{11}\text{B}$  NMR experiments, solid  $\text{NaBH}_4$  was used as a secondary chemical shift reference, with  $\delta_{\text{iso}}(^{11}\text{B}) = -42.06$  ppm, setting the chemical shift scale against the primary reference which is neat liquid  $(\text{C}_2\text{H}_5)_2\text{O} \cdot \text{BF}_3$  with  $\delta_{\text{iso}}(^{11}\text{B}) = 0.00$  ppm.<sup>[17]</sup> Proton-decoupled  $^{11}\text{B}$  MAS NMR spectra were acquired with spinning frequencies ranging from 5000 to 20000 Hz, a pulse width of  $1.5 \mu\text{s}$ ,  $\nu_1 = 83$  kHz and

recycle delays of 1 s. Proton-decoupled  $^{11}\text{B}$  Hahn echo experiments were conducted with inter-pulse delays of 50 – 100  $\mu\text{s}$  and similar pulse widths and recycle delays as above.

### 2.2.2.3 $^{13}\text{C}$ NMR Experiments

$^{13}\text{C}$  single-pulse and cross-polarization (CP) MAS NMR experiments were conducted using the same spectrometers as above, operating at  $\nu_0(^{13}\text{C}) = 90.54$  MHz, and with high-power proton decoupling during acquisition.  $^{13}\text{C}$  NMR spectra were referenced to TMS ( $\delta_{\text{iso}}(^{13}\text{C}) = 0.0$  ppm) by setting the high frequency resonance of adamantane to 38.57 ppm. Spectra were acquired at two different spinning frequencies (2000 and 4723 Hz) with a 3.5  $\mu\text{s}$  pulse width and  $\nu_1 = 71.4$  kHz rf field for  $[\text{Cp}^*_2\text{Al}][\text{AlCl}_4]$ . For  $[\text{Cp}^*_2\text{Al}][\text{AlCl}_4]$  and  $\text{Cp}^*_2\text{BMe}$ , proton-decoupled  $^{13}\text{C}$  MAS, CP/MAS and variable amplitude (VA) CP/MAS NMR spectra were acquired at spinning frequencies of 2000 – 6000 Hz with proton  $90^\circ$  pulse widths of 2.5  $\mu\text{s}$ , recycle delays of 2 – 8 s and contact times ranging from 0.1 to 10 ms. Rotor-synchronized  $^{13}\text{C}/^{11}\text{B}/^1\text{H}$  CP/TRAPDOR experiments were conducted in a similar manner to the  $^{13}\text{C}$  CP/MAS experiments above, except with strong on-resonance irradiation of the  $^{11}\text{B}$  peaks ( $\nu_1 = 80$  kHz) over one, three and five rotor periods.

### 2.2.3 Spectral Simulations

Analytical simulations of static and MAS NMR spectra were carried out on a Pentium III computer using the WSOLIDS simulation package.<sup>[18]</sup> This software incorporates the space-tiling method of Alderman and co-workers for the generation of

frequency domain solid-state NMR powder patterns.<sup>[19]</sup> Prior to simulating the  $^{11}\text{B}$  MAS NMR spectra, the spinning sidebands were summed into the isotropic center-band to produce a powder pattern resembling that at infinite spinning speeds. Carbon shielding tensors were extracted from  $^{13}\text{C}$  MAS NMR spectra using the method of Herzfeld and Berger.<sup>[20,21]</sup>

The SIMPSON<sup>[22]</sup> software package was used to simulate the  $^{27}\text{Al}$  SATRAS NMR spectrum of  $[\text{Cp}^*_2\text{Al}][\text{AlCl}_4]$ , as well as the full central transition spinning sideband manifolds for  $[\text{Cp}^*_2\text{B}][\text{AlCl}_4]$  and  $\text{Cp}^*_2\text{BMe}$ . Simulations were accomplished by the *gcompute* method of powder averaging using the *zcw4180* crystal file provided in the package. For simplicity, the start and detect operators were set to  $I_{1x}$  and  $I_{1p}$ , respectively. Simulated spectra were saved as free induction decays (FIDs) in ASCII format without any mathematical manipulation and converted to files readable by the NUTS (Acorn NMR) software for processing.

#### 2.2.4 Theoretical Calculations

Calculations of EFG and CS tensors were performed using Gaussian 98<sup>[23]</sup> on a Dell Precision workstation running Red Hat Linux 6.2. The molecular coordinates of  $\text{Cp}^*_2\text{Al}^+$ ,  $\text{Cp}^*_2\text{BMe}$  and  $\text{Cp}^*_2\text{B}^+$  used in calculations were obtained from crystal structures resolved by X-ray diffraction studies respectively from the present work (Appendix A) and Reference [1]. Computations were carried out using standard methods (restricted Hartree-Fock (RHF) and density functional theory (DFT) with the B3LYP functional<sup>[24-26]</sup>) and basis sets (6-31G\*\*, 6-311G\*\*, 6-311+G\*\*) provided within the package.

Quadrupole coupling constants in Hz were calculated by multiplying the largest component of the EFG tensor ( $V_{33}$ ) in atomic units with  $eQ/h \times 9.7177 \times 10^{21} \text{ V m}^{-2}$ ,<sup>[27, 28]</sup> where  $e = 1.602 \times 10^{-19} \text{ C}$ ,  $h = 6.626 \times 10^{-34} \text{ J s}$ ,  $Q(^{27}\text{Al}) = 1.403 \times 10^{-29} \text{ m}^2$ ,<sup>[4, 5]</sup> and  $Q(^{11}\text{B}) = 0.04100 \times 10^{-28} \text{ m}^2$ .<sup>[5]</sup> Chemical shielding values were calculated using the gauge-including atomic orbital (GIAO) method.<sup>[29, 30]</sup> Theoretical  $^{27}\text{Al}$  chemical shielding values were referenced to the calculated absolute chemical shielding of  $\text{Al}(\text{H}_2\text{O})_6^{3+}$  with its shift set to  $\delta_{\text{iso}} = 0.0 \text{ ppm}$ ,<sup>[31]</sup> whereas for  $^{11}\text{B}$  CS data,  $\text{BH}_4^-$  was used as a secondary reference with  $\delta_{\text{iso}} = -42.06 \text{ ppm}$ , which sets calculated boron shift values to the  $(\text{C}_2\text{H}_5)_2\text{O}\cdot\text{BF}_3$  scale ( $\delta_{\text{iso}} = 0.0 \text{ ppm}$ ). Carbon chemical shielding parameters were converted to carbon chemical shifts by referencing to the absolute chemical shielding of the carbon nucleus in CO which is set to  $\delta_{\text{iso}} = 187.1 \text{ ppm}$  with respect to the carbon nucleus in TMS ( $\delta_{\text{iso}} = 0.0 \text{ ppm}$ ).<sup>[32]</sup>

The rotational barrier of the  $\eta^5\text{-Cp}^*$  ring in  $\text{Cp}^*_2\text{B}^+$  was determined by calculating the self consistent field (SCF) energy of the molecule, keeping all other atoms fixed and rotating the  $\eta^5\text{-Cp}^*$  ring in six degree intervals. Manipulation of the  $\eta^5\text{-Cp}^*$  ring movement was accomplished using a z-matrix. Rotational barrier calculations were also conducted for molecules with fully optimized geometries, except for the angle responsible for the relative orientation of the  $\text{Cp}^*$  rings.

Theoretical contributions to aluminum chemical shielding due to mixing of molecular orbitals were calculated for  $\text{Cp}^*_2\text{Al}^+$ ,  $\text{Al}(\text{H}_2\text{O})_6^{3+}$  and  $\text{AlCl}_4^-$  using the Amsterdam Density Functional software package version 2000.02 (ADF2000.02).<sup>[33, 34]</sup> Pure exchange was used for the Local Density Approximation (LDA) and Becke's<sup>[24, 25]</sup>

exchange with the Lee-Yang-Parr<sup>[26]</sup> correlation functionals were applied for the generalized gradient approximation (GGA). Calculations were performed on crystal structure molecular coordinates using the all-electron ADF standard basis sets V, which are triple- $\zeta$  basis sets with two polarization functions for H–Ar.

<sup>13</sup>C powder patterns affected by molecular motion were simulated using a custom-written C++ chemical exchange program. Hemispherical Zaremba, Conroy and Wolfsberg (ZCW) angle sets were used for powder averaging,<sup>[35]</sup> and inversion and diagonalization routines for square matrices were performed with release 3.0 of the LAPACK linear algebra package.

## 2.3 Results and Discussion

### 2.3.1 Solid-State <sup>27</sup>Al and <sup>11</sup>B NMR

The <sup>27</sup>Al MAS NMR spectrum of [Cp\*<sub>2</sub>Al][AlCl<sub>4</sub>] reveals three different aluminum-containing species (Figure 2.1a). The normal range of <sup>27</sup>Al chemical shifts falls between 0 ppm (hexacoordinate aluminum) and 100 ppm (tetra-coordinate aluminum).<sup>[6, 36]</sup> Accordingly, the peak at 101.0 ppm, with a line-width at half-height ( $\Delta\nu_{1/2}$ ) of 80 Hz (without apodization of the FID) is assigned to the AlCl<sub>4</sub><sup>-</sup> anions. This peak is expected to be relatively narrow, because the quadrupolar interaction in a pseudo-tetrahedral environment is relatively small due to the high spherical symmetry. Expansion of the low-frequency portion of the spectrum (Figure 2.1b) reveals two sharp resonances arising from the two crystallographically distinct Cp\*<sub>2</sub>Al<sup>+</sup> cations in the unit



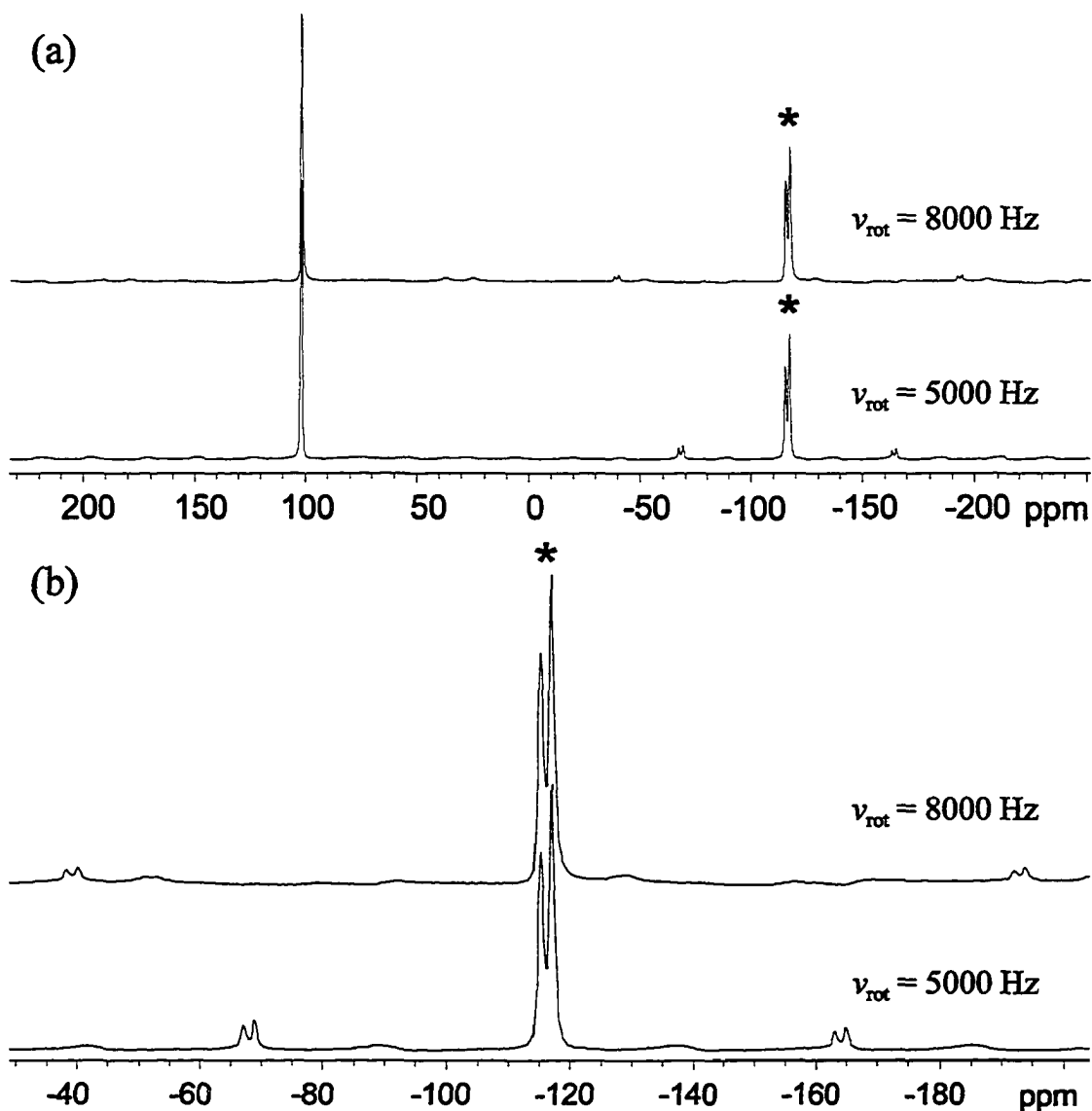


**Figure 2.1** (a)  $^{27}\text{Al}$  MAS NMR spectra of  $[\text{Cp}^*_2\text{Al}][\text{AlCl}_4]$ . (b) Expansion of the  $\text{Cp}^*_2\text{Al}^+$  region. Asterisks denote the isotropic resonances of  $\text{Cp}^*_2\text{Al}^+$ .

cell, with slightly different chemical shifts of  $-115.3 \text{ ppm}$  and  $-117.0 \text{ ppm}$ , and slightly different line-widths ( $\Delta\nu_{1/2} = 80 \text{ Hz}$  and  $70 \text{ Hz}$ , respectively). These shifts are similar to those measured in solution  $^{27}\text{Al}$  NMR experiments on  $\text{Cp}^*_2\text{Al}^+$ , and fall well outside of the usual aluminum chemical shift range. There is no visible second order quadrupolar powder pattern for these peaks; however,  $C_Q$  is non-zero since there is evidence of

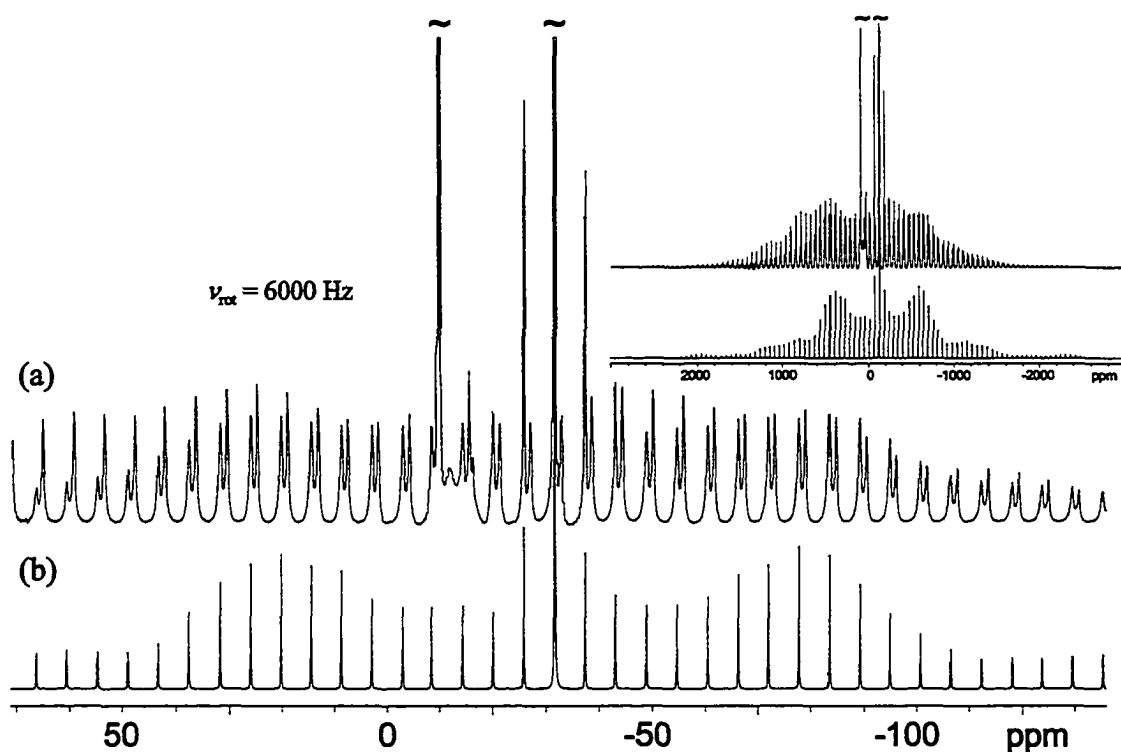


**Figure 2.2** (a)  $^{27}\text{Al}$  SATRAS NMR spectrum of  $[\text{Cp}^*_2\text{Al}][\text{AlCl}_4]$  with (b) numerical simulation of one  $\text{Cp}^*_2\text{Al}^+$  site. Inset shows the full satellite transition pattern and accompanying simulation.

spinning sidebands resulting from satellite transitions observed in the spectra.

The full  $^{27}\text{Al}$  NMR spectrum including central and satellite transitions is displayed in Figure 2.2. The pattern is extremely complex, due to overlap of satellite transition spinning sidebands from the different aluminum sites. Additionally, the overall shape of the pattern and exact position and intensity of each spinning sideband is dependent upon both the anisotropic chemical shielding and quadrupolar parameters. Careful simulation of the full  $^{27}\text{Al}$  central and satellite transition patterns of the  $\text{Cp}^*_2\text{Al}^+$  cation, including CS tensor parameters obtained from analysis of the static  $^{27}\text{Al}$  NMR powder pattern, allow for the determination of  $C_Q(^{27}\text{Al}) = 0.86$  MHz and  $\eta_Q = 0.0$ .

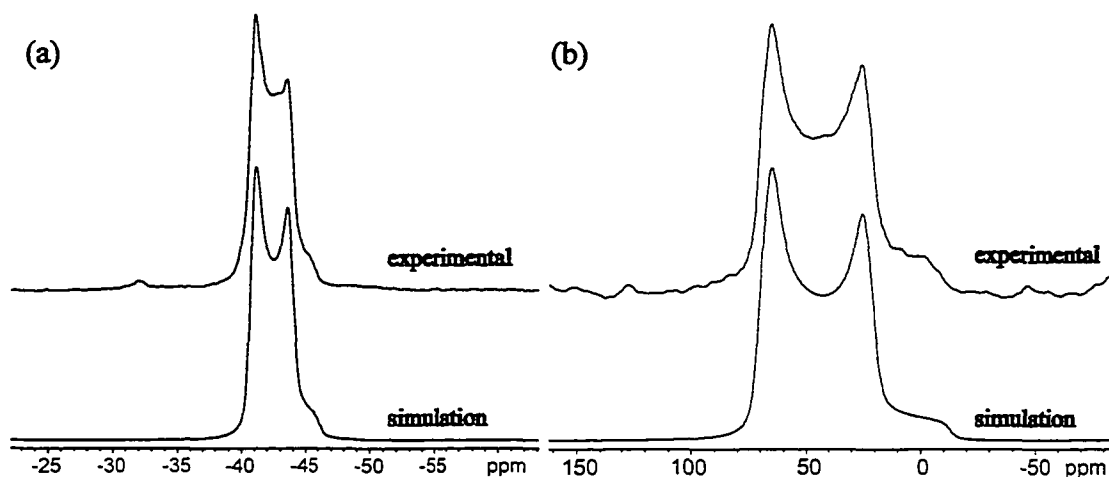


**Figure 2.3** Experimental and simulated  $^{11}\text{B}$  MAS NMR spectra at 8.46 T of (a)  $[\text{Cp}^*_2\text{B}][\text{AlCl}_4]$  at  $\nu_{\text{rot}} = 6000$  Hz and (b)  $\text{Cp}^*_2\text{BMe}$  at  $\nu_{\text{rot}} = 20000$  Hz.

The  $^{11}\text{B}$  MAS NMR spectra of  $\text{Cp}^*_2\text{B}^+$  and  $\text{Cp}^*_2\text{BMe}$  along with best-fit simulations are shown in Figure 2.3. The NMR parameters (Table 2.1) are obtained from comparison of simulations with complimentary MAS and static NMR spectra. A small distortion is visible in the  $^{11}\text{B}$  MAS NMR spectra of  $\text{Cp}^*_2\text{B}^+$ , which is identified as arising from impurities in the accompanying static spectra (*vide infra*).

**Table 2.1**  
Experimental Chemical Shielding and Quadrupolar Parameters  
Derived from Simulation of NMR Spectra

Parameter	$\text{Cp}^*_2\text{Al}^+$	$\text{Cp}^*_2\text{B}^+$	$\text{Cp}^*_2\text{BMe}$
nucleus	$^{27}\text{Al}$	$^{11}\text{B}$	$^{11}\text{B}$
$C_Q$ [MHz]	0.86(10)	1.14(1)	4.52(2)
$\eta_Q$	0	0.10(4)	0.11(1)
$\delta_{\text{iso}}$ [ppm]	-116.3(7)	-41.3(1)	81.9(1)
$\Omega$ [ppm]	83.0(30)	73.0(3)	146.1(3)
$\kappa$	0.88(3)	0.98(2)	0.75(4)
$\delta_{11}$ [ppm]	-87.0	-16.7	136.7
$\delta_{22}$ [ppm]	-92.0	-17.5	118.4
$\delta_{33}$ [ppm]	-170.0	-89.7	-9.4

Notably, as the coordination and local environment of the metal nuclei changes from  $\eta^5, \eta^5\text{-Cp}^*$  in  $\text{Cp}^*_2\text{Al}^+$  to  $\eta^1, \eta^5\text{-Cp}^*$  in  $\text{Cp}^*_2\text{B}^+$ , and finally to  $\eta^1, \eta^1\text{-Cp}^*$ , Me- in  $\text{Cp}^*_2\text{BMe}$ , there are two differences apparent in the NMR parameters: (i) substantial increase in  $C_Q$ 's, and (ii) considerable deshielding of the nuclei. Both  $C_Q$  and  $\delta_{\text{iso}}$  increase in the order  $\text{Cp}^*_2\text{Al}^+$ ,  $\text{Cp}^*_2\text{B}^+$  and  $\text{Cp}^*_2\text{BMe}$  ( $C_Q$ : 0.86  $\rightarrow$  1.14  $\rightarrow$  4.52 MHz;  $\delta_{\text{iso}}$ : -116.3  $\rightarrow$  -41.3  $\rightarrow$  81.9 ppm). The latter  $C_Q(^{11}\text{B})$  is comparable to that measured in trimesitylborane ( $C_Q(^{11}\text{B}) = 4.75$  MHz),<sup>[12]</sup> with which it is structurally similar.

The geometrical shape of the aluminumocenium cation can be visualized as a centro-symmetric dodecahedron which has twelve sides and twenty vertices (Figure 2.4), with the aluminum at the center and each of the 10  $\text{Cp}^*$  ring carbons superimposed on the two opposing sets of pentagonally arranged vertices. It has been demonstrated that there should be a null EFG at the center,  $S_0$ , of a centro-symmetric polyhedron, if  $V/2$  equal charges are distributed among  $V$  vertices in such a way that no two charges are related by

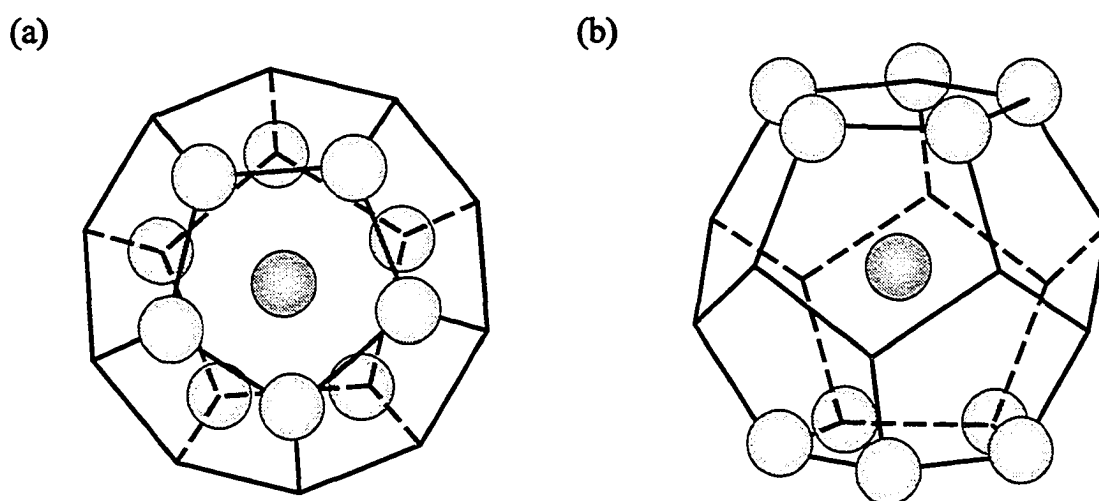


**Figure 2.4** (a) Top view and (b) side view of the superposition of  $\text{Cp}^*_2\text{Al}^+$  onto a centro-symmetric dodecahedron with Al at the center and carbon atoms located on 10 of the 20 vertices.

reflection through  $S_0$ .<sup>[37-39]</sup> The Cp\* carbon atoms of Cp\*<sub>2</sub>Al<sup>+</sup> do not fit perfectly onto the vertices of a centro-symmetric dodecahedron, accounting for the presence of a non-zero EFG at the aluminum nucleus. The combination of this arrangement of carbon atoms about the aluminum atom and rapid rotation of the Cp\* rings at ambient temperatures (which normally serve to reduce nuclear quadrupole coupling constants)<sup>[40]</sup> results in a very small aluminum nuclear quadrupole interaction. A similar model can also be used to rationalize the differences in nuclear quadrupolar coupling constants for [Cp\*<sub>2</sub>B][AlCl<sub>4</sub>] and Cp\*<sub>2</sub>BMe. In the case of Cp\*<sub>2</sub>B<sup>+</sup>, we can imagine the boron nucleus at the center of an icosahedron (i.e., 12 vertices, 20 faces), with the nearest neighbor carbons (i.e., five from the η<sup>5</sup>-Cp\* ring and one from the η<sup>1</sup>-Cp\* ring) approximately positioned on six of the twelve vertices. However, this is of course not exactly the case for this molecule, since (i) the η<sup>5</sup>-Cp\* ring carbons are not positioned *exactly* on the icosahedron vertices and possess different charges than the η<sup>1</sup>-coordinated Cp\* ring carbon, and (ii) the EFG at the boron is sensitive to the presence of second-coordination sphere atoms, such as methyl carbons, non-coordinated η<sup>1</sup>-ring carbons, protons, etc. Nonetheless, this pseudo-spherical symmetry likely accounts for the smaller quadrupolar interaction in Cp\*<sub>2</sub>B<sup>+</sup> compared to that in Cp\*<sub>2</sub>BMe. In the case of Cp\*<sub>2</sub>BMe, the boron C<sub>3</sub> skeletal geometry is trigonal planar; however, overall the molecular symmetry is C<sub>1</sub> and consequently the observed value of C<sub>Q</sub>(<sup>11</sup>B) is very large.

Of equal interest is the correlation between nuclear shielding and ligand coordination. The boron chemical shift range is typically quoted as being ca. +20 ppm to -130 ppm for four-coordinate boron compounds and ca. +100 ppm to -10 ppm for three-

coordinate boron.<sup>[14]</sup> The three-coordinate Cp\*<sub>2</sub>BMe has a boron chemical shift of 81.9 ppm, which agrees with the high chemical shift values of most three-coordinate organometallic boron complexes. In Cp\*<sub>2</sub>B<sup>+</sup>, the presence of one η<sup>5</sup>-Cp\* ring and one η<sup>1</sup>-Cp\* ring results in a large increase in nuclear shielding, with δ<sub>iso</sub>(<sup>11</sup>B) = -41.3 ppm. Such a change in shielding in the presence of the η<sup>5</sup>-Cp\* ring is not surprising, as a rough survey of solution NMR literature quickly shows that the majority of bis(η<sup>5</sup>-Cp) coordinated main group metals have unusually large negative isotropic chemical shifts. For instance, the magnesium chemical shifts normally range from 0 to 100 ppm (from reference compound MgSO<sub>4</sub>·7H<sub>2</sub>O to Et<sub>2</sub>Mg),<sup>[41]</sup> however, Cp<sub>2</sub>Mg has a chemical shift of -85.4 ppm.<sup>[42]</sup> Substitution of various Lewis bases at the Mg site, which cause bending of the metallocene structure, result in decreased nuclear shielding (i.e., higher chemical shifts).<sup>[43]</sup> Similar results have been observed for main group metallocenes such as the aluminumocenium cation, δ<sub>iso</sub>(<sup>27</sup>Al) = -114.5 ppm,<sup>[44]</sup> (standard shift range 0 to 300 ppm from Al(H<sub>2</sub>O)<sub>6</sub><sup>3+</sup>), stannocene, δ<sub>iso</sub>(<sup>119</sup>Sn) = -2199 ppm,<sup>[45]</sup> (organometallic tin complexes from -400 to 200 ppm; δ<sub>iso</sub>(SnMe<sub>4</sub>) = 0 ppm), and plumbocene, δ<sub>iso</sub>(<sup>207</sup>Pb) = -6150 ppm,<sup>[45]</sup> (organometallic lead complexes from -400 to +400 ppm; δ<sub>iso</sub>(PbMe<sub>4</sub>) = 0 ppm). A metal with a single η<sup>5</sup>-coordinated Cp' ring should have a chemical shift somewhere between the limits of three-coordinate planar and bis-η<sup>5</sup>-Cp' coordinated metallocenes, such as, the aluminum isotropic shift observed herein for Cp\*<sub>2</sub>Al<sup>+</sup> (-116.3 ppm).

One might suspect that if the <sup>27</sup>Al quadrupolar interaction is small for a molecule of this relatively high symmetry, that the degree of anisotropic chemical shielding must also be small. However, examination of the symmetry of Cp\*<sub>2</sub>Al<sup>+</sup> makes it evident that

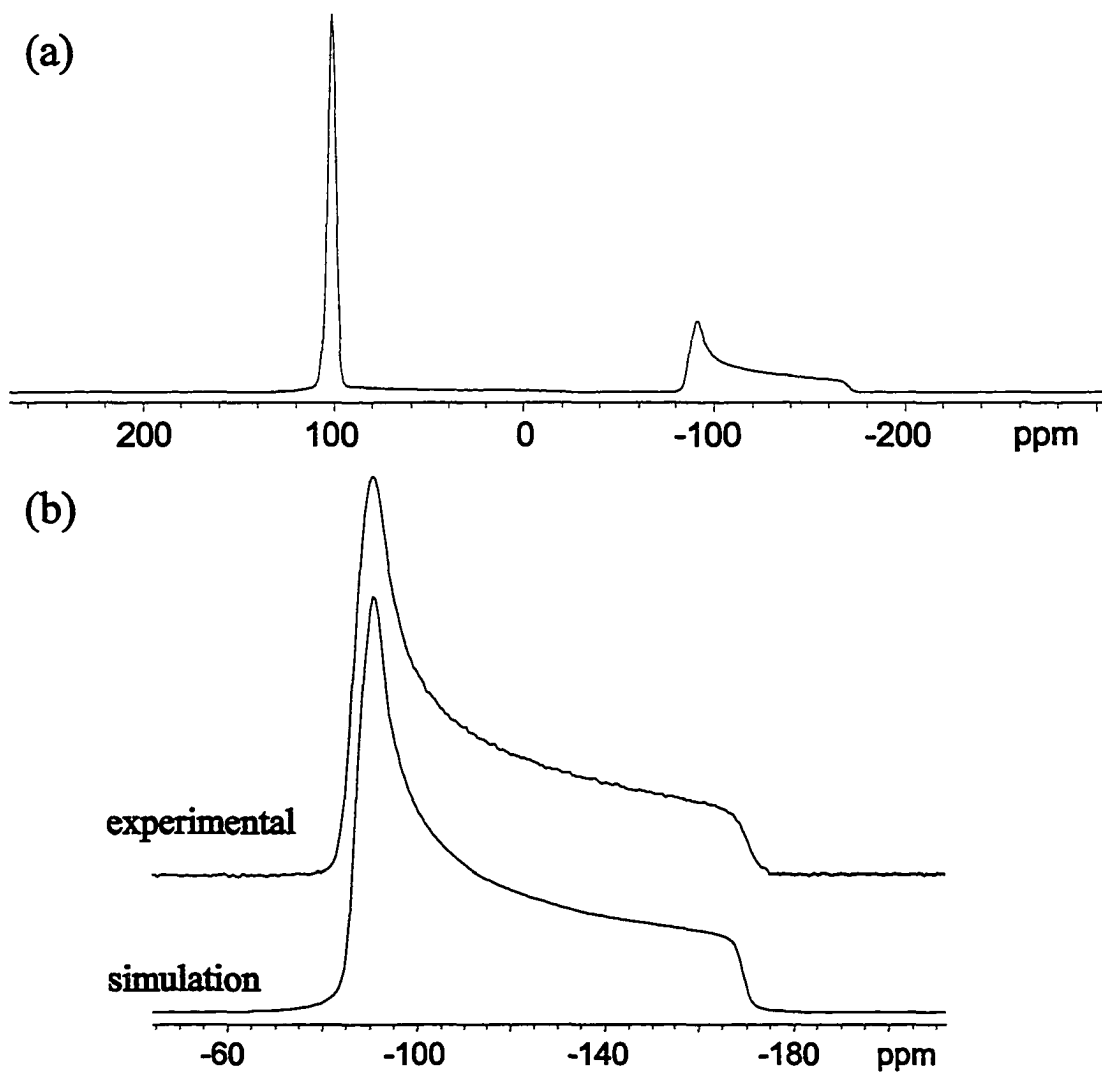


**Figure 2.5** (a) Static  $^{27}\text{Al}$  NMR spectrum of  $[\text{Cp}^*_2\text{Al}][\text{AlCl}_4]$ . (b) Expansion of the  $\text{Cp}^*_2\text{Al}^+$  CSA pattern with accompanying simulation.

the chemical shielding along the  $C_3$  axis of the molecule must be different from shielding perpendicular to this axis, and indeed, the aluminum CSA in the  $\text{Cp}^*_2\text{Al}^+$  cation is substantial. The static  $^{27}\text{Al}$  NMR spectrum (Figure 2.5a) reveals a classical CSA powder pattern for the  $\text{Cp}^*_2\text{Al}^+$  aluminum nuclei which spans approximately 83 ppm, as well as a relatively symmetric broad peak centered at ca. 101 ppm corresponding to the  $\text{AlCl}_4^-$  ions. Shielding patterns similar to that of the  $\text{Cp}^*_2\text{Al}^+$  cation are rarely observed for

quadrupolar nuclei with sizeable quadrupole moments, since static powder patterns are typically influenced by both anisotropic quadrupolar and chemical shielding interactions, as well as their relative orientation.<sup>[46,47]</sup> Spectral simulation of the Cp\*<sub>2</sub>Al<sup>+</sup> static pattern (Figure 2.5b) reveal an almost axially symmetric chemical shielding tensor ( $\delta_{\text{iso}} = -116.3$  ppm,  $\Omega = 83$  ppm and  $\kappa = 0.88$ ). This is the largest aluminum CSA measured by solid-state NMR to date. The static CSA pattern results from the overlap of two indistinguishable CSA patterns with very similar isotropic chemical shifts; consequently, two separate shielding tensors cannot be extracted by simulation of the static spectrum. The axial symmetry of the tensor can immediately be correlated to the high symmetry of the molecule: the most shielded principal component,  $\delta_{33}$ , is oriented along the C<sub>5</sub> axis of the molecule, while the other two components are oriented perpendicular to this axis.

Simulation of the static <sup>11</sup>B NMR spectra of [Cp\*<sub>2</sub>B][AlCl<sub>4</sub>] and Cp\*<sub>2</sub>BMe using only the quadrupolar parameters obtained from MAS NMR spectra indicate the presence of anisotropic chemical shielding (Figure 2.6, bottom traces). The boron CS tensor in Cp\*<sub>2</sub>B<sup>+</sup> derived from simulation can be described by the parameters:  $\delta_{\text{iso}} = -41.3$  ppm,  $\Omega = 73.0$  ppm and  $\kappa = 0.98$  (Figure 2.6a). A small “hump” in the spectrum is visible at approximately -40 ppm, which results from an impurity with a relatively sharp resonance, and constitutes < 1% of the total integrated signal (included in the simulated spectra). Similarly, a larger boron chemical shielding anisotropy is observed in the static <sup>11</sup>B NMR spectra of Cp\*<sub>2</sub>BMe (Fig. 2.6b;  $\delta_{\text{iso}} = 81.9$  ppm,  $\Omega = 146.0$  ppm and  $\kappa = 0.75$ ). The magnitude of chemical shielding anisotropy, described by the span, is comparable to that



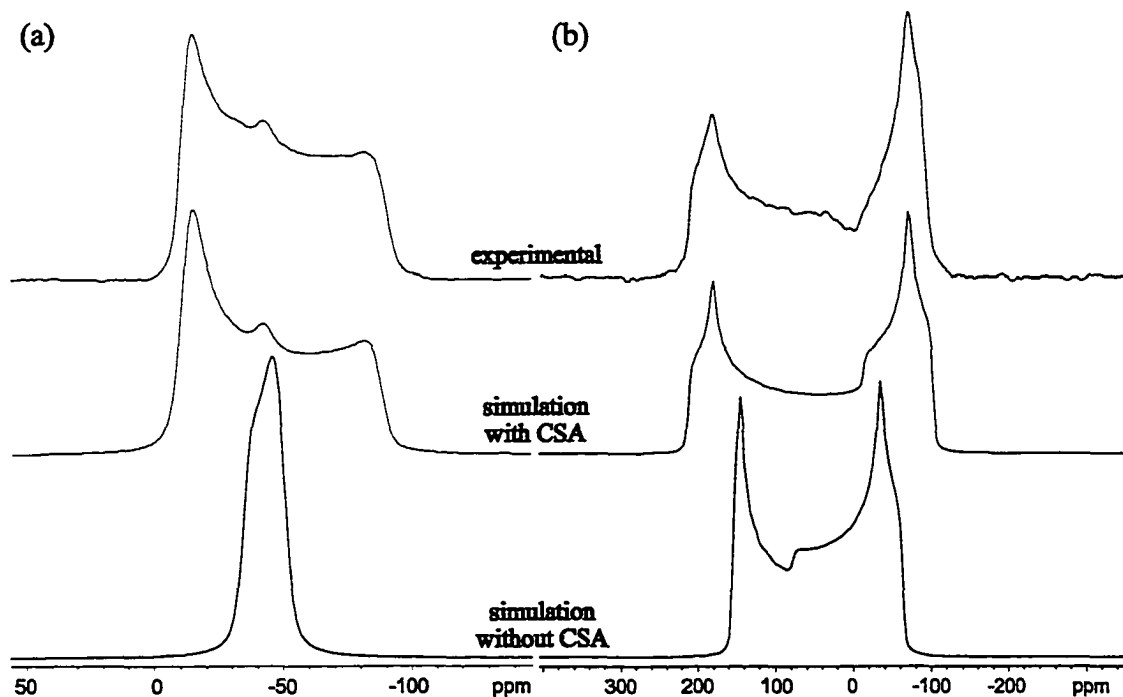


**Figure 2.6** Experimental and simulated static  $^{11}\text{B}$  NMR spectra at 8.46 T of (a)  $\text{Cp}^*_2\text{B}^+$  and (b)  $\text{Cp}^*_2\text{BMe}$ . Simulations with and without the effects of boron chemical shielding anisotropy are included for comparison.

previously reported for trimesitylborane ( $\Omega = 121$  ppm),<sup>[12]</sup> and represents the largest boron CSA measured by solid state NMR to date. The origin of the anisotropic boron shielding in these molecules is further investigated using computational methods discussed in the next section of this chapter.

Experimental and best-fit numerical simulations of  $^{11}\text{B}$  MAS NMR spectra for  $\text{Cp}^*_2\text{B}^+$  ( $\nu_{\text{rot}} = 6000$  Hz) and  $\text{Cp}^*_2\text{BMe}$  ( $\nu_{\text{rot}} = 20000$  Hz) are shown in Figure 2.7. Numerically simulated MAS spectra using the quadrupolar and chemical shielding parameters from time-independent analytical simulations are in good agreement with experimental data. The presence of CSA at the boron center in  $\text{Cp}^*_2\text{B}^+$  can easily be confirmed by the dramatic disappearance of spinning sidebands upon neglect of anisotropic shielding contributions to the powder pattern. A small satellite peak arising

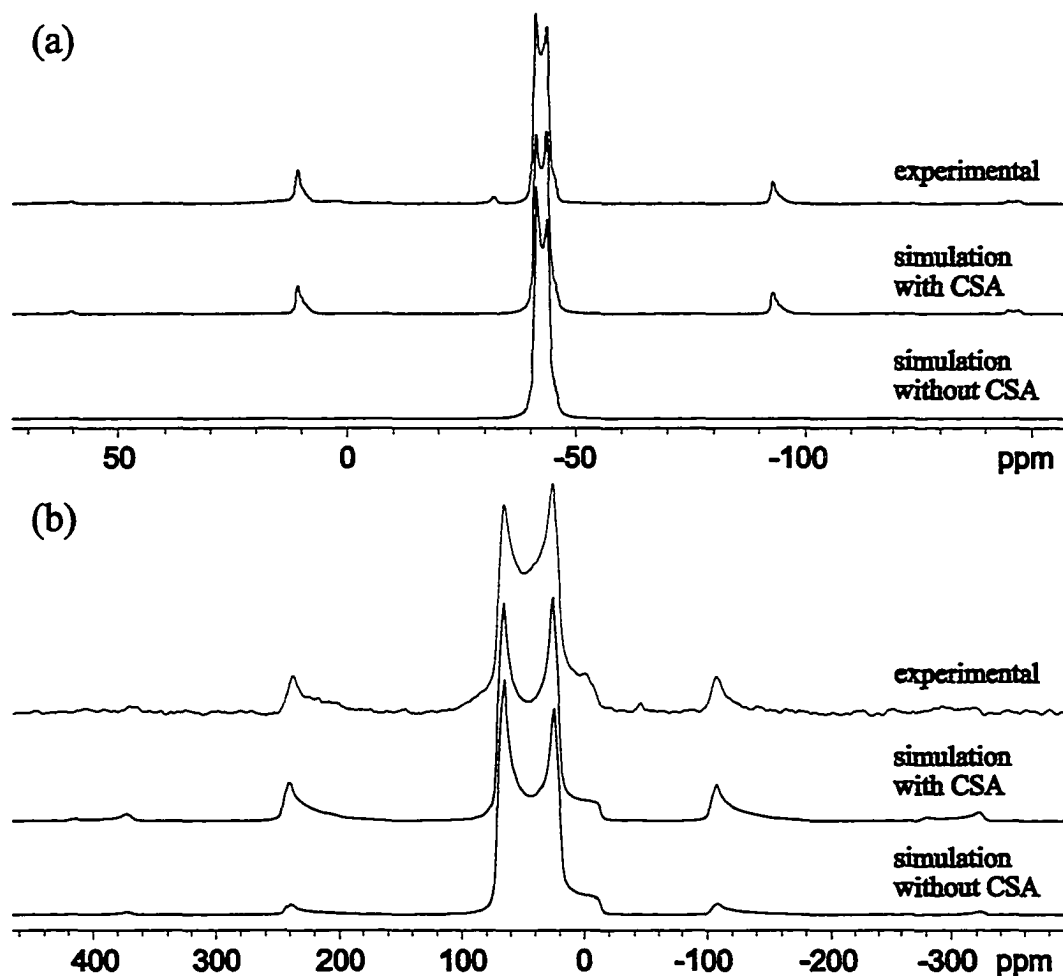


**Figure 2.7** Experimental and numerical simulations of  $^{11}\text{B}$  MAS NMR spectra of (a)  $\text{Cp}^*_2\text{B}^+$  and (b)  $\text{Cp}^*_2\text{BMe}$ .

from the  $\pm 3/2 \rightarrow \pm 1/2$  satellite transitions is observed slightly to the left of the isotropic resonance of the central transition MAS spectrum. The spinning sidebands in the  $^{11}\text{B}$  MAS NMR spectrum of  $\text{Cp}^*_2\text{BMe}$  do not disappear completely, but are much reduced in intensity in the absence of boron chemical shielding anisotropy.

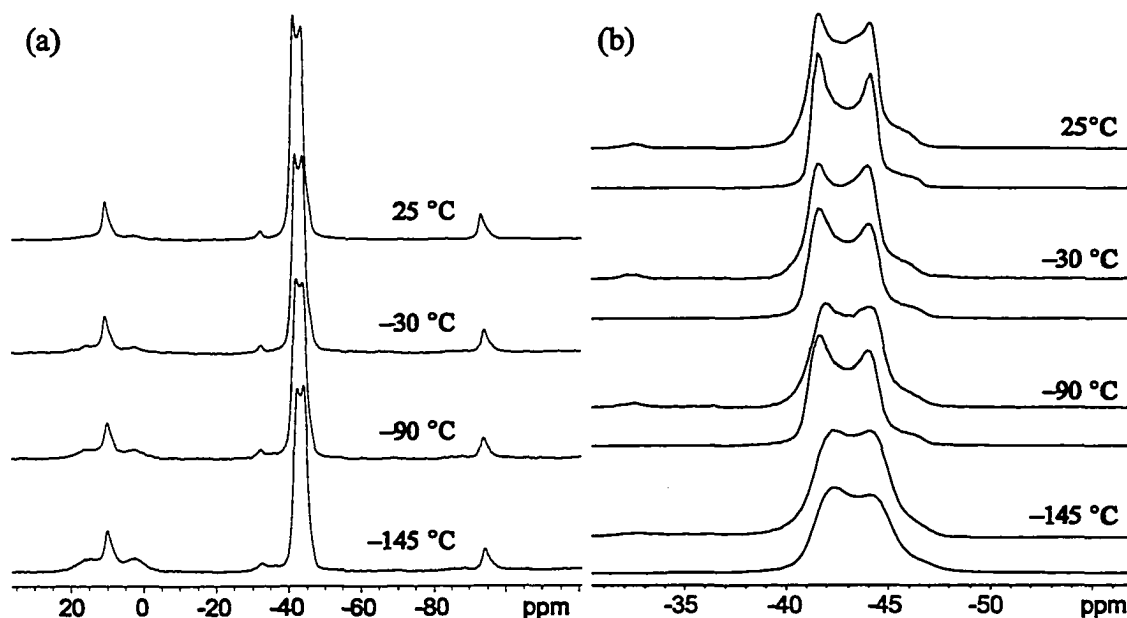


**Figure 2.8**  $^{11}\text{B}$  VT MAS NMR spectra of  $\text{Cp}^*_2\text{B}^+$  at 8.46 T. (a) Full spectral width. (b) Expanded isotropic resonances with corresponding simulations shown as the lower traces for each temperature.

### 2.3.1.1 Variable-Temperature $^{11}\text{B}$ MAS NMR

Lowering the temperature from 25 °C to -145 °C leads to very subtle changes in the  $^{11}\text{B}$  MAS NMR spectra of  $\text{Cp}^*_2\text{B}^+$  (Figure 2.8). Typically, the slowing molecular motions resulting from temperature decreases are associated with increases in  $C_Q$ .  $^{11}\text{B}$  VT NMR spectra indicate that upon lowering the temperature, only a negligible increase from about 1.14 MHz to 1.17 MHz is observed. A similarly subtle yet noticeable change in  $\eta_Q$  (0.10  $\rightarrow$  0.24) is also seen. The isotropic chemical shift ( $\delta_{\text{iso}}$ ) appears to correlate with temperature in a linear fashion:  $\delta_{\text{iso}}$  increases (-41.3 - -40.4 - -40.6 - -40.8 ppm) as temperature decreases (25 - -30 - -90 - -145 °C). These experimental results are in qualitative agreement with theoretical predictions of a low rotational barrier and the general insensitivity of the anisotropic NMR interactions in  $\text{Cp}^*_2\text{B}^+$  to different rotational conformations of the  $\eta^5\text{-Cp}^*$  ring.

### 2.3.2 Solid-State $^{13}\text{C}$ NMR

Examination of the  $^{13}\text{C}$  CP/MAS NMR spectra for  $\text{Cp}^*_2\text{Al}^+$  (Figure 2.9a) reveals two types of carbon sites: the  $\text{Cp}^*$  ring carbons at 118.7 ppm and the  $\text{Cp}^*$  methyl carbons at 10.4 ppm. Sharp isotropic resonances and spinning sidebands imply magnetic

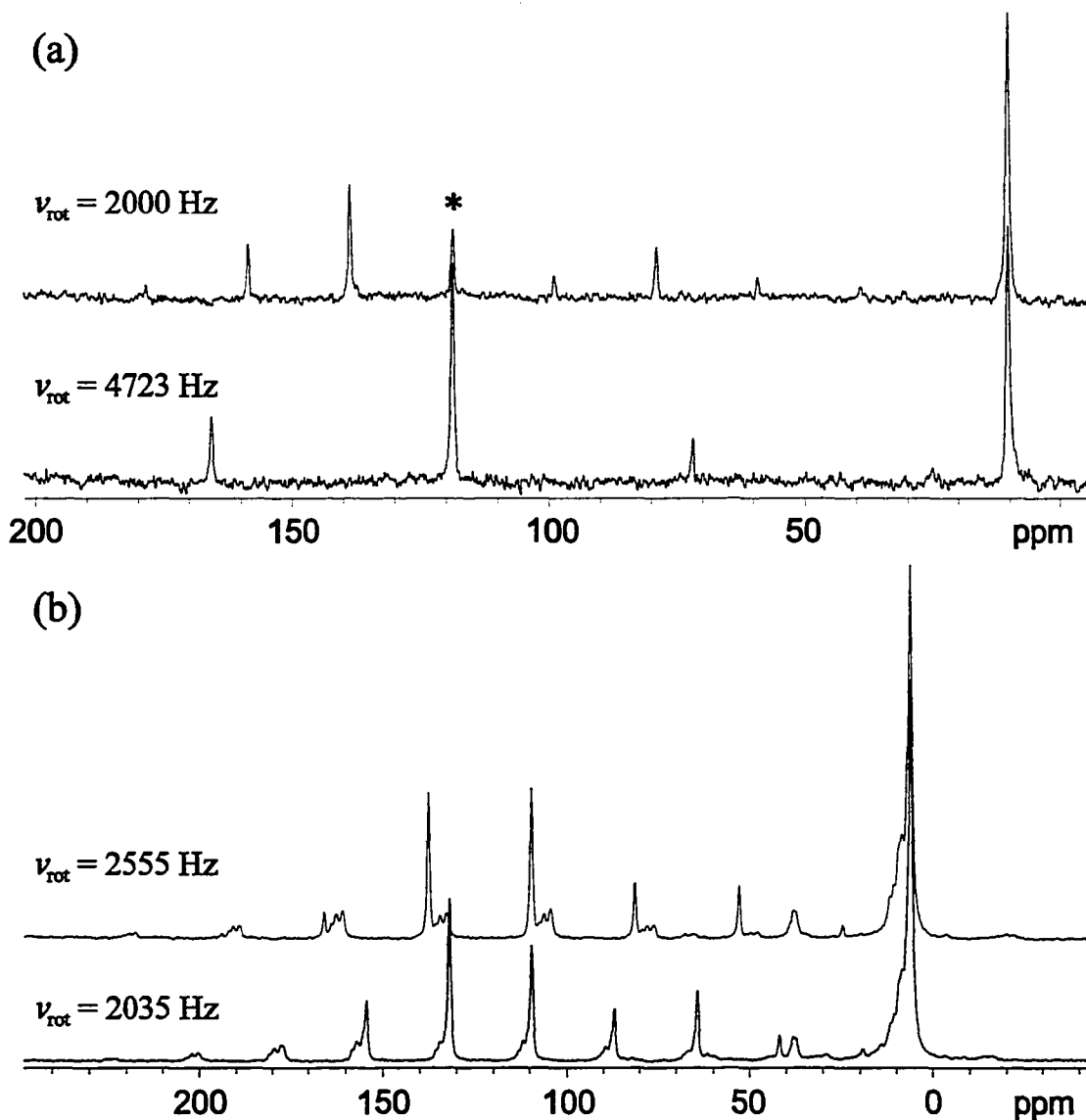


**Figure 2.9**  $^{13}\text{C}$  CP/MAS NMR spectra of (a)  $[\text{Cp}^*_2\text{Al}][\text{AlCl}_4]$  at 9.4 T and (b)  $[\text{Cp}^*_2\text{B}][\text{AlCl}_4]$  at 8.46 T at different spinning frequencies. Asterisk denotes the isotropic signal for the  $\text{Cp}^*$  ring carbons in  $\text{Cp}^*_2\text{Al}^+$ .

equivalence of all of the carbon sites, which is only possible if dynamic exchange of carbon sites is occurring as the result of ring motion. The Cp\* aromatic carbons are observed to have a significant carbon chemical shielding anisotropy with axial CS tensors described by  $\Omega = 108$  ppm and  $\kappa = 1.0$ . These values are comparable to  $^{13}\text{C}$  chemical shielding tensors that were previously measured in  $\text{Cp}_2\text{Mg}$  and related complexes.<sup>[48-50]</sup> The axial symmetry of the CS tensor is believed to arise from rapid rotation of the Cp\* rings – this aspect of ring dynamics is further discussed in the theoretical section of this chapter.

$^{13}\text{C}$  CP/MAS experiments were conducted on  $\text{Cp}^*_2\text{B}^+$  (Figure 2.9b) in order to determine carbon CS tensors. The  $\eta^5\text{-Cp}^*$  ring is rapidly rotating, so that only one resonance is observed for each of the Cp\* ring and methyl carbons, at 109.3 ppm and 5.8 ppm, respectively. All of the  $\eta^1\text{-Cp}^*$  ring carbon sites are resolved as well, with chemical shifts in close agreement to those observed in solution.<sup>[1]</sup> Ambient temperature  $^{13}\text{C}$  CP/MAS experiments with variable contact times ranging from 3 to 15 ms showed little variation in cross polarization efficiency. A number of spinning sidebands are observed for the  $\eta^5\text{-Cp}^*$  ring carbons as well as for the  $\alpha$ - and  $\beta$ -carbons in the  $\eta^1\text{-Cp}^*$  ring, which are due to chemical shielding anisotropy; Table 2.2 lists results from Herzfeld-Berger analysis.<sup>[20, 21]</sup> For the  $\eta^5\text{-Cp}^*$  ring, results are comparable to CS tensors reported for other  $\text{Cp}'_2\text{M}$  systems,<sup>[48-50]</sup> with principal components  $\delta_{11} = 157$  ppm,  $\delta_{22} = 140$  ppm,  $\delta_{33} = 32$  ppm. Chemical shielding parameters for the  $\alpha$ - and  $\beta$ -carbons on the  $\eta^1\text{-Cp}^*$  ring are similar, the main difference being a decrease in  $\delta_{11}$  of about 67 ppm which increases the span of the chemical shielding tensor to  $\Omega = 181$  ppm and 186 ppm, respectively. These

parameters correspond closely with previously measured carbon shielding tensors for the  $\eta^1$ -rings in tetrakis(cyclopentadienyl)titanium.<sup>[51]</sup>

**Table 2.2**  
Experimental  $^{13}\text{C}$  Chemical Shielding Tensors in  $\text{Cp}^*_2\text{B}^+$

Site	$\delta_{11}$ [ppm]	$\delta_{22}$ [ppm]	$\delta_{33}$ [ppm]	$\delta_{\text{iso}}$ [ppm]	$\Omega$ [ppm]	$\kappa$
$\eta^5$ : $\text{C}_5(\underline{\text{C}}\text{H}_3)_5$	—	—	—	5.9	—	—
$\eta^5$ : $\underline{\text{C}}_5(\text{CH}_3)_5$	157	140	32	109.3	124	0.73
$\eta^1$ : $i$ - $\underline{\text{C}}_5(\text{CH}_3)_5$	—	—	—	37.7	—	—
$\eta^1$ : $\alpha$ - $\underline{\text{C}}_5(\text{CH}_3)_5$	224	135	43	134.2	181	0
$\eta^1$ : $\beta$ - $\underline{\text{C}}_5(\text{CH}_3)_5$	224	144	38	135.5	186	0.14

### 2.3.2.1 $^{13}\text{C}/^{11}\text{B}/^1\text{H}$ TRAPDOR NMR of $\text{Cp}^*_2\text{B}^+$

$^{13}\text{C}/^{11}\text{B}/^1\text{H}$  CP/TRAPDOR MAS NMR spectra and control spectra (i.e., standard  $^{13}\text{C}$  CP/MAS NMR spectra) of  $\text{Cp}^*_2\text{B}^+$  acquired at 25 °C and -150 °C are shown in Figure 2.10. Not only are TRAPDOR effects visible at both temperatures, there is also considerable variation in the efficiency of cross polarization. In the room-temperature control spectrum, CP is efficient to both the aromatic and methyl  $^{13}\text{C}$  nuclei of the  $\text{Cp}^*$  rings. Upon irradiating on the  $^{11}\text{B}$  channel using the TRAPDOR sequence, all of the aromatic  $^{13}\text{C}$  signals disappear almost completely, while the  $^{13}\text{C}$  methyl signals remain relatively unchanged. This is indicative of relatively strong dipolar coupling between the  $^{11}\text{B}$  and aromatic  $^{13}\text{C}$  nuclei in both  $\text{Cp}^*$  rings, even in light of the rapid rotation of the  $\eta^5$ - $\text{Cp}^*$  ring and the large inter-nuclear distances between boron and ortho- and meta- (or  $\alpha$ - and  $\beta$ -) carbons in the  $\eta^1$ - $\text{Cp}^*$  ring. Dipolar coupling constants may easily be calculated from the crystal structure of the  $\text{Cp}^*_2\text{B}^+$  cation, and scale as the inverse cube of the inter-

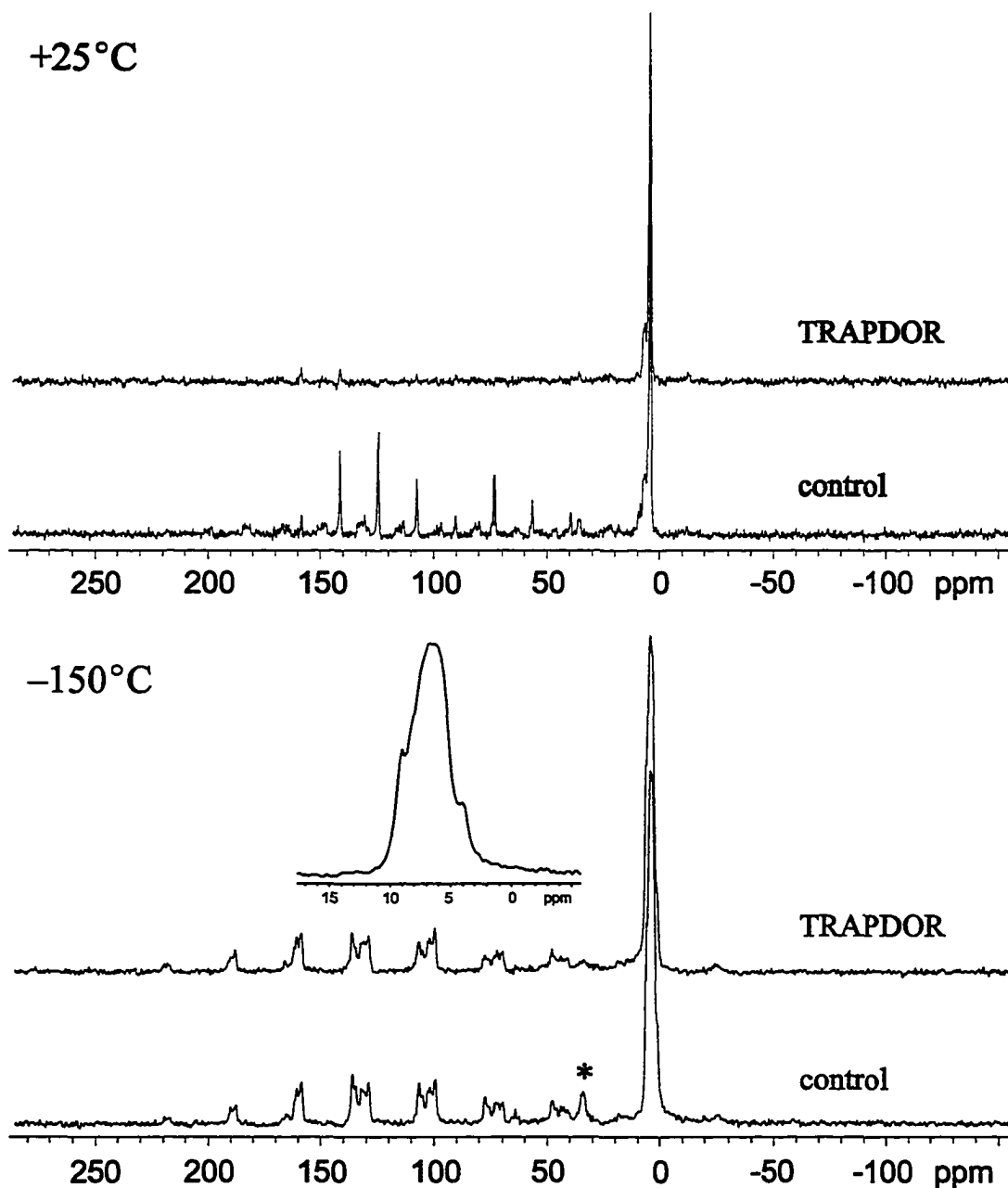


**Figure 2.10**  $^{13}\text{C}/^{11}\text{B}/^1\text{H}$  CP/MAS TRAPDOR and control CP/MAS NMR spectra of  $[\text{Cp}^*_2\text{B}][\text{AlCl}_4]$  at  $+25\text{ }^\circ\text{C}$  and  $-150\text{ }^\circ\text{C}$ . Inset of spectrum acquired at  $-150\text{ }^\circ\text{C}$  shows detail of individual methyl carbon sites on the  $\eta^1\text{-Cp}^*$  ring.

nuclear distance. The dipolar coupling constant between the  $\eta^5\text{-Cp}^*$  ring carbons and boron is quite large ( $R_{\text{DD}}(^{11}\text{B}, ^{13}\text{C}) = 1760\text{ Hz}$ ), as is the boron–“*ipso*”-carbon ( $R_{\text{DD}}(^{11}\text{B}, ^{13}\text{C}) = 2430\text{ Hz}$ ) coupling.  $^{11}\text{B}$ – $^{13}\text{C}$  dipolar coupling constants range from 250 – 650 Hz for

the remainder of the  $^{13}\text{C}$  nuclei in the molecule. At  $-150\text{ }^{\circ}\text{C}$ , with various spinning speeds and contact times, cross polarization to the  $\eta^5\text{-Cp}^*$  aromatic and methyl carbons drops substantially (though peaks can still be distinguished), and the  $\eta^1\text{-Cp}^*$  carbon sites can be seen clearly. Notably, much definition can be seen in the methyl group region (see inset, Figure 2.10). The only clearly discernible difference in the CP/TRAPDOR spectrum at  $-150\text{ }^{\circ}\text{C}$  is at the *ipso*-carbon ( $\delta_{\text{iso}} = 37.0\text{ ppm}$ , marked with an asterisk), indicating that it is the only carbon nucleus still strongly dipolar coupled to boron. Closer examination reveals that there is a 25 – 40% decrease in signal intensity for the  $\eta^5\text{-Cp}^*$  aromatic carbons, much less than observed at room temperature (though this is difficult to strictly quantify due to the reduction in CP efficiency). Signal intensity decrease is not observed for the remaining carbon sites in the  $-150\text{ }^{\circ}\text{C}$  TRAPDOR spectra.

This set of results initially seems to be counterintuitive, as stronger dipolar couplings between  $^{11}\text{B}$  and  $^{13}\text{C}$  are expected at lower temperatures as the  $\eta^5\text{-Cp}^*$  ring motion slows down, perhaps leading to a stronger TRAPDOR effect. In addition, variable contact time CP/MAS experiments at various spinning speeds fail to improve the CP efficiency to the  $\eta^5\text{-Cp}^*$  carbons at low temperatures. However, the TRAPDOR results do suggest that a sigmatropic exchange mechanism is occurring for the  $\eta^1\text{-Cp}^*$  ring at ambient temperatures. The exchange process involves “jump-like” rotation of the  $\eta^1\text{-Cp}^*$  ring such that each of the aromatic  $\eta^1\text{-Cp}^*$  carbons spends a finite amount of time (shorter than the time scale of the TRAPDOR experiment) proximate to the boron nucleus. As a consequence, a very large TRAPDOR effect is experienced by all of the aromatic  $\eta^1\text{-Cp}^*$  carbon nuclei, since  $^{11}\text{B}$  and  $^{13}\text{C}$  will be dipolar coupled for a finite



amount of time. At lower temperatures, the exchange rate is slower than the timescale of the TRAPDOR experiment (irradiation occurs over a single 100  $\mu\text{s}$  rotor period), and thus only the directly bound aromatic *i*-carbon nucleus experiences the TRAPDOR effect, while no intensity loss is observed for the remainder of the carbon sites in the  $\eta^1\text{-Cp}^*$  ring. This preliminary interpretation of NMR data and chemical exchange is consistent with the concept of a reorienting  $\eta^1\text{-Cp}^*$  ring (perhaps passing through an  $\eta^2\text{-Cp}^*$  transition state).<sup>[51]</sup> Such sigmatropic rearrangements have been previously studied by  $^1\text{H}$  wide-line and  $^{13}\text{C}$  CP/MAS NMR experiments in a number of  $\eta^1\text{-Cp}$  containing transition metal metallocenes such as  $(\eta^5\text{-Cp})_2\text{Ti}(\eta^1\text{-Cp})_2$ ,<sup>[51]</sup>  $\text{CpHgX}$  ( $\text{X} = \text{Cl, Br, I}$ ) and  $\text{Cp}_2\text{Fe}(\text{CO})_2$ .<sup>[52]</sup> Double- and triple-resonance NMR experiments of this nature seem very promising for examining such intra-molecular motions.

### 2.3.3 Theoretical Study of $^{27}\text{Al}$ and $^{11}\text{B}$ EFG and Chemical Shielding Tensors

Calculations of the  $^{27}\text{Al}$  EFG tensor in the isolated  $D_{5d}$   $\text{Cp}^*_2\text{Al}^+$  cation are summarized at the top of Table 2.3. There is not very good agreement between the experimentally determined values of  $C_Q(^{27}\text{Al})$  and computed results. RHF calculations seem to approach the experimental value of  $C_Q$  as the basis set increases in size, whereas the B3LYP calculations consistently overestimate  $C_Q$ . In all cases, an axially symmetric EFG tensor is predicted, in good agreement with our experimental results.

**Table 2.3**  
Experimental and Theoretical Quadrupolar Parameters

Source	$V_{11}$ [a.u.]	$V_{22}$ [a.u.]	$V_{33}$ [a.u.]	$ C_Q $ [MHz]	$\eta_Q$
<b>Cp*<sub>2</sub>Al<sup>+</sup></b>					
<b>Experimental<sup>[a]</sup></b>	0.0130	0.0130	-0.0261	0.86(10)	0
<b><i>D</i><sub>sd</sub> - staggered</b>					
RHF					
6-31G**	-0.0058	-0.0058	0.0117	0.38	0.0
6-311G**	0.0106	0.0106	-0.0213	0.70	0.0
DFT(B3LYP)					
6-31G**	0.0220	0.0220	-0.0439	1.44	0.0
6-311G**	0.0229	0.0229	-0.0458	1.51	0.0
<b><i>D</i><sub>sh</sub> - eclipsed</b>					
RHF					
6-31G**	-0.0032	-0.0032	0.0065	0.21	0.0
6-311G**	0.0092	0.0092	-0.0184	0.61	0.0
DFT(B3LYP)					
6-31G**	0.0269	0.0269	-0.0537	1.77	0.0
6-311G**	0.0292	0.0292	-0.0583	1.92	0.0
-----					
<b>Cp*<sub>2</sub>B<sup>+</sup></b>					
<b>Experimental</b>	-0.0532	-0.0651	0.1183	1.14(1)	0.10(4)
RHF					
6-31G**	-0.0720	-0.0794	0.1514	1.46	0.05
6-311G**	-0.0752	-0.0826	0.1578	1.52	0.05
6-311+G**	-0.0749	-0.0826	0.1575	1.52	0.05
DFT(B3LYP)					
6-31G**	-0.0622	-0.0665	0.1287	1.24	0.03
6-311G**	-0.0664	-0.0714	0.1378	1.33	0.04
6-311+G**	-0.0660	-0.0710	0.1370	1.32	0.04
-----					
<b>Cp*<sub>2</sub>BMe</b>					
<b>Experimental</b>	0.2088	0.2604	-0.4692	4.52(2)	0.11(1)
RHF					
6-31G**	0.2502	0.2896	-0.5399	5.20	0.07
6-311G**	0.2590	0.3035	-0.5625	5.42	0.08
6-311+G**	0.2590	0.3038	-0.5628	5.42	0.08

**Table 2.3 (cont.)**

Source	$V_{11}$ [a.u.]	$V_{22}$ [a.u.]	$V_{33}$ [a.u.]	$ C_Q $ [MHz]	$\eta_Q$
DFT(B3LYP)					
6-31G**	0.2235	0.2671	-0.4906	4.73	0.09
6-311G**	0.2403	0.2974	-0.5377	5.18	0.11
6-311+G**	0.2400	0.2974	-0.5374	5.18	0.11

<sup>[a]</sup> The sign (+/-) and significant figures of experimental EFG tensor components ( $V_{11}$ ,  $V_{22}$  and  $V_{33}$ ) are set according to most proximate theoretical values for comparison.

Calculations of the  $^{11}\text{B}$  EFG tensors for an isolated  $\text{Cp}^*_2\text{B}^+$  cation and an isolated  $\text{Cp}^*_2\text{BMe}$  molecule are also shown and compared with experimental data in Table 2.3. The values of  $C_Q(^{11}\text{B})$  are overestimated by both methods, but EFG tensors with almost axial symmetry ( $\eta_Q = 0.03$  to  $0.11$ ) are predicted for both molecules, in close agreement with experimental results. The B3LYP calculations are closer to the experimental results than RHF calculations, and as the basis set size is increased, the  $C_Q(^{11}\text{B})$  moves further away from the experimental value. The discrepancy between experimentally determined and theoretically calculated quadrupolar parameters likely arise from the fact that intramolecular motions are not taken into account, although it is possible that there are some contributions to the EFG tensor from distant point charges in the solid lattice. The overestimation of the  $C_Q(^{11}\text{B})$  is therefore not surprising, as rapid molecular motion is most often observed to significantly decrease the magnitude of nuclear quadrupole coupling constants, due to averaging of atomic positions within the molecule or ionic solid.<sup>[40]</sup> Calculations predict that the  $C_Q(^{11}\text{B})$  in  $\text{Cp}^*_2\text{BMe}$  is ca. 3.9 MHz larger than that in  $\text{Cp}^*_2\text{B}^+$ , in reasonable agreement with experimental results (3.38 MHz difference).

Experimental and theoretical aluminum CS tensors in  $\text{Cp}^*_2\text{Al}^+$  are compared in Table 2.4. Both RHF and B3LYP calculations on the  $D_{3d}$   $\text{Cp}^*_2\text{Al}^+$  cation correspond very

closely with experimental results, with the RHF calculations slightly underestimating  $\Omega$ , and calculations with the larger 6-311G\*\* basis set overestimating the isotropic chemical shift. In all cases, an axially symmetric shielding tensor is predicted (i.e.,  $\kappa = 1.0$ , so  $\delta_{11} = \delta_{22}$  and  $\delta_{33}$  is the unique component). Interestingly, calculations on the  $D_{5h}$  Cp\*<sub>2</sub>Al<sup>+</sup> cation, in which the Cp\* rings are eclipsed, indicate that the span of the aluminum CS tensor decreases (by ca. 25 – 30 ppm) in this rotational conformation. This suggests that at room temperature, if the barrier to rotation for the Cp\* rings is small enough, we may be observing an average aluminum chemical shielding tensor.

**Table 2.4**  
Experimental and Theoretical Aluminum Chemical Shielding Tensors in Cp\*<sub>2</sub>Al<sup>+</sup>

	$\delta_{11}$ [ppm]	$\delta_{22}$ [ppm]	$\delta_{33}$ [ppm]	$\delta_{iso}$ [ppm]	$\Omega$ [ppm]	$\kappa$
<b>Experimental</b>	-87(1)	-92(1)	-170(1)	-116.3(7)	83(3)	0.88(3)
<b><math>D_{5d}</math> - staggered</b>						
RHF/6-31G**	-86.52	-86.52	-157.85	-110.30	71.33	1.00
RHF/6-311G**	-102.06	-102.06	-172.49	-125.54	70.44	1.00
B3LYP/6-31G**	-74.60	-74.95	-156.11	-101.89	81.50	0.99
B3LYP/6-311G**	-93.46	-93.66	-180.33	-122.48	86.87	1.00
<b><math>D_{5h}</math> - eclipsed</b>						
RHF/6-31G**	-105.26	-105.26	-150.92	-120.48	45.66	1.00
RHF/6-311G**	-119.68	-119.68	-168.50	-135.96	48.82	1.00
B3LYP/6-31G**	-95.74	-96.41	-144.01	-112.05	48.27	0.97
B3LYP/6-311G**	-113.87	-114.12	-171.65	-133.21	57.78	0.99

There is remarkably good agreement between experimental boron CS tensors and those calculated by both RHF and B3LYP methods (Table 2.5). All chemical shielding tensor values have been converted to the boron chemical shift scale (see section 2.2.4) for ease of comparison with experimental results. For Cp\*<sub>2</sub>B<sup>+</sup>,  $\delta_{iso}$  and  $\Omega$  are predicted

satisfactorily, and the experimental and theoretical skews match almost identically. RHF calculations overestimate the nuclear magnetic shielding in the directions of  $\delta_{11}$  and  $\delta_{33}$ , while B3LYP calculations underestimate the nuclear shielding along  $\delta_{11}$ . In the case of  $\text{Cp}^*_2\text{BMe}$ , RHF calculations seem slightly better than B3LYP methods in predicting experimental values. Notably, there is excellent agreement between experimental and RHF boron isotropic shifts and spans.

**Table 2.5**  
Experimental and Theoretical Boron Chemical Shielding Tensors  
in  $\text{Cp}^*_2\text{B}^+$  and  $\text{Cp}^*_2\text{BMe}$

Source	$\delta_{11}$ [ppm]	$\delta_{22}$ [ppm]	$\delta_{33}$ [ppm]	$\delta_{\text{iso}}$ [ppm]	$\Omega$ [ppm]	$\kappa$
$\text{Cp}^*_2\text{B}^+$						
<b>Experimental</b>	-16.7	-17.5	-89.7	-41.3(1)	73.0(3)	0.98(2)
RHF						
6-31G**	-22.0	-24.8	-101.9	-49.6	79.9	0.93
6-311G**	-22.1	-24.4	-103.4	-50.0	81.3	0.94
6-311+G**	-20.5	-23.1	-102.0	-48.5	81.4	0.94
B3LYP						
6-31G**	-10.5	-14.5	-89.8	-38.3	79.3	0.90
6-311G**	-10.7	-14.0	-93.0	-39.2	82.3	0.92
6-311+G**	-8.6	-11.5	-89.7	-36.6	81.1	0.93
$\text{Cp}^*_2\text{BMe}$						
<b>Experimental</b>	136.7	118.4	-9.4	81.9(1)	146.1(3)	0.75(4)
RHF						
6-31G**	130.9	100.0	-12.7	72.8	143.6	0.57
6-311G**	140.4	107.9	-10.6	79.3	151.0	0.57
6-311+G**	141.8	109.5	-9.3	80.7	151.1	0.57
B3LYP						
6-31G**	143.8	108.9	-5.2	82.5	149.0	0.53
6-311G**	161.6	122.6	-2.3	93.9	163.9	0.53
6-311+G**	164.9	124.4	-0.1	96.4	164.9	0.51

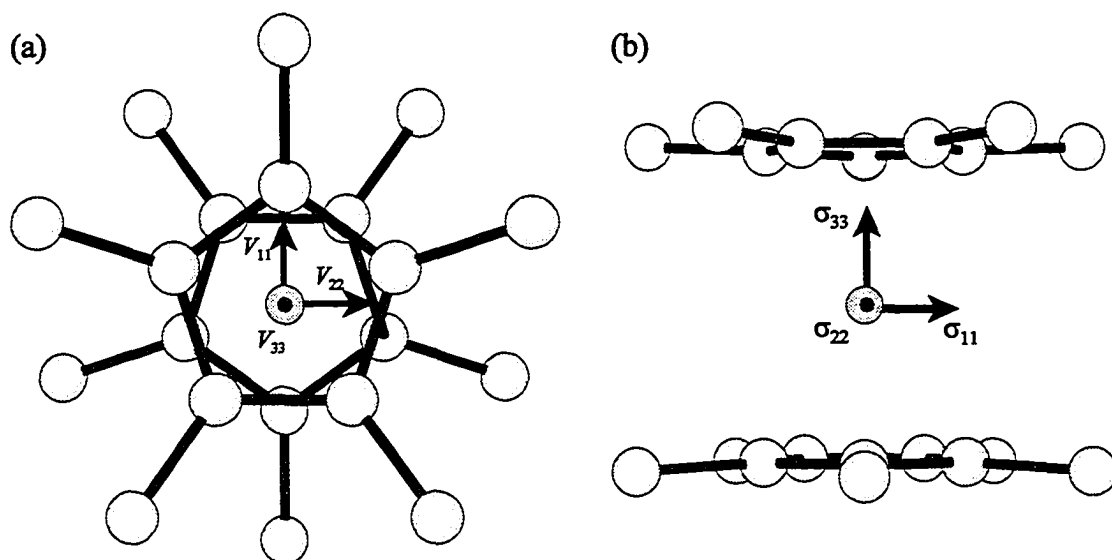


**Figure 2.11** Orientation of the (a) electric field gradient and (b) chemical shielding tensors in  $\text{Cp}^*_2\text{Al}^+$ , as determined by RHF calculations with the 6-31G\*\* basis set. Hydrogen atoms are omitted for clarity.

The EFG tensor orientation of  $\text{Cp}^*_2\text{Al}^+$  is pictured in Figure 2.11 a, with the largest, distinct component of the EFG ( $V_{33}$ ) along the  $C_5$  symmetry axis. The lack of accuracy of theoretical values may stem from the reason discussed earlier, with the largest discrepancies perhaps arising from motion of  $\text{Cp}^*$  rings. The orientation of the aluminum CS tensor is similar to that of the EFG tensor, with the most shielded component,  $\sigma_{33}$ , oriented along the  $C_5$  symmetry axis of the molecule (Figure 2.11 b).

The EFG tensor orientations in  $\text{Cp}^*_2\text{B}^+$  and  $\text{Cp}^*_2\text{BMe}$  are pictured in Figure 2.12a. In  $\text{Cp}^*_2\text{B}^+$ , the largest component of the EFG tensor ( $V_{33}$ ) is coincident with the  $\eta^5\text{-Cp}^*$  ring's pseudo-five-fold axis of symmetry ( $C_5$ ), while in  $\text{Cp}^*_2\text{BMe}$  it is aligned with a pseudo-three-fold axis ( $C_3$ ) perpendicular to the plane of the coordinated ligands. The EFG tensor is observed to be almost axially symmetric by both experimental and theoretical methods for both  $\text{Cp}^*_2\text{B}^+$  and  $\text{Cp}^*_2\text{BMe}$ , meaning that  $V_{11}$  and  $V_{22}$  are similar in magnitude and positioned perpendicular to the  $C_5$  and  $C_3$  axes in  $\text{Cp}^*_2\text{B}^+$  and

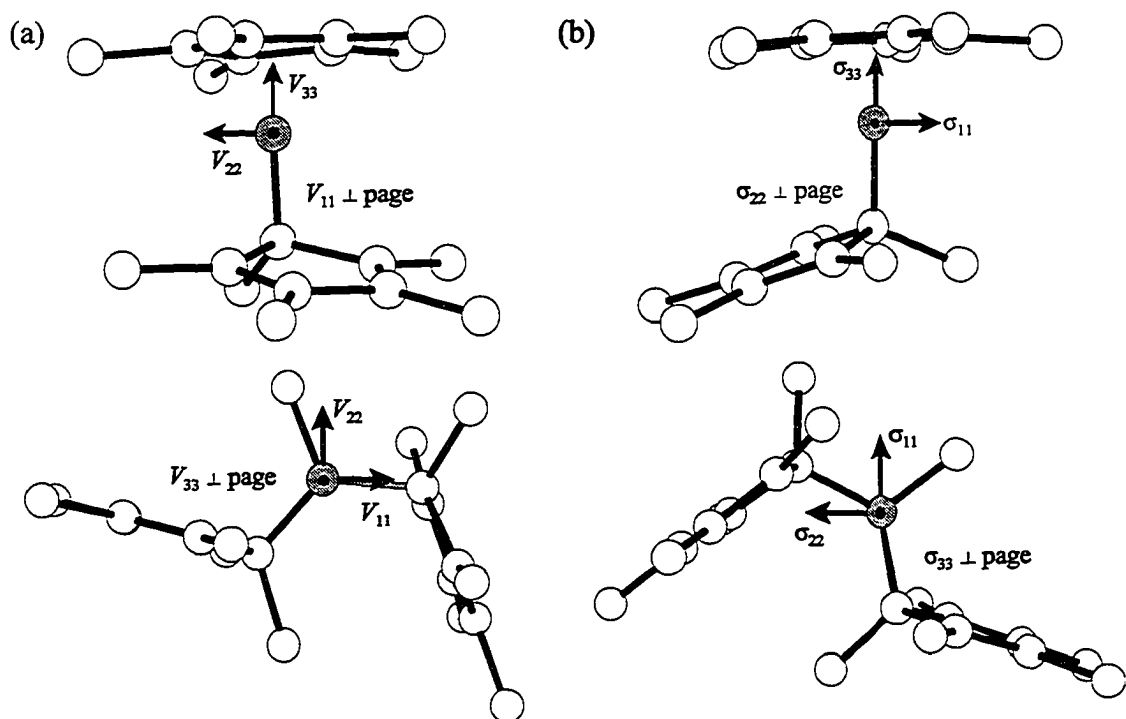


**Figure 2.12** Theoretical  $^{11}\text{B}$  (a) EFG tensor and (b) CS tensor orientations in  $\text{Cp}^*_2\text{B}^+$  and  $\text{Cp}^*_2\text{BMe}$ .

$\text{Cp}^*_2\text{BMe}$ , respectively. The orientations of the boron chemical shielding tensors in  $\text{Cp}^*_2\text{B}^+$  and  $\text{Cp}^*_2\text{BMe}$  are pictured in Figure 2.12b. In  $\text{Cp}^*_2\text{B}^+$ , the largest component,  $\sigma_{33}$ , is once again directed towards the  $\eta^5$ - $\text{Cp}^*$  ring centroid, while  $\sigma_{11}$  points along the direction of the *ipso*-methyl carbon which “bends” away from the boron atom. The near-axial symmetry of the boron chemical shielding tensor is easily justified when one considers the relatively homogeneous electronic environment perpendicular to the  $\eta^5$ - $\text{Cp}^*$ -boron bond axis. The most shielded principal component in  $\text{Cp}^*_2\text{BMe}$  is directed from the boron nucleus perpendicular to a plane containing the three directly bound carbons, while  $\sigma_{11}$  approximately bisects the angle between the methyl carbon and one of the boron-bound  $\text{Cp}^*$  ring carbons. In this case,  $\sigma_{11}$  and  $\sigma_{22}$  point into electronically distinct environments due to the different orientations of the  $\eta^1$ - $\text{Cp}^*$  rings, thereby

resulting in a non-axially symmetric chemical shielding tensor; however,  $\kappa = 0.57$ , indicating that these two components are relatively similar to one another, and  $\sigma_{33}$  is the distinct principal component.

In Figure 2.13, theoretically calculated rotational barriers are pictured for the  $\text{Cp}^*_2\text{Al}^+$  cation. Initial calculations of the rotational barrier involved changing the relative orientation of the  $\text{Cp}^*$  rings by adjusting the position of one ring. B3LYP calculations with both the 6-31G\*\* and 6-311G\*\* basis sets displayed an unusual discontinuity for the staggered  $D_{5d}$  species (energies for different conformers are signified by rectangular and circular points), making it apparent that it was necessary to conduct a geometry optimization for each rotational conformer. A rotational barrier of 4.15 kJ mol<sup>-1</sup> was calculated from B3LYP/6-311G\*\* geometry optimizations, with the staggered

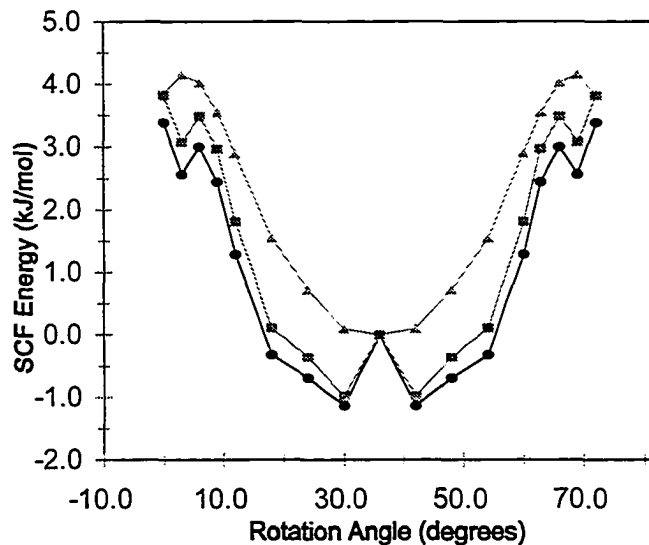


**Figure 2.13** Rotational barrier: SCF energy versus relative dihedral angle between  $\text{Cp}^*$  rings with  $D_{5h}$  being  $0^\circ$  from Gaussian 98 (▲) B3LYP/6-311G\*\* geometry optimization, and (●) B3LYP/6-31G\*\* and (■) B3LYP/6-311G\*\* NMR calculations.



$D_{5d}$  conformation possessing the lowest energy. This result is comparable to energy barriers which have been determined for different solid-state phases of ferrocene, which vary from 5.4 – 24.8 kJ mol<sup>-1</sup>.<sup>[53]</sup> The highest energy conformation is almost eclipsed, with the dihedral angle between methyl groups on opposing Cp\* rings equal to 3°. The shape of the rotational barrier can be fit to the function  $f(\theta) = A + B\cos(\theta-\pi/5)^2 + C\cos(\theta-\pi/5)^4 + D\cos(\theta-\pi/5)^6$ , where  $A = 4.124(0.036)$ ,  $B = -7.787(0.534)$ ,  $C = 5.34(1.42)$ ,  $D = -1.714(0.969)$ . The expectation (or average) value for the angle theta is  $\langle\theta\rangle = 8.8576^\circ$ , meaning that the rings sit with methyl groups staggered at an angle of 27.14° with respect to one another. If the experimental rotational barrier is similar at room temperature in the solid state, the rings are undergoing restricted rotation, spending most of their time in a staggered conformation. Free rotation of the Cp\* rings would require temperatures in excess of 498 K. The predominantly staggered conformation at room temperature is reflected by the measured anisotropic chemical shielding spans at room temperature (refer to Table 2.4).

In a similar fashion, theoretical calculations (B3LYP/6-31G\*\*) predict the rotational barrier of the  $\eta^5$ -Cp\* ring in Cp\*<sub>2</sub>B<sup>+</sup> to be approximately 7.3 kJ mol<sup>-1</sup>. The lowest energy conformer has one of the  $\eta^5$ -Cp\* ring carbons eclipsed with the proton attached to the *ipso*-carbon of the  $\eta^1$ -Cp\* ring. The highest energy conformation is when the  $\eta^5$ -Cp\* ring is rotated 30° from this position. A slight decrease in  $\Omega$  of -1.4 ppm with an increase in  $\delta_{iso}$  of approximately 1.0 ppm is predicted as the  $\eta^5$ -ring is rotated into a position which is staggered compared to its original low energy conformation. Similarly,  $C_Q$  is predicted to vary by only about 6 kHz. Owing to the ease and speed at which rings

of penta-hapticity are able to rotate in the absence of bulky ligands, it is very unlikely that these relatively low magnitude changes in the chemical shielding and quadrupolar interactions could be observed even at low temperatures ( $< 140$  K).

To examine the origin of the chemical shielding interaction, it is useful to compare the diamagnetic and paramagnetic shielding contributions (Table 2.6). Calculations on the staggered  $D_{5d}$  conformer of  $\text{Cp}^*_2\text{Al}^+$  reveal that negative paramagnetic contributions responsible for de-shielding the nucleus are much larger perpendicular rather than parallel to the  $C_5$  molecular axis. This implies that there must be occupied and virtual molecular orbitals (MOs) which are relatively close in energy that mix in the plane of the molecular axis to de-shield the nucleus perpendicular to the molecular axis. Similar results are observed in the  $D_{5h}$  species, though the negative paramagnetic shielding contributions are reduced. Interestingly, comparison of calculations on both metallocene conformers with those on the hydrated  $\text{Al}^{3+}$  cation reveal that the latter has much larger negative paramagnetic shielding contributions, resulting in a de-shielded aluminum nucleus (i.e., a high frequency NMR shift).

An analogous breakdown of theoretical paramagnetic and diamagnetic magnetic shielding contributions at the boron nuclei in  $\text{Cp}^*_2\text{B}^+$ ,  $\text{Cp}^*_2\text{BMe}$  and  $\text{BH}_4^-$  is given in Table 2.7. In  $\text{Cp}^*_2\text{B}^+$ , magnetic dipole allowed mixing of energetically close occupied and virtual orbitals is responsible for magnetic de-shielding perpendicular to the pseudo- $C_3$  molecular axis. Such mixing is absent perpendicular to the  $C_3$ , as evidenced by the much higher shielding value in this direction. It is interesting to note that both

**Table 2.6**  
Theoretical Diamagnetic and Paramagnetic Contributions to Shielding at the Aluminum in  $\text{Cp}^*_2\text{Al}^+$  and  $\text{Al}(\text{H}_2\text{O})_6^{3+}$

	$\sigma_{11}^d$	$\sigma_{11}^p$	$\sigma_{22}^d$	$\sigma_{22}^p$	$\sigma_{33}^d$	$\sigma_{33}^p$	$\sigma_{\text{iso}}^d$	$\sigma_{\text{iso}}^p$	$\sigma_{\text{iso}}^{\text{total}}$
<b><math>\text{Cp}^*_2\text{Al}^+</math></b>									
<b><math>D_{5d}</math> - staggered</b>									
RHF/6-31G**	798.36	-76.80	798.36	-76.80	812.50	-19.61	803.08	-57.74	745.34
RHF/6-311G**	789.48	-70.15	789.48	-70.15	806.59	-16.82	795.19	-52.38	742.81
B3LYP/6-31G**	809.81	-126.84	809.81	-126.49	815.22	-50.75	811.62	-101.40	710.22
B3LYP/6-311G**	796.84	-124.68	796.84	-124.48	814.29	-55.25	802.66	-101.50	701.16
<b><math>D_{5h}</math> - eclipsed</b>									
RHF/6-31G**	795.81	-55.51	795.81	-55.51	811.99	-26.03	801.21	-45.68	755.53
RHF/6-311G**	786.64	-49.68	786.64	-49.68	805.49	-19.71	792.92	-39.69	753.23
B3LYP/6-31G**	807.70	-103.60	807.70	-102.92	814.89	-62.51	810.10	-89.67	720.43
B3LYP/6-311G**	794.64	-102.10	794.64	-101.81	813.29	-62.93	800.85	-88.94	711.91
<b><math>\text{Al}(\text{H}_2\text{O})_6^{3+}</math></b>									
RHF/6-31G**	785.57	-150.52	785.57	-150.52	785.57	-150.52	785.57	-150.52	635.05
RHF/6-311G**	781.79	-164.52	781.79	-164.52	781.79	-164.52	781.79	-164.52	617.27
B3LYP/6-31G**	789.71	-181.34	789.71	-181.34	789.71	-181.34	789.71	-181.34	608.37
B3LYP/6-311G**	787.40	-208.70	787.40	-208.70	787.40	-208.70	787.40	-208.70	578.70

**Table 2.7**  
Theoretical Diamagnetic and Paramagnetic Contributions to Shielding at the Boron in  $\text{Cp}^*_2\text{B}^+$ ,  $\text{Cp}^*_2\text{BMe}$  and  $\text{BH}_4^-$

	$\sigma_{11}^d$	$\sigma_{11}^p$	$\sigma_{22}^d$	$\sigma_{22}^p$	$\sigma_{33}^d$	$\sigma_{33}^p$	$\sigma_{\text{iso}}^d$	$\sigma_{\text{iso}}^p$	$\sigma_{\text{iso}}^{\text{total}}$
<b><math>\text{Cp}^*_2\text{B}^+</math></b>									
RHF/6-31G**	196.70	-57.38	199.61	-57.49	219.07	0.10	205.12	-38.25	166.87
RHF/6-311G**	191.29	-54.48	193.97	-54.86	220.30	-2.16	201.85	-37.17	164.69
RHF/6-311+G**	68.26	68.20	112.12	26.84	121.01	96.86	100.46	63.97	164.43
B3LYP/6-31G**	201.94	-77.22	203.27	-74.59	224.37	-20.32	209.86	-57.37	152.49
B3LYP/6-311G**	195.34	-74.31	196.87	-72.50	222.91	-19.61	205.04	-55.47	149.57
B3LYP/6-311+G**	70.67	50.98	108.83	15.69	122.36	80.34	100.62	49.00	149.62
<b><math>\text{Cp}^*_2\text{BMe}</math></b>									
RHF/6-31G**	171.39	-185.01	201.18	-183.85	208.85	-78.87	193.81	-149.24	44.56
RHF/6-311G**	170.13	-195.86	197.04	-190.25	209.20	-83.93	192.12	-156.68	35.44
RHF/6-311+G**	150.28	-176.15	178.06	-171.64	180.43	-55.21	169.59	-134.34	35.26
B3LYP/6-31G**	180.19	-209.80	211.42	-206.08	213.69	-94.26	201.77	-170.05	31.72
B3LYP/6-311G**	174.45	-225.69	204.77	-217.08	212.34	-99.67	197.18	-180.81	16.37
B3LYP/6-311+G**	156.02	-207.85	179.49	-190.82	196.03	-82.92	177.18	-160.53	16.65
<b><math>\text{BH}_4^-</math></b>									
RHF/6-31G**	186.52	-27.15	186.52	-27.15	186.52	-27.15	186.52	-27.15	159.37
RHF/6-311G**	183.63	-26.87	183.63	-26.87	183.63	-26.87	183.63	-26.87	156.76
RHF/6-311+G**	185.16	-27.19	185.16	-27.19	185.16	-27.19	185.16	-27.19	157.97
B3LYP/6-31G**	189.23	-32.96	189.23	-32.96	189.23	-32.96	189.23	-32.96	156.27
B3LYP/6-311G**	185.49	-33.11	185.49	-33.11	185.49	-33.11	185.49	-33.11	152.38
B3LYP/6-311+G**	188.29	-33.20	188.29	-33.20	188.29	-33.20	188.29	-33.20	155.09

RHF and B3LYP calculations predict very small negative paramagnetic shielding contributions in  $\text{Cp}^*_2\text{B}^+$ ; notably, calculations using the 6-311+G\*\* basis set actually predict positive paramagnetic shielding contributions. There are numerous small positive paramagnetic contributions resulting from mixing of both occupied with virtual, and occupied with occupied orbitals, which result in the high shielding at the boron nucleus in this molecule. Further discussion of high magnetic shielding in metallocenes can be found in a recent theoretical study of ferrocene.<sup>[54]</sup> The origin of anisotropic magnetic shielding of the boron nucleus in the trigonal planar  $\text{Cp}^*_2\text{BMe}$  molecule is analogous to that discussed by Wasylishen and co-workers for the trimesitylborane species,<sup>[12]</sup> and will not be discussed here in detail. However, it should be noted that the magnetic shielding in  $\text{Cp}^*_2\text{BMe}$  has large negative paramagnetic shielding contributions in comparison to  $\text{Cp}^*_2\text{B}^+$  (Table 2.7).

In order to gain insight into which  $\text{Cp}^*_2\text{Al}^+$  MOs are responsible for the aluminum chemical shielding anisotropy and high shielding of the aluminum nucleus, calculations were carried out with the ADF software package (see section 2.2.4 for details). The results of ADF BLYP calculations using basis set V are presented in Table 2.8 for three aluminum-containing species with markedly different isotropic chemical shifts,  $\text{AlCl}_4^-$ ,  $\text{Al}(\text{H}_2\text{O})_6^{3+}$  and  $\text{Cp}^*_2\text{Al}^+$ . The isotropic chemical shielding values are in qualitative agreement with experimental data, with  $\text{Cp}^*_2\text{Al}^+$  possessing the most magnetically shielded aluminum nucleus.

Under the GIAO formalism, diamagnetic and paramagnetic contributions are calculated independently from one another, with the former arising solely from ground

state electron circulation, and the latter arising from contributions from both the ground state and magnetic-dipole allowed mixing of ground and excited state wavefunctions. Commonly, the paramagnetic contribution arising from mixing of occupied and virtual molecular orbitals (occ-vir contribution) is the main factor leading to variation in magnetic shielding among chemically distinct nuclei. However, ADF calculations indicate that a positive contribution (i.e., shielding) from the mixing of occupied wavefunctions (occ-occ) is of great significance for magnetic shielding at the aluminum nucleus as well. The apparent origin of chemical shielding at the metal site in this *p*-block metallocene stands in stark contrast to that in a transition metal metallocene such as ferrocene.<sup>[54]</sup>

**Table 2.8**  
ADF Numerical Calculations of Contributions to Aluminum  
Chemical Shielding from Orbital Mixing

	AlCl <sub>4</sub> <sup>-</sup>	Al(H <sub>2</sub> O) <sub>6</sub> <sup>3+</sup>	Cp* <sub>2</sub> Al <sup>+</sup>
σ <sup>tot</sup> (isotropic chemical shielding)	443.179	565.118	694.196
σ <sup>d</sup> (total)	794.350	770.152	784.803
σ <sup>d</sup> (core)	0.000	0.000	0.000
σ <sup>d</sup> (valence)	794.350	770.152	784.803
σ <sup>p</sup> (total)	-351.171	-205.034	-90.607
Gauge Invariance Terms	-3.861	1.728	5.714
Frozen Core Terms	0.000	0.000	0.000
σ <sup>p</sup> (occ-occ) <sup>a</sup>	-70.642	2.589	132.316
σ <sup>p</sup> (occ-vir) <sup>a</sup>	-276.668	-209.351	-228.637

<sup>[a]</sup> Occ-occ and occ-vir refer to contributions to paramagnetic shielding stemming from mixing of occupied MOs with occupied and virtual MOs, respectively.

Before examining Cp\*<sub>2</sub>Al<sup>+</sup>, the calculation of shielding tensors for AlCl<sub>4</sub><sup>-</sup> and Al(H<sub>2</sub>O)<sub>6</sub><sup>3+</sup> are considered. Calculations on AlCl<sub>4</sub><sup>-</sup> indicate a large negative paramagnetic

contribution to aluminum magnetic shielding from mixing of occupied MOs with occupied (occ-occ) and virtual (occ-vir) MOs. The large occ-vir value arises from MOs with contributions mainly from aluminum atomic orbitals (AOs). Specifically, occupied hybrid  $2p$ -aluminum orbitals mix with virtual hybrid aluminum  $2p$  and  $3p$  orbitals, which are separated by approximately 10.3 eV. In the pseudo-octahedral  $\text{Al}(\text{H}_2\text{O})_6^{3+}$  complex the situation is similar, except that the occupied and virtual MOs which mix to give the largest negative paramagnetic contributions are separated by approximately 18.3 eV. There is also a small positive paramagnetic occ-occ contribution. In both cases, the high spherical symmetry of these complexes results in negligible magnetic shielding anisotropy.

The  $D_{5d}$  symmetry of  $\text{Cp}^*_2\text{Al}^+$  lends itself to extremely different magnetic shielding environments parallel and perpendicular to the  $C_5$  axis of the molecule. In this

**Table 2.9**  
Major Paramagnetic Shielding Contributions in  $\text{Cp}^*_2\text{Al}^+$  from Molecular Orbital Mixing

Occ	Vir	$\sigma_{\text{iso}}$	$\sigma_{\perp}$	$\sigma_{\parallel}$
$2E_{1u}$ (1)	$6A_{2u}$	-17.95	-53.9	0.0
$2E_{1u}$ (2)	$6A_{2u}$	-18.03	-54.1	0.0
$2E_{1u}$ (1)	$8A_{2u}$	-19.70	-59.1	0.0
$2E_{1u}$ (2)	$8A_{2u}$	-19.80	-59.4	0.0
$2E_{1u}$ (1)	$10A_{2u}$	30.32	90.9	0.0
$2E_{1u}$ (2)	$10A_{2u}$	30.44	91.3	0.0
Occ	Occ	$\sigma_{\text{iso}}$	$\sigma_{\perp}$	$\sigma_{\parallel}$
$2E_{1u}$ (1)	$2E_{1u}$ (2)	37.58	0.0	112.7
$2E_{1u}$ (1)	$3A_{2u}$	-39.98	-119.9	0.0
$2E_{1u}$ (2)	$3A_{2u}$	-40.14	-120.4	0.0
$5A_{2u}$	$5E_{1u}$ (1)	38.01	114.0	0.0
$5A_{2u}$	$5E_{1u}$ (2)	37.92	113.8	0.0
$5E_{1u}$ (1)	$5E_{1u}$ (2)	49.78	0.0	149.3

cation, the complicated  $p$ - $\pi$  bonding at the aluminum center results in a multitude of positive and negative contributions to paramagnetic shielding from a variety of occ-occ and occ-vir symmetry-allowed mixing. For simplicity, only contributions to the isotropic chemical shielding in excess of 18 ppm in absolute magnitude will be considered. There are many smaller contributions from occ-occ and occ-vir MO mixing with similar symmetries which have not been included. The shielding contributions and

**Table 2.10**  
List of Molecular Orbitals and Most Significant Symmetrized Fragment Orbitals

MO <sup>[a]</sup>	Occ	Energy [eV]	% <sup>[b]</sup>	SFO <sup>[c]</sup>	Fragment
2E <sub>1u</sub> (1,2)	2	-74.50	99.98	2p <sub>x,y</sub>	Al
3A <sub>2u</sub>	2	-26.46	78.47	2s	C
			19.26	2p <sub>y</sub>	C
			8.31	3p <sub>z</sub>	Al
5A <sub>2u</sub>	2	-14.11	83.50	2p <sub>z</sub>	C
			6.82	3p <sub>z</sub>	Al
5E <sub>1u</sub> (1,2)	2	-11.30	72.28	2p <sub>z</sub>	C
			16.79	3p <sub>x,y</sub>	Al
6A <sub>2u</sub>	0	-2.74	57.30	4p <sub>z</sub>	Al
			25.56	1s	H
			14.87	3p <sub>z</sub>	Al
8A <sub>2u</sub>	0	1.25	53.85	4p <sub>z</sub>	Al
			28.40	3p <sub>z</sub>	C
			20.66	2p <sub>z</sub>	C
			18.77	3p <sub>z</sub>	Al
10A <sub>2u</sub>	0	5.74	36.44	3p <sub>z</sub>	C
			20.54	2s	H
			20.25	5p <sub>z</sub>	Al

<sup>[a]</sup> Molecular orbitals have symmetry labels corresponding to the  $D_{5d}$  point group. The “Occ” column lists the occupation of occupied (2 electrons) and virtual (0 electrons) MOs. <sup>[b]</sup> The % column denotes percent contribution to MOs from symmetry adapted atomic orbitals (AOs). <sup>[c]</sup> In the ADF software package, SFOs (symmetrized fragment orbitals) serve as the symmetry adapted basis set for the calculation (see ADF User’s Guide).



corresponding MOs are summarized in Tables 2.9 and 2.10, with three-dimensional contour images of the molecular orbitals pictured in Figure 2.14. Moderately large negative shielding contributions (ca. -19 ppm) perpendicular to the  $C_5$  molecular axis arise from mixing of two degenerate occupied  $2E_{1u}$  MOs (comprised largely of contributions from the aluminum  $2p_{x,y}$  AOs) with the virtual  $6A_{2u}$  and  $8A_{2u}$  MOs, both of which have significant contributions from  $3p_z$  and  $4p_z$  aluminum AOs and smaller contributions from ring carbon  $p_z$  orbitals and hydrogen  $s$  orbitals. However, in comparison to  $AlCl_4^-$  and  $Al(H_2O)_6^{3+}$ , the energy separation between these occupied and virtual MOs are immense, with  $E(2E_{1u}-6A_{2u}) = 71.75$  eV and  $E(2E_{1u}-8A_{2u}) = 75.74$  eV. Furthermore, mixing of the occupied  $2E_{1u}$  MOs with the virtual  $10A_{2u}$  MO results in a positive paramagnetic shielding contribution perpendicular to the molecular axis (ca. +30 ppm). Along the  $C_5$  axis there are no comparable large negative paramagnetic contributions, although there are a series of positive contributions arising from mixing of the occupied  $2E_{1u}$  MOs with virtual MOs that possess substantial aluminum  $p$ -character.

Interestingly, occ-occ mixing of MOs with high  $2p_z$  AO character from the Cp\* ring carbons gives rise to both positive and negative paramagnetic shielding contributions. For instance, mixing of the degenerate  $2E_{1u}$  MOs with the  $3A_{2u}$  MO produce large deshielding contributions (ca. -40 ppm, -120 ppm perpendicular to the molecular axis), while mixing of the degenerate  $2E_{1u}$  MOs with one another shields the nucleus along the direction of molecular axis (ca. +40 ppm, +120 ppm parallel to the molecular axis). In addition, occ-occ mixing of the  $5A_{2u}$  MO (large contributions from Cp\* carbon  $2p_z$  AOs and small contribution from the  $2p_z$  Al orbital) with two degenerate

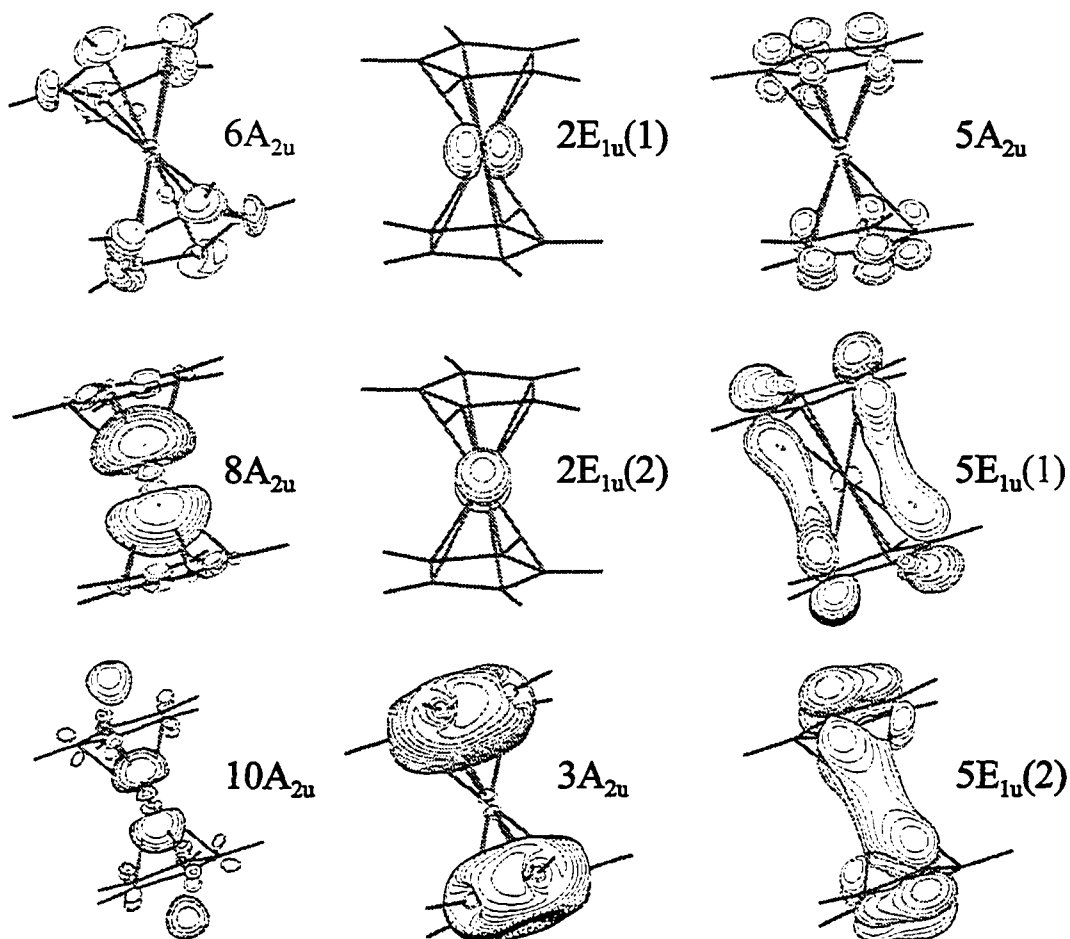


**Figure 2.14** Occupied ( $2E_{1u}(1, 2)$ ,  $3A_{2u}$ ,  $5A_{2u}$  and  $5E_{1u}(1, 2)$ ) and virtual ( $6A_{2u}$ ,  $8A_{2u}$  and  $10A_{2u}$ ) molecular orbitals in  $Cp^*_2Al^+$ , which mix to make the largest aluminum paramagnetic shielding contributions.

$5E_{1u}$  MOs (Cp carbon  $2p_z$  AOs and small contribution from the  $3p_z$  Al orbital) provides heavy magnetic shielding of the aluminum nucleus (ca. +38 ppm, +114 ppm perpendicular to the molecular axis). Occ-occ mixing of the  $5E_{1u}$  orbitals with one another shields the nucleus in the direction of the molecular axis as well (ca. +50 ppm, +149 ppm parallel to the molecular axis). Virtual rotation of ground and excited state orbitals is commonly used as a physical picture of magnetic-field induced orbital mixing associated with a paramagnetic shielding contribution in a direction perpendicular to that

rotation. However, there is no similar physical picture for mixing of occupied orbitals, although the shielding contributions occur in a direction perpendicular to their mixing. Nonetheless, occ-occ mixing of MOs localized on the Cp\* rings and not on the aluminum atom seem to play a major role in shielding the aluminum nucleus, as witnessed from the large positive paramagnetic contributions to the shielding tensor.

### 2.3.4 Theoretical Study of Carbon Shielding Tensors and Cp\* Ring Dynamics

A comparison of experimental and theoretical carbon CS tensors for Cp\*<sub>2</sub>Al<sup>+</sup> is presented in Table 2.11. With the exception of  $\delta_{iso}$  and  $\delta_{33}$ , comparison of the chemical shielding tensor parameters reveals discrepancies between experimental and theoretical values. In all cases, the orientation of carbon CS tensors at the Cp\* ring carbons have the most shielded component,  $\sigma_{33}$ , perpendicular to the plane of the Cp\* ring, and the least shielded component,  $\sigma_{11}$ , oriented along the direction of the methyl carbon. The discrepancy between experimental and theoretical values arises from the fact that the Cp\*

**Table 2.11**  
Experimental and Theoretical <sup>13</sup>C Chemical Shielding Tensors in Cp\*<sub>2</sub>Al<sup>+</sup>

	$\delta_{11}$ [ppm]	$\delta_{22}$ [ppm]	$\delta_{33}$ [ppm]	$\delta_{iso}$ [ppm]	$\Omega$ [ppm]	$\kappa$
<b>Experimental</b>	154.8(1)	154.8(1)	46.7(1)	118.7	108.1	1.00
<b>Theoretical</b>						
RHF/6-31G**	174.77	127.54	22.49	108.27	152.28	0.38
RHF/6-311G**	173.63	123.68	11.93	103.08	161.69	0.38
B3LYP/6-31G**	182.47	141.30	44.28	122.68	138.19	0.40
B3LYP/6-311G**	182.35	141.27	44.22	122.61	138.13	0.41

rings are undergoing rapid reorientation about the Cp\* axis. It has previously been demonstrated that NMR powder patterns manifesting first- and second-order effects from anisotropic CS<sup>[55-57]</sup> and EFG tensors<sup>[58, 59]</sup> are influenced by both molecular motions and chemical exchange. Herein, a previously described semi-classical exchange formalism is used to treat the effects of chemical exchange on a powder pattern strongly influenced by first-order anisotropic chemical shielding.<sup>[57, 59]</sup>

A series of calculations of the <sup>13</sup>C chemical shift tensors in Cp\*<sub>2</sub>B<sup>+</sup> is presented in Table 2.12. For the η<sup>5</sup>-Cp\* aromatic carbons, RHF calculations tend to exaggerate the magnitude of Ω by overestimating the shielding perpendicular to the ring plane (i.e., δ<sub>33</sub>). B3LYP calculations seem to predict the span more closely. Furthermore, the B3LYP calculations are also superior in predicting values of δ<sub>iso</sub> and Ω for the η<sup>1</sup>-Cp\* ring. In the case of the pentahapto ring, there is a discrepancy between the experimental and theoretical skews, likely resulting from averaging of the observed CS tensor due to ring motion. For the η<sup>1</sup>-ring, skews are more accurately calculated by both methods.

**Table 2.12**  
Experimental and Theoretical <sup>13</sup>C Chemical Shielding Tensors in Cp\*<sub>2</sub>B<sup>+</sup>

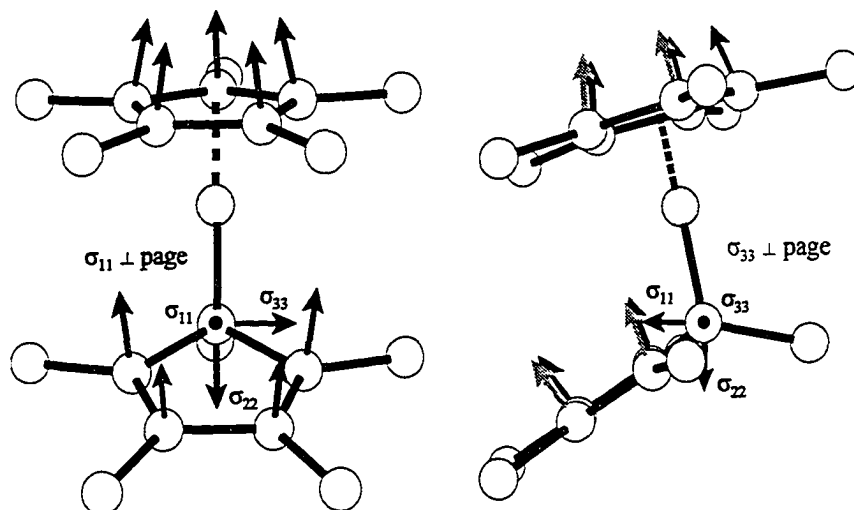
Site	δ <sub>11</sub> [ppm]	δ <sub>22</sub> [ppm]	δ <sub>33</sub> [ppm]	δ <sub>iso</sub> [ppm]	Ω [ppm]	κ
<b>Experimental</b>						
η <sup>5</sup> : C <sub>5</sub> ( <u>C</u> H <sub>3</sub> ) <sub>5</sub>	—	—	—	5.9	—	—
η <sup>5</sup> : <u>C</u> <sub>5</sub> (CH <sub>3</sub> ) <sub>5</sub>	157	140	32	109.3	124	0.73
η <sup>1</sup> : <i>i</i> - <u>C</u> <sub>5</sub> (CH <sub>3</sub> ) <sub>5</sub>	—	—	—	37.7	—	—
η <sup>1</sup> : α- <u>C</u> <sub>5</sub> (CH <sub>3</sub> ) <sub>5</sub>	224	135	43	134.2	181	0
η <sup>1</sup> : β- <u>C</u> <sub>5</sub> (CH <sub>3</sub> ) <sub>5</sub>	224	144	38	135.5	186	0.14

Table 2.12 (cont.)

Site	$\delta_{11}$ [ppm]	$\delta_{22}$ [ppm]	$\delta_{33}$ [ppm]	$\delta_{iso}$ [ppm]	$\Omega$ [ppm]	$\kappa$
RHF/6-31G**						
$\eta^5$ : $\underline{C}_5(\text{CH}_3)_5$	151.0	139.7	19.3	103.3	131.7	0.83
	149.4	147.6	15.9	104.3	133.5	0.97
	149.2	145.4	15.1	103.2	134.1	0.94
	147.7	144.6	15.2	102.5	132.5	0.95
	148.8	145.1	17.3	103.7	131.5	0.94
$\eta^1$ : $i$ - $\underline{C}_5(\text{CH}_3)_5$	41.7	35.6	10.3	29.2	31.4	0.61
$\eta^1$ : $\alpha$ - $\underline{C}_5(\text{CH}_3)_5$	238.8	129.6	28.7	132.4	210.2	-0.04
	236.7	127.8	29.1	131.2	207.6	-0.05
$\eta^1$ : $\beta$ - $\underline{C}_5(\text{CH}_3)_5$	244.2	120.2	39.8	134.7	204.4	-0.21
	240.9	121.3	39.6	133.9	201.3	-0.19
-----						
RHF/6-311G**						
$\eta^5$ : $\underline{C}_5(\text{CH}_3)_5$	148.0	134.4	9.2	97.2	138.8	0.80
	146.6	143.1	5.5	98.4	141.1	0.95
	146.3	140.9	5.0	97.4	141.3	0.92
	144.7	140.1	5.1	96.7	139.6	0.93
	145.3	140.4	7.1	97.6	138.2	0.93
$\eta^1$ : $i$ - $\underline{C}_5(\text{CH}_3)_5$	33.3	26.4	-0.9	19.6	34.2	0.59
$\eta^1$ : $\alpha$ - $\underline{C}_5(\text{CH}_3)_5$	245.8	125.0	20.0	130.3	225.7	-0.07
	243.6	123.2	20.5	129.1	223.2	-0.08
$\eta^1$ : $\beta$ - $\underline{C}_5(\text{CH}_3)_5$	249.3	113.0	30.5	130.9	218.8	-0.25
	245.5	114.1	30.4	130.0	215.2	-0.22
-----						
RHF/6-311+G**						
$\eta^5$ : $\underline{C}_5(\text{CH}_3)_5$	148.3	134.9	9.5	97.6	138.8	0.81
	147.2	143.7	5.8	98.9	141.4	0.95
	146.9	141.4	5.3	97.8	141.6	0.92
	145.4	140.5	5.4	97.1	140.0	0.93
	145.8	141.0	7.3	98.0	138.5	0.93
$\eta^1$ : $i$ - $\underline{C}_5(\text{CH}_3)_5$	33.5	27.0	-0.6	20.0	34.1	0.62
$\eta^1$ : $\alpha$ - $\underline{C}_5(\text{CH}_3)_5$	246.3	126.0	20.3	130.9	226.0	-0.06
	244.2	124.3	20.7	129.7	223.5	-0.07
$\eta^1$ : $\beta$ - $\underline{C}_5(\text{CH}_3)_5$	249.6	113.7	30.8	131.4	218.7	-0.24
	245.8	114.8	30.7	130.4	215.1	-0.22

Table 2.12 (cont.)

Site	$\delta_{11}$ [ppm]	$\delta_{22}$ [ppm]	$\delta_{33}$ [ppm]	$\delta_{\text{iso}}$ [ppm]	$\Omega$ [ppm]	$\kappa$
B3LYP/6-31G**						
$\eta^5$ : $\underline{\text{C}}_5(\text{CH}_3)_5$	158.0	152.1	39.1	116.4	118.9	0.90
	160.5	156.7	35.5	117.6	125.0	0.94
	158.5	154.4	34.6	115.8	123.9	0.93
	157.7	153.8	34.9	115.4	122.9	0.94
	157.7	155.6	37.1	116.8	120.6	0.96
$\eta^1$ : <i>i</i> - $\underline{\text{C}}_5(\text{CH}_3)_5$	61.0	55.2	30.8	49.0	30.2	0.62
$\eta^1$ : $\alpha$ - $\underline{\text{C}}_5(\text{CH}_3)_5$	224.3	148.5	47.5	140.1	176.8	0.14
	223.2	146.2	48.0	139.1	175.3	0.12
$\eta^1$ : $\beta$ - $\underline{\text{C}}_5(\text{CH}_3)_5$	231.6	141.3	57.4	143.4	174.2	-0.04
	228.6	142.2	57.1	142.6	171.4	-0.01
B3LYP/6-311G**						
$\eta^5$ : $\underline{\text{C}}_5(\text{CH}_3)_5$	156.2	146.9	25.0	109.3	131.2	0.86
	156.3	154.5	21.7	110.8	134.6	0.97
	154.1	151.8	21.1	109.0	133.0	0.97
	153.3	151.5	21.4	108.7	131.8	0.97
	153.1	152.7	23.0	109.6	130.2	0.99
$\eta^1$ : <i>i</i> - $\underline{\text{C}}_5(\text{CH}_3)_5$	51.2	44.8	16.1	37.4	35.1	0.64
$\eta^1$ : $\alpha$ - $\underline{\text{C}}_5(\text{CH}_3)_5$	232.3	143.2	36.1	137.2	196.2	0.09
	231.1	140.9	36.5	136.1	194.6	0.07
$\eta^1$ : $\beta$ - $\underline{\text{C}}_5(\text{CH}_3)_5$	238.1	135.1	44.8	139.3	193.3	-0.07
	234.4	136.2	44.7	138.4	189.7	-0.03
B3LYP/6-311+G**						
$\eta^5$ : $\underline{\text{C}}_5(\text{CH}_3)_5$	157.5	149.8	25.6	111.0	132.0	0.88
	158.0	156.7	23.8	112.8	134.2	0.98
	156.5	153.2	22.6	110.8	133.8	0.95
	155.2	153.6	22.8	110.5	132.4	0.98
	155.6	154.2	23.9	111.2	131.7	0.98
$\eta^1$ : <i>i</i> - $\underline{\text{C}}_5(\text{CH}_3)_5$	52.5	44.6	16.4	37.8	36.1	0.57
$\eta^1$ : $\alpha$ - $\underline{\text{C}}_5(\text{CH}_3)_5$	234.4	147.1	36.2	139.2	198.2	0.12
	233.1	144.3	36.5	137.9	196.5	0.10
$\eta^1$ : $\beta$ - $\underline{\text{C}}_5(\text{CH}_3)_5$	240.6	136.7	45.5	140.9	195.0	-0.07
	236.3	137.7	45.9	140.0	190.5	-0.04



**Figure 2.15** Orientation of theoretical carbon CS tensors of aromatic carbons in  $\text{Cp}^*_2\text{B}^+$ . Arrows signify direction of  $\sigma_{33}$  at all carbons with  $\sigma_{11}$  and  $\sigma_{22}$  components omitted for clarity. The full CS tensor orientation is shown for the *ipso*-carbon in the  $\eta^1\text{-Cp}^*$  ring.

Similar to the case of  $\text{Cp}^*_2\text{Al}^+$ , theoretically obtained  $^{13}\text{C}$  shielding tensors for the  $\text{Cp}^*$  ring carbons of  $\text{Cp}^*_2\text{B}^+$  are all oriented so the largest principal component,  $\sigma_{33}$ , is directed approximately perpendicular to the  $\text{Cp}^*$  rings while the less shielded components,  $\sigma_{11}$  and  $\sigma_{22}$ , lie within the ring planes. This is the case for all except the *ipso*-carbon on the  $\eta^1\text{-Cp}^*$  ring, which has  $\sigma_{11}$  and  $\sigma_{22}$  positioned in such a way that the  $\eta^1\text{-Cp}^*$  ring nearly bisects the angle between them, and  $\sigma_{33}$  is perpendicular to the boron-(*ipso*-carbon)-(methyl carbon) plane (Figure 2.15).

A static  $^{13}\text{C}$  NMR powder pattern was simulated for the  $\text{Cp}^*$  aromatic carbons in  $\text{Cp}^*_2\text{Al}^+$  using the chemical shift principal values from the B3LYP/6-311G\*\* calculation (Figure 2.16). Using the CS tensor orientations described previously, the Euler angles for a five site exchange are:  $\alpha = 0, 2\pi/5, 4\pi/5, 6\pi/5, 8\pi/5$ ;  $\beta = 0$ ;  $\gamma = 0$ . This corresponds to rotation of the orthogonal  $\sigma_{11}$  and  $\sigma_{22}$  components about a five-fold axis in  $72^\circ$

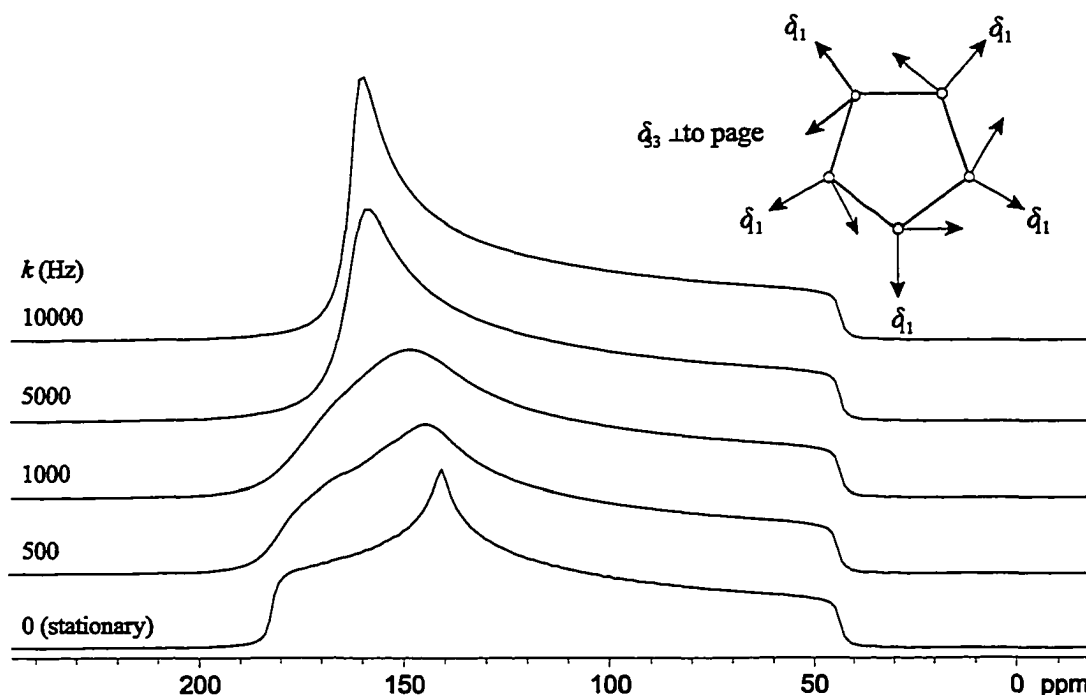


**Figure 2.16** Simulations of  $^{13}\text{C}$  static NMR powder patterns undergoing five-fold chemical exchange. Inset: Picture of five-fold ring and orientations of CS tensors determined from B3LYP/6-311G\*\* calculations.

increments, leaving  $\sigma_{33}$  pointing along the axis of rotation, as illustrated in the inset of Figure 2.16. As the exchange rate is increased, the high frequency portion of the powder pattern begins to collapse upon itself. At an exchange rate of  $k = 5000$  Hz (half the breadth of the powder pattern), an axially symmetric pattern begins to take shape. Finally, at  $k = 10000$  kHz, a powder pattern with a single sharp high frequency discontinuity is present. The CS tensor is analysed to yield  $\delta_{11} = \delta_{22} = 160$  ppm and  $\delta_{33} = 44$  ppm, with  $\delta_{\text{iso}} = 121.3$  ppm,  $\Omega = 116$  ppm and  $\kappa = 1.0$ , in very close agreement with experimental values.

Given the reliability of theoretical calculations of magnetic shielding tensors of first-row elements and the remarkable correspondence between experimental and



theoretical results, we believe that the combination of variable-temperature solid-state NMR, chemical exchange powder pattern simulations and theoretical calculations of NMR interaction tensors may prove to be an excellent means of probing rotational barriers in a variety of organometallic complexes.

## 2.4 Conclusion

A combination of solid-state NMR experiments and theoretical calculations of NMR interaction tensors has been used to study the anisotropic NMR interaction tensors of the metal nuclei in  $\text{Cp}^*_2\text{Al}^+$ ,  $\text{Cp}^*_2\text{B}^+$  and  $\text{Cp}^*_2\text{BMe}$ .

The  $\text{Cp}^*_2\text{Al}^+$  cation has a very small  $^{27}\text{Al}$  quadrupolar interaction due to the high ( $D_{5d}$ ) symmetry, but a large aluminum chemical shielding anisotropy due to the cylindrical symmetry of this cation. Full analysis of the  $^{27}\text{Al}$  satellite transition NMR spectra is required to measure the  $C_Q(^{27}\text{Al})$ , since no second-order lineshape is visible in the central transition MAS NMR spectra. The solid-state  $^{11}\text{B}$  MAS and static NMR spectra of  $\text{Cp}^*_2\text{B}^+$  and  $\text{Cp}^*_2\text{BMe}$  are greatly affected by anisotropic quadrupolar and CS interactions, which in turn are strongly influenced by the local symmetry and structure. These structurally different metallocenes exhibit vastly different quadrupolar coupling constants and chemical shielding tensor spans and symmetries, suggesting that chemically similar metallocenes may also be differentiated by simple solid-state NMR methods (albeit with less noticeable changes in the anisotropic NMR parameters). Notably, clear correlations can be seen between the magnitude of  $C_Q$  and the degree of spherical

symmetry about the metal nuclei (symmetry decrease  $\Rightarrow C_Q$  increase), as well as between  $\delta_{\text{iso}}$  and the hapticity of coordinated  $\eta^x\text{-Cp}^*$  ligands ( $x$  increase  $\Rightarrow \delta_{\text{iso}}$  decrease).

Ab initio calculations of aluminum chemical shielding tensors are in excellent agreement with experimental values, while calculated  $^{27}\text{Al}$  EFG tensors show discrepancies which can most likely be attributed to the exclusion of  $\text{Cp}^*$  ring motion. Calculation of  $^{11}\text{B}$  CS and EFG tensors are in very good agreement with experimentally determined parameters, demonstrating the useful predictive nature of calculations for these type of compounds.

Detailed RHF, B3LYP and ADF BLYP calculations help to explain the large chemical shielding anisotropy and high magnetic shielding of the aluminum nucleus in  $\text{Cp}^*_2\text{Al}^+$ . In addition to negative paramagnetic shielding contributions from symmetry-allowed mixing of occupied and virtual orbitals, mixing between occupied MOs make positive paramagnetic shielding contributions.

Double- and triple-resonance  $^{13}\text{C}/^{11}\text{B}/^1\text{H}$  NMR experiments performed at various temperatures support previously observed sigmatropic rearrangements of  $\eta^1\text{-Cp}'$  rings and show promise for further examinations of ring motion in metallocene complexes. However, for metallocenes with low internal rotation barriers, such as  $\text{Cp}^*_2\text{Al}^+$ , it may be necessary to drop to very low temperatures (e.g.,  $< 50 - 60$  K) to observe any significant effects on solid-state NMR spectra of the central metal nucleus. Calculation of carbon shielding tensors and chemical exchange simulations show that rapid rotation of the  $\text{Cp}^*$  rings results in an averaged chemical shielding tensor, which is observed experimentally for  $\text{Cp}^*_2\text{Al}^+$ .

It is believed that acquiring and analyzing NMR spectra of metal quadrupolar nuclei in metallocenes, in combination with theoretical computation of anisotropic NMR interaction tensors, provides an excellent means of probing metallocene structure, dynamics and chemistry. It is hoped that the work presented herein will encourage further work of this nature on the important class of organometallic compounds comprised by metallocenes.

# Bibliography

- [1] A. Voigt, S. Filipponi, C. L. B. Macdonald, J. D. Gordon, A. H. Cowley, *Chemical Communications* **2000**, 911.
- [2] P. Jutzi, A. Seufert, *Journal of Organometallic Chemistry* **1978**, *161*, C5.
- [3] O. Kwon, M. L. McKee, *Journal of Physical Chemistry A* **2001**, *105*, 10133.
- [4] D. Sundholm, J. Olsen, *Physical Review A* **1993**, *47*, 2672.
- [5] P. Pyykko, *Zeitschrift Fur Naturforschung Section A - a Journal of Physical Sciences* **1992**, *47*, 189.
- [6] M. E. Smith, *Applied Magnetic Resonance* **1993**, *4*, 1.
- [7] J. J. Delpuech, *NMR of Newly Accessible Nuclei - Volume 2: Chemically and Biochemically Important Elements, Vol. 2*, Academic Press, New York, **1983**.
- [8] J. W. Akitt, *Progress in Nuclear Magnetic Resonance Spectroscopy* **1989**, *21*, 1.
- [9] T. Vosegaard, H. J. Jakobsen, *Journal of Magnetic Resonance* **1997**, *128*, 135.
- [10] R. W. Schurko, R. E. Wasylshen, A. D. Phillips, *Journal of Magnetic Resonance* **1998**, *133*, 388.
- [11] R. W. Schurko, R. E. Wasylshen, H. Foerster, *Journal of Physical Chemistry A* **1998**, *102*, 9750.
- [12] D. L. Bryce, R. E. Wasylshen, M. Gee, *Journal of Physical Chemistry A* **2001**, *105*, 3633.
- [13] S. Kroeker, J. F. Stebbins, *Inorganic Chemistry* **2001**, *40*, 6239.

- [14] J. D. Kennedy, in *Multinuclear NMR* (Ed.: J. Mason), Plenum Press, New York, **1987**, pp. 221.
- [15] C. P. Grey, W. S. Veeman, *Chemical Physics Letters* **1992**, *192*, 379.
- [16] C. P. Grey, W. S. Veeman, A. J. Vega, *Journal of Chemical Physics* **1993**, *98*, 7711.
- [17] S. Hayashi, K. Hayamizu, *Bulletin of the Chemical Society of Japan* **1989**, *62*, 2429.
- [18] K. Eichele, R. E. Wasylshen, WSOLIDS, v.1.17.28 - Software for simulations of solid state NMR powder patterns, Dalhousie University, Dalhousie, **2000**.
- [19] D. W. Alderman, M. S. Solum, D. M. Grant, *Journal of Chemical Physics* **1986**, *84*, 3717.
- [20] J. Herzfeld, A. E. Berger, *Journal of Chemical Physics* **1980**, *73*, 6021.
- [21] M. M. Maricq, J. S. Waugh, *Journal of Chemical Physics* **1979**, *70*, 3300.
- [22] M. Bak, J. T. Rasmussen, N. C. Nielsen, *Journal of Magnetic Resonance* **2000**, *147*, 296.
- [23] M. J. Frisch, G. W. Trucks, H. B. Schlegel, G. E. Scuseria, M. A. Robb, J. R. Cheeseman, V. G. Zakrzewski, J. Montgomery, J. A., R. E. Stratmann, J. C. Burant, S. Dapprich, J. M. Millam, A. D. Daniels, K. N. Kudin, M. C. Strain, O. Farkas, J. Tomasi, V. Barone, M. Cossi, R. Cammi, B. Mennucci, C. Pomelli, C. Adamo, S. Clifford, J. Ochterski, G. A. Petersson, P. Y. Ayala, Q. Cui, K. Morokuma, D. K. Malick, A. D. Rabuck, K. Raghavachari, J. B. Foresman, J. Cioslowski, J. V. Ortiz, A. G. Baboul, B. B. Stefanov, G. Liu, A. Liashenko, P. Piskorz, I. Komaromi, R. Gomperts, R. L. Martin, D.

J. Fox, T. Keith, M. A. Al-Laham, C. Y. Peng, A. Nanayakkara, M. Challacombe, P. M. W. Gill, B. Johnson, W. Chen, M. W. Wong, J. L. Andres, C. Gonzalez, M. Head-Gordon, E. S. Replogle, J. A. Pople, Gaussian 98, Revision A.9. Gaussian, Inc., Pittsburgh, PA, 1998.

[24] A. D. Becke, *Physical Review A* **1988**, *38*, 3098.

[25] A. D. Becke, *Journal of Chemical Physics* **1993**, *98*, 5648.

[26] C. T. Lee, W. T. Yang, R. G. Parr, *Physical Review B* **1988**, *37*, 785.

[27] R. D. Brown, M. P. Headgordon, *Molecular Physics* **1987**, *61*, 1183.

[28] P. L. Cummins, G. B. Bacskay, N. S. Hush, *Molecular Physics* **1987**, *62*, 193.

[29] R. Ditchfield, *Molecular Physics* **1974**, *27*, 789.

[30] K. Wolinski, J. F. Hinton, P. Pulay, *Journal of the American Chemical Society* **1990**, *112*, 8251.

[31] H. Noth, *Zeitschrift Fur Naturforschung Section B-a Journal of Chemical Sciences* **1980**, *35*, 119.

[32] A. K. Jameson, C. J. Jameson, *Chemical Physics Letters* **1987**, *134*, 461.

[33] G. Schreckenbach, T. Ziegler, *Journal of Physical Chemistry* **1995**, *99*, 606.

[34] S. Patchkovskii, T. Ziegler, *Journal of Physical Chemistry A* **2001**, *105*, 5490.

[35] M. Eden, M. H. Levitt, *Journal of Magnetic Resonance* **1998**, *132*, 220.

[36] J. W. Akitt, in *Multinuclear NMR* (Ed.: J. Mason), Plenum Press, New York, **1987**, pp. 259.

[37] O. Knop, *Acta Crystallographica Section A* **1976**, *32*, 147.

- [38] O. Knop, E. M. Palmer, R. W. Robinson, *Acta Crystallographica Section A* **1975**, *31*, 19.
- [39] J. W. Akitt, W. S. McDonald, *Journal of Magnetic Resonance* **1984**, *58*, 401.
- [40] E. A. C. Lucken, *Nuclear Quadrupole Coupling Constants*, Academic Press, New York, **1969**.
- [41] J. W. Akitt, in *Multinuclear NMR* (Ed.: J. Mason), Plenum Press, New York, **1987**, pp. 189.
- [42] I. Hung, R. W. Schurko, *Solid State Nuclear Magnetic Resonance* **2003**, *24*, 78.
- [43] R. Benn, H. Lehmkuhl, K. Mehler, A. Rufinska, *Angewandte Chemie-International Edition in English* **1984**, *23*, 534.
- [44] C. Dohmeier, H. Schnockel, C. Robl, U. Schneider, R. Ahlrichs, *Angewandte Chemie-International Edition in English* **1993**, *32*, 1655.
- [45] C. Janiak, H. Schumann, C. Stader, B. Wrackmeyer, J. J. Zuckerman, *Chemische Berichte-Recueil* **1988**, *121*, 1745.
- [46] J. T. Cheng, J. C. Edwards, P. D. Ellis, *Journal of Physical Chemistry* **1990**, *94*, 553.
- [47] W. P. Power, R. E. Wasylshen, S. Mooibroek, B. A. Pettitt, W. Danchura, *Journal of Physical Chemistry* **1990**, *94*, 591.
- [48] A. M. Orendt, J. C. Facelli, Y. J. Jiang, D. M. Grant, *Journal of Physical Chemistry A* **1998**, *102*, 7692.
- [49] D. E. Wemmer, D. J. Ruben, A. Pines, *Journal of the American Chemical Society* **1981**, *103*, 28.

- [50] D. E. Wemmer, A. Pines, *Journal of the American Chemical Society* **1981**, *103*, 34.
- [51] S. J. Heyes, C. M. Dobson, *Journal of the American Chemical Society* **1991**, *113*, 463.
- [52] A. J. Campbell, C. A. Fyfe, *Journal of the American Chemical Society* **1972**, *94*, 8387.
- [53] A. Kubo, R. Ikeda, D. Nakamura, *Chemistry Letters* **1981**, 1497.
- [54] G. Schreckenbach, *Journal of Chemical Physics* **1999**, *110*, 11936.
- [55] H. W. Spiess, R. Groseescu, U. Haeberlen, *Chemical Physics* **1974**, *6*, 226.
- [56] H. W. Spiess, *Chemical Physics* **1974**, *6*, 217.
- [57] M. Mehring, *Principles of High Resolution NMR in Solids*, 2nd ed., Springer-Verlag, New York, **1983**.
- [58] M. Witschas, H. Eckert, H. Freiheit, A. Putnis, G. Korus, M. Jansen, *Journal of Physical Chemistry A* **2001**, *105*, 6808.
- [59] R. W. Schurko, S. Wi, L. Frydman, *Journal of Physical Chemistry A* **2002**, *106*, 51.



# Chapter 3

## Correlation of Anisotropic NMR Interaction Tensors With the Structure and Dynamics of Homoleptic Beryllocenes

### 3.1 Introduction

Due to its unusual structure, much work has been devoted to the study of bis(cyclopentadienyl)beryllium,  $\text{Cp}_2\text{Be}$  ( $\text{Cp} = \text{C}_5\text{H}_5$ ), since its preparation in 1959.<sup>[1]</sup> From the outset it was clear that  $\text{Cp}_2\text{Be}$  did not possess a highly symmetric geometry (as ferrocene does) because of the dipole moment observed in solution.<sup>[1]</sup> However,  $\text{Cp}_2\text{Be}$  was found to crystallize in the space group  $P2_1/c$  with two molecules per unit cell ( $Z = 2$ ), making it isomorphous with  $\text{Cp}_2\text{Fe}$  and suggesting a centro-symmetric geometry in the solid state.<sup>[2]</sup> The bonding in  $\text{Cp}_2\text{Be}$  was initially determined to be predominantly ionic by IR spectroscopy,<sup>[3]</sup> and a structure for the compound was first postulated by Almenningen and co-workers based upon data from vapor phase electron diffraction.<sup>[4]</sup> The hypothesized structure consisted of two parallel, staggered Cp rings and a beryllium atom lying at one of two alternate positions along the five-fold principal axis of the molecule, 1.485(5) Å from one ring and 1.98(1) Å from the other (Figure 3.1, I). The report of such an unusual  $C_{5v}$  structure quickly drew the attention of many researchers. A semi-empirical molecular orbital (MO) study, in which the position of Be is varied along the molecular  $C_5$  axis, was unsuccessful in determining the most energetically favourable Be position.<sup>[5]</sup> However, the calculations suggested that UV spectroscopy could be used

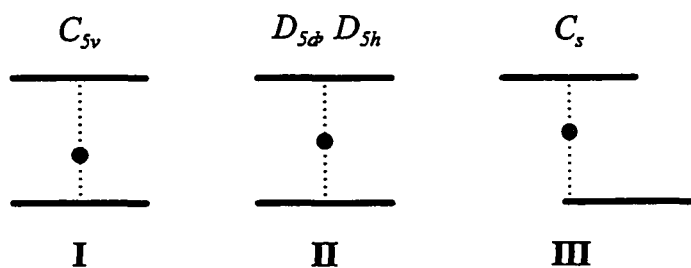


**Figure 3.1** Schematic of proposed  $\text{Cp}_2\text{Be}$  structures with different point symmetries.

to discern if the Be was asymmetrically (**I**) or symmetrically (**II**) disposed along the  $C_5$  axis. Further investigation of  $\text{Cp}_2\text{Be}$  by IR spectroscopy in the vapor,<sup>[6]</sup> solution and solid phases,<sup>[7]</sup> as well as a least-square refinement of the vapor phase diffraction intensities recorded by Almenningen,<sup>[4]</sup> provided support for the existence of structure **I**. Furthermore, a LCAO MO study comparing **I** and **II** for  $\text{Cp}_2\text{Be}$  found the  $C_{5v}$  geometry to have a lower total electronic energy,<sup>[8]</sup> and analysis of Raman and IR spectral data estimated the average time spent by the Be at each of the alternate positions to be on the order of  $10^{-13}$  to  $10^{-12}$  s.<sup>[9]</sup>

In 1972, Wong and co-workers reported the first low-temperature ( $-120^\circ\text{C}$ ) X-ray crystal structure of  $\text{Cp}_2\text{Be}$ .<sup>[10]</sup> The two Cp rings were found to be more or less parallel (as in ferrocene) and staggered with respect to each other, however, one of the rings appeared as if it had “slipped” sideways with its centroid  $1.20\text{ \AA}$  away from the ideal  $D_{5d}$  five-fold axis, resulting in a structure with the Be atom roughly equidistant from all five carbons of one Cp ring and bound to only one carbon on the other Cp ring (dubbed the ‘slip’ sandwich structure; **III** in Figure 3.1). The distances from the Be atom to the  $\eta^5$ -Cp ring centroid and the closest carbon on the  $\eta^1$ -Cp ring were found to be  $1.53\text{ \AA}$  and  $1.81\text{ \AA}$ , respectively. The discovery of a new  $\text{Cp}_2\text{Be}$  structure quickly led researchers to

reevaluate previous data. Previously reported vapor phase electron diffraction data were re-examined using the geometrical parameters for the 'slip' sandwich structure;<sup>[11]</sup> it was demonstrated that the data did not support a "slip" of 0.6 Å or more from the  $D_{5h}$  position of the Cp ring. It was also noted that the bonding in the 'slip' sandwich should be described more appropriately as having polyhapto  $\pi$ -coordination ( $\eta^x$ ) rather than a  $\sigma$ -bond between Be and the singly-bound Cp ring, due to the parallel arrangement of the Cp rings. Wong and co-workers went on to re-examine the crystal structure of  $Cp_2Be$  at room temperature,<sup>[12, 13]</sup> and found a similar structure to the one reported at  $-120^\circ C$ , but with notable differences. The Cp rings were found to be intermediate between the staggered and eclipsed conformations, and the  $Be-(\eta^5-Cp)$  and  $Be-(\eta^1-Cp)$  distances were found to be shorter than and longer than, respectively, those observed in the low-temperature structure. These observations, along with the appearance of a single resonance in solution  $^1H$  NMR spectra, led to the proposition that  $Cp_2Be$  had a highly fluxional structure which underwent rapid ring reorientation about their centroids *and* possibly exchange of the Be atom between the two half-occupied crystallographic positions. Solution  $^1H$  and  $^9Be$  NMR spectra revealed a single resonance,<sup>[14]</sup> and even upon lowering the temperature to  $-135^\circ C$  a single peak remained in  $^1H$  NMR spectra.<sup>[15]</sup> A number of theoretical studies were performed in order to examine the bonding in  $Cp_2Be$  and determine its lowest energy structure.<sup>[16-26]</sup> In contrast to previous results, all calculations favoured structures **II** and **III** energetically over the  $C_{5v}$ -type structures. Further investigation of  $Cp_2Be$  by Raman spectroscopy in solution and the solid state,<sup>[27]</sup> solution IR spectroscopy,<sup>[28]</sup> microwave dielectric loss measurements,<sup>[29]</sup> solution  $^{13}C$  and

$^9\text{Be}$  NMR spectroscopy,<sup>[30, 31]</sup> as well as more accurate low-temperature (128 K) X-ray crystal diffraction,<sup>[32]</sup> all contributed increasing support for structure **III**. In fact, comparison of IR spectra of vapor, solution and solid  $\text{Cp}_2\text{Be}$  suggests that some form of **III** actually persists in all phases.<sup>[33]</sup>

More recently, studies using Car-Parrinello molecular dynamics (MD) calculations,<sup>[34]</sup> and the synthesis of various other beryllocenes with substituted Cp rings have been performed in order to examine the structure and dynamics of  $\text{Cp}_2\text{Be}$  and features common to beryllocenes. MD calculations predict that the ground state for  $\text{Cp}_2\text{Be}$  should have a structure resembling that of **III**, and that this structure is energetically favoured over both the  $D_{5d}$  and  $D_{5h}$  geometries by approximately 10  $\text{kJ mol}^{-1}$ .<sup>[35]</sup> Furthermore, two dynamic processes are observed in accordance with the initial proposition by Wong and co-workers:<sup>[13]</sup> (1) 1,2-sigmatropic rearrangement of the  $\eta^1$ -ring wherein the Be-( $\eta^1$ -Cp) bond moves from one carbon atom to an adjacent carbon atom, and (2) intra-molecular exchange caused by ‘inversion’ of the coordination modes between the  $\eta^5$ - and  $\eta^1$ -Cp rings.<sup>[36]</sup> Notably, these two processes are calculated to have activation barriers of 5 and 8  $\text{kJ mol}^{-1}$  at 400 K, and rates of 1 – 4 and 0.3 – 1.5  $\text{ps}^{-1}$ , respectively, in close agreement with the barrier (5.2  $\text{kJ mol}^{-1}$ ) for Cp ring inversion determined from variable temperature  $^{13}\text{C}$  solution NMR spectra of  $\text{Cp}_2\text{Be}$ .<sup>[31]</sup> A number of substituted- and mixed-Cp’ beryllocenes have been prepared by Conejo and co-workers, including  $\text{Cp}^*_2\text{Be}$  ( $\text{Cp}^* = \text{C}_5\text{Me}_5$ ),  $(\text{C}_5\text{Me}_4\text{H})_2\text{Be}$  and  $\text{Cp}^*\text{Be}(\text{C}_5\text{Me}_4\text{H})$ .<sup>[37-39]</sup> Through the reaction of  $\text{Cp}^*_2\text{Be}$  and  $(\text{C}_5\text{Me}_4\text{H})_2\text{Be}$  with 2,6-dimethylphenyl isocyanide (CNXyl), Conejo and co-workers have provided experimental chemical evidence for the

presence of the  $\eta^5, \eta^1$ -isomer of  $\text{Cp}^*_2\text{Be}$  in solution and sigmatropic rearrangement of the  $\eta^1$ -ring in  $(\text{C}_5\text{Me}_4\text{H})_2\text{Be}$ .<sup>[40]</sup> This conclusion rests on the reasonable assumption that the observed iminoacyl products result from coupling of the  $\eta^5, \eta^1$  isomers of the corresponding beryllocenes with CNXyl. Similarly, evidence for molecular rearrangement ('inversion') of the  $\eta^5$ - and  $\eta^1$ -rings has also been provided by reactions of  $\text{Cp}^*\text{Be}(\text{C}_5\text{Me}_4\text{H})$  with CNXyl.<sup>[41]</sup>

$^9\text{Be}$  is a spin-3/2 quadrupolar nucleus with a small nuclear quadrupole moment ( $Q(^9\text{Be}) = 5.288 \times 10^{-30} \text{ m}^2$ ),<sup>[42, 43]</sup> 100% natural abundance and receptivity of 78.7 compared to  $^{13}\text{C}$ . However, there are relatively few examples of solid-state  $^9\text{Be}$  NMR in the literature, likely because of the extreme toxicity of beryllium-containing compounds. Solid-state  $^9\text{Be}$  NMR spectra of  $\text{Be}(\text{acac})_2$  have been reported,<sup>[44]</sup> along with studies that focus mainly upon the characterization of beryllium sites in minerals.<sup>[44-54]</sup> The  $^9\text{Be}$  quadrupole coupling constants measured for these compounds all fall within the relatively narrow range of 30 – 700 kHz. To the best of our knowledge, there are no reported solid-state  $^9\text{Be}$  NMR studies on organometallic beryllium complexes, although various organometallic complexes have been studied by solution  $^9\text{Be}$  NMR and quantum mechanical calculations.<sup>[14, 31, 44, 55-57]</sup>

Herein we present the solid-state  $^9\text{Be}$  and  $^{13}\text{C}$  NMR study of  $\text{Cp}_2\text{Be}$  (1),  $\text{Cp}^*_2\text{Be}$  (2) and  $(\text{C}_5\text{Me}_4\text{H})_2\text{Be}$  (3) (Figure 3.2). Theoretical and experimental  $^9\text{Be}$  electric field gradient (EFG) and chemical shielding (CS) tensors are reported, as well as the relationship between these NMR interaction tensors and the molecular structure of the beryllocenes. There has been much recent progress in understanding the fluxional

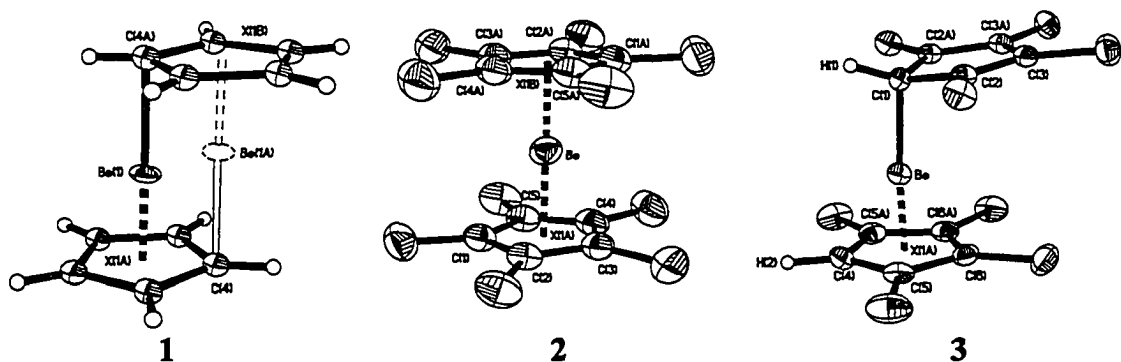


**Figure 3.2** Molecules of (1)  $\text{Cp}_2\text{Be}$ , (2)  $\text{Cp}^*_2\text{Be}$  and (3)  $(\text{C}_5\text{Me}_4\text{H})_2\text{Be}$  from their respective crystal structures.

structures of beryllocenes, yet not much work studying the intra-molecular dynamics present in the solid state has been reported. To address this, variable-temperature (VT)  $^9\text{Be}$  and  $^{13}\text{C}$  NMR, as well as  $^{13}\text{C}/^9\text{Be}/^1\text{H}$  triple-resonance experiments, are utilized to probe the changes in the NMR interaction tensors and isotropic NMR signals with intra-molecular dynamics which occur on the dynamic NMR timescale.

## 3.2 Experimental

### 3.2.1 Sample Preparation and Handling

Compounds 1, 2 and 3 were prepared using literature procedures.<sup>[3, 37]</sup> **CAUTION:** *Extreme care must be taken in dealing with beryllium compounds because they are very toxic and can cause serious irreversible effects.*

### 3.2.2 Solid-State NMR Spectroscopy

$^9\text{Be}$  and  $^{13}\text{C}$  NMR spectra were acquired on a Varian Infinity+ NMR spectrometer with an Oxford 9.4 T ( $\nu_0(^1\text{H}) = 400$  MHz) wide-bore magnet operating at 56.2 MHz and

100.5 MHz for  $^9\text{Be}$  and  $^{13}\text{C}$ , respectively. Samples were finely powdered and packed under a nitrogen atmosphere into 4 mm outer diameter  $\text{ZrO}_2$  rotors.

Central transition selective  $\pi/2$  pulse widths of 0.75, 2.0 and 2.2  $\mu\text{s}$  with rf fields of  $\nu_1 = 166.7, 62.5$  and  $56.8$  kHz, spectral widths (sw) of 20, 40 and 20 kHz, and recycle delays of 10, 10 and 20 s were employed, respectively, for the static  $^9\text{Be}$  NMR spectra of **1**, **2** and **3**. Central transition selective pulse widths are non-selective pulse widths which have been scaled by a factor of  $(I + 1/2)^{-1}$ , where  $I$  is the nuclear spin quantum number. The  $^9\text{Be}$  MAS spectrum of **3** was acquired with the same parameters as the static spectrum but with a 10 kHz spectral window. For the  $^9\text{Be}$  SATRAS spectra of **1** and **2**, central transition selective  $\pi/2$  pulse widths of 1.5 and 2.25  $\mu\text{s}$  with rf fields of  $\nu_1 = 83.3$  and 55.6 kHz and recycle delays of 4 and 15 s were employed, respectively.

The  $^{13}\text{C}$  CP/MAS spectra of **1** were acquired at  $\nu_{\text{rot}} = 1415$  and 4500 Hz with a proton  $\pi/2$  pulse of 5.5  $\mu\text{s}$ , contact time (ct) of 15 ms, sw = 40 kHz and recycle delay of 10 s; for **2**:  $\nu_{\text{rot}} = 1040$  and 3500 Hz, proton  $\pi/2$  pulse = 2.75  $\mu\text{s}$ , ct = 9 ms, sw = 50 kHz and recycle delay = 15s, while for **3**:  $\nu_{\text{rot}} = 4000$  and 15000 Hz, proton  $\pi/2$  pulse = 4.5  $\mu\text{s}$ , ct = 15 ms, sw = 50 kHz and recycle delay = 20 s. Variable-temperature (VT)  $^{13}\text{C}/^9\text{Be}/^1\text{H}$  CP/TRAPDOR (TRANSfer of Populations in DOuble Resonance) experiments on all three species were recorded in a similar fashion as CP/MAS spectra with additional on-resonance irradiation of beryllium nuclei over one rotor period with rf fields of ca. 30, 40 and 60 kHz for **1**, **2** and **3**.

Beryllium chemical shifts were referenced to a concentrated aqueous solution of  $\text{BeCl}_2$  ( $\delta_{\text{iso}} = 0.0$  ppm); carbon shifts are reported with respect to the  $\text{Si}(\text{CH}_3)_4$  scale ( $\delta_{\text{iso}} =$

0.0 ppm) by setting the chemical shift of the adamantane high-frequency resonance to 38.57 ppm. Variable-temperature experiments were performed within a temperature range of 110 °C to -120 °C with an accuracy of  $\pm 1$  °C at the extremes.

### 3.2.3 Spectral Simulations

Analytical simulations of  $^9\text{Be}$  static and MAS NMR spectra were performed with the WSOLIDS software package.<sup>[58]</sup> Further refinement of quadrupolar parameters for the SATRAS NMR spectra of **1** and **2** was performed via numerical simulations with the SIMPSON software package.<sup>[59]</sup> SIMPSON simulations were performed by the *direct* method of powder averaging using the *zcw4180* crystal file provided with the package. The gamma angles parameter was set to  $(sw/v_{\text{rot}})$ , where *sw* is the spectral width and  $v_{\text{rot}}$  is the rate of spinning; in the case of **2**, *sw* had to be increased to 301.5 kHz to accommodate the equation for the gamma angles. The start and detect operators were set to  $I_{1z}$  and  $I_{1p}$ , respectively, while all other parameters were set equal to those employed experimentally. Simulated spectra were saved in ASCII format as free induction decay (FID) files without any mathematical manipulation and converted to files readable by the NUTS (Acorn NMR) software for further processing. Best-fit spectra were obtained by comparison of root-mean-square difference spectra, and experimental errors for the extracted NMR parameters were determined by bidirectional variation. All experimental carbon chemical shift tensors were obtained by analysis of  $^{13}\text{C}$  NMR spectra with the method of Herzfeld and Berger.<sup>[60, 61]</sup>

Conventions used for the specification of EFG and chemical shift parameters



differ between the WSOLIDS and SIMPSON simulation programs, and therefore, the reader is alerted to these differences. Whereas WSOLIDS uses the right-handed EFG and chemical shift tensors given by ( $|V_{zz}| \geq |V_{yy}| \geq |V_{xx}|$ ;  $C_Q = eV_{zz}Q/h$ ;  $\eta_Q = (V_{xx} - V_{yy})/V_{zz}$ ) and ( $\delta_{11} \geq \delta_{22} \geq \delta_{33}$ ;  $\Omega = \delta_{11} - \delta_{33}$ ;  $\kappa = 3(\delta_{22} - \delta_{iso})/\Omega$ ), respectively, the conventions employed in SIMPSON differ ( $|V_{zz}| \geq |V_{xx}| \geq |V_{yy}|$ ;  $C_Q = eV_{zz}Q/h$ ;  $\eta_Q = (V_{yy} - V_{xx})/V_{zz}$ ;  $|\delta_{zz} - \delta_{iso}| \geq |\delta_{xx} - \delta_{iso}| \geq |\delta_{yy} - \delta_{iso}|$ ;  $\delta = \delta_{zz} - \delta_{iso}$ ;  $\kappa = (\delta_{yy} - \delta_{xx})/\delta$ ). In cases where the chemical shift and EFG tensors do not coincide, Euler angles are implemented to describe their relative orientation. One must be cautious in selecting Euler angles appropriate to the convention implemented within the simulation software. The WSOLIDS conventions are followed in the present work. Namely, the Euler angles  $\alpha$ ,  $\beta$  and  $\gamma$  are employed for unitary transformations in the order  $\mathbf{R}_z(\gamma)\mathbf{R}_y(\beta)\mathbf{R}_z(\alpha)$ ,<sup>[62, 63]</sup> where  $\mathbf{R}_i(\theta)$  performs a counter-clockwise (positive) rotation about the positive  $i$ -axis by angle  $\theta$ , producing a new rotation axis  $i'$ , such that a coordinate system initially coincident with the EFG principal axis system (PAS) ends up coincident with the chemical shift PAS after the transformation (i.e., an active transformation).

### 3.2.4 Theoretical Calculations

Calculations of EFG and chemical shielding tensors were performed using Gaussian 98<sup>[64]</sup> on a Dell Precision 420 workstation with dual 733 MHz Pentium III processors running the Red Hat Linux 6.2 operating system. Calculations were done on isolated molecules with molecular coordinates obtained from the crystal structures resolved by X-ray diffraction.<sup>[32, 37]</sup> Computations were carried out using restricted

Hartree-Fock (RHF) and hybrid density functional theory (DFT) with the B3LYP functional,<sup>[65-67]</sup> and the 6-31G\*\*, 6-311G\*\* and 6-311+G\*\* basis sets for all nuclei.<sup>[43]</sup> Quadrupole coupling constants ( $C_Q$ ) were converted from atomic units (a.u.) to Hz by multiplying the largest component of the EFG tensor,  $V_{33}$ , by  $eQ/h \times 9.71736 \times 10^{21} \text{ V m}^{-2}$ , where  $Q(^9\text{Be}) = 5.3 \times 10^{-30} \text{ m}^2$ ,<sup>[42, 43]</sup>  $h = 6.626 \times 10^{-34} \text{ J s}$  and  $e = 1.602188 \times 10^{-19} \text{ C}$ . Chemical shielding tensors were calculated using the gauge-including atomic orbital (GIAO) method<sup>[68, 69]</sup> excluding relativistic effects. Calculated beryllium shielding data was referenced by setting the theoretical isotropic chemical shielding of  $\text{Be}(\text{H}_2\text{O})_4^{2+}$  to  $\delta_{\text{iso}} = 0.0 \text{ ppm}$ . Similarly, carbon CS tensors were referenced to the theoretical shielding of CO as a secondary reference by subtracting the theoretical shielding data of the compound from that of CO (calculated with the corresponding theoretical method and basis set) and then adding  $\delta_{\text{iso}}(\text{CO}) = 187.1 \text{ ppm}$ .<sup>[70]</sup>

## 3.3 Results and Discussion

### 3.3.1 Solid-State $^9\text{Be}$ NMR

Experimental  $^9\text{Be}$  MAS NMR spectra of **1**, **2** and **3** are shown in Figure 3.3 along with corresponding numerical (a, b) and analytical (c) simulations. The  $^9\text{Be}$  quadrupolar coupling constants of **1** and **2** are relatively small in magnitude (0.41 and 0.23 MHz, respectively), resulting in the absence of observable second-order quadrupolar effects in the central transition powder pattern. Thus, acquisition of satellite transition (SATRAS) NMR spectra is necessary to extract the  $^9\text{Be}$  quadrupolar parameters (EFG and CS

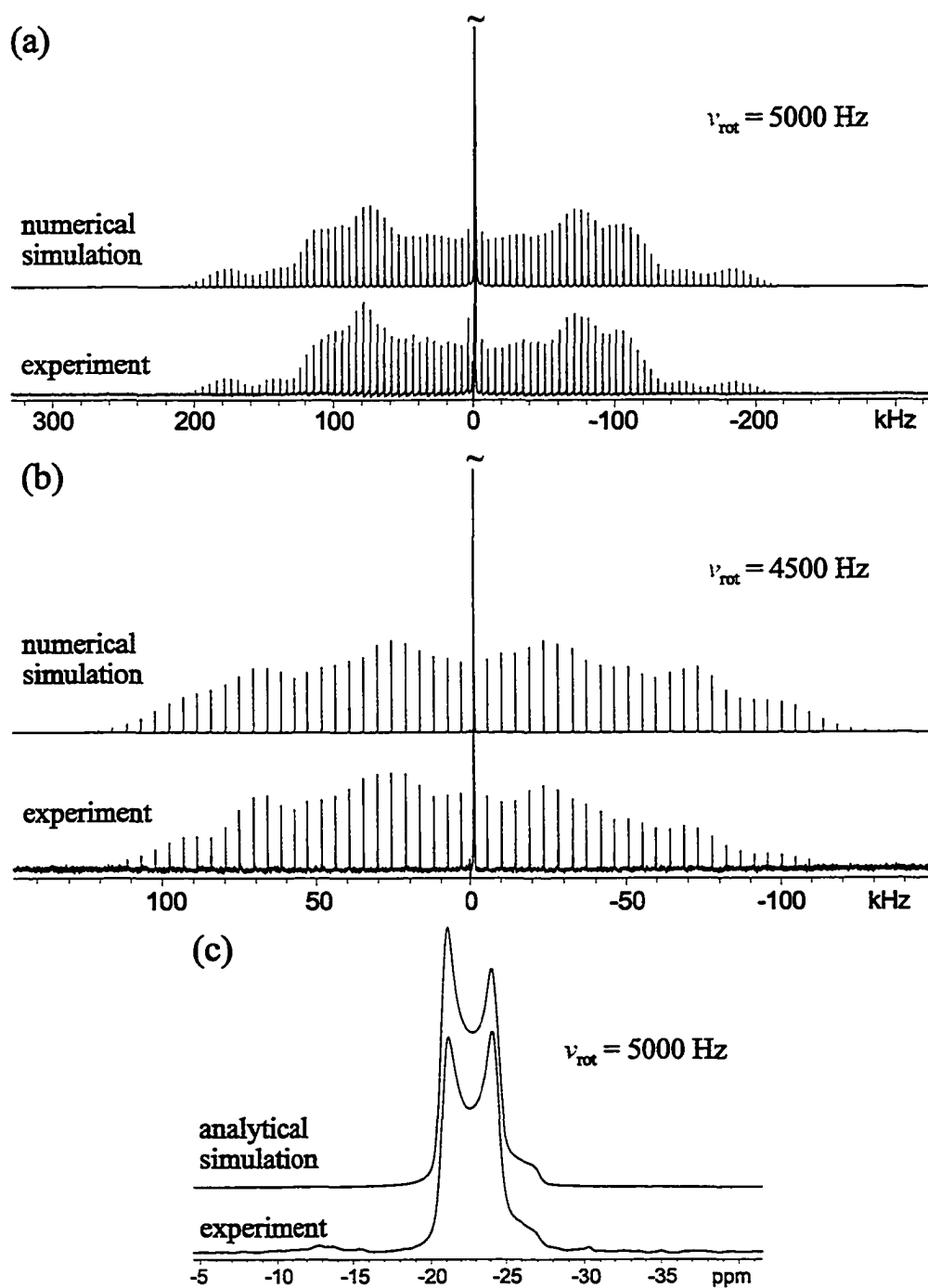


**Figure 3.3**  $^9\text{Be}$  MAS NMR spectra of (a) **1**, (b) **2** and (c) **3**. Simulations of **1** and **2** were performed with SIMPSON and that of **3** with WSOLIDS.

parameters derived from spectral simulations for **1**, **2** and **3** are shown in Table 3.1). In contrast to **1** and **2**, the spectrum of **3** displays a characteristic second-order quadrupolar

powder pattern which yields  $C_Q = 0.61$  MHz and  $\eta_Q = 0.13$ . Notably, as the spherical symmetry decreases in the order  $2 \rightarrow 1 \rightarrow 3$ , the magnitude of  $C_Q(^9\text{Be})$  increases correspondingly:  $0.23 \rightarrow 0.41 \rightarrow 0.61$  MHz. It is intriguing that the  $C_Q(^9\text{Be})$  of **1** has an intermediate value compared to **2** and **3**, which possibly reflects its unusual equilibrium geometry consisting of  $\eta^5, \eta^x$  coordination to the Cp rings.

**Table 3.1**  
Experimental  $^9\text{Be}$  and  $^{13}\text{C}$  NMR Parameters

Parameter	<b>1</b>		<b>2</b>		<b>3</b> <sup>[a]</sup>
	$^9\text{Be}$	$^{13}\text{C}$	$^9\text{Be}$	$^{13}\text{C}$ <sup>[b]</sup>	$^9\text{Be}$
$ C_Q $ [MHz]	0.41(2)	—	0.23(2)	—	0.61(5)
$\eta_Q$	0.25(5)	—	0.55(5)	—	0.13(7)
$\delta_{\text{iso}}$ [ppm]	-21(1)	108.2(2)	-24.4(7)	110(3)	-19.8(5)
$\Omega$ [ppm]	65(2)	130(2)	55(5)	112(1)	54(4)
$\kappa$	0.83(4)	1.0	0.86(7)	1.0	0.85(8)
$\delta_{11}$ [ppm]	2.5	151.5	-4.8	147.3	-0.5
$\delta_{22}$ [ppm]	-3	151.5	-8.6	147.3	-4.5
$\delta_{33}$ [ppm]	-62.5	21.5	-59.8	35.3	-54.5
$\alpha$ [°]	0	—	90	—	90
$\beta$ [°]	38(5)	—	28	—	4(2)
$\gamma$ [°]	0	—	44	—	0

<sup>[a]</sup> Carbon CS parameters for  $(\text{C}_5\text{Me}_4\text{H})_2\text{Be}$  are shown in Table 3.2. <sup>[b]</sup> Carbon chemical shift tensor corresponds to aromatic carbons.

The experimental static  $^9\text{Be}$  NMR spectra of **1**, **2** and **3** are shown in Figure 3.4 along with simulations including and excluding the effects of CSA. Comparison of simulated spectra which only take into account the  $^9\text{Be}$  nuclear quadrupolar interaction (top traces) with the experimental spectra (bottom traces) indicates the presence of beryllium CSA (confirmed by the simulations shown in the middle traces). Although  $^9\text{Be}$  EFG parameters for the three species are markedly different, the CS parameters (i.e.,  $\delta_{\text{iso}}$ ,

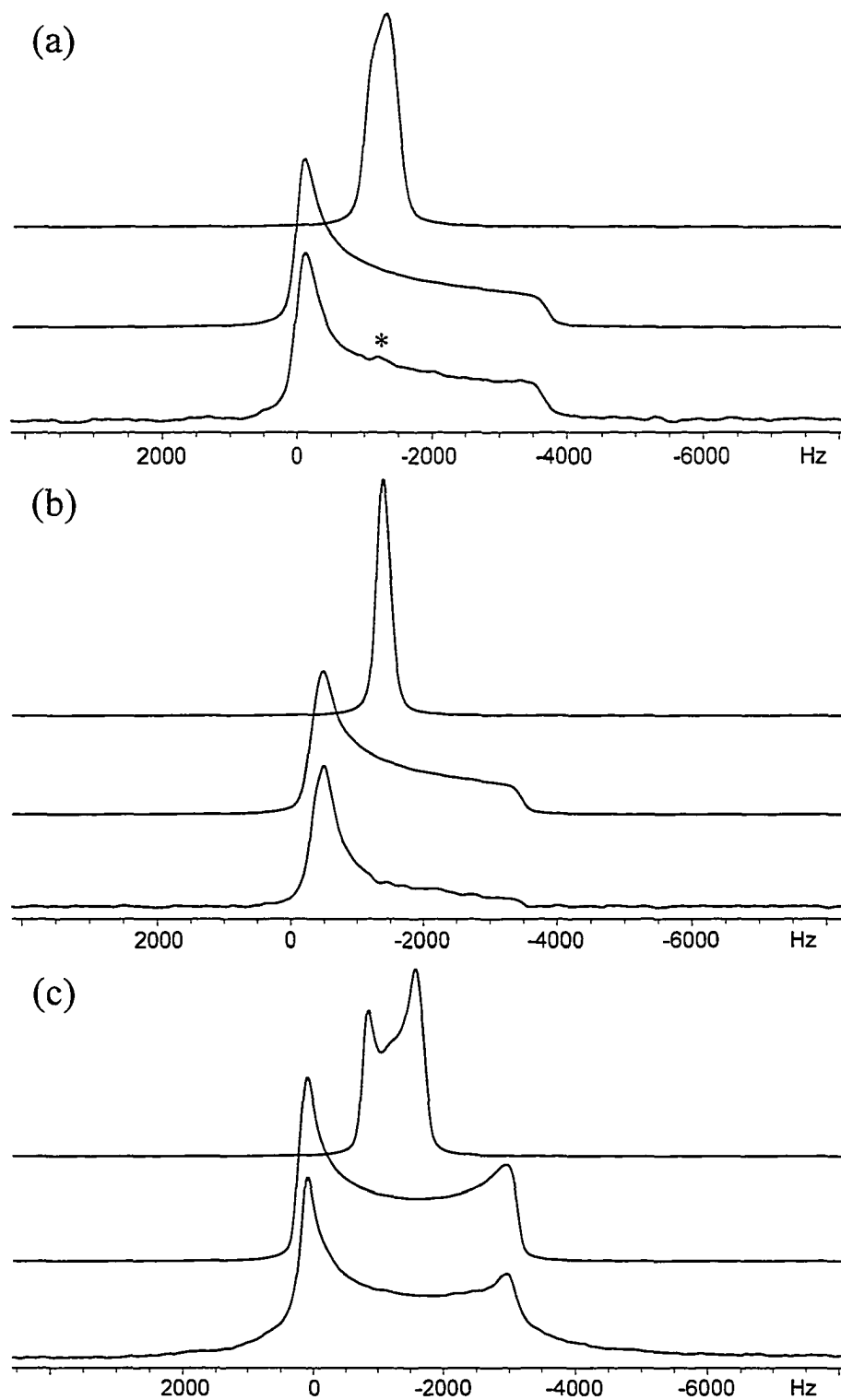


**Figure 3.4** Static  $^9\text{Be}$  NMR spectra of (a) **1**, (b) **2** and (c) **3**. Traces: bottom – experimental; middle – simulation including CSA; top – simulation excluding CSA. Asterisk (\*) points out resonance at the isotropic position.

$\Omega$  and  $\kappa$  in Table 3.1) appear to be relatively similar. These differences appear small because of the relatively small beryllium chemical shift range (ca. +25 to -25 ppm).<sup>[71, 72]</sup> In light of this, we note that the CSA of **1** is significantly greater than the other two compounds, and that all three species display chemical shielding spans on the order of the entire known Be chemical shift range for diamagnetic complexes. The large metal CSA caused by coordination to Cp' ligands are consistent with observations from Cp\*<sub>2</sub>Al<sup>+</sup>,<sup>[73]</sup> Cp\*<sub>2</sub>B<sup>+</sup> and Cp\*<sub>2</sub>BMe.<sup>[74]</sup> It is also interesting to note that the Be nuclei become more shielded with increasing hapticity (i.e.,  $\delta_{\text{iso}}(\mathbf{3}) : \eta^5, \eta^1 > \delta_{\text{iso}}(\mathbf{1}) : \eta^5, \eta^x > \delta_{\text{iso}}(\mathbf{2}) : \eta^5, \eta^5$ ), which also corresponds to the trend observed for Cp\*<sub>2</sub>Al<sup>+</sup>, Cp\*<sub>2</sub>B<sup>+</sup> and Cp\*<sub>2</sub>BMe.

Aside from the expected anisotropic powder pattern, the static <sup>9</sup>Be NMR spectrum of **1** reveals a small additional peak at the isotropic position of the powder pattern (marked with an asterisk in Figure 3.4a). Variable-temperature static <sup>9</sup>Be NMR experiments were performed on **1** in order to explore the possibility of observing the effects of intra-molecular dynamics on the powder pattern (Figure 3.5). As the temperature is raised, the isotropic peak gradually increases in magnitude until about 60 °C, where the anisotropic powder pattern completely collapses leaving a very sharp isotropic signal; this process is reversible and no dynamic “coalescence point” is observed. The lack of a coalescence temperature suggests the onset of a phase change in which the Cp<sub>2</sub>Be molecules start to undergo motion(s) capable of completely averaging both the CS and EFG tensors. The large <sup>9</sup>Be CSA patterns for all of the beryllocenes suggest that this peak does not result from an intermediate structure of higher symmetry,

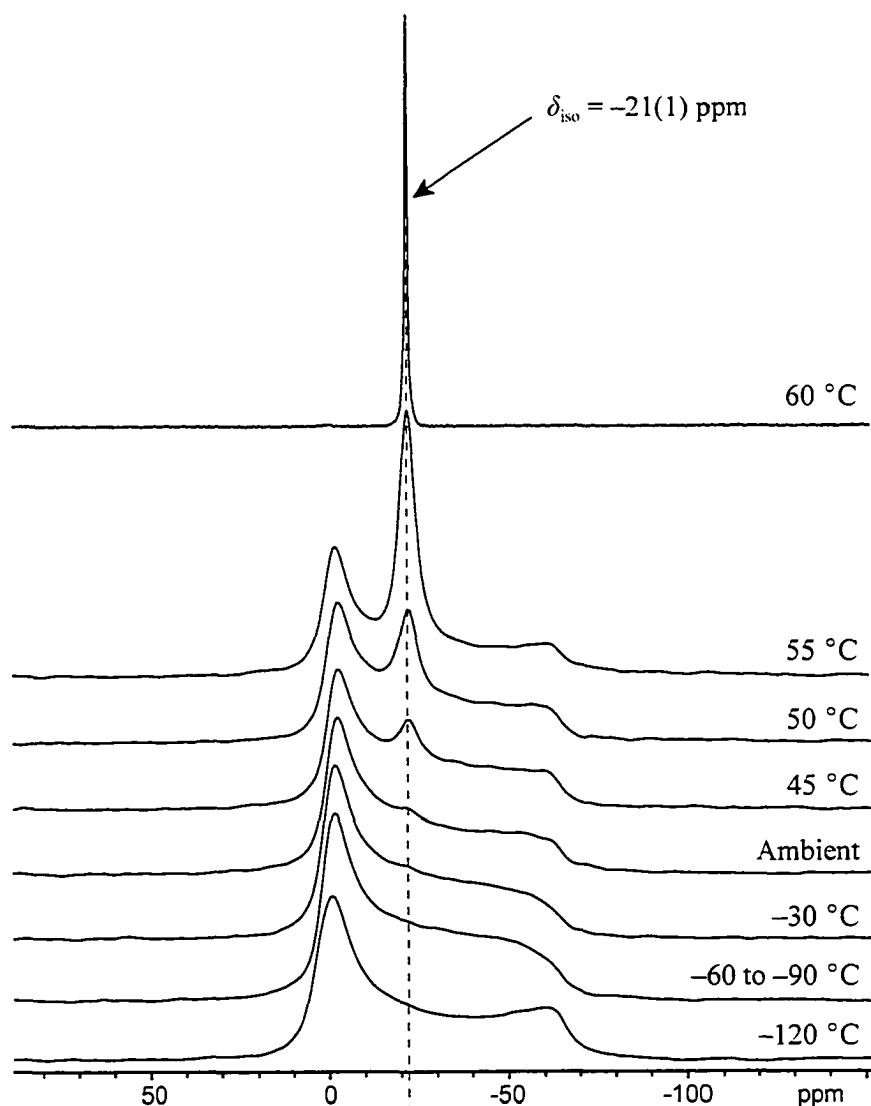


**Figure 3.5** Static  $^9\text{Be}$  VT NMR spectra of **1**.

but rather from a portion of the molecules in the condensed phase undergoing isotropic “solution-like” motion (even at ambient temperature). The sharp isotropic peak and complete absence of CSA effects in the spectrum acquired at 60 °C result from melting of the sample (m.p. 59 °C).<sup>[75]</sup> This process is reversible, since identical static spectra are obtained after cooling the sample from 60 °C, indicating that it is possible to recrystallize  $\text{Cp}_2\text{Be}$  from the melt.

VT  $^9\text{Be}$  NMR experiments were also performed for **2** and **3**. The VT  $^9\text{Be}$  SATRAS NMR spectra of **2** show a change in isotropic shift from  $-23.1$  ppm to  $-25.7$  ppm, as well as an apparent increase in  $C_Q(^9\text{Be})$ , as the temperature is decreased from  $110$  °C to  $-100$  °C (Appendix B, Figure B.1). The origin of the temperature-dependent chemical shift variation is unknown; however, the lower values of  $C_Q$  with increased temperature is well understood, and normally attributed to motional averaging of the EFG tensors due to increased intra-molecular motions at higher temperatures.<sup>[76, 77]</sup> VT  $^9\text{Be}$  NMR experiments on **3** do not show any observable changes with temperature.

### 3.3.2 Solid-State $^{13}\text{C}$ NMR

The  $^{13}\text{C}$  CP/MAS NMR spectra of **1** and **2** (Figures 3.6a, 3.6b) display spinning-sideband manifolds indicative of carbon CSA in the aromatic region, which is common for metallocenes. The aromatic carbon sites have the following CSA parameters: **1**:  $\delta_{\text{iso}} = 108.2$  ppm,  $\Omega = 130$  ppm,  $\kappa = 1.0$ ; **2**:  $\delta_{\text{iso}} = 110$  ppm,  $\Omega = 112$  ppm,  $\kappa = 1.0$ , while the Me carbon nuclei in **2** have  $\delta_{\text{iso}} = 10.7$  ppm – comparable to data reported for other metallocenes. Both the axial symmetry of the aromatic carbon CS tensors (i.e.,  $\kappa = 1.0$ ) and the observation of a single Cp' resonance are attributed to the fast reorientation of the Cp' moieties about their ring centroids.<sup>[73, 78-80]</sup> Due to the lower overall molecular symmetry of **3**, its  $^{13}\text{C}$  NMR spectra (Figure 3.6c) are relatively complex compared to those of **1** and **2**. By spinning the sample at a frequency of  $\nu_{\text{rot}} = 15$  kHz, the spinning sidebands are removed, leaving only the isotropic peaks for each of the distinct carbon environments. Analysis of the sideband manifolds in the slow-spinning ( $\nu_{\text{rot}} = 4.0$  kHz)



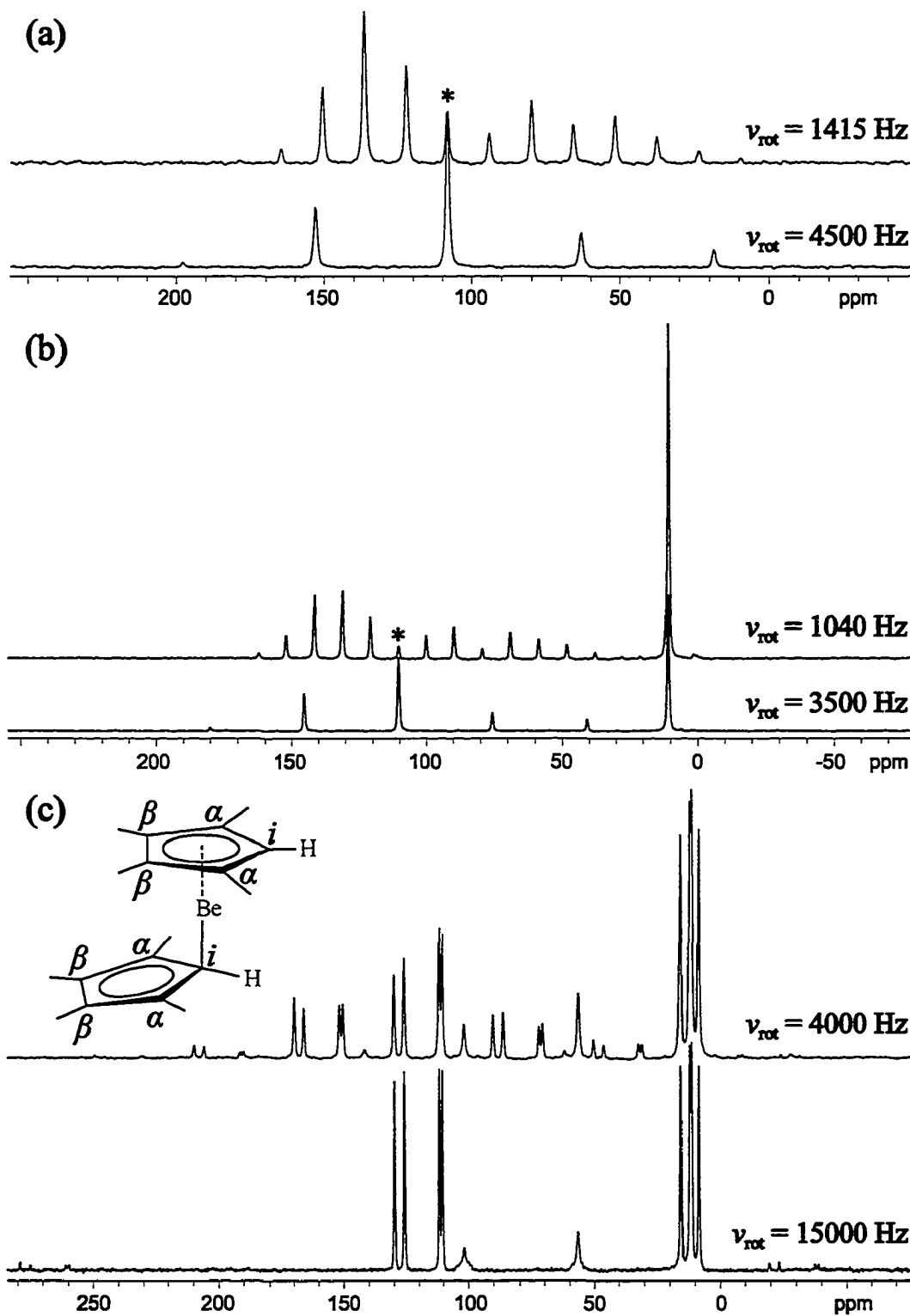


**Figure 3.6**  $^{13}\text{C}$  CP/MAS NMR spectra of (a) 1, (b) 2 and (c) 3 at different spinning frequencies. Inset in (c) shows the labelling scheme of the carbon sites in 3.

spectrum by the method of Herzfeld and Berger yields the carbon CS parameters shown in Table 3.2. From high to low frequency, the  $^{13}\text{C}$  signals are assigned to the  $\eta^1$ :  $\alpha$ - (130.1 ppm),  $\eta^1$ :  $\beta$ - (126.0 ppm),  $\eta^5$ :  $\beta$ - (112.0 ppm),  $\eta^5$ :  $\alpha$ - (110.6 ppm),  $\eta^5$ :  $i$ - (101.9 ppm) and  $\eta^1$ :  $i$ -( $\text{C}_5\text{Me}_4\text{H}$ ) $_2\text{Be}$  carbons (56.8 ppm); the four remaining peaks are collectively assigned to the eight methyl groups. These assignments were based primarily on the values of the CS parameters (i.e.,  $\delta_{\text{iso}}$ ,  $\Omega$  and  $\kappa$ ) of each carbon site. As mentioned above, the axial symmetry ( $\kappa = 1$ ) of Cp' carbon CS tensors has been shown to arise from time-averaging of the  $\delta_{11}$  and  $\delta_{22}$  components caused by reorientation of the carbocycles,<sup>[73, 78-80]</sup> which is also in agreement with the observation of a single  $^{13}\text{C}$  NMR resonance for both rings in solution.<sup>[37]</sup> The signals at 112.0 and 110.6 ppm are therefore assigned to the  $\eta^5$ -Cp' carbons and those at 130.1 and 126.0 ppm can be attributed to the  $\eta^1$ -Cp' carbons. Differentiation of the  $\alpha$ - and  $\beta$ - sites in each of the  $\text{C}_5\text{Me}_4\text{H}$  rings was accomplished by comparison of experimental  $\Omega$  and  $\kappa$  values with theoretical values obtained from ab initio calculations (Table 3.2). Based upon  $^{13}\text{C}/^9\text{Be}/^1\text{H}$  CP/TRAPDOR<sup>[81]</sup> experiments (*vide infra*) and their chemical shifts ( $\delta_{\text{iso}} \sim 100 - 130$  ppm is characteristic of  $\eta^5$ -Cp' carbons), the signals at 101.9 and 56.8 ppm are assigned to the  $\eta^5$ :  $i$ -Cp' and  $\eta^1$ :  $i$ -Cp' sites, respectively.

The  $^{13}\text{C}$  VT CP/MAS spectra of **1** are shown in Figure 3.7. The resonance at  $\delta_{\text{iso}} = 108.2$  ppm gradually splits into two peaks upon cooling to  $-2$  °C ( $\delta_{\text{iso}} = 110.0$  and 106.3 ppm) and remains as such all the way down to  $-110$  °C. The average  $\delta_{\text{iso}}$  of the two peaks found at low temperature is equal to the isotropic shift of the carbon signal at ambient temperature, being highly indicative of chemical exchange. A detailed analysis of the

**Table 3.2**  
Experimental and Theoretical  $^{13}\text{C}$  NMR CS Parameters of **3**

Site	$\delta_{11}$ [ppm]	$\delta_{22}$ [ppm]	$\delta_{33}$ [ppm]	$\delta_{\text{iso}}$ [ppm]	$\Omega$ [ppm]	$\kappa$
<b>Experimental</b>						
$\eta^5$ : $\alpha$ - $\underline{\text{C}}_5\text{Me}_4\text{H}^{[a]}$	151.6	151.6	28.7	110.6	122.9	1.00
$\eta^5$ : $\beta$ - $\underline{\text{C}}_5\text{Me}_4\text{H}$	151.5	151.5	32.9	112.0	118.6	1.00
$\eta^5$ : $i$ - $\underline{\text{C}}_5\text{Me}_4\text{H}$	153.1	115.4	37.2	101.9	115.9	0.35
$\eta^1$ : $\alpha$ - $\underline{\text{C}}_5\text{Me}_4\text{H}$	212.0	145.6	32.7	130.1	179.3	0.26
$\eta^1$ : $\beta$ - $\underline{\text{C}}_5\text{Me}_4\text{H}$	204.8	129.8	43.5	126.0	161.3	0.07
$\eta^1$ : $i$ - $\underline{\text{C}}_5\text{Me}_4\text{H}$	—	—	—	56.8	—	—
<b>RHF/6-31G**</b>						
$\eta^5$ : $\alpha$	165.0	125.8	15.2	102.0	149.8	0.48
$\eta^5$ : $\beta$	165.1	130.9	20.1	105.4	145.0	0.53
$\eta^5$ : $i$	153.4	91.7	15.3	86.8	138.1	0.11
$\eta^1$ : $\alpha$	225.6	135.9	16.0	125.8	209.7	0.14
$\eta^1$ : $\beta$	206.3	116.9	29.6	117.6	176.7	-0.01
$\eta^1$ : $i$	73.0	19.3	9.4	33.9	63.6	-0.69
<b>RHF/6-311G**</b>						
$\eta^5$ : $\alpha$	159.8	117.6	0.5	92.6	159.3	0.47
$\eta^5$ : $\beta$	158.9	122.7	5.4	95.6	153.5	0.53
$\eta^5$ : $i$	146.5	80.3	2.7	76.5	143.8	0.08
$\eta^1$ : $\alpha$	226.5	127.9	1.8	118.8	224.7	0.12
$\eta^1$ : $\beta$	206.1	106.3	15.2	109.2	190.9	-0.05
$\eta^1$ : $i$	61.9	6.9	-3.8	21.7	65.7	-0.67
<b>RHF/6-311+G**</b>						
$\eta^5$ : $\alpha$	161.1	119.0	1.7	93.9	159.4	0.47
$\eta^5$ : $\beta$	160.4	124.3	6.7	97.1	153.7	0.53
$\eta^5$ : $i$	147.5	81.6	3.8	77.6	143.6	0.08
$\eta^1$ : $\alpha$	227.6	129.5	3.2	120.1	224.4	0.13
$\eta^1$ : $\beta$	207.5	108.3	16.5	110.8	191.0	-0.04
$\eta^1$ : $i$	63.4	8.4	-2.4	23.2	65.8	-0.67
<b>B3LYP/6-31G**</b>						
$\eta^5$ : $\alpha$	167.1	135.0	34.4	112.1	132.7	0.52
$\eta^5$ : $\beta$	167.9	140.6	40.2	116.2	127.7	0.57
$\eta^5$ : $i$	157.7	98.8	29.9	95.5	127.8	0.08
$\eta^1$ : $\alpha$	210.9	143.8	34.6	129.8	176.2	0.24
$\eta^1$ : $\beta$	201.0	133.8	48.0	127.6	153.0	0.12
$\eta^1$ : $i$	91.7	32.9	26.6	50.4	65.0	-0.81

**Table 3.2 (cont.)**

Site	$\delta_{11}$ [ppm]	$\delta_{22}$ [ppm]	$\delta_{33}$ [ppm]	$\delta_{\text{iso}}$ [ppm]	$\Omega$ [ppm]	$\kappa$
B3LYP/6-311G**						
$\eta^5: \alpha$	172.0	134.2	24.3	110.2	147.7	0.49
$\eta^5: \beta$	171.3	140.1	30.7	114.0	140.6	0.56
$\eta^5: i$	160.2	94.5	23.6	92.8	136.6	0.04
$\eta^1: \alpha$	222.3	143.2	25.8	130.5	196.5	0.20
$\eta^1: \beta$	210.9	131.4	39.4	127.2	171.6	0.07
$\eta^1: i$	89.6	27.3	19.1	45.3	70.4	-0.77
B3LYP/6-311+G**						
$\eta^5: \alpha$	172.9	135.4	25.1	111.1	147.8	0.49
$\eta^5: \beta$	172.7	142.1	30.8	115.2	141.9	0.57
$\eta^5: i$	160.3	96.2	24.2	93.5	136.1	0.06
$\eta^1: \alpha$	223.2	143.7	25.7	130.9	197.6	0.20
$\eta^1: \beta$	212.8	132.6	40.7	128.7	172.2	0.07
$\eta^1: i$	92.7	25.9	18.6	45.7	74.1	-0.80

<sup>[a]</sup> Labelling scheme of carbon sites can be found in inset of Figure 3.6c.

spectra between the temperatures +3 °C to -5 °C (Appendix B, Figure B.2) reveals the coalescence point ( $\approx -1$  °C) and activation energy ( $E_a = 36.9$  kJ mol<sup>-1</sup>) for the chemical exchange process. The measured  $E_a$  for the ‘inversion’ process lies intermediate to values calculated with the PRDDO method (62.8 – 129.7 kJ mol<sup>-1</sup>),<sup>[17]</sup> and those obtained from MD calculations at 400 K (8 kJ mol<sup>-1</sup>)<sup>[36]</sup> and <sup>9</sup>Be-<sup>13</sup>C spin-spin coupling in solution <sup>13</sup>C VT NMR (5.2 kJ mol<sup>-1</sup>).<sup>[31]</sup> It is worth mentioning that although the <sup>13</sup>C CP/MAS spectra of **1** at higher temperatures (ca. 40 °C – 60 °C) resemble the spectrum obtained at ambient temperature, the optimal contact time was shorter (5 ms) and required the acquisition of many more transients to achieve reasonable intensity than spectra at lower temperatures. The apparent loss in cross-polarization efficiency at higher temperatures may be caused by increased rates of motion which serve to partially average <sup>1</sup>H-<sup>13</sup>C

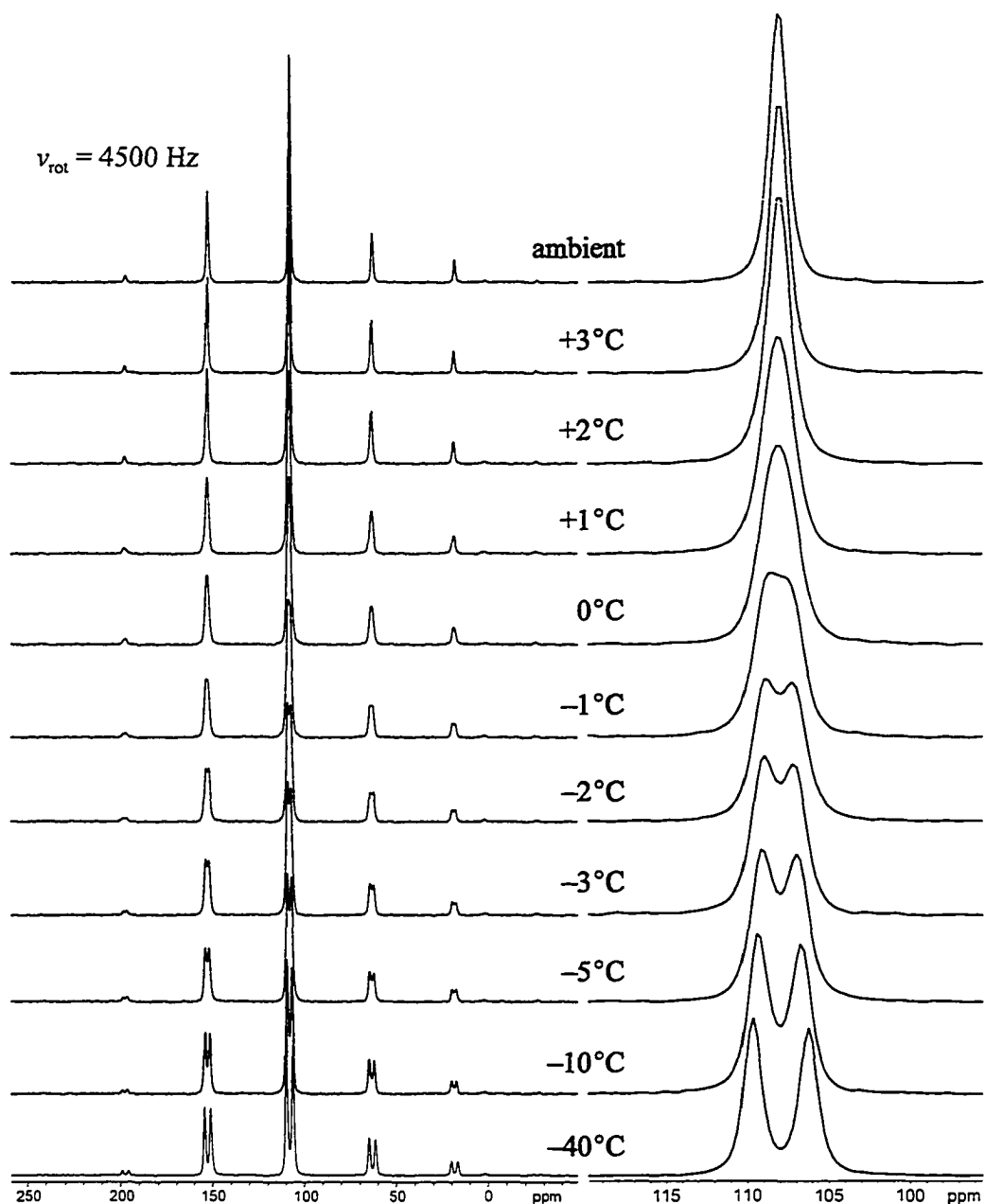


**Figure 3.7**  $^{13}\text{C}$  VT CP/MAS spectra employed for calculation of the activation energy ( $E_a = 36.9 \text{ kJ mol}^{-1}$ ) for Cp ring ‘inversion’ in **1**. Expansion of the isotropic resonances for each of the spectra are shown on the right.

dipolar coupling. The effects of chemical exchange in the  $^{13}\text{C}$  NMR spectra of **1** correlate well with observations from  $^9\text{Be}$  VT NMR spectra: as the temperature is lowered, the time spent by the Be atom at each crystallographic site increases compared to the time

scale of the NMR experiment, resulting in the observation of a single Be site. At the same time, the equivalence of the Cp carbons caused by rapid motion of the Be is nullified and results in observation of the two non-equivalent Cp rings. However, the low temperatures employed are insufficient to slow down the very rapid reorientation of the Cp rings about their five-fold axes, and therefore, the carbon sites within each of the Cp rings cannot be differentiated.

$^{13}\text{C}/^9\text{Be}/^1\text{H}$  VT CP/TRAPDOR NMR experiments were performed in order to examine the intra-molecular dynamics present in all three compounds. By examining the loss in intensity observed in TRAPDOR spectra, it is possible to determine the presence and relative magnitudes of dipolar couplings between beryllium and various carbon nuclei. The  $^{13}\text{C}/^9\text{Be}/^1\text{H}$  CP/TRAPDOR spectrum of **1** (not shown) yields an integrated intensity, including the spinning sidebands, of 0.7 compared to the CP/MAS experiment (normalized integrated intensity of 1.0). Only slight increases in the TRAPDOR effect were observed upon lowering the temperature, and are not very diagnostic of temperature-dependent dynamics.

The  $^{13}\text{C}/^9\text{Be}/^1\text{H}$  CP/TRAPDOR spectrum of **3** is shown in Figure 3.8. As expected, the TRAPDOR effect is most pronounced for the  $\eta^1$ : *i*-Cp' carbon (marked with \*), which is directly bound to the beryllium. Interestingly, the methyl resonances show a larger decrease in intensity under TRAPDOR conditions than the aromatic Cp' carbons; the origin of this effect is unknown at this time. VT experiments (not shown) from 80 °C to -100 °C do not display any differences in the TRAPDOR effect compared to spectra acquired at ambient temperature. This suggests that the carbocycles in **3**

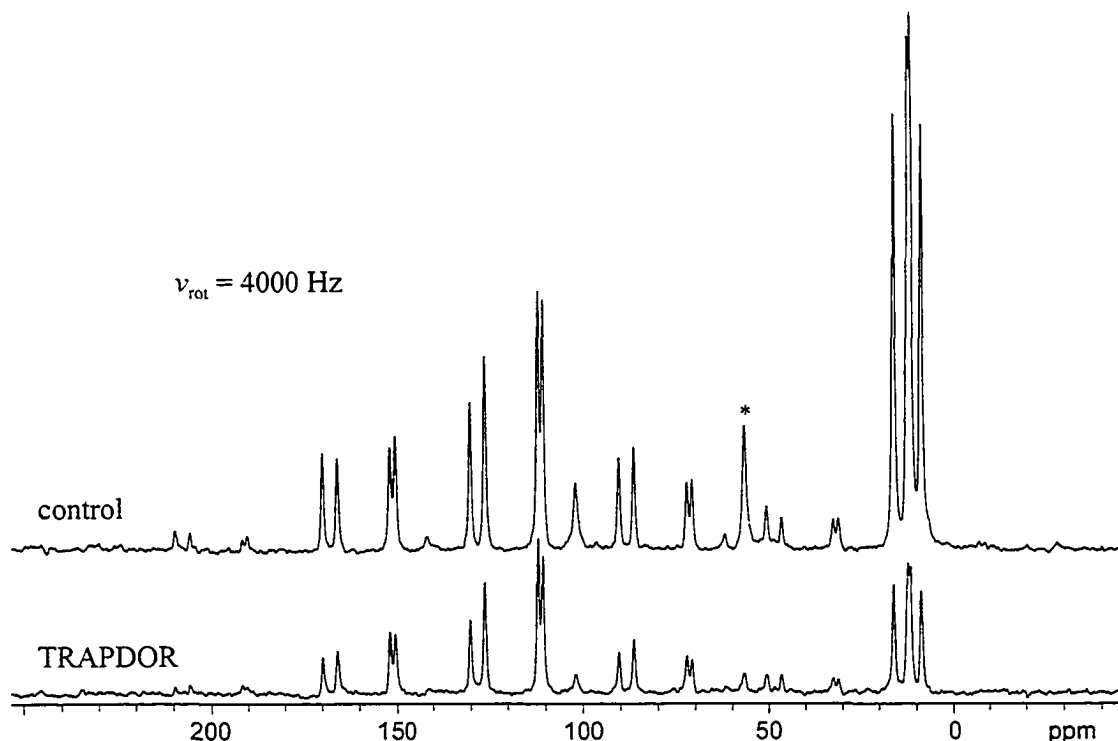


**Figure 3.8**  $^{13}\text{C}/^9\text{Be}/^1\text{H}$  CP/TRAPDOR spectra of **3**; asterisk (\*) marks the  $\eta^1\text{-}i\text{-C}_5\text{Me}_4\text{H}$  carbon resonance.

display relatively little motion and are rather rigid in contrast to **1** and **2**.

$^{13}\text{C}/^9\text{Be}/^1\text{H}$  VT CP/TRAPDOR experiments for **2** are shown in Figure 3.9. At ambient temperature and higher, TRAPDOR and control spectra are almost identical, perhaps indicating little or motionally averaged  $^{13}\text{C}\text{-}^9\text{Be}$  dipolar coupling. Upon cooling, CP conditions change such that the Cp\* and Me resonances quickly diminish until reaching  $-60\text{ }^\circ\text{C}$  when both signals can no longer be detected. With further cooling, the Me and Cp\* peaks slowly reappear with broader line-widths. The width at half-height ( $\Delta\nu_{1/2}$ ) of the Cp\* and Me isotropic peaks change from 81 and 84 Hz at ambient temperature to 540 and 176 Hz at  $-100\text{ }^\circ\text{C}$ , respectively. The dramatic change in CP conditions and broad peak widths at lower temperatures suggest a change in the rate of

the Cp\* five-fold reorientation. Furthermore, the significantly increased TRAPDOR effect at low temperatures indicates an increase in  $^{13}\text{C}$ - $^9\text{Be}$  dipolar coupling, supporting the notion of decelerating Cp\* ring motion (at  $-100\text{ }^\circ\text{C}$ , the methyl and aromatic Cp\*

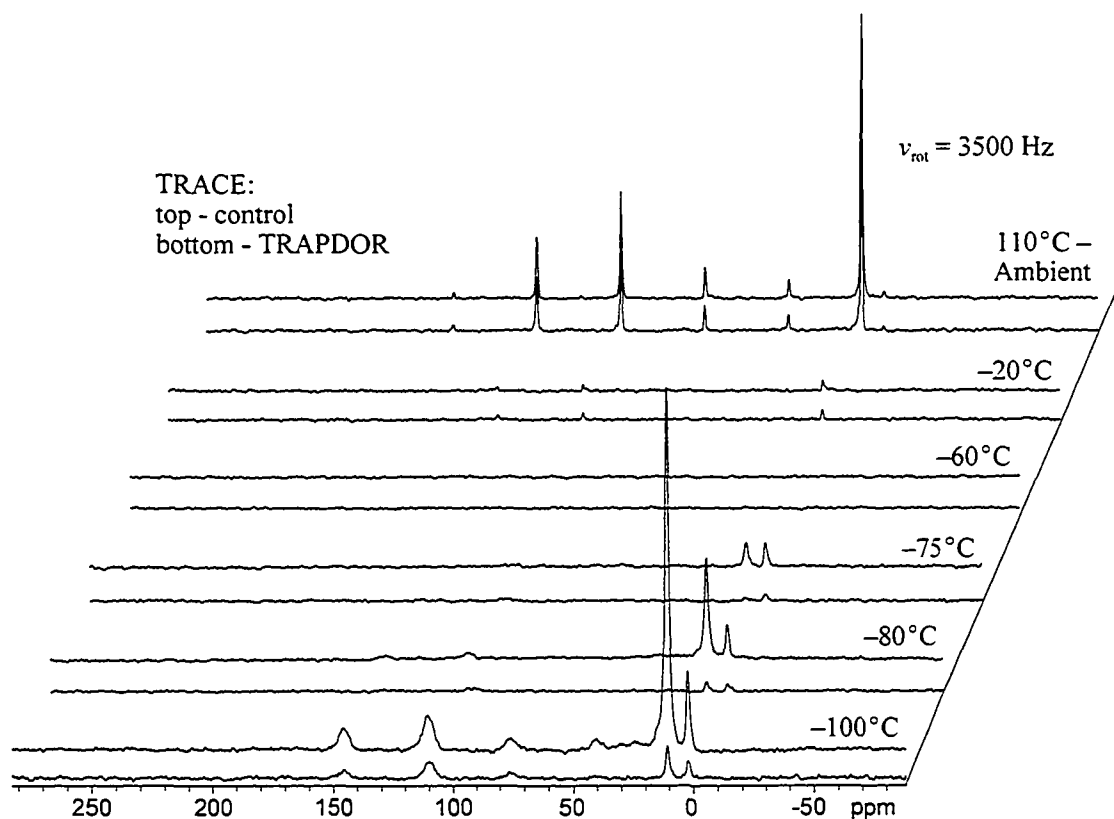


**Figure 3.9**  $^{13}\text{C}/^9\text{Be}/^1\text{H}$  VT CP/TRAPDOR spectra of **2**. Variable contact time experiments display no difference compared to the spectra shown.

signals retain ca. 8% and 46% of their integrated intensity compared to the control experiment). Variable contact time experiments (ct = 0.1 – 25.0 ms) were also performed (not shown) in order to examine the reason for loss in CP efficiency between  $-20\text{ }^\circ\text{C}$  and  $-80\text{ }^\circ\text{C}$ , however, spectra displayed no difference to those shown in Figure 3.9. The peak at  $\delta_{\text{iso}} = 2\text{ ppm}$ , which becomes more prevalent at lower temperatures, most likely arises from an impurity in the sample.



### 3.3.3 Theoretical Calculations

Theoretical  $^9\text{Be}$  CS tensors (Table 3.3), obtained from calculations with standard methods and basis sets show remarkable agreement with experimental data. In particular, both the RHF and B3LYP methods perform exceptionally well in calculating  $\delta_{\text{iso}}$  and  $\Omega$

**Table 3.3**  
Experimental and Theoretical Beryllium Chemical Shielding Tensors

Source	$\delta_{11}$ [ppm]	$\delta_{22}$ [ppm]	$\delta_{33}$ [ppm]	$\delta_{\text{iso}}$ [ppm]	$\Omega$ [ppm]	$\kappa$
<b>1</b>						
<b>Experimental</b>	2.5	-3.0	-62.5	-21(1)	65(2)	0.83(4)
RHF/6-31G**	4.7	2.8	-62.3	-18.3	67.0	0.94
/6-311G**	4.2	2.5	-64.0	-19.1	68.1	0.95
/6-311+G**	4.7	2.7	-63.9	-18.8	68.6	0.94
B3LYP/6-31G**	3.8	1.4	-62.0	-18.9	65.8	0.93
/6-311G**	3.3	1.5	-64.5	-19.9	67.8	0.95
/6-311+G**	3.3	1.4	-64.5	-19.9	67.8	0.95
<b>2</b>						
<b>Experimental</b>	-4.8	-8.6	-59.8	-24.4(7)	55(5)	0.86(7)
RHF/6-31G**	-8.9	-9.3	-65.0	-27.7	56.1	0.98
/6-311G**	-13.4	-13.7	-68.3	-31.8	54.9	0.99
/6-311+G**	-13.1	-13.5	-68.2	-31.6	55.1	0.99
B3LYP/6-31G**	2.4	1.6	-51.2	-15.8	53.6	0.97
/6-311G**	-2.1	-2.7	-54.2	-19.7	52.0	0.98
/6-311+G**	1.2	-1.2	-53.0	-17.7	54.1	0.91
<b>3</b>						
<b>Experimental</b>	-0.5	-4.5	-54.5	-19.8(5)	54(4)	0.85(8)
RHF/6-31G**	1.8	-2.8	-54.0	-18.4	55.8	0.83
/6-311G**	0.9	-3.0	-55.8	-19.3	56.6	0.86
/6-311+G**	1.2	-2.8	-55.5	-19.0	56.7	0.86
B3LYP/6-31G**	1.5	-3.2	-53.0	-18.2	54.5	0.83
/6-311G**	0.8	-3.3	-55.5	-19.3	56.3	0.86
/6-311+G**	1.7	-3.2	-55.2	-18.9	56.8	0.83

for all three compounds. The values of  $\kappa$  show the largest discrepancy with measured values, however, even those deviations are minute.

Calculated values of  $C_Q$  and  $\eta_Q$  (Table 3.4) also show very good agreement with experimental values. Notably, B3LYP/6-31G\*\* calculations yield the best agreement

**Table 3.4**  
Experimental and Theoretical  $^9\text{Be}$  EFG Parameters

Source	$V_{11}$ [a.u.]	$V_{22}$ [a.u.]	$V_{33}$ [a.u.]	$ C_Q $ [MHz]	$\eta_Q$
<b>1</b>					
<b>Experimental<sup>[a]</sup></b>	-0.0123	-0.0206	0.0329	0.41(2)	0.25(5)
RHF/6-31G**	-0.0129	-0.0182	0.0311	0.39	0.17
/6-311G**	-0.0092	-0.0148	0.0240	0.30	0.23
/6-311+G**	-0.0093	-0.0148	0.0241	0.30	0.23
B3LYP/6-31G**	-0.0125	-0.0205	0.0330	0.41	0.24
/6-311G**	-0.0103	-0.0193	0.0296	0.37	0.30
/6-311+G**	-0.0104	-0.0192	0.0296	0.37	0.30
<b>2</b>					
<b>Experimental</b>	0.0042	0.0143	-0.0185	0.23(2)	0.55(5)
RHF/6-31G**	0.0102	0.0263	-0.0364	0.45	0.44
/6-311G**	0.0155	0.0308	-0.0464	0.58	0.33
/6-311+G**	0.0155	0.0309	-0.0464	0.58	0.33
B3LYP/6-31G**	0.0103	0.0245	-0.0349	0.43	0.41
/6-311G**	0.0164	0.0307	-0.0470	0.59	0.30
/6-311+G**	0.0163	0.0306	-0.0469	0.58	0.30
<b>3</b>					
<b>Experimental</b>	-0.0213	-0.0277	0.0490	0.61(5)	0.13(7)
RHF/6-31G**	-0.0270	-0.0315	0.0585	0.73	0.08
/6-311G**	-0.0270	-0.0290	0.0559	0.70	0.04
/6-311+G**	-0.0268	-0.0296	0.0563	0.70	0.05
B3LYP/6-31G**	-0.0235	-0.0306	0.0541	0.67	0.13
/6-311G**	-0.0269	-0.0301	0.0571	0.71	0.06
/6-311+G**	-0.0267	-0.0308	0.0574	0.72	0.07

<sup>[a]</sup> The sign (+/-) and significant figures of experimental EFG tensor components ( $V_{11}$ ,  $V_{22}$  and  $V_{33}$ ) are set according to most proximate theoretical values for comparison.

with measured values for **1** and **3**, although all other calculations also perform well. Relatively large deviations are seen for the calculated  $C_Q$  and  $\eta_Q$  values of **2**. These discrepancies are attributed to rapid reorientation of the Cp\* rings in **2**, which motionally averages the  $V_{33}$  component of the  $^9\text{Be}$  EFG tensor and is unaccounted for in calculations (*vide infra*).

Not surprisingly, theoretical  $^9\text{Be}$  EFG and CS tensor orientations do not vary due to the methods and basis sets used. In all three cases the beryllium CS tensor has near-axial symmetry (**1**:  $\kappa = 0.83$ ; **2**:  $\kappa = 0.86$ ; **3**:  $\kappa = 0.85$ ) indicating that the  $\sigma_{11}$  and  $\sigma_{22}$  components are similar in magnitude while  $\sigma_{33}$  is distinct. Therefore,  $\sigma_{11}$  and  $\sigma_{22}$  should point towards similar electronic environments, while  $\sigma_{33}$  assumes an orientation along a unique symmetry element or molecular axis. Indeed,  $\sigma_{33}$  points in the general direction of the Cp' ring centroid for all three compounds, while the  $\sigma_{11}$  and  $\sigma_{22}$  components lie on a plane parallel to the  $\eta^5\text{-Cp}'$  moieties (Figure 3.10). The  $^9\text{Be}$  EFG tensors of **1** and **3** are also indicative of high cylindrical ground state electronic symmetry (**1**:  $\eta_Q = 0.25$ ; **3**:  $\eta_Q = 0.13$ ), consequently, theoretical EFG tensors have the  $V_{33}$  component aligned toward the Cp' centroid as well. However, the NMR interaction tensors for both **1** and **3** are not coincident. In **3**,  $V_{11}$  and  $\sigma_{22}$  are coincident, while  $\Delta V_{33}\text{-Be-}\sigma_{33}$  and  $\Delta V_{22}\text{-Be-}\sigma_{11}$  are equal to  $4.3^\circ$  (Figure 3.10c); the corresponding Euler angles describing the relative orientation of the two theoretical tensors are  $\alpha = 90.0^\circ$ ,  $\beta = 4.3^\circ$  and  $\gamma = 0.0^\circ$ , in very good agreement with experimentally measured values ( $\alpha = 90^\circ$ ,  $\beta = 4^\circ$ ,  $\gamma = 0^\circ$ ). For **1**,  $V_{33}$  and  $\sigma_{33}$  are offset by a  $V_{33}\text{-Be-}\sigma_{33}$  angle of  $7^\circ$ , while  $\Delta V_{22}\text{-Be-}\sigma_{11}$  and  $\Delta V_{11}\text{-Be-}\sigma_{22}$  are both approximately  $28^\circ$  apart (Figure 3.10a); the theoretical Euler angles obtained are

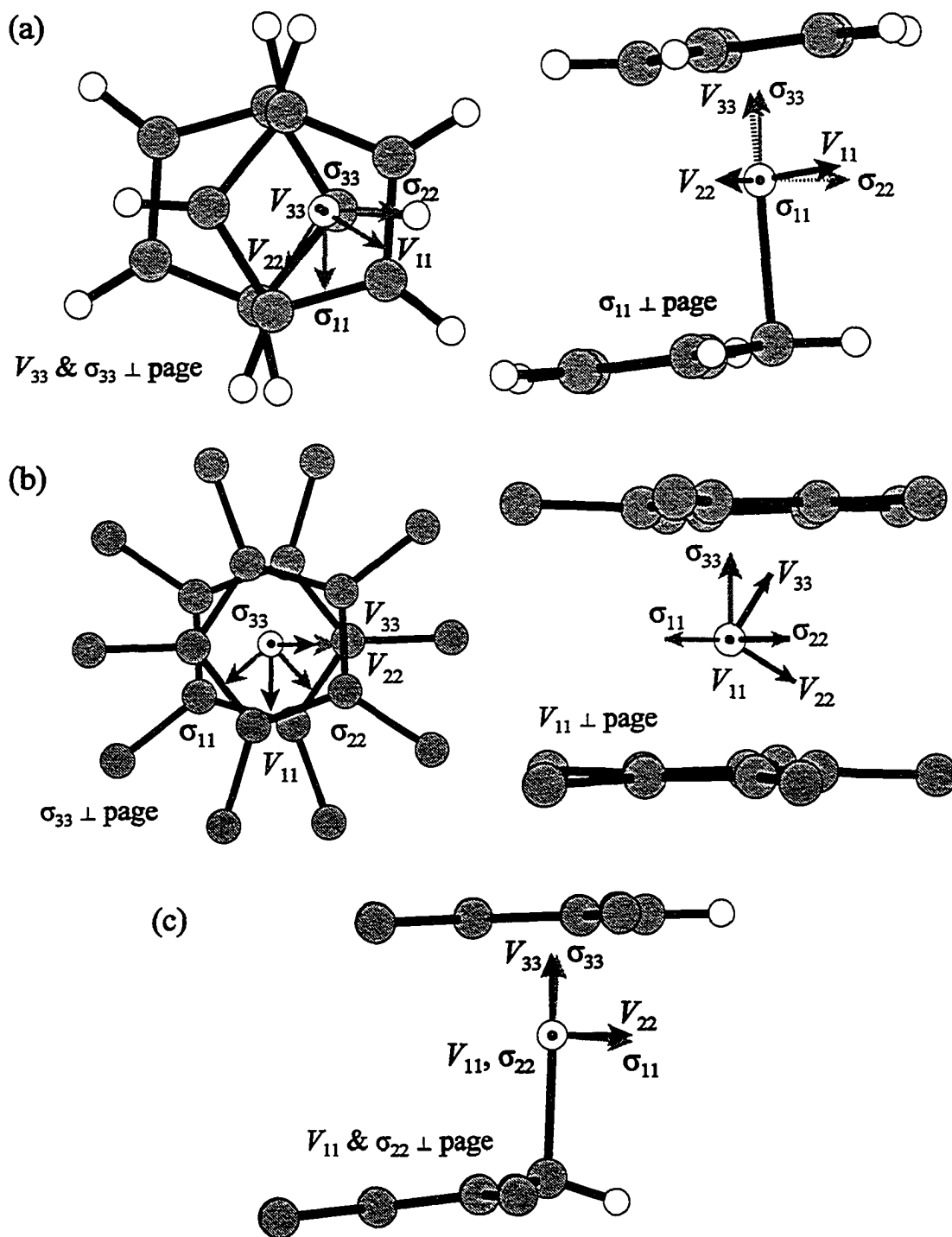


**Figure 3.10** Theoretical  $^9\text{Be}$  EFG and CS tensors of (a) 1 (top and side view of molecule) (b) 2 (top and side view of molecule) and (c) 3. Methyl hydrogen atoms have been omitted in 2 and 3 for clarity.

$\alpha = 3.8^\circ$ ,  $\beta = 7.0^\circ$  and  $\gamma = 57.9^\circ$ . These stand in contrast to the relative orientation measured experimentally; however, one must bear in mind that simulation parameters extracted from NMR spectra are from a motionally averaged structure wherein different intra-molecular dynamic processes obviously affect the NMR interactions observed, whereas theoretical results are derived from purely stationary structures. Furthermore, since both the experimental  $^9\text{Be}$  EFG and CS tensors are axial and the magnitudes of both the span and quadrupolar interaction result in rather small anisotropic frequency spreads, the relative orientation of the lesser components ( $V_{ii}$  and  $\delta_{ii}$ ;  $i = 1, 2$ ) with respect to each other is of minor influence and experimental observations ( $\alpha = 0^\circ$ ,  $\beta = 38^\circ$ ,  $\gamma = 0^\circ$ ) show misalignment only between  $V_{33}$  and  $\delta_{33}$ .

The theoretical  $^9\text{Be}$  EFG tensor of **2** takes on a very distinct orientation compared to those of **1** and **3** as shown in Figure 3.10b. In particular, the plane in which  $V_{22}$ ,  $V_{33}$  and the Be atom lie makes an angle of  $46^\circ$  with  $\sigma_{22}$ , while  $V_{11}$  approximately bisects the angle between  $\sigma_{11}$  and  $\sigma_{22}$ . The corresponding theoretical Euler angles relating the orientation of the EFG and CS tensors are  $\alpha = 89.3^\circ$ ,  $\beta = 29.8^\circ$  and  $\gamma = 46.9^\circ$ .

Simulations of the static  $^9\text{Be}$  NMR spectrum of **2** using the theoretical Euler angles provide very good agreement; in fact, the experimental values ( $\alpha = 90^\circ$ ,  $\beta = 28^\circ$ ,  $\gamma = 44^\circ$ ) were arrived at by only minor refinement of the calculated values. As in the case of  $\text{Cp}_2\text{Mg}$ ,<sup>[80]</sup> offset of  $V_{33}$  from the  $\text{Cp}^*$  centroid suggests slight distortions in the spherical/cylindrical ground state symmetry of the molecule. Indeed, the crystal structure of **2**<sup>[37]</sup> reveals that the  $\text{Cp}^*_2\text{Be}$  unit has  $C_i$  rather than  $D_{5d}$  symmetry. For **2**, the  $V_{33}$  component tilts towards the two  $\text{Cp}^*$  carbon atoms which lie farthest from the Be (Be–C

distances range from 1.969 to 2.114 Å). Because of the misalignment of  $V_{33}$  from the ring centroid, five-fold reorientation of the Cp\* rings reduces  $C_Q(^9\text{Be})$  so that only an average value is detected, in contrast to the values obtained from calculations.

To further explore the effects upon the  $^9\text{Be}$  NMR interaction tensors from movement of the Be atom between the two half-occupied crystallographic sites of  $\text{Cp}_2\text{Be}$ , a series of B3LYP/6-311G\*\* calculations were performed attempting to simulate the suspected ‘inversion’ process or “shuttling” motion of the Be atom. For each calculation, the Be atom was positioned at a different distance (a multiple of 1/8 of the total distance between the two crystallographic Be sites) along a straight line which joins the two crystallographic Be sites in the low temperature structure. Calculations for five different Be positions were done in total, beginning at one of the crystallographic sites and ending at the midpoint between the two crystallographic sites (hitherto referred to as the “midpoint”); the remaining points on the other side of the midpoint were assumed to be equivalent to those calculated. The calculated  $^9\text{Be}$  NMR parameters at each of the points are shown in Table 3.5, where the Be positions are labelled by their distance from the midpoint, i.e., the 0.652 Å site is the crystallographic site. According to calculations, the ‘inversion’ process has a classical energy barrier of 11.07 kJ mol<sup>-1</sup> with the lowest and highest energies found for 0.489 Å and the midpoint, respectively. The calculated barrier is comparable to values determined from MD calculations (8 kJ mol<sup>-1</sup>)<sup>[36]</sup> and solution  $^{13}\text{C}$  VT NMR (5.2 kJ mol<sup>-1</sup>).<sup>[31]</sup> Variation of the self-consistent field energy along the reaction coordinate can be fit to the function  $f(r) = A + B\cos^2(r) + C\cos^4(r) + D\cos^6(r)$  within the range  $r = 0.652$  to  $-0.652$  Å, where  $r$  is the distance from the midpoint,  $A =$

212.1(1.7),  $B = -645.9(6.3)$ ,  $C = 602.0(7.8)$  and  $D = -157.2(3.2)$ . The expectation value for  $r$  is 0.5996 Å as opposed to the lowest energy position which lies 0.4894 Å from the midpoint. If the trends observed from calculations are representative of the solid-state ‘inversion’ barrier, the beryllium in  $\text{Cp}_2\text{Be}$  would be undergoing hindered passage between the two half-occupied sites, spending the majority of the time approximately 0.052 Å from each of the crystallographic sites.

**Table 3.5**  
Theoretical (B3LYP/6-311G\*\*)  $^9\text{Be}$  EFG and CS Parameters at Different Beryllium Stationary Points Along the Reaction Coordinates of the ‘Inversion’ Process

Parameter	Absolute Distance from Center Position [Å]				
	0.000	0.163	0.326	0.489	0.652
$ C_Q $ [MHz]	1.58	1.48	1.21	0.83	0.49
$\eta_Q$	0.77	0.74	0.63	0.39	0.05
$V_{11}$ [a.u.]	-0.014539	-0.015539	-0.017930	-0.020133	-0.018486
$V_{22}$ [a.u.]	-0.112587	-0.103642	-0.079196	-0.046134	-0.020617
$V_{33}$ [a.u.]	0.127126	0.119180	0.097126	0.066267	0.039103
$\delta_{\text{iso}}$ [ppm]	-22.99	-22.79	-22.22	-21.24	-19.62
$\Omega$ [ppm]	67.96	67.35	66.11	65.50	66.95
$\kappa$	0.976	0.976	0.974	0.961	0.924
$\delta_{11}$ [ppm]	-0.06	-0.07	0.11	1.02	3.55
$\delta_{22}$ [ppm]	-0.89	-0.89	-0.77	-0.26	0.99
$\delta_{33}$ [ppm]	-68.02	-67.42	-66.00	-64.48	-63.40

In addition, according to calculations the  $^9\text{Be}$  NMR interactions are also expected to vary because of the ‘inversion’ process (Table 3.5, see Figure B.3 of Appendix B for details). In moving from one of the crystallographic sites to the other,  $C_Q(^9\text{Be})$  and  $\eta_Q$  vary within the ranges 0.49 – 1.58 MHz and 0.05 – 0.77, respectively, being greatest at the midpoint in both cases. Similarly, in going from 0.652 Å to the midpoint,  $\kappa$  increases

to 0.976 from 0.924, while  $\Omega$  varies by merely 2.46 ppm. As discussed above, the Be atom spends most of its time at or near the crystallographic sites rather than at the midpoint, explaining why NMR parameters calculated using the atomic positions from the crystal structure display such good agreement with experimental values. Thus, the observed  $^9\text{Be}$  NMR signal arises almost entirely from beryllium occupying the crystallographic sites (or nearby positions). The orientation of both the theoretical  $^9\text{Be}$  EFG and CS tensors display little variation along the chosen Be atom trajectory.

### 3.4 Conclusion

Through a combination of solid-state  $^9\text{Be}$  and  $^{13}\text{C}$  NMR spectroscopy, X-ray diffraction and quantum mechanical calculations, the relationships between anisotropic NMR interactions and molecular structure and dynamics in  $\text{Cp}_2\text{Be}$ ,  $\text{Cp}^*_2\text{Be}$  and  $(\text{C}_5\text{Me}_4\text{H})_2\text{Be}$  are elucidated. Notably, parameters measured by solid-state MAS and static  $^9\text{Be}$  NMR experiments are correlated with molecular structure (which confirm geometries measured by X-ray diffraction): (i)  $C_Q(^9\text{Be})$  increases in magnitude as the degree of spherical symmetry about the Be nuclei decreases, (ii) large beryllium chemical shift anisotropy comparable to the entire known beryllium chemical shift range are consistent with p- $\pi$  bonding to Cp' moieties, and (iii) the isotropic  $^9\text{Be}$  chemical shift increases as the overall hapticity is decreased, i.e.,  $\delta_{\text{iso}}$  increases in the order:  $\text{Cp}^*_2\text{Be}$  ( $\eta^5, \eta^5$ ),  $\text{Cp}'_2\text{Be}$  ( $\eta^5, \eta^{1-3}$ ), and  $(\text{C}_5\text{Me}_4\text{H})_2\text{Be}$  ( $\eta^5, \eta^1$ ). On the other hand, variable-temperature NMR experiments allow examination of intra-molecular dynamics: VT  $^9\text{Be}$  NMR experiments reveal that a small portion of  $\text{Cp}_2\text{Be}$  molecules undergo rapid isotropic



motion even at ambient temperature and that  $\text{Cp}^*_2\text{Be}$  and  $(\text{C}_5\text{Me}_4\text{H})_2\text{Be}$  undergo relatively small variation in their molecular geometries with changing temperature.  $^{13}\text{C}$  VT CP/MAS NMR spectra of  $\text{Cp}_2\text{Be}$  reveal chemical exchange, indicating that the hapticity of the Cp rings is 'inverted' through the motion of the beryllium atom between the crystallographically equivalent sites; the activation energy associated with this 'inversion' process is measured to be  $36.9 \text{ kJ mol}^{-1}$ . In the case of  $\text{Cp}^*_2\text{Be}$ ,  $^{13}\text{C}/^9\text{Be}/^1\text{H}$  VT CP/TRAPDOR spectra show dramatic changes upon cooling, which indicate a slowing down of the five-fold reorientation of the Cp\* ring.

Ab initio (RHF) and hybrid density functional theory (B3LYP) calculations yield excellent agreement with experimental NMR interaction parameters. In combination with experimental data, theoretical calculations give a particularly good indication as to the equilibrium geometry found in the condensed phase of  $\text{Cp}_2\text{Be}$ , namely, that the Be atom spends most of its time located at one of the two related crystallographic sites and a relatively insignificant amount of time in transit. Theoretical calculations aid in determining the orientation of anisotropic NMR interaction tensors in the molecular frame, which further correlates NMR parameters with molecular structure. We hope to have shown that solid-state NMR spectroscopy is an excellent complimentary technique to X-ray diffraction for confirming molecular symmetry, rapid checking of sample purity, relating magnetic shielding tensors to molecular structure and enabling the observation of unique solid-state intra-molecular dynamics.

# Bibliography

- [1] E. O. Fischer, H. P. Hofmann, *Chemische Berichte* **1959**, 92, 482.
- [2] H. P. Fritz, R. Schneider, *Chemische Berichte* **1960**, 93, 1171.
- [3] H. P. Fritz, *Chemische Berichte* **1959**, 92, 780.
- [4] A. Almenningen, O. Bastiansen, A. Haaland, *Journal of Chemical Physics* **1964**, 40, 3434.
- [5] M. Sundbom, *Acta Chemica Scandinavica* **1966**, 20, 1608.
- [6] G. B. McVicker, G. L. Morgan, *Spectrochimica Acta Part A* **1970**, 26A, 23.
- [7] H. P. Fritz, D. Sellmann, *Journal of Organometallic Chemistry* **1966**, 5, 501.
- [8] O. Y. Lopatko, N. M. Klimenko, M. E. Dyatkina, *Journal of Structural Chemistry* **1972**, 13, 1044.
- [9] S. P. Ionov, G. V. Ionova, *Izvestiia Akademii nauk SSR, Seriya Khimiia* **1970**, 2836.
- [10] C.-H. Wong, T.-Y. Lee, K.-J. Chao, S. Lee, *Acta Crystallogr., Sect. B* **1972**, 28, 1662.
- [11] D. A. Drew, A. Haaland, *Acta Crystallogr., Sect. B* **1972**, 28, 3671.
- [12] C.-H. Wong, K. J. Chao, C. Chih, T. Y. Lee, *Journal of the Chinese Chemical Society* **1969**, 16, 15.
- [13] C. Wong, T. Y. Lee, T. J. Lee, T. W. Chang, C. S. Liu, *Inorganic & Nuclear Chemistry Letters* **1973**, 9, 667.
- [14] G. L. Morgan, G. B. McVicker, *Journal of the American Chemical Society* **1968**, 90, 2789.

- [15] C.-H. Wong, S.-M. Wang, *Inorganic & Nuclear Chemistry Letters* **1975**, *11*, 677.
- [16] J. B. Collins, P. V. R. Schleyer, *Inorganic Chemistry* **1977**, *16*, 152.
- [17] D. S. Marynick, *Journal of the American Chemical Society* **1977**, *99*, 1436.
- [18] C.-S. Liu, *Journal of the Chinese Chemical Society* **1977**, *24*, 79.
- [19] J. Demuynck, M. M. Rohmer, *Chemical Physics Letters* **1978**, *54*, 567.
- [20] M. J. S. Dewar, H. S. Rzepa, *Journal of the American Chemical Society* **1978**, *100*, 777.
- [21] N.-S. Chiu, L. Schaefer, *Journal of the American Chemical Society* **1978**, *100*, 2604.
- [22] E. D. Jemmis, S. Alexandratos, P. v. R. Schleyer, A. Streitwieser, Jr., H. F. Schaefer, III, *Journal of the American Chemical Society* **1978**, *100*, 5695.
- [23] O. P. Charkin, A. Veillard, J. Demuynck, M. M. Rohmer, *Koordinatsionnaya Khimiya* **1979**, *5*, 501.
- [24] R. Gleiter, M. C. Boehm, A. Haaland, R. Johansen, J. Lusztyk, *Journal of Organometallic Chemistry* **1979**, *170*, 285.
- [25] C. Glidewell, *Journal of Organometallic Chemistry* **1981**, *217*, 273.
- [26] L. A. Gribov, M. M. Raikhshtat, V. V. Zhogina, *Koordinatsionnaya Khimiya* **1988**, *14*, 1368.
- [27] J. Lusztyk, K. B. Starowieyski, *Journal of Organometallic Chemistry* **1979**, *170*, 293.
- [28] S. J. Pratten, M. K. Cooper, M. J. Aroney, *Polyhedron* **1984**, *3*, 1347.
- [29] S. J. Pratten, M. K. Cooper, M. J. Aroney, S. W. Filipczuk, *Journal of the Chemical*

*Society, Dalton Transactions* **1985**, 1761.

[30] K. W. Nugent, J. K. Beattie, *Journal of the Chemical Society, Chemical Communications* **1986**, 186.

[31] K. W. Nugent, J. K. Beattie, L. D. Field, *Journal of Physical Chemistry* **1989**, *93*, 5371.

[32] K. W. Nugent, J. K. Beattie, T. W. Hambley, M. R. Snow, *Australian Journal of Chemistry* **1984**, *37*, 1601.

[33] K. W. Nugent, J. K. Beattie, *Inorganic Chemistry* **1988**, *27*, 4269.

[34] R. Car, M. Parrinello, *Physical Review Letters* **1985**, *55*, 2471.

[35] P. Margl, K. Schwarz, P. E. Blochl, *Journal of the American Chemical Society* **1994**, *116*, 11177.

[36] P. Margl, K. Schwarz, P. E. Blochl, *Journal of Chemical Physics* **1995**, *103*, 683.

[37] M. D. Conejo, R. Fernandez, E. Gutierrez-Puebla, A. Monge, C. Ruiz, E. Carmona, *Angewandte Chemie-International Edition* **2000**, *39*, 1949.

[38] M. D. Conejo, R. Fernandez, D. del Rio, E. Carmona, A. Monge, C. Ruiz, *Chemical Communications* **2002**, 2916.

[39] M. D. Conejo, R. Fernandez, D. del Rio, E. Carmona, A. Monge, C. Ruiz, A. M. Marquez, J. F. Sanz, *Chemistry-a European Journal* **2003**, *9*, 4452.

[40] M. D. Conejo, R. Fernandez, E. Carmona, E. Gutierrez-Puebla, A. Monge, *Organometallics* **2001**, *20*, 2434.

[41] M. D. Conejo, R. Fernandez, E. Carmona, R. A. Andersen, E. Gutierrez-Puebla, M. A. Monge, *Chemistry-a European Journal* **2003**, *9*, 4462.

- [42] D. Sundholm, J. Olsen, *Chemical Physics Letters* **1991**, *177*, 91.
- [43] P. Pyykko, *Zeitschrift Fur Naturforschung Section A-a Journal of Physical Sciences* **1992**, *47*, 189.
- [44] D. L. Bryce, R. E. Wasylshen, *Journal of Physical Chemistry A* **1999**, *103*, 7364.
- [45] L. C. Brown, D. Williams, *Journal of Chemical Physics* **1956**, *24*, 751.
- [46] J. F. Hon, *Physical Review* **1961**, *124*, 1368.
- [47] G. J. Troup, J. Walter, *Journal of Nuclear Materials* **1964**, *14*, 272.
- [48] H. L. Reaves, T. E. Gilmer, Jr., *Journal of Chemical Physics* **1965**, *42*, 4138.
- [49] R. Blinc, J. Slak, J. Stepisnik, *Journal of Chemical Physics* **1971**, *55*, 4848.
- [50] W. J. Dell, R. V. Mulkern, P. J. Bray, M. J. Weber, S. A. Brawer, *Physical Review B: Condensed Matter and Materials Physics* **1985**, *31*, 2624.
- [51] E. T. Ahrens, P. C. Hammel, R. H. Heffner, A. P. Reyes, J. L. Smith, W. G. Clark, *Physical Review B: Condensed Matter and Materials Physics* **1993**, *48*, 6691.
- [52] T. H. Yeom, A. R. Lim, S. H. Choh, K. S. Hong, Y. M. Yu, *Journal of Physics: Condensed Matter* **1995**, *7*, 6117.
- [53] J. Skibsted, P. Norby, H. Bildsoe, H. J. Jakobsen, *Solid State Nuclear Magnetic Resonance* **1995**, *5*, 239.
- [54] V. D. Kodibagkar, P. A. Fedders, C. D. Browning, R. C. Bowman, Jr., N. L. Adolphi, M. S. Conradi, *Physical Review B: Condensed Matter and Materials Physics* **2003**, *67*, Art. no. 045107.
- [55] D. A. Drew, G. L. Morgan, *Inorganic Chemistry* **1977**, *16*, 1704.
- [56] M. Kanakubo, H. Ikeuchi, G. P. Sato, *Journal of the Chemical Society, Faraday*

*Transactions* **1998**, *94*, 3237.

[57] D. A. Saulys, D. R. Powell, *Organometallics* **2003**, *22*, 407.

[58] K. Eichele, R. E. Wasylshen, WSOLIDS, v.1.17.28 - Software for simulations of solid state NMR powder patterns, Dalhousie University, Dalhousie, **2000**.

[59] M. Bak, J. T. Rasmussen, N. C. Nielsen, *Journal of Magnetic Resonance* **2000**, *147*, 296.

[60] M. M. Maricq, J. S. Waugh, *Journal of Chemical Physics* **1979**, *70*, 3300.

[61] J. Herzfeld, A. E. Berger, *Journal of Chemical Physics* **1980**, *73*, 6021.

[62] M. Mehring, *Principles of High Resolution NMR in Solids*, Springer-Verlag, New York, **1983**.

[63] R. N. Zare, *Angular Momentum: Understanding Spatial Aspects in Chemistry and Physics*, John Wiley & Sons, Inc., Toronto, **1988**.

[64] M. J. Frisch, G. W. Trucks, H. B. Schlegel, G. E. Scuseria, M. A. Robb, J. R. Cheeseman, V. G. Zakrzewski, J. Montgomery, J. A., R. E. Stratmann, J. C. Burant, S. Dapprich, J. M. Millam, A. D. Daniels, K. N. Kudin, M. C. Strain, O. Farkas, J. Tomasi, V. Barone, M. Cossi, R. Cammi, B. Mennucci, C. Pomelli, C. Adamo, S. Clifford, J. Ochterski, G. A. Petersson, P. Y. Ayala, Q. Cui, K. Morokuma, D. K. Malick, A. D. Rabuck, K. Raghavachari, J. B. Foresman, J. Cioslowski, J. V. Ortiz, A. G. Baboul, B. B. Stefanov, G. Liu, A. Liashenko, P. Piskorz, I. Komaromi, R. Gomperts, R. L. Martin, D. J. Fox, T. Keith, M. A. Al-Laham, C. Y. Peng, A. Nanayakkara, M. Challacombe, P. M. W. Gill, B. Johnson, W. Chen, M. W. Wong, J. L. Andres, C. Gonzalez, M. Head-Gordon, E. S. Replogle, J. A. Pople, Gaussian 98, Revision A.9. Gaussian, Inc.,

Pittsburgh, PA, **1998**.

[65] A. D. Becke, *Physical Review A* **1988**, 38, 3098.

[66] C. Lee, W. Yang, R. G. Parr, *Physical Review B* **1988**, 37, 785.

[67] A. D. Becke, *Journal of Chemical Physics* **1993**, 98, 5648.

[68] R. Ditchfield, *Molecular Physics* **1974**, 27, 789.

[69] K. Wolinski, J. F. Hinton, P. Pulay, *Journal of the American Chemical Society* **1990**, 112, 8251.

[70] A. K. Jameson, C. J. Jameson, *Chemical Physics Letters* **1987**, 134, 461.

[71] R. A. Kovar, G. L. Morgan, *Journal of the American Chemical Society* **1970**, 92, 5067.

[72] D. F. Gaines, K. M. Coleson, D. F. Hillenbrand, *Journal of Magnetic Resonance* **1981**, 44, 84.

[73] R. W. Schurko, I. Hung, C. L. B. Macdonald, A. H. Cowley, *Journal of the American Chemical Society* **2002**, 124, 13204.

[74] R. W. Schurko, I. Hung, S. Schauff, C. L. B. Macdonald, A. H. Cowley, *Journal of Physical Chemistry A* **2002**, 106, 10096.

[75] A. Almenningen, A. Haaland, J. Lusztyk, *Journal of Organometallic Chemistry* **1979**, 170, 271.

[76] T. P. Das, E. L. Hahn, *Nuclear Quadrupole Resonance Spectroscopy*, Academic Press, Inc., New York, **1958**.

[77] E. A. C. Lucken, *Nuclear Quadrupole Coupling Constants*, Academic Press, Inc., New York, **1969**.

- [78] D. E. Wemmer, D. J. Ruben, A. Pines, *Journal of the American Chemical Society* **1981**, *103*, 28.
- [79] D. E. Wemmer, A. Pines, *Journal of the American Chemical Society* **1981**, *103*, 34.
- [80] I. Hung, R. W. Schurko, *Solid State Nuclear Magnetic Resonance* **2003**, *24*, 78.
- [81] C. P. Grey, A. J. Vega, *Journal of the American Chemical Society* **1995**, *117*, 8232.



# Chapter 4

## Signal Enhancement in the NMR Spectra of Half-Integer Quadrupolar Nuclei Through the Combination of DFS and RAPT with QCPMG

### 4.1 Introduction

Experimental and technological advances in the past fifteen years have brought solid-state NMR of half-integer quadrupolar nuclei to the forefront of solid-state characterization methods.<sup>[1]</sup> Perhaps most notable was the introduction of the multiple-quantum magic-angle spinning (MQMAS) experiment in 1995,<sup>[2]</sup> which enabled high-resolution NMR of half-integer quadrupolar nuclei in the solid state.<sup>[3]</sup> Another focus has been the development of pulse sequences aimed at improving the signal-to-noise ratio in solid-state NMR experiments on half-integer quadrupolar nuclei. Examples include the quadrupolar Carr-Purcell Meiboom-Gill (QCPMG) sequence,<sup>[4]</sup> the rotor assisted population transfer (RAPT) scheme<sup>[5]</sup> and the application of adiabatic frequency sweeps (notably, the fast amplitude-modulated (FAM) pulses<sup>[6]</sup> and double-frequency sweeps (DFS)).<sup>[7, 8]</sup> The impetus for much of this research is that many of the half-integer quadrupolar nuclei, which constitute 73% of NMR-active nuclides in the periodic table, are relatively unreceptive nuclei, making the NMR experiment inherently insensitive due to their low natural abundance, low gyromagnetic ratios, large nuclear quadrupole moments, dilution of the nuclide of interest and/or any combination of the preceding.<sup>[9, 10]</sup>

The QCPMG pulse sequence, which consists of an initial  $\pi/2$  pulse followed by a

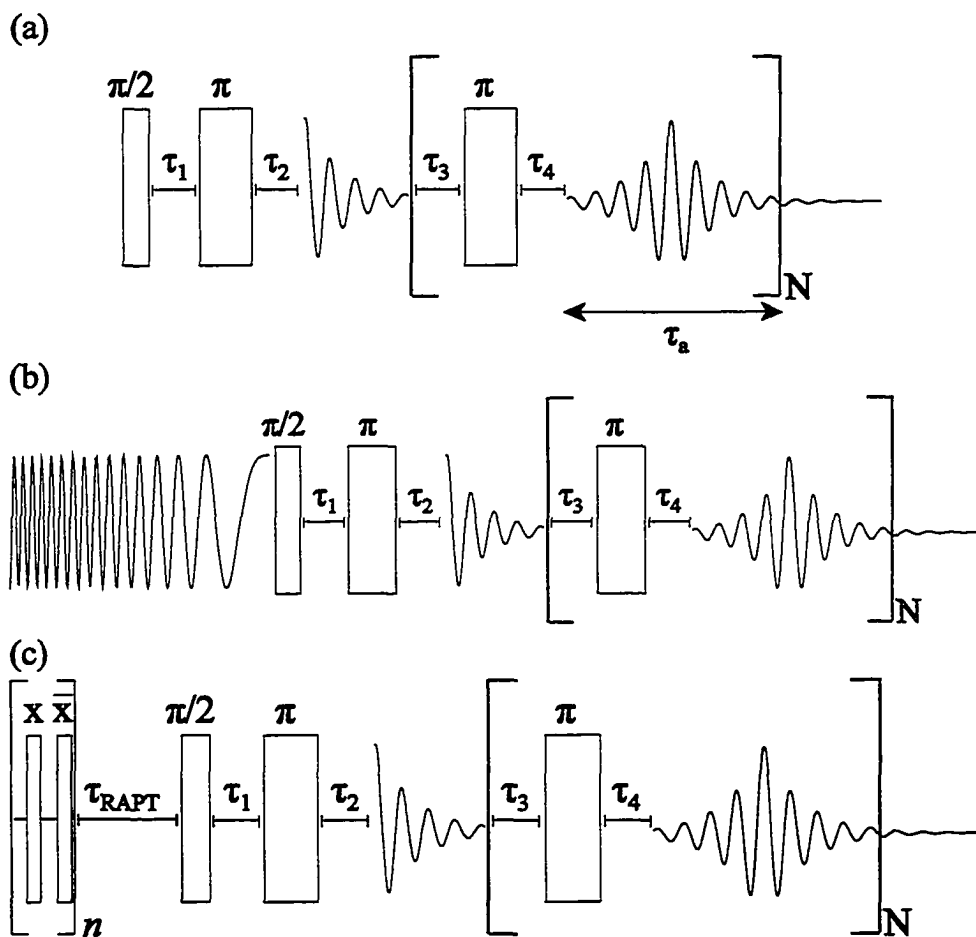


**Figure 4.1** The (a) QCPMG, (b) DFS/QCPMG, and (c) RAPT/QCPMG pulse sequences.

train of  $\pi$  pulses, is pictured in Figure 4.1a. With judicious choice of phase cycling, interpulse delays ( $\tau_i$ ,  $i = 1, 2, 3, 4$ ) and pulse durations, the QCPMG sequence can be used to acquire a long train of spin echoes, which when Fourier transformed, yields a spectrum composed of echo spikelets. Depending on the desired resolution, these spectra can exhibit increases in signal of greater than an order of magnitude. The QCPMG sequence has been implemented in experiments on stationary samples<sup>[4]</sup> and in magic-angle spinning (MAS) experiments,<sup>[11]</sup> and has also been employed for the detection of the direct dimension in MQMAS-QCPMG NMR experiments.<sup>[12]</sup> A number of often

neglected half-integer quadrupolar nuclei have been studied with this technique, including  $^{67}\text{Zn}$  in model compounds for metalloproteins,<sup>[13]</sup>  $^{25}\text{Mg}$ ,  $^{39}\text{K}$ ,  $^{67}\text{Zn}$  and  $^{87}\text{Sr}$  in a series of inorganic polycrystalline solids<sup>[14]</sup> and  $^{35}\text{Cl}$  in a high-field NMR study of organic hydrochloride salts.<sup>[15]</sup>

Frequency-swept rf fields and their effects on nuclear spin polarization of the central transition of half-integer quadrupolar nuclei were explored in detail by Haase and co-workers.<sup>[16]</sup> They found that by using weak rf fields and/or fast sweep rates (i.e., adiabatic frequency sweeps), it is possible to create  $\Delta m = 1$  level crossings (adiabatic passage), which result in pair-wise population interchanges, while  $\Delta m = 2$  crossings remain unaltered (sudden passage). The net result is a transfer of nuclear spin populations from outer Zeeman levels to the  $+1/2$  and  $-1/2$  levels, yielding a theoretical signal enhancement of a factor of  $2I$ , where  $I$  is the spin of the quadrupolar nucleus. Kentgens and co-workers demonstrated that the application of time-dependent AM-DFS is efficient for central-transition enhancement in NMR experiments on single-crystals and polycrystalline solids,<sup>[7,17]</sup> as well as for enhancement of multiple-quantum (MQ) to single-quantum (SQ) conversion in MQMAS NMR experiments.<sup>[8]</sup>

The RAPT pulse sequence was introduced as an alternative to adiabatic frequency-swept passages for MAS experiments on spin- $3/2$  nuclei. It is similar to the fast-amplitude modulated pulses of Vega and co-workers,<sup>[6]</sup> who applied such pulses for enhancing MQ-SQ transfer in MQMAS. The RAPT sequence consists of a phase-alternating  $X-\bar{X}$  pulse train followed by a short delay ( $\tau_{\text{RAPT}}$ ) prior to applying a central-transition selective  $\pi/2$  pulse. In these experiments, the frequency is not swept as in the

DFS-type experiments; rather, the frequency is held constant and the coherence transfers result from the adiabatic motion of the rotor. The effect of these rotor-synchronized amplitude-modulated pulses is to saturate the satellite transitions, thereby providing a theoretical maximum central transition enhancement of 2 for spin-3/2 nuclei. This methodology was recently extended to spin-5/2 nuclei (satellite saturation pulse sequences have theoretical signal enhancements of a factor of  $I + 1/2$ , and experimental signal enhancements as high as 2.5 were reported).<sup>[18]</sup>

In this chapter, we present an experimental study of combinations of the aforementioned pulse sequences aimed at achieving overall signal gains ranging from one to two orders of magnitude. Specifically, the DFS/QCPMG and RAPT/QCPMG schemes (Figures 4.1b, 4.1c), and their application to the study of two spin-3/2 nuclei ( $^{87}\text{Rb}$  and  $^{39}\text{K}$ ) and one spin-5/2 nucleus ( $^{85}\text{Rb}$ ) are presented. In each case, a RAPT or DFS sequence is used as a preparatory sequence serving to saturate and/or invert the satellite transition populations as described above. The QCPMG sequence is then used to enhance the signal of the resulting population-enhanced central transition. A comparison of Hahn echo, RAPT/Hahn echo, DFS/Hahn echo, QCPMG, RAPT/QCPMG and DFS/QCPMG NMR experiments is presented, along with full details of the optimized experimental parameters. In all cases, the DFS/QCPMG and RAPT/QCPMG experiments provide signal enhancements close to those predicted by theory.

## 4.2 Experimental

### 4.2.1 Sample Preparation and Handling

KHCO<sub>3</sub> samples were obtained from Aldrich and used without further purification. Samples of RbClO<sub>4</sub> were precipitated from a concentrated aqueous solution of RbCl and NaClO<sub>4</sub>, which were obtained from Aldrich and Alfa Aesar, respectively. Samples were finely ground before packing into 4 mm outer diameter ZrO<sub>2</sub> NMR rotors.

### 4.2.2 Solid-State NMR Spectroscopy

Solid-state <sup>87</sup>Rb, <sup>39</sup>K and <sup>85</sup>Rb NMR spectra were acquired on a Varian Infinity+ spectrometer with a wide-bore 9.4 T ( $\nu_0(^1\text{H}) = 400$  MHz) Oxford magnet operating at 130.80 MHz, 18.65 MHz and 38.59 MHz for <sup>87</sup>Rb, <sup>39</sup>K and <sup>85</sup>Rb, respectively. A Varian/Chemagnetics 4 mm double-resonance (HX) MAS NMR probe was used for <sup>87</sup>Rb NMR experiments, while a Varian/Chemagnetics 4 mm triple-resonance (HXY) MAS NMR probe was used to acquire <sup>39</sup>K and <sup>85</sup>Rb NMR spectra. Achievement of high forward-to-reflected power while tuning to the low <sup>39</sup>K Larmor frequency was accomplished by attaching a Varian/Chemagnetics Low Gamma Tuning Box to the T3-HXY 4 mm probe.

Static and MAS Hahn echo experiments utilized a pulse sequence of the form  $\pi/2 - \tau_1 - \pi - \tau_2 - \text{acquire}$ , with central-transition selective  $\pi/2$  and  $\pi$  pulses (i.e., non-selective pulses scaled by  $(I + 1/2)^{-1}$ ) and inter-pulse delays  $\tau_1$  and  $\tau_2$ . For all MAS echo experiments, the first inter-pulse delay ( $\tau_1$ ) and the spinning speed ( $\nu_{\text{rot}}$ ) are synchronized,

by setting  $\tau_1$  to  $N(\nu_{\text{rot}})^{-1}$ , where  $N$  is an integer. For  $^{87}\text{Rb}$ ,  $^{39}\text{K}$  and  $^{85}\text{Rb}$ , the  $\pi/2$  pulse widths were 3.5  $\mu\text{s}$ , 5.25  $\mu\text{s}$  and 1.75  $\mu\text{s}$ , respectively, with corresponding rf fields of  $\nu_1(^{87}\text{Rb}) = 35.7$  kHz,  $\nu_1(^{39}\text{K}) = 23.8$  kHz and  $\nu_1(^{85}\text{Rb}) = 47.6$  kHz. All  $^{87}\text{Rb}$  NMR experiments featured a recycle delay of 1.0 s and spectral width of 100 kHz.  $^{39}\text{K}$  static and MAS NMR experiments were acquired with 80 kHz and 30 kHz spectral windows, respectively, and a recycle delay of 3.0 s. Spectral widths of 200 kHz and 100 kHz were employed for  $^{85}\text{Rb}$  static and MAS NMR experiments, respectively, with a recycle delay of 0.5 s. The static  $^{87}\text{Rb}$  Hahn echo was acquired with inter-pulse delays  $\tau_1 = 60$   $\mu\text{s}$  and  $\tau_2 = 40$   $\mu\text{s}$ . All  $^{87}\text{Rb}$  MAS experiments were performed at a spinning frequency of  $\nu_{\text{rot}} = 10$  kHz; the rotor-synchronized Hahn echo was recorded with  $\tau_1 = 100$   $\mu\text{s}$  and  $\tau_2 = 30$   $\mu\text{s}$ . For the static  $^{39}\text{K}$  Hahn echo experiment  $\tau_1$  was set to 200  $\mu\text{s}$  in order to minimize the effects of acoustic ringing and a pre-acquisition delay ( $\tau_2$ ) of 100  $\mu\text{s}$  was employed. All  $^{39}\text{K}$  MAS NMR experiments were performed at  $\nu_{\text{rot}} = 10$  kHz; the MAS Hahn echo employed  $\tau_1 = 400$   $\mu\text{s}$  and  $\tau_2 = 200$   $\mu\text{s}$ .  $^{85}\text{Rb}$  static and MAS ( $\nu_{\text{rot}} = 15$  kHz) Hahn echo experiments used  $\tau_1 = 50$   $\mu\text{s}$  and  $\tau_2 = 40$   $\mu\text{s}$  and  $\tau_1 = 66.7$   $\mu\text{s}$  and  $\tau_2 = 36.7$   $\mu\text{s}$ , respectively.

Hahn echo experiments were all processed by shifting to the top of the echo before Fourier transformation and using exponential multiplication with Lorentzian broadening (LB). All variations of QCPMG experiments were processed with LB between 2 – 5 Hz, except for static  $^{39}\text{K}$  and  $^{85}\text{Rb}$  QCPMG and DFS/QCPMG spectra, where LB of 20 Hz was employed. Relative signal intensities were compared by numerical integration of the spectra using NUTS software (Acorn NMR).

## 4.3 Results and Discussion

### 4.3.1 $^{87}\text{Rb}$ NMR Experiments

The  $^{87}\text{Rb}$  nucleus was chosen for initial tests of these sequences due to its high receptivity and moderate nuclear quadrupole moment ( $Q(^{87}\text{Rb}) = 1.3 \times 10^{-29} \text{ m}^2$ ); as a result, all static and MAS NMR experiments required collection of only 128 transients.  $\text{RbClO}_4$  is an ideal sample for such studies due to the fact that there is a single Rb site with  $C_Q(^{87}\text{Rb}) = 3.3 \text{ MHz}$  and  $\eta_Q = 0.2$ .<sup>[19]</sup> Comparison of the static Hahn echo and DFS/Hahn echo spectra (Figure 4.2a) reveals a signal enhancement of 2.1, in agreement with predicted enhancements for DFS static spectra of spin-3/2 nuclei<sup>[8]</sup> (the integrated intensity of the static Hahn echo experiment is normalized to 1.0 and all signal enhancements are reported with respect to this normalized value). The DFS/Hahn echo scheme consists of a DFS followed by the Hahn echo sequence for detection of the signal. The DFS are implemented using a converging amplitude-modulated pulse described in Reference [7], with starting frequency,  $\nu_s$ , and final frequency,  $\nu_f$ , where  $\nu_s > \nu_f$  (Figure 4.3a). The starting frequency,  $\nu_s = 1.7 \text{ MHz}$ , lies just outside the extremities of the  $\pm 1/2 - \pm 3/2$  satellite transition powder patterns and is approximately equal to, or a bit greater than the quadrupolar frequency ( $\nu_Q = 3C_Q/(2I(2I - 1))$ ). The  $^{87}\text{Rb}$  DFS pulse swept a frequency range of ca. 1.6 MHz over a period of 400  $\mu\text{s}$ , which was divided into 3460 steps. This corresponds to a sweep rate,  $\lambda$ , of 4.0  $\text{GHz s}^{-1}$ , and an adiabaticity parameter of  $A = 0.32$ , where the adiabaticity parameter,  $A$ , is defined as  $A = \nu_1^2/\lambda$ .<sup>[20]</sup> For a very fast sweep rate, the value of  $A$  will be low (e.g., 0.001) and the passage of the satellite

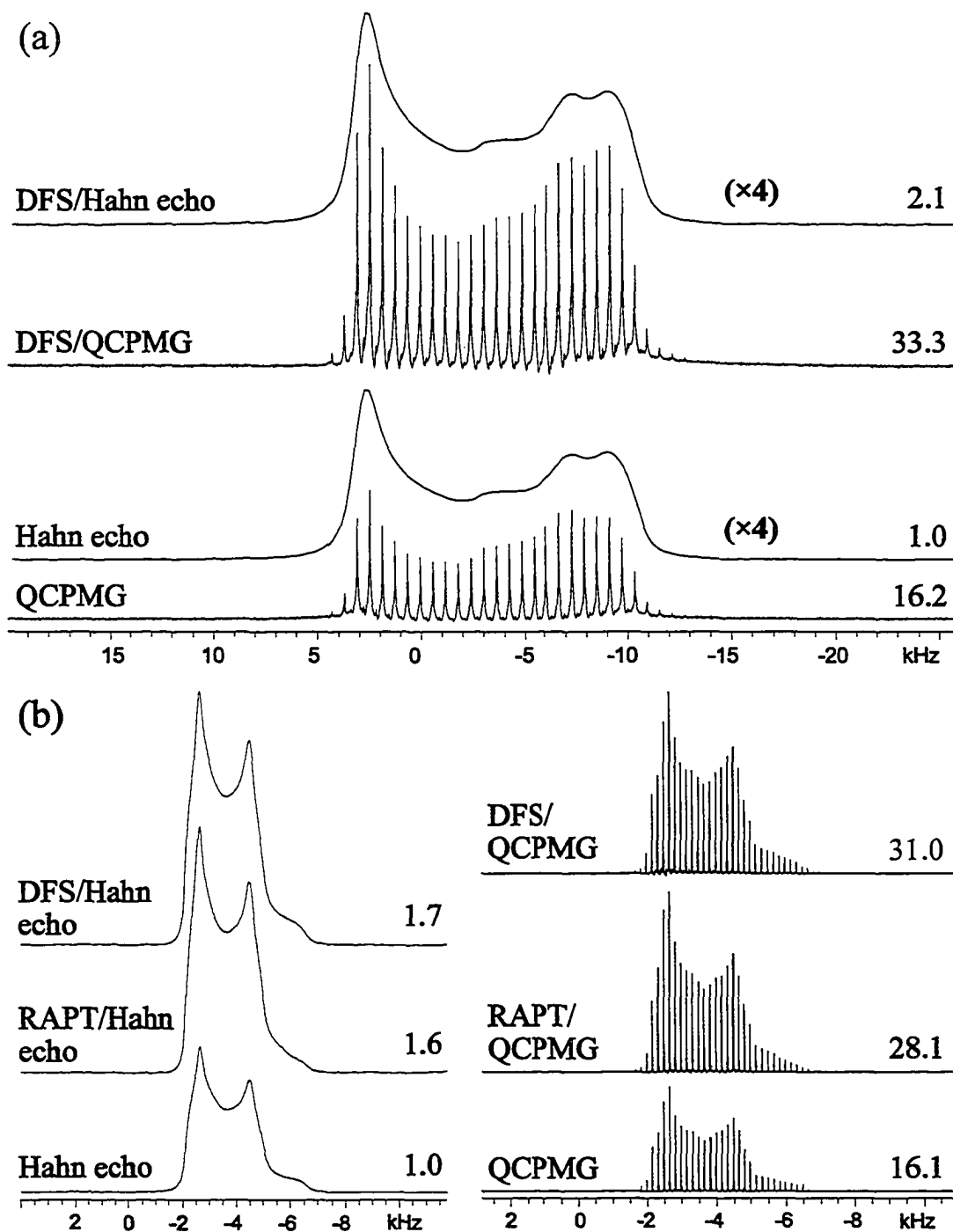


**Figure 4.2** (a) Static  $^{87}\text{Rb}$  Hahn echo and DFS/Hahn echo NMR spectra of  $\text{RbClO}_4$ , along with corresponding QCPMG experiments. The vertical scales of both echo spectra are augmented by a factor of 4. (b)  $^{87}\text{Rb}$  MAS Hahn echo, RAPT/Hahn echo, DFS/Hahn echo, QCPMG, RAPT/QCPMG and DFS/QCPMG NMR spectra of  $\text{RbClO}_4$ . All spectra were acquired with 128 scans. Integrated intensities with respect to the static and MAS  $^{87}\text{Rb}$  Hahn echo experiments are located to the right of each spectrum.



transitions with the frequency sweep is sudden. In this condition, the spin populations are not observed to change in the laboratory frame and no central transition signal enhancement is observed. A higher value of  $A$  (e.g.,  $A > 0.1$ ) may correspond to an adiabatic passage, where the sweep rate through the satellite transitions is slow enough that the level populations become saturated or inverted in the laboratory frame. The adiabaticity parameter must also be chosen such that adiabatic passage occurs for the single-quantum transitions (i.e.,  $\pm 1/2 \rightarrow \pm 3/2$  for spin-3/2) but is sudden with respect to double-quantum and higher-order transitions. Further information regarding the optimization of DFS pulse sequences is thoroughly explained elsewhere.<sup>[8, 20]</sup>

Careful choice of the final frequency,  $\nu_f$ , is integral in maximizing signal enhancement and ensuring that there is minimal distortion of the central transition powder pattern. For example, the  $^{87}\text{Rb}$  central transition powder pattern of  $\text{RbClO}_4$  has a breadth of approximately 15 kHz, which theoretically requires the DFS to halt at ca.  $\nu_f = 10$  kHz; however, a series of experiments testing signal enhancement as a function of  $\nu_f$  reveal that the end of the sweep must occur far from the edge of the central transition pattern (not shown). For example, optimum signal enhancement with minimal distortion of the powder pattern (i.e., most resembling the pure Hahn echo pattern) was obtained when the DFS ended at  $\nu_f = 146$  kHz. The reason for this is that the DFS pulse does not perfectly sweep the predefined frequency range, as evidenced by performing a Fourier Transform of the complete DFS time-domain waveform (Fig 4.3b). The frequency representation of the DFS does not have well-defined boundaries; rather, both the inner and outer edges are gradual in their descent.

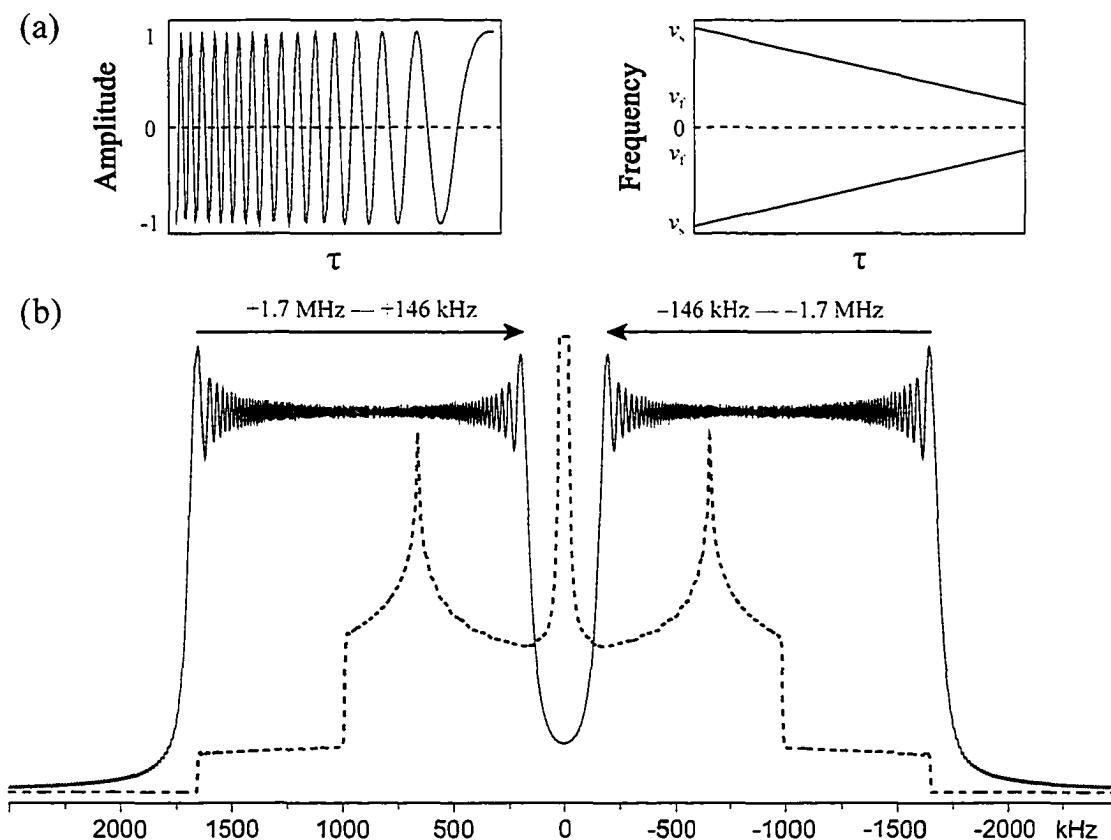


**Figure 4.3** (a) Time-domain representation of a converging DFS pulse and corresponding schematic representation of the DFS in the frequency domain. (b) Fourier transformed frequency-domain representation of the DFS pulse used in  $^{87}\text{Rb}$  NMR experiments (—) along with simulation of the  $\text{RbClO}_4$  powder pattern including the  $\pm 1/2 - \pm 3/2$  satellite transitions (- - -).

The static  $^{87}\text{Rb}$  QCPMG and DFS/QCPMG spectra (Figure 4.2a) were acquired with 24 Meiboom-Gill (MG) loops, an acquisition period per echo ( $\tau_a$ ) of 1.64 ms and inter-pulse and inter-acquisition delays  $\tau_1, \tau_2, \tau_3, \tau_4$  of 30  $\mu\text{s}$ , 40  $\mu\text{s}$ , 20  $\mu\text{s}$  and 30  $\mu\text{s}$ , respectively (see Figure 4.1a, 4.1b). For the DFS/QCPMG experiment, the applied DFS pulse has the same parameters as described for the static DFS/Hahn echo experiment. It is noted that in all cases reported herein, the use of DFS as a preparation pulse does not appear to influence the application of the subsequent pulse sequences, nor the shape of the powder patterns. Integration of the  $^{87}\text{Rb}$  QCPMG static spectrum reveals a signal

enhancement of a factor of 16 in comparison to the standard Hahn echo experiment. Variable degrees of signal-to-noise (S/N) enhancement are possible with the QCPMG experiment, depending upon the desired resolution of the spikelet manifold. The QCPMG parameters were chosen to provide close resemblance of the spikelet manifold to the static NMR powder patterns. The DFS/QCPMG experiment yields a signal enhancement factor of 33; thus, the DFS pulse sequence preceding the Hahn echo or QCPMG sequence provides similar signal enhancement of the central transition (i.e., approximately a factor of 2.1).

The Hahn echo, RAPT/Hahn echo and DFS/Hahn echo experiments and their QCPMG counterparts under conditions of magic-angle spinning are now compared. The QCPMG MAS sequence employed  $\tau_1 = \tau_2 = 100 \mu\text{s}$ ,  $\tau_3 = \tau_4 = 96.5 \mu\text{s}$ , 72 MG loops and  $\tau_a = 6.0 \text{ ms}$ .  $\tau_3$  and  $\tau_4$  were set according to the equation  $2N\tau_r = \tau_a + \tau_3 + \tau_4 + \tau_\pi$ , where  $N$  is an integer,  $\tau_r$  is the rotor period,  $\tau_3 = \tau_4$ , and  $\tau_\pi$  is the duration of the “selective”  $\pi$  pulse.<sup>[11]</sup> DFS MAS experiments were performed in the same manner as the non-spinning experiments. The RAPT pulse sequence (Figure 4.1c) consists of a series of repeating X- $\bar{X}$  units comprised of two oppositely phased ( $0^\circ$ ,  $180^\circ$ ) pulses of equal duration, each of which is preceded by a 100 ns delay. As suggested by a previous study,<sup>[5]</sup> the time for one X- $\bar{X}$  unit was initially set to a value of approximately  $4/C_Q$ , and subsequently optimized to  $1.6 \mu\text{s}$  (i.e., the duration of each pulse was  $0.7 \mu\text{s}$ ) and for simplicity, the duration of the complete RAPT sequence was set equal to the rotor period. The X- $\bar{X}$  unit was repeated 62 times and a delay of  $0.8 \mu\text{s}$  (which is denoted as  $\tau_{\text{RAPT}}$ ) was employed before the initial  $\pi/2$  pulse of the succeeding pulse sequences. Little variation was found in the

signal enhancement upon lengthening or shortening the overall RAPT train duration, in accordance with a previous report.<sup>[5]</sup> The RAPT and DFS pulse sequences provide signal enhancements of 1.6 and 1.7, respectively, in comparison to the Hahn echo MAS NMR spectrum which has a normalized integrated intensity of 1.0 (Figure 4.2b). The QCPMG MAS NMR experiment has an enhancement factor of 16, and preparatory RAPT and DFS sequences nearly double that signal enhancement.

The <sup>87</sup>Rb NMR experiments on RbClO<sub>4</sub> provide a fast and efficient means of optimizing QCPMG, RAPT and DFS parameters. In all cases, the RAPT and DFS preparatory sequences are equally successful in providing approximately double the signal enhancement of standard QCPMG NMR experiments. It is obvious that a significant augmentation of the powder pattern S/N can be achieved with QCPMG and in the case of <sup>87</sup>Rb, this enhancement is clearly superfluous due to the inherently high sensitivity of the nucleus; however, this is an invaluable aid to the NMR characterization of less favourable nuclei such as <sup>39</sup>K and <sup>85</sup>Rb (*vide infra*).

### 4.3.2 <sup>39</sup>K NMR Experiments

Rapid acquisition of solid-state <sup>39</sup>K NMR experiments is highly desirable, due to the common occurrence of potassium in many biological and inorganic materials of interest. <sup>39</sup>K has a high natural abundance (93.1%) and relatively small quadrupole moment ( $Q(^{39}\text{K}) = 5.5 \times 10^{-30} \text{ m}^2$ ). However, its small gyromagnetic ratio makes it a challenging nucleus for solid-state NMR experiments (i.e., at 9.4 T,  $\nu_0 = 18.65 \text{ MHz}$ ). In addition, NMR experiments at low frequencies such as this are often plagued by acoustic

probe ringing. Even in  $^{39}\text{K}$  spin-echo experiments, which have the potential of reducing the deleterious effects of probe ringing, echo delays must often be prohibitively long, thereby decreasing the effective signal.

A comparison of static  $^{39}\text{K}$  Hahn echo, DFS/Hahn echo, QCPMG and DFS/QCPMG NMR spectra of  $\text{KHCO}_3$  ( $C_Q = 1.49$  MHz,  $\eta_Q = 0.24$ )<sup>[21]</sup> are shown in Figure 4.4a. In this set of experiments, the collection of 18144 transients (over 908 minutes) was required for the Hahn echo and DFS/Hahn echo experiments in order to obtain a reasonable S/N ratio. All  $^{39}\text{K}$  DFS experiments were acquired with  $\nu_s = 850$  kHz and  $\nu_r = 85$  kHz over a period of  $508 \mu\text{s}$  with 2200 steps, meaning  $\lambda = 1.51$  GHz  $\text{s}^{-1}$  and  $A = 0.38$ . For the QCPMG and DFS/QCPMG experiments, spectra with comparable or superior S/N ratios were obtained with only 1824 transients (92 minutes). Static QCPMG experiments employed 19 MG loops, a  $\tau_a$  of 1.25 ms and inter-pulse and inter-acquisition delays of  $\tau_1 = \tau_2 = 200 \mu\text{s}$  and  $\tau_3 = \tau_4 = 100 \mu\text{s}$ . The integrated intensities of the static Hahn echo and QCPMG spectra are coincidentally equal to 1.0; however, the QCPMG experiment provides a signal enhancement of greater than an order of magnitude, as evidenced by acquisition times which are reduced by a factor of ca. 10. Both the DFS/Hahn echo and DFS/QCPMG sequences provided signal enhancements of ca. 1.9 with respect to corresponding “non-DFS” experiments, indicating that the preparatory DFS pulse is an attractive and important addition to the standard QCPMG sequence in this case.

A comparison of  $^{39}\text{K}$  MAS Hahn echo, RAPT/Hahn echo, DFS/Hahn echo and corresponding QCPMG NMR spectra is shown in Figure 4.4b. All of the QCPMG

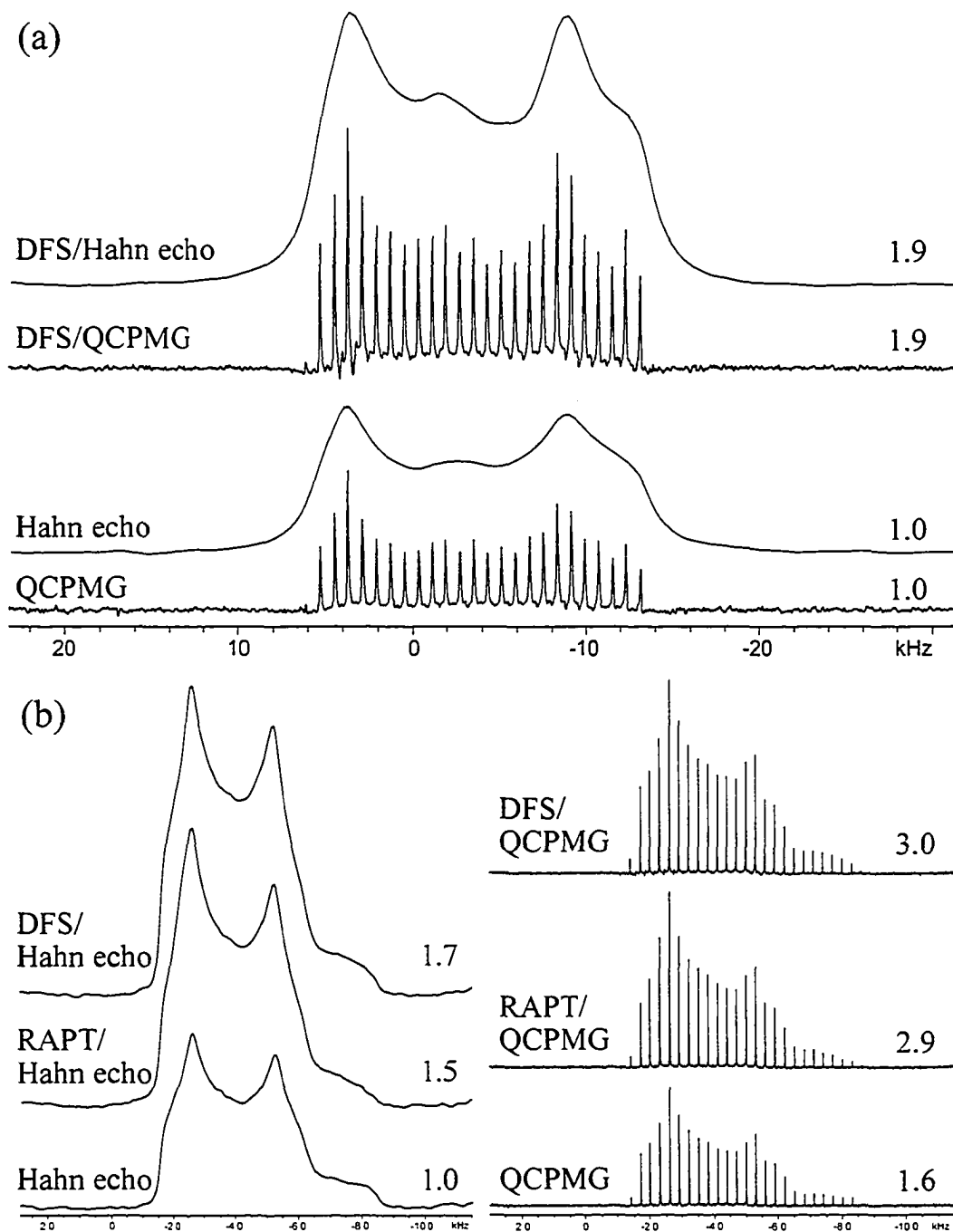


**Figure 4.4** (a) Static  $^{39}\text{K}$  Hahn echo and DFS/Hahn echo NMR spectra of  $\text{KHCO}_3$  and corresponding QCPMG experiments. (b)  $^{39}\text{K}$  MAS Hahn echo, RAPT/Hahn echo, DFS/Hahn echo and corresponding QCPMG NMR spectra of  $\text{KHCO}_3$ . Integrated intensities with respect to the static and MAS Hahn echo experiments are located to the right of each spectrum. QCPMG experiments were acquired with ca. 10 times fewer scans than corresponding echo experiments.

experiments were completed in 41 minutes (752 scans), whereas corresponding echo experiments took 372 minutes to complete (7392 scans). In the  $^{39}\text{K}$  RAPT MAS experiments, the time for each  $X\text{-}\bar{X}$  unit was optimized to  $3.9\ \mu\text{s}$  (pulse duration  $1.85\ \mu\text{s}$ ) and was repeated 25 times, with  $\tau_{\text{RAPT}} = 2.5\ \mu\text{s}$ . QCPMG MAS NMR experiments utilized 81 MG loops,  $\tau_a = 3.33\ \text{ms}$ ,  $\tau_1 = \tau_2 = 200\ \mu\text{s}$  and  $\tau_3 = \tau_4 = 128.25\ \mu\text{s}$ . Despite our best attempts at optimizing the pulse sequence parameters, a signal enhancement of only 1.5 was achieved with the RAPT/Hahn echo experiment. However, a signal enhancement close to two times (with respect to the QCPMG experiment) was obtained in the corresponding RAPT/QCPMG experiment. DFS/Hahn echo and DFS/QCPMG experiments resulted in signal enhancements of 1.7 and 3.0, respectively. It is important to stress that the QCPMG spectra presented in Figure 4.4 were all acquired with ca. 10 times less scans than their echo counterparts, implying overall signal enhancements of ca. 20 – 30 times.

### 4.3.3 $^{85}\text{Rb}$ NMR Experiments

Despite the high natural abundance of  $^{85}\text{Rb}$  (72.15%), it has a larger quadrupole moment ( $Q(^{85}\text{Rb}) = 2.7 \times 10^{-29}\ \text{m}^2$ ) and a significantly lower gyromagnetic ratio ( $\nu_0 = 38.59\ \text{MHz}$  at 9.4 T) than  $^{87}\text{Rb}$ , and is accordingly less often examined in solid-state NMR experiments. We chose to conduct experiments on  $^{85}\text{Rb}$  due to the fact that it is less receptive, but more importantly because it is a spin-5/2 nucleus, which will have different central transition signal enhancement factors from the RAPT and DFS pulse sequences. For instance, two separate amplitude-modulated RAPT sequences with

different modulation frequencies affect the outer and inner satellite transitions consecutively, resulting in partial saturation of all satellites of a spin-5/2 nucleus, which yields signal enhancements of ca. 2.5.<sup>[18]</sup> A converging DFS pulse, which first inverts populations of the outer satellites followed by inner satellite population inversion has the potential of providing a maximum signal enhancement of 5 times for single crystals or ca. 3 times for polycrystalline powder samples.<sup>[18]</sup>

Static <sup>85</sup>Rb Hahn echo and DFS/Hahn echo NMR spectra involved the acquisition of 8480 transients, whereas corresponding QCPMG experiments were completed with the collection of 848 scans (Figure 4.5a). The DFS experiments were optimized for maximum signal enhancement using  $\nu_s = 1.95$  MHz and  $\nu_f = 200$  kHz over a period of 1200  $\mu$ s and 6120 steps, hence  $\lambda = 1.458$  GHz  $s^{-1}$  and  $A = 1.59$ . Static QCPMG experiments employed 95 MG loops,  $\tau_a = 0.85$  ms, and  $\tau_1, \tau_2, \tau_3$  and  $\tau_4$  all set to 40  $\mu$ s. Comparison of Hahn echo and DFS/Hahn echo experiments reveal a signal enhancement of 2.9 in the latter. Surprisingly, in the corresponding QCPMG spectra (which have an overall signal enhancement of 15 times), a signal enhancement of ca. 3.8 times is obtained with DFS/QCPMG. The reason for this additional signal enhancement is unknown at this time. It is noteworthy that the <sup>85</sup>Rb nucleus in RbClO<sub>4</sub> has transverse relaxation properties well suited for QCPMG experiments, as very long trains of spin echoes are easily obtained which result in immense signal enhancements.

All <sup>85</sup>Rb Hahn echo and QCPMG MAS spectra (Figure 4.5b) were acquired with collection of 3360 and 336 transients, respectively. In RAPT experiments the length of the X- $\bar{X}$  unit was set to 2.08  $\mu$ s and repeated 31 times;  $\tau_{\text{RAPT}}$  was set to 2.18  $\mu$ s. The



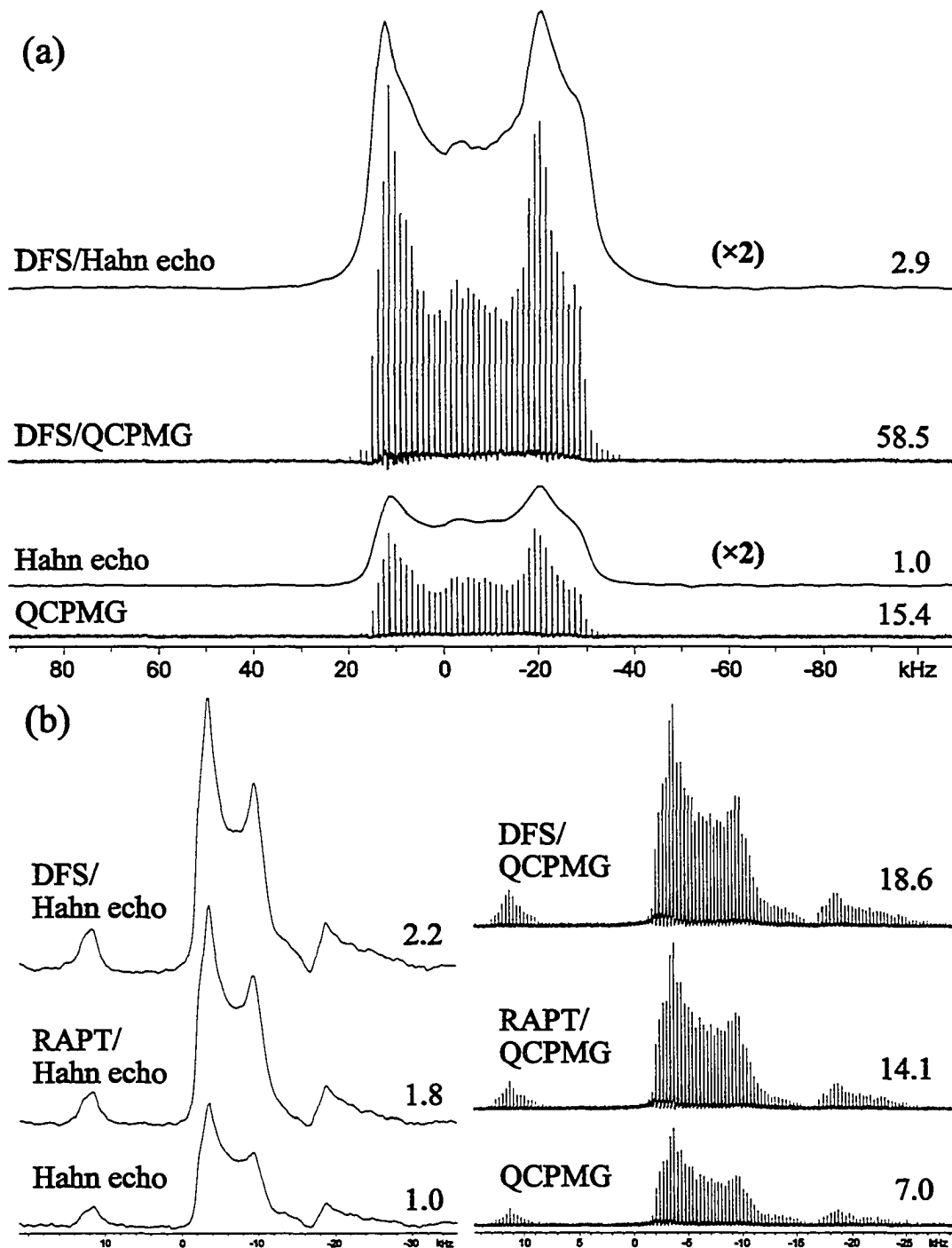


**Figure 4.5** (a) Static  $^{85}\text{Rb}$  Hahn echo and DFS/Hahn echo NMR spectra of  $\text{RbClO}_4$  and corresponding QCPMG experiments. The vertical scale of both echo spectra is augmented by a factor of 2. (b)  $^{85}\text{Rb}$  MAS Hahn echo, RAPT/Hahn echo, DFS/Hahn echo and corresponding QCPMG NMR spectra of  $\text{RbClO}_4$ . Integrated intensities with respect to the static and MAS  $^{85}\text{Rb}$  Hahn echo experiments are located to the right of each spectrum. QCPMG experiments were acquired with 10 times fewer scans than corresponding echo experiments.

recently published technique featuring two distinct consecutive amplitude-modulated RAPT sequences<sup>[18]</sup> was not applied in the set of experiments reported herein, though this method is expected to provide further signal enhancements. The QCPMG MAS NMR experiments utilized 53 MG loops,  $\tau_a = 3$  ms,  $\tau_1 = \tau_2 = 66.7$   $\mu$ s and  $\tau_3 = \tau_4 = 98.25$   $\mu$ s. RAPT/ and DFS/Hahn echo experiments resulted in signal enhancements of 1.8 and 2.2, respectively. The QCPMG MAS NMR experiments were conducted to produce very high resolution spectra, so a signal enhancement of only 7 times is obtained (modification of the QCPMG parameters could easily result in further signal enhancements of two or three times). RAPT/QCPMG and DFS/QCPMG experiments provide additional enhancement factors of 2.0 and 2.6, respectively.

#### 4.4 Conclusions

The DFS pulse sequence has been successfully combined with the QCPMG pulse sequence for both static and MAS NMR experiments. The DFS/QCPMG scheme provides signal enhancements of approximately a factor of 2 for spin-3/2 nuclei and 2.6 – 3.8 times for spin-5/2 nuclei compared to the standard QCPMG experiments. Similarly, the combination of RAPT with the QCPMG sequence for MAS experiments yields signal enhancements of 1.5 – 2.0 for spin-3/2 and spin-5/2 nuclei. The RAPT sequence generally provides slightly less signal enhancement in comparison to the DFS experiment; however, the former is trivial to implement whereas the latter requires a fair degree of optimization. At the very least, the DFS experiments require a rough estimate of  $C_Q$  in order to properly set the DFS parameters (notably, the success of the DFS pulse

depends on prudent selection of the final frequency,  $\nu_f$ ). The QCPMG experiments provide greater than an order of magnitude of signal enhancement, with the coupled RAPT or DFS preparatory sequences offering the potential of reducing experimental times further by close to an order of magnitude (since  $S/N$  scales as the square root of the total number of transients acquired) thereby making these pulse schemes extremely attractive for the study of unreceptive half-integer quadrupolar nuclei. Of equal importance is the potential application of the DFS/ and RAPT/QCPMG sequences in further work on optimization of RAPT and DFS pulse sequences, due to the greatly reduced experimental times afforded by these sequences.

# Bibliography

- [1] M. E. Smith, E. R. H. van Eck, *Prog. Nucl. Magn. Reson. Spectrosc.* **1999**, *34*, 159.
- [2] A. Medek, J. S. Harwood, L. Frydman, *J. Am. Chem. Soc.* **1995**, *117*, 12779.
- [3] L. Frydman, J. S. Harwood, *J. Am. Chem. Soc.* **1995**, *117*, 5367.
- [4] F. H. Larsen, H. J. Jakobsen, P. D. Ellis, N. C. Nielsen, *J. Phys. Chem. A* **1997**, *101*, 8597.
- [5] Z. Yao, H. T. Kwak, D. Sakellariou, L. Emsley, P. J. Grandinetti, *Chem. Phys. Lett.* **2000**, *327*, 85.
- [6] P. K. Madhu, A. Goldbourn, L. Frydman, S. Vega, *J. Chem. Phys.* **2000**, *112*, 2377.
- [7] A. P. M. Kentgens, R. Verhagen, *Chem. Phys. Lett.* **1999**, *300*, 435.
- [8] D. Iuga, H. Schafer, R. Verhagen, A. P. M. Kentgens, *J. Magn. Reson.* **2000**, *147*, 192.
- [9] M. E. Smith, in *Annual Reports on Nmr Spectroscopy, Vol 43, Vol. 43*, **2001**, pp. 121.
- [10] A. S. Lipton, J. A. Sears, P. D. Ellis, *J. Magn. Reson.* **2001**, *151*, 48.
- [11] F. H. Larsen, H. J. Jakobsen, P. D. Ellis, N. C. Nielsen, *J. Magn. Reson.* **1998**, *131*, 144.
- [12] F. H. Larsen, N. C. Nielsen, *J. Phys. Chem. A* **1999**, *103*, 10825.
- [13] A. S. Lipton, M. D. Smith, R. D. Adams, P. D. Ellis, *J. Am. Chem. Soc.* **2002**,

124, 410.

- [14] F. H. Larsen, J. Skibsted, H. J. Jakobsen, N. C. Nielsen, *J. Am. Chem. Soc.* **2000**, *122*, 7080.
- [15] D. L. Bryce, M. Gee, R. E. Wasylshen, *J. Phys. Chem. A* **2001**, *105*, 10413.
- [16] J. Haase, M. S. Conradi, C. P. Grey, A. J. Vega, *J. Magn. Reson. Ser. A* **1994**, *109*, 90.
- [17] H. Schafer, D. Iuga, R. Verhagen, A. P. M. Kentgens, *J. Chem. Phys.* **2001**, *114*, 3073.
- [18] P. K. Madhu, K. J. Pike, R. Dupree, M. H. Levitt, M. E. Smith, **2003**, *367*, 150.
- [19] T. Vosegaard, J. Skibsted, H. Bildsoe, H. J. Jakobsen, *J. Magn. Reson. Ser. A* **1996**, *122*, 111.
- [20] E. Van Veenendaal, B. H. Meier, A. P. M. Kentgens, *Mol. Phys.* **1998**, *93*, 195.
- [21] T. J. Bastow, *J. Chem. Soc.-Faraday Trans.* **1991**, *87*, 2453.

# Chapter 5

## Application of the Carr-Purcell Meiboom-Gill Pulse Sequence for the Acquisition of Solid-State NMR Spectra of Spin-1/2 Nuclei

### 5.1 Introduction

A large number of solid-state NMR studies on materials containing unreceptive nuclei have recently been published due to the increasing availability of high magnetic fields, sophisticated NMR hardware and the development of new pulse sequences and methodologies for acquiring NMR spectra of low-gamma nuclei.<sup>[1,2]</sup> Unreceptive nuclei are nuclei which are not amenable to standard NMR experiments due to (i) low magnetogyric ratios ( $\gamma$ ), (ii) low natural abundances, (iii) large nuclear quadrupole moments (in the case of quadrupolar nuclei), (iv) dilution of the nuclide of interest, (v) large longitudinal relaxation time constants, (vi) exceedingly broad powder patterns or (vii) any combination of the above properties. Common means of circumventing such difficulties are running NMR experiments at ultra-high magnetic field strengths, at very low temperatures (e.g., below 50 K), and/or isotopic labelling. However, many of these measures are very costly, to the point of being prohibitive for many scientists interested in routinely conducting solid-state NMR experiments on unreceptive nuclei.

Recently, the quadrupolar Carr-Purcell Meiboom-Gill (QCPMG) sequence was introduced as a means of enhancing signal intensity in the NMR spectra of half-integer

quadrupolar nuclei (i.e., nuclear spins of 3/2, 5/2, 7/2 and 9/2).<sup>[3]</sup> The QCPMG sequence is very similar to the traditional CPMG sequence utilized for measuring transverse relaxation time constants.<sup>[4,5]</sup> The QCPMG sequence (Figure 5.1a) consists of a single  $\pi/2$  pulse followed by a train of alternating  $\pi$  pulses (which produce spin echoes) and

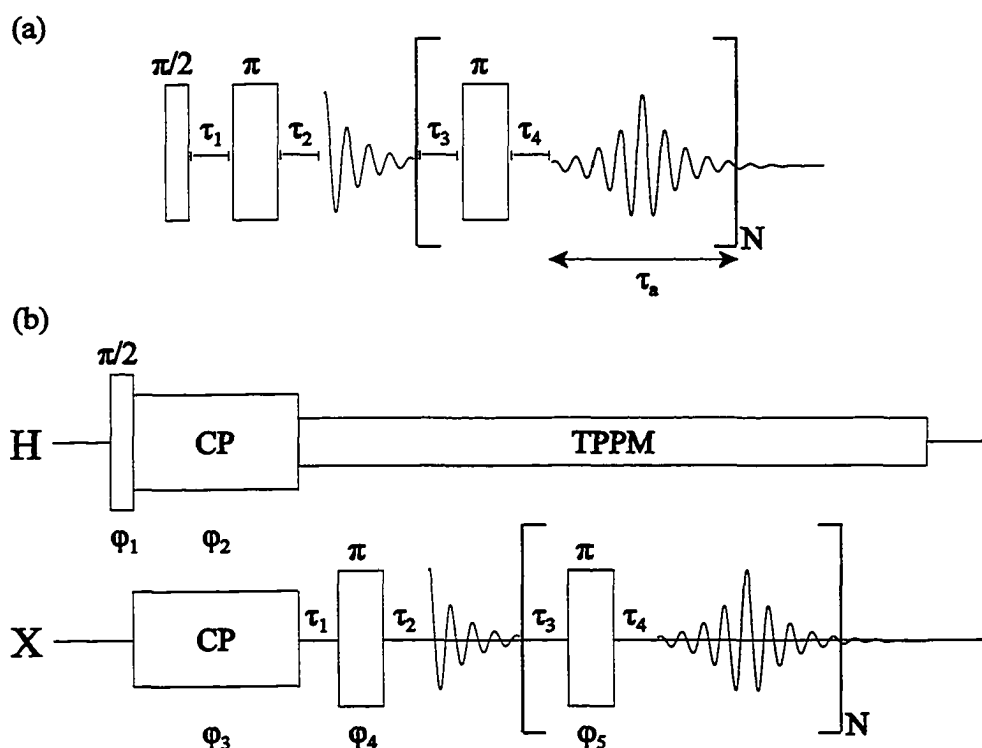


**Figure 5.1** Schematics of the (a) (Q)CPMG and (b) CP/CPMG with TPPM decoupling pulse sequences. The phases for each of the pulses in the CP/CPMG sequence are:  $\varphi_1 = 2, 0, 0, 2$ ;  $\varphi_2 = 1$ ;  $\varphi_3 = 3, 2$ ;  $\varphi_4 = 1, 0, 1, 0, 3, 2, 3, 2$ ;  $\varphi_5 = 1, 0, 1, 0, 3, 2, 3, 2, 3, 2, 3, 2, 1, 0, 1, 0$ ; with receiver phase list  $\varphi_r = (2, 3, 0, 1) \times 4$ , where  $\{n\pi/2 \mid n = 0, 1, 2, 3\}$

detection periods (in which the echo FIDs are acquired). By acquiring the spin echoes multiple times within a single scan, large signal enhancements can be obtained over the course of an experiment, making this technique advantageous for all types of unreceptive nuclei. The QCPMG FID consists of a series of echoes in the time domain which may be Fourier transformed to produce a manifold of spikelets in the frequency domain. For

most half-integer quadrupolar nuclei, the shape of this manifold corresponds to the shape of the central-transition powder pattern. The timing of the pulse sequence can be adjusted to produce a train of echoes with variable spacing in the time domain, such that close spacing in the time domain leads to a spectrum of high signal-to-noise ratio (S/N) but low resolution and far spacing leads to the opposite situation. The echoes from a CPMG train may be co-added to produce a central transition pattern of increased intensity compared to the standard Hahn echo pattern and/or processed with sawtooth apodization functions.<sup>[6]</sup>

The QCPMG sequence has been applied to quadrupolar nuclei in stationary samples and under conditions of magic-angle spinning (MAS) in a number of standard samples<sup>[3]</sup> and interesting biological,<sup>[7, 8]</sup> organic,<sup>[9, 10]</sup> organometallic<sup>[11, 12]</sup> and inorganic materials.<sup>[13, 14]</sup> QCPMG has also been utilized as a means of detecting the direct dimension in the MQMAS experiment (which is used for obtaining high-resolution NMR spectra of half-integer quadrupolar nuclei),<sup>[15]</sup> and has been implemented in wide-line piecewise acquisitions of spectra of quadrupolar nuclei with powder patterns exceeding standard excitation bandwidth.<sup>[8]</sup> Cross-polarization (CP) QCPMG sequences have been used to acquire spectra of half-integer nuclei in proton-containing systems,<sup>[2]</sup> and amplitude modulated double-frequency sweep (DFS) and rotor assisted population transfer (RAPT) pulse sequences have been coupled with the QCPMG sequence as preparatory sequences for further signal enhancements.<sup>[16]</sup>

An interesting application of the QCPMG sequence for signal enhancement was reported by Farnan and co-workers in a <sup>17</sup>O and <sup>29</sup>Si NMR study of  $\alpha$ -cristobalite.<sup>[17]</sup> The QCPMG sequence was applied to obtain high quality <sup>17</sup>O (spin = 5/2) MAS NMR



spectra, but also of interest, was the application of the pulse sequence to acquire the  $^{29}\text{Si}$  (spin = 1/2) NMR spectra. The  $^{29}\text{Si}$  NMR resonances in question are quite broad due to chemical shift distributions which result from the amorphous nature of the materials under examination. The implications of these experiments are significant, since there are many spin-1/2 nuclei which have broad powder patterns resulting from large chemical shift anisotropy, chemical shift distributions or other line broadening mechanisms.<sup>[18, 19]</sup> Many of these spin-1/2 nuclei also have low natural abundances, low magnetogyric ratios and/or long spin-lattice relaxation times ( $T_1$ ). The work of Farnan et al. is not the only application of CPMG-type sequences to spin-1/2 nuclei, but rather, one that closely resembles the recent QCPMG work in the literature. Aside from the typical use of the CPMG-type sequences to measure spin-spin relaxation time constants ( $T_2$ 's), they have also been used to enhance the  $^{89}\text{Y}$  NMR signal of  $\text{YBa}_2\text{Cu}_3\text{O}_{7-\delta}$ ,<sup>[20]</sup> study dipolar-induced spin-lattice relaxation,<sup>[21]</sup> enhance signal within the magic-angle hopping experiment,<sup>[22]</sup> double-quantum NMR experiments<sup>[23]</sup> and the ME-PHORMAT sequence,<sup>[24]</sup> as well as for resolving dipolar splittings between nuclei like  $^1\text{H}$  and  $^{19}\text{F}$ .<sup>[25]</sup>

In this chapter, we present examples of the CPMG pulse sequence applied to the study of five different nuclei:  $^{113}\text{Cd}$ ,  $^{199}\text{Hg}$ ,  $^{207}\text{Pb}$ ,  $^{15}\text{N}$  and  $^{109}\text{Ag}$  (Table 5.1). The CPMG NMR spectra of stationary samples of  $\text{Cd}(\text{NO}_3)_2 \cdot 4\text{H}_2\text{O}$ ,  $(\text{CH}_3\text{COO})_2\text{Hg}$ ,  $(\text{CH}_3\text{COO})_2\text{Pb} \cdot 3\text{H}_2\text{O}$ , doubly  $^{15}\text{N}$ -labelled  $\text{NH}_4\text{NO}_3$  and  $\text{AgSO}_3\text{CH}_3$  are presented. CP/CPMG NMR spectra are acquired with high-power two-pulse phase modulated (TPPM) proton-decoupling<sup>[26]</sup> throughout the train of  $\pi$ -pulses and acquisition periods.

**Table 5.1**  
Nuclear Properties of Studied Nuclei

nucleus	natural abundance [%]	$\gamma$ [ $10^7$ rad s <sup>-1</sup> T <sup>-1</sup> ]	$\nu_0$ at $B_0 = 9.4$ T [MHz]	$T_1$ [s] <sup>[a]</sup>	<sup>1</sup> H $T_1$ [s] <sup>[b]</sup>
<sup>15</sup> N	0.37	-2.7126	40.52	—	—
<sup>109</sup> Ag	48.18	-1.2519	18.60	—	< 5 <sup>[c]</sup>
<sup>113</sup> Cd	12.26	-5.9609	88.65	> 300 <sup>[d]</sup>	< 0.5 <sup>[d]</sup>
<sup>199</sup> Hg	16.84	4.8458	71.42	290 <sup>[e]</sup>	25 <sup>[e]</sup>
<sup>207</sup> Pb	22.60	5.6264	83.51	—	0.56 <sup>[f]</sup>

<sup>[a]</sup> Spin-lattice relaxation time of relevant nuclei in compounds studied. <sup>[b]</sup> Hydrogen spin-lattice relaxation times in studied compounds. <sup>[c]</sup> Reference [27]. <sup>[d]</sup> Reference [28]. <sup>[e]</sup> Reference [29]. <sup>[f]</sup> Reference [30].

Comparison of the CPMG and CP/CPMG spectra with conventional MAS and CP/MAS NMR spectra are presented. Full details of experimental parameters used in each experiment are also provided. The aim of this work is to demonstrate that the CPMG sequence can be used to efficiently acquire high-quality static spectra of spin-1/2 nuclei with broad powder patterns arising from chemical shielding anisotropy or other sources of line-broadening. Notably, this sequence is useful for samples with long spin-lattice relaxation times, unusual spinning-speed dependent CP behaviour, low NMR frequencies, low natural abundances or a combination of these factors.

## 5.2 Experimental

### 5.2.1 Sample Preparation and Handling

Samples of ammonium nitrate ( $^{15}\text{NH}_4^{15}\text{NO}_3$ , 98%  $^{15}\text{N}$ ), silver methanesulfonate ( $\text{AgSO}_3\text{CH}_3$ ), cadmium nitrate tetrahydrate ( $\text{Cd}(\text{NO}_3)_2 \cdot 4\text{H}_2\text{O}$ ) and mercury(II) acetate ( $(\text{CH}_3\text{COO})_2\text{Hg}$ ) were purchased from Sigma-Aldrich Canada Ltd. and used without further purification. Lead(II) acetate trihydrate ( $(\text{CH}_3\text{COO})_2\text{Pb} \cdot 3\text{H}_2\text{O}$ ) was obtained from the same company and recrystallized from aqueous solution, since it has been shown by  $^{13}\text{C}$  CP/MAS NMR that  $(\text{CH}_3\text{COO})_2\text{Pb} \cdot 3\text{H}_2\text{O}$  undergoes dehydration and phase transformation over time at room temperature.<sup>[31]</sup>  $^{207}\text{Pb}$  NMR spectra of a mixture of pure lead acetate trihydrate and the partially or completely dehydrated lead acetate are shown in Appendix B (Figure B.4). Samples were finely powdered and packed into 4 mm outer diameter  $\text{ZrO}_2$  rotors for  $^{15}\text{N}$  and  $^{109}\text{Ag}$  experiments, and 5 mm outer diameter rotors for

$^{113}\text{Cd}$ ,  $^{199}\text{Hg}$  and  $^{207}\text{Pb}$  experiments.

## 5.2.2 Solid-State NMR Spectroscopy

Solid-state NMR spectra were acquired on a Varian Infinity+ NMR spectrometer with an Oxford 9.4 T ( $\nu_0(^1\text{H}) = 400$  MHz) wide-bore magnet operating at  $\nu_0(^{15}\text{N}) = 40.52$  MHz,  $\nu_0(^{109}\text{Ag}) = 18.60$  MHz,  $\nu_0(^{113}\text{Cd}) = 88.65$  MHz,  $\nu_0(^{199}\text{Hg}) = 71.42$  MHz and  $\nu_0(^{207}\text{Pb}) = 83.47$  MHz. When working at the low  $^{109}\text{Ag}$  Larmor frequency, high forward-to-reflected power was achieved by employing a Varian/Chemagnetics low gamma tuning box.

$^{113}\text{Cd}$  chemical shifts are reported with respect to an external saturated solution of  $\text{Cd}(\text{NO}_3)_2 \cdot 4\text{H}_2\text{O}$  with its isotropic shift ( $\delta_{\text{iso}}$ ) set to 0.0 ppm, though an alternative referencing system features setting  $\delta_{\text{iso}} = -102.2$  ppm for solid  $\text{Cd}(\text{NO}_3)_2 \cdot 4\text{H}_2\text{O}$  with respect to solid  $\text{Cd}(\text{ClO}_4)_2$ .<sup>[32]</sup>  $^{199}\text{Hg}$  chemical shifts were referenced to  $\text{Hg}(\text{CH}_3)_2$  ( $\delta_{\text{iso}} = 0.0$  ppm) by setting the chemical shift of a concentrated  $\text{Hg}(\text{ClO}_4)_2$  aqueous solution to  $-2253$  ppm.<sup>[33]</sup>  $^{207}\text{Pb}$  NMR spectra were referenced to  $\text{Pb}(\text{CH}_3)_2$  by setting an external 0.5 M aqueous solution of  $\text{Pb}(\text{NO}_3)_2$  to  $\delta_{\text{iso}} = -2941$  ppm.<sup>[34]</sup> Nitrogen chemical shifts were referenced to liquid ammonia at 20 °C by setting the isotropic shift of the ammonium resonance in  $^{15}\text{NH}_4^{15}\text{NO}_3$  to 23.8 ppm.<sup>[35, 36]</sup> The  $^{109}\text{Ag}$  shift of  $\text{AgSO}_3\text{CH}_3(\text{s})$  was set to  $\delta_{\text{iso}} = 87.2$  ppm, such that it is referenced to 9 M  $\text{AgNO}_3(\text{aq})$  with  $\delta_{\text{iso}} = 0.0$  ppm.<sup>[27]</sup>

Spectral widths of 40, 50, 80, 400 and 400 kHz were employed for  $^{15}\text{N}$ ,  $^{109}\text{Ag}$ ,  $^{113}\text{Cd}$ ,  $^{199}\text{Hg}$  and  $^{207}\text{Pb}$  experiments, respectively. Recycle delays of 12, 5, 30, 90 and 4 s were used for all  $^{15}\text{N}$ ,  $^{109}\text{Ag}$ ,  $^{113}\text{Cd}$ ,  $^{199}\text{Hg}$  and  $^{207}\text{Pb}$  CP experiments, while for  $^{113}\text{Cd}$ ,  $^{199}\text{Hg}$

and  $^{207}\text{Pb}$  non-CP experiments the recycle delays were 60, 1450 and 20 s. For  $^{113}\text{Cd}$ ,  $^{199}\text{Hg}$  and  $^{207}\text{Pb}$  non-CP NMR spectra,  $\pi/2$  pulses of 4.4, 3.1 and 3.0  $\mu\text{s}$  with radio frequency (rf) fields of  $\nu_1 = 56.8, 80.6$  and  $83.3$  kHz were utilized, respectively, along with corresponding  $\pi$  pulses (where applicable). The TPPM heteronuclear decoupling scheme<sup>[26]</sup> was employed in all cases with typical  $^1\text{H}$  decoupling field strengths of 13 – 29 kHz.

$^{15}\text{N}$  CP NMR spectra were acquired with a 35 ms contact time (ct), a proton  $\pi/2$  pulse ( $\tau_{\pi/2}^{\text{H}}$ ) of 2.87  $\mu\text{s}$ , a rf field of  $\nu_{1\text{H}} = 87.1$  kHz, and matched radio frequency fields ( $\nu_{\text{CP}}$ ) of 58.4 kHz for CP.  $^{15}\text{N}$  CP/Hahn echo and CP/CPMG experiments employed a  $\pi$  pulse of 6.6  $\mu\text{s}$  and a rf field of 75.8 kHz. Furthermore, inter-pulse ( $\tau_1, \tau_3$ ) and pre-acquisition ( $\tau_2, \tau_4$ ) delays of 60  $\mu\text{s}$ , 408 Meiboom-Gill loops (MG) and an acquisition time per echo ( $\tau_a$ ) of 2.0 ms were employed for the CP/CPMG experiment, while  $\tau_1 = 75$   $\mu\text{s}$  and  $\tau_2 = 25$   $\mu\text{s}$  were used for the CP/Hahn echo spectrum. In particular,  $1/\tau_a$  represents the inter-spikelet separation in the frequency domain of CPMG type spectra. The CP/CPMG sequence is shown in Figure 5.1b with phase cycling details given in the figure caption.

$^{109}\text{Ag}$  CP experiments employed  $\tau_{\pi/2}^{\text{H}} = 2.8$   $\mu\text{s}$ ,  $\nu_{1\text{H}} = 89.3$  kHz, ct = 40 ms and  $\nu_{\text{CP}} = 31.6$  kHz. The  $^{109}\text{Ag}$  CP/Hahn echo spectrum was acquired with a 13.5  $\mu\text{s}$   $\pi$  pulse, rf field of 37.0 kHz,  $\tau_1 = 300$   $\mu\text{s}$  and  $\tau_2 = 160$   $\mu\text{s}$ , while the CP/CPMG experiment employed MG = 162,  $\tau_1 = \tau_2 = 300$   $\mu\text{s}$ ,  $\tau_3 = \tau_4 = 250$   $\mu\text{s}$ ,  $\tau_a = 2.0$  ms and the same  $\pi$  pulse.

For  $^{113}\text{Cd}$  CP spectra,  $\tau_{\pi/2}^{\text{H}} = 5.7$   $\mu\text{s}$ ,  $\nu_{1\text{H}} = 43.9$  kHz, ct = 6 ms and  $\nu_{\text{CP}} = 63.6$  kHz. For both CP and non-CP  $^{113}\text{Cd}$  Hahn echo and CPMG experiments, a  $\pi$  pulse of 8.8  $\mu\text{s}$

and rf field of 56.8 kHz were employed. Further,  $\tau_1 = 77.5 \mu\text{s}$  and  $\tau_2 = 40.0 \mu\text{s}$  for the Hahn echo spectra, and  $\text{MG} = 101$ ,  $\tau_a = 0.5 \text{ ms}$  and  $\tau_1 = \tau_2 = \tau_3 = \tau_4 = 70 \mu\text{s}$  for the CPMG experiments.

The  $^{199}\text{Hg}$  CP/MAS spectrum at 3 kHz spinning frequency ( $\nu_{\text{rot}}$ ) was acquired with  $\tau_{\pi/2}^{\text{H}} = 6.5 \mu\text{s}$ ,  $\nu_{1\text{H}} = 38.5 \text{ kHz}$ ,  $\text{ct} = 32 \text{ ms}$  and  $\nu_{\text{CP}} = 42.9 \text{ kHz}$ , while the CP/Hahn echo and CP/CPMG were recorded with  $\tau_{\pi/2}^{\text{H}} = 2.5 \mu\text{s}$ ,  $\nu_{1\text{H}} = 100 \text{ kHz}$ ,  $\text{ct} = 32 \text{ ms}$  and  $\nu_{\text{CP}} = 48.6 \text{ kHz}$ . For both the  $^{199}\text{Hg}$  CPMG and CP/Hahn echo experiments, a  $6.2 \mu\text{s}$   $\pi$  pulse and 80.6 kHz rf field were employed, while for the CP/CPMG spectrum, a  $\pi$  pulse of  $11.5 \mu\text{s}$  and rf field of 43.5 kHz were used. The CPMG experiments were recorded with  $\text{MG} = 247$ ,  $\tau_1 = \tau_2 = \tau_3 = \tau_4 = 20 \mu\text{s}$  and  $\tau_a = 330 \mu\text{s}$ ; the Hahn echo spectrum with  $\tau_1 = 60 \mu\text{s}$  and  $\tau_2 = 20 \mu\text{s}$ ; and each piece of the wideline CP/CPMG spectrum with  $\text{MG} = 81$ ,  $\tau_1 = \tau_2 = \tau_3 = \tau_4 = 20 \mu\text{s}$  and  $\tau_a = 250 \mu\text{s}$ . The transmitter frequency was varied through the 71.471 – 71.331 MHz and 71.440 – 71.343 MHz frequency ranges in 28 and 48.5 kHz steps for acquisition of the  $^{199}\text{Hg}$  wideline CP/CPMG and CPMG spectra, respectively.

For  $^{207}\text{Pb}$  CP/CPMG spectra,  $\tau_{\pi/2}^{\text{H}} = 3.5 \mu\text{s}$ ,  $\nu_{1\text{H}} = 71.4 \text{ kHz}$ ,  $\text{ct} = 2 \text{ ms}$  and  $\nu_{\text{CP}} = 35 \text{ kHz}$  were employed along with  $\text{MG} = 326$ ,  $\tau_1 = \tau_2 = \tau_3 = \tau_4 = 40 \mu\text{s}$  and  $\tau_a = 250 \mu\text{s}$ . Similar parameters were employed for the CPMG experiment except for pulses and the rf field, which were already mentioned earlier in the experimental section. Similar to the  $^{199}\text{Hg}$  wideline CP/CPMG spectrum, the  $^{207}\text{Pb}$  wideline CPMG and CP/CPMG spectra were acquired in 40 kHz steps within the 83.387 – 83.547 MHz transmitter frequency range.

### 5.2.3 Spectral Simulations

Simulations of static NMR spectra were accomplished with the WSOLIDS software package.<sup>[37]</sup> Manifolds of spinning sidebands (ssbs) were analysed using the method of Herzfeld and Berger,<sup>[38]</sup> which is incorporated into the aforementioned software. Spectra obtained from co-addition of the time-domain spin-echoes and subsequent Fourier transformation generally resemble the envelope of CPMG echo spikelet spectra, which in turn resemble conventional Hahn echo spectra (Appendix B, Figure B.5). Consequently, extraction of CSA parameters from CPMG spectra was simply accomplished by analytical simulation of their envelopes.

## 5.3 Results and Discussion

The results and discussion are presented in five different sub-sections divided by nuclei. The  $^{113}\text{Cd}$  NMR spectra of  $\text{Cd}(\text{NO}_3)_2 \cdot 4\text{H}_2\text{O}$  are examined first due to the high receptivity of  $^{113}\text{Cd}$ , the relatively narrow pattern and good CP efficiency. Then, the performance of the CP/CPMG pulse sequence is described for the  $^{199}\text{Hg}$  NMR of  $(\text{CH}_3\text{COO})_2\text{Hg}$  and  $^{207}\text{Pb}$  NMR of  $(\text{CH}_3\text{COO})_2\text{Pb} \cdot 3\text{H}_2\text{O}$ . Spectra of these nuclei typically have very broad powder patterns influenced by large chemical shielding anisotropy (CSA), and are often very difficult to acquire due to very long spin-lattice relaxation times ( $T_1$ 's). Application of the CP/CPMG pulse sequence to unreceptive nuclei with low Larmor frequencies and/or low natural abundances ( $^{15}\text{N}$  and  $^{109}\text{Ag}$ ) is then discussed.

### 5.3.1 $^{113}\text{Cd}$ NMR

$^{113}\text{Cd}$  NMR is quite common for the study of Cd coordination compounds as well as the investigation of model biological systems;<sup>[39]</sup> the latter is notably important due to the use of the receptive  $^{113}\text{Cd}$  nucleus as a surrogate for the unreceptive  $^{67}\text{Zn}$  nucleus.<sup>[40]</sup> Solid-state  $^{113}\text{Cd}$  NMR studies are often aimed at characterizing cadmium chemical shielding tensors,<sup>[41]</sup> which lend insight into the relationship between cadmium coordination environments and experimental cadmium chemical shifts. Initial  $^{113}\text{Cd}$  solid-state NMR experiments on  $\text{Cd}(\text{NO}_3)_2 \cdot 4\text{H}_2\text{O}$  were first reported by Gerstein and co-workers in 1980,<sup>[28]</sup> and later studies were reported by two other groups.<sup>[32, 42]</sup>  $^{113}\text{Cd}$  CP/MAS NMR experiments are preferable to MAS NMR experiments due to long  $T_1$ 's of close to 300 s, as well as the potential sensitivity enhancement afforded by  $^1\text{H}$ - $^{113}\text{Cd}$  cross polarization.

In Figures 5.2a and 5.2b,  $^{113}\text{Cd}$  CP/MAS NMR spectra of  $\text{Cd}(\text{NO}_3)_2 \cdot 4\text{H}_2\text{O}$  are shown at spinning speeds of 7000 Hz and 2000 Hz, respectively. Acquisitions of spectra at two spinning speeds are used to identify the isotropic chemical shift, while Herzfeld-Berger analysis can be applied to obtain anisotropic chemical shielding parameters. Cadmium CS tensors obtained from analysis of the various types of NMR spectra are shown in Table 5.2. A  $^{113}\text{Cd}$  CP/Hahn echo NMR spectrum (Figure 5.2c) is required to obtain an accurate CS pattern for the stationary sample, since standard static CP experiments result in missing points at the beginning of the FID, which lead to baseline distortions and other abnormalities in the experimental powder patterns. Cadmium CS parameters obtained from experiments on stationary samples (e.g.,  $\delta_{\text{iso}} = -4$  ppm,  $\Omega = 205$



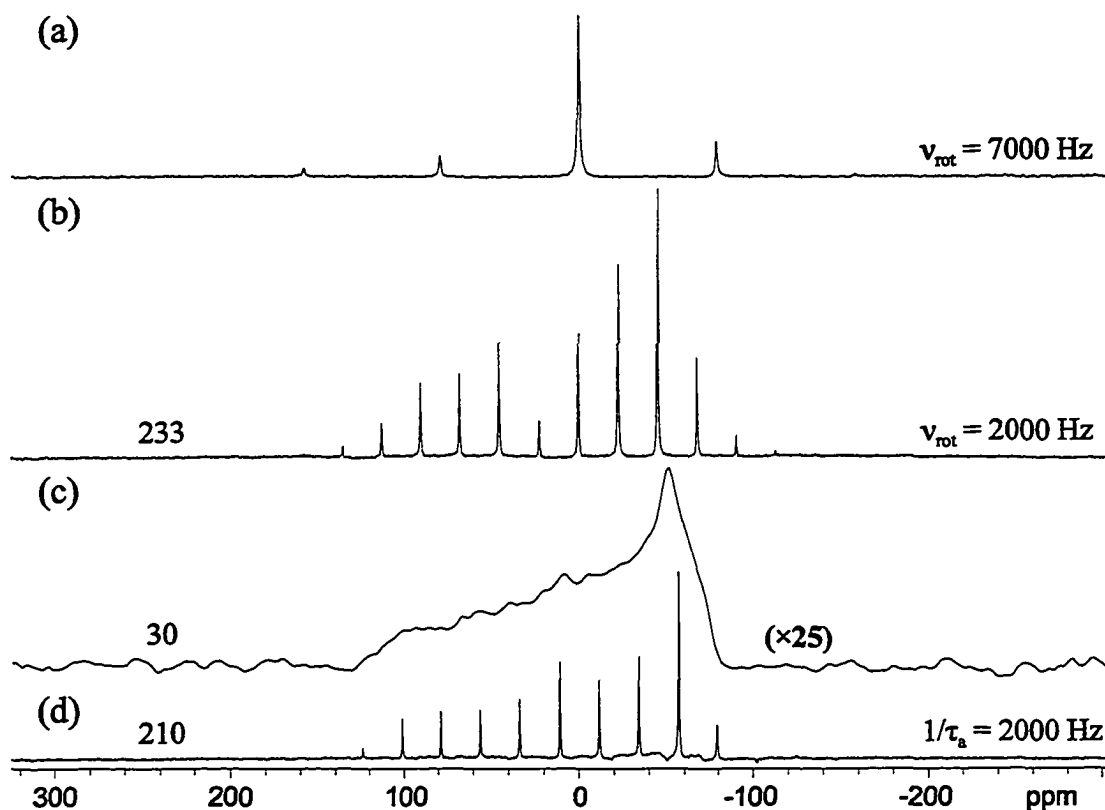


**Figure 5.2**  $^{113}\text{Cd}$  CP/MAS at (a)  $\nu_{\text{rot}} = 7000$  Hz and (b)  $\nu_{\text{rot}} = 2000$  Hz, (c) static CP/Hahn echo and (d) static CP/CPMG ( $1/\tau_a = 2000$  Hz) NMR spectra of  $\text{Cd}(\text{NO}_3)_2 \cdot 4\text{H}_2\text{O}$ ; all recorded with a total of 16 transients. Scaling factors used in modifying the vertical scale of spectra are shown in parentheses, otherwise, all spectra are shown on the same scale. The relevant S/N ratios are shown at the left of each spectrum.

ppm,  $\kappa = -0.78$ ) are in good agreement with parameters obtained from single-crystal  $^{113}\text{Cd}$  NMR,<sup>[32]</sup> while the values obtained from Herzfeld-Berger analysis of  $^{113}\text{Cd}$  CP/MAS or MAS spectra are somewhat less reliable. Increasingly accurate CS tensor parameters can indeed be deduced from simulations of static NMR spectra, however, acquisition of high S/N static spectra often requires long experimental times. Although the static  $^{113}\text{Cd}$  CP/CPMG (Figure 5.2d) and CP/Hahn echo spectra have been acquired over the same amount of time, the S/N in the former (210) is comparable to the CP/MAS (233) spectrum pictured in Figure 5.2b, while the latter (30) is much less intense (the S/N for

**Table 5.2**  
Anisotropic Chemical Shielding Parameters of Investigated Compounds

compound	experiment	$\delta_{\text{iso}}$ [ppm]	$\Omega$ [ppm]	$\kappa$	$\delta_{11}$ [ppm]	$\delta_{22}$ [ppm]	$\delta_{33}$ [ppm]
Cd(NO <sub>3</sub> ) <sub>2</sub> ·4H <sub>2</sub> O	CP/MAS ( $\nu_{\text{rot}} = 7000$ Hz)	0	159	-1.00	106(3)	-53(3)	-53(3)
	CP/MAS ( $\nu_{\text{rot}} = 2000$ Hz)	0	175	-0.84	112(2)	-49(2)	-63(2)
	CP/Hahn echo	0	205	-0.75	128(2)	-51(2)	-77(2)
	CP/CPMG	-4	205	-0.78	125(5)	-57(5)	-83(5)
	MAS ( $\nu_{\text{rot}} = 2000$ Hz)	0	209	-0.73	130(3)	-51(3)	-79(3)
	Hahn echo	0	200	-0.80	127(4)	-53(4)	-73(4)
	CPMG	-4	205	-0.78	125(5)	-57(5)	-83(5)
	single-crystal <sup>[a]</sup>	0	196.6	-0.80	124.4	-52.1	-72.2
(CH <sub>3</sub> COO) <sub>2</sub> Hg	CP/MAS ( $\nu_{\text{rot}} = 3000$ Hz)	-2488	1770	0.87	-1860(40)	-1975(40)	-3630(40)
	wideline CP/CPMG	-2496	1850	0.87	-1840(30)	-1957(30)	-3690(30)
	MAS ( $\nu_{\text{rot}} = 3000$ Hz)	-2495	1810	0.86	-1850(30)	-1975(30)	-3660(30)
	CPMG	-2508	1810	0.88	-1870(30)	-1975(30)	-3680(30)
	CP/MAS ( $\nu_{\text{rot}} = 3100$ Hz) <sup>[b]</sup>	-2497	1826	0.90	-1859	-1947	-3685
(CH <sub>3</sub> COO) <sub>2</sub> Pb·3H <sub>2</sub> O	wideline CP/CPMG	-1881	1690	0.65	-1220(10)	-1513(10)	-2910(10)
	wideline CPMG	-1898	1693	0.60	-1220(10)	-1561(10)	-2913(10)
	MAS ( $\nu_{\text{rot}} = 7000$ Hz)	-1868	1590	0.63	-1241(5)	-1532(5)	-2832(5)
	Hahn echo <sup>[c]</sup>	-1904	1728	0.62	-1217	-1549	-2945

Table 5.2 (cont.)

compound	experiment	$\delta_{\text{iso}}$ [ppm]	$\Omega$ [ppm]	$\kappa$	$\delta_{11}$ [ppm]	$\delta_{22}$ [ppm]	$\delta_{33}$ [ppm]
$\text{NH}_4\text{NO}_3$	CP/MAS ( $\nu_{\text{rot}} = 5300$ Hz)	377	220	0.96	452(3)	447(3)	232(3)
	CP/MAS ( $\nu_{\text{rot}} = 500$ Hz)	377	216	0.58	464(2)	419(2)	248(2)
	CP/Hahn echo	377	232	0.72	465(1)	433(1)	233(1)
	CP/CPMG	377	235	0.68	468(2)	430(2)	233(2)
	CP <sup>[d]</sup>	363	222	0.77	446	420	224
$\text{AgSO}_3\text{CH}_3$	CP/MAS ( $\nu_{\text{rot}} = 500$ Hz)	87	197	-0.50	202(5)	54(5)	5(5)
	CP/Hahn echo	82	192	-0.30	187(3)	63(3)	-5(3)
	CP/CPMG ( $1/\tau_a = 500$ Hz)	80	218	-0.49	207(4)	45(4)	-11(4)
	CP/CPMG ( $1/\tau_a = 200$ Hz)	80	219	-0.45	206(4)	47(4)	-13(4)
	CP <sup>[e]</sup>	87.2	183	-0.39	191	63	8

<sup>[a]</sup> Reference [32]. <sup>[b]</sup> Reference [29]. <sup>[c]</sup> Reference [43]. <sup>[d]</sup> Reference [44]. <sup>[e]</sup> Reference [27].

the most intense peak or discontinuity is shown to the left of each spectrum). The manifold of “echo-spikelets” in the CP/CPMG spectrum closely resembles the static  $^{113}\text{Cd}$  NMR pattern. We emphasize that it is quite difficult to make precise quantitative comparisons of signal enhancement between static, CP/MAS and CPMG spectra, due to changes in CP conditions and variation in spectral parameters such as dwell times, acquisition times, total number of points, etc.

Suitable conditions for cross polarization are often not available for many samples. Unfortunately, the long  $T_1$ 's encountered for many nuclei in systems of this sort result in very long overall experimental times and poor S/N. For example, the  $^{113}\text{Cd}$  CP

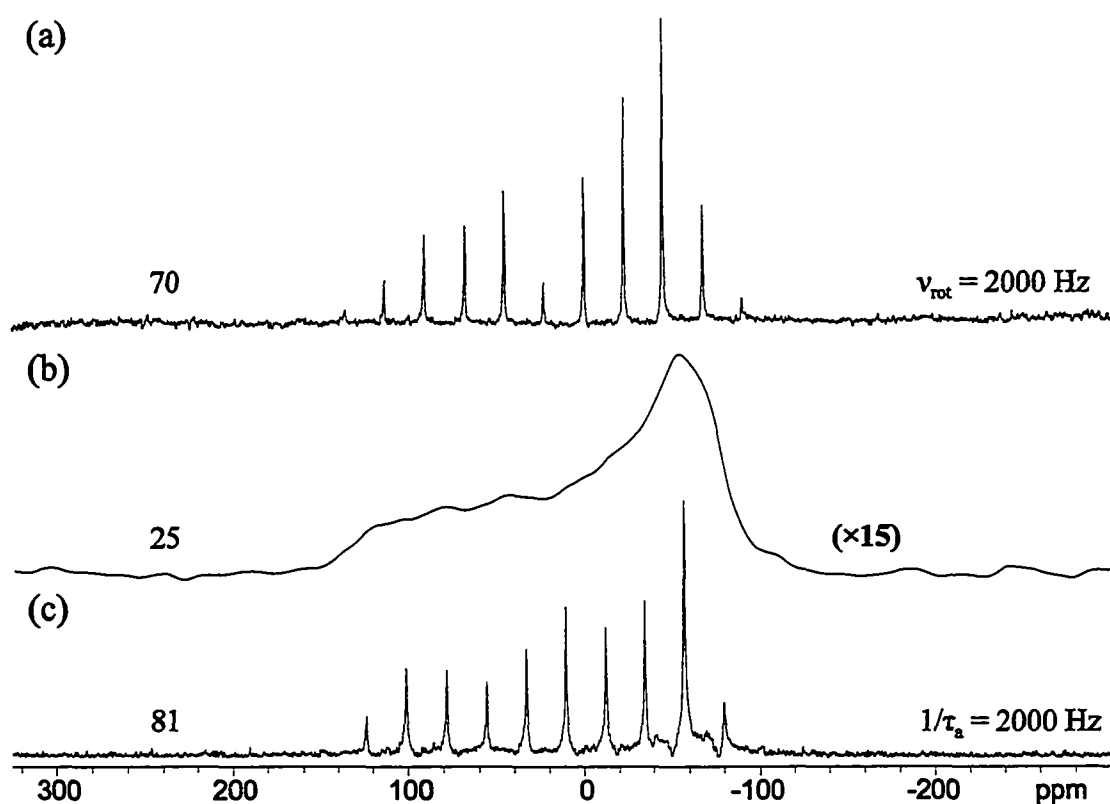


**Figure 5.3**  $^{113}\text{Cd}$  (a) MAS at  $\nu_{\text{rot}} = 2000$  Hz, (b) Hahn echo and (c) CPMG ( $1/\tau_a = 2000$  Hz) NMR spectra of  $\text{Cd}(\text{NO}_3)_2 \cdot 4\text{H}_2\text{O}$ ; 164 transients were averaged for all three spectra.

NMR spectra shown in Figure 5.2 were acquired in eight minutes, whereas the corresponding NMR spectra obtained without CP (Figure 5.3) required 164 minutes to obtain comparable S/N. In Figures 5.3a and 5.3b, standard  $^{113}\text{Cd}$  MAS and static NMR spectra are shown. The corresponding CPMG spectrum (Figure 5.3c) was acquired under non-spinning conditions, but has a S/N comparable to the MAS NMR spectrum (81 and 70, respectively). The CPMG experiment is potentially very useful for obtaining high S/N spectra of stationary samples, however, it has the disadvantage that isotropic shifts for samples with multiple Cd sites cannot be differentiated (in contrast to MAS NMR experiments). It is possible that the combination of MAS and stationary CPMG experiments may be useful in acquiring isotropic chemical shifts and accurate CS tensor parameters for samples with multiple sites.

### 5.3.2 $^{199}\text{Hg}$ NMR

Solid-state  $^{199}\text{Hg}$  NMR studies used to be uncommon, due to the large chemical shielding anisotropy associated with linear mercury(II) compounds and long spin-lattice relaxation time constants.<sup>[45,46]</sup> Harris and Sebald first suggested  $(\text{CH}_3\text{COO})_2\text{Hg}$  as a standard set-up sample for optimizing  $^{199}\text{Hg}$  CP/MAS NMR experiments:<sup>[18]</sup> they reported two closely-spaced isotropic  $^{199}\text{Hg}$  resonances for this sample. Santos et al. used the mercuric acetate as a primary reference and setup sample, and noted that the multiple isotropic peaks likely resulted from a magic-angle mis-set.<sup>[47]</sup> Groombridge conducted further experiments on this compound and demonstrated that even slight mis-setting of the magic angle can result in the appearance of additional peaks, which may spuriously

suggest the existence of multiple species.<sup>[48]</sup> It was further suggested that this would be the case for many heavy metal spin-1/2 nuclei with large CSAs. Most recently, Wasylshen and co-workers reported the following mercury CSA parameters for mercury(II) acetate:  $\delta_{\text{iso}} = -2497$  ppm,  $\Omega = 1826$  ppm and  $\kappa = 0.90$ .<sup>[29]</sup>

The  $^{199}\text{Hg}$  CP/MAS spectrum (Figure 5.4a) acquired at  $\nu_{\text{rot}} = 3$  kHz has a manifold of ssbs which resembles previously reported spectra. Unfortunately, this pattern is difficult to correctly analyse by the method of Herzfeld and Berger, since the pattern has a breadth of 130 kHz, is not uniformly excited and has ssb intensities which may not accurately reflect the mercury CSA. The static  $^{199}\text{Hg}$  CP/Hahn echo and CP/CPMG spectra of  $(\text{CH}_3\text{COO})_2\text{Hg}$  are shown in Figures 5.4b and 5.4c, respectively. Notably, the CP/Hahn echo spectrum was recorded with ten times the number of scans used to acquire the CP/MAS and CP/CPMG spectra, and yet its S/N is approximately six times less than that of the corresponding CP/CPMG spectrum. The powder patterns in the  $^{199}\text{Hg}$  CP/Hahn echo and CP/CPMG spectra bear little resemblance to the powder pattern in the CP/MAS spectrum, due to the difficulty in uniformly exciting the broad powder pattern over the entire span of the chemical shielding anisotropy (1800 ppm = 128 kHz at 9.4 T).

Due to limitations in the attainable excitation bandwidth, which is dependent upon pulse width and the magnitude of  $\omega_1$ ,<sup>[49, 50]</sup> as well as orientation-dependent CP efficiency, only a portion of the total powder pattern can be excited. In this case, piecewise wideline experiments are required to observe the complete lineshape (shown in Figure 5.4d for comparison, and detailed in Figure 5.5). Acquisition of wideline solid-state NMR spectra consists of acquiring segments of the spectrum at suitably fixed transmitter frequency

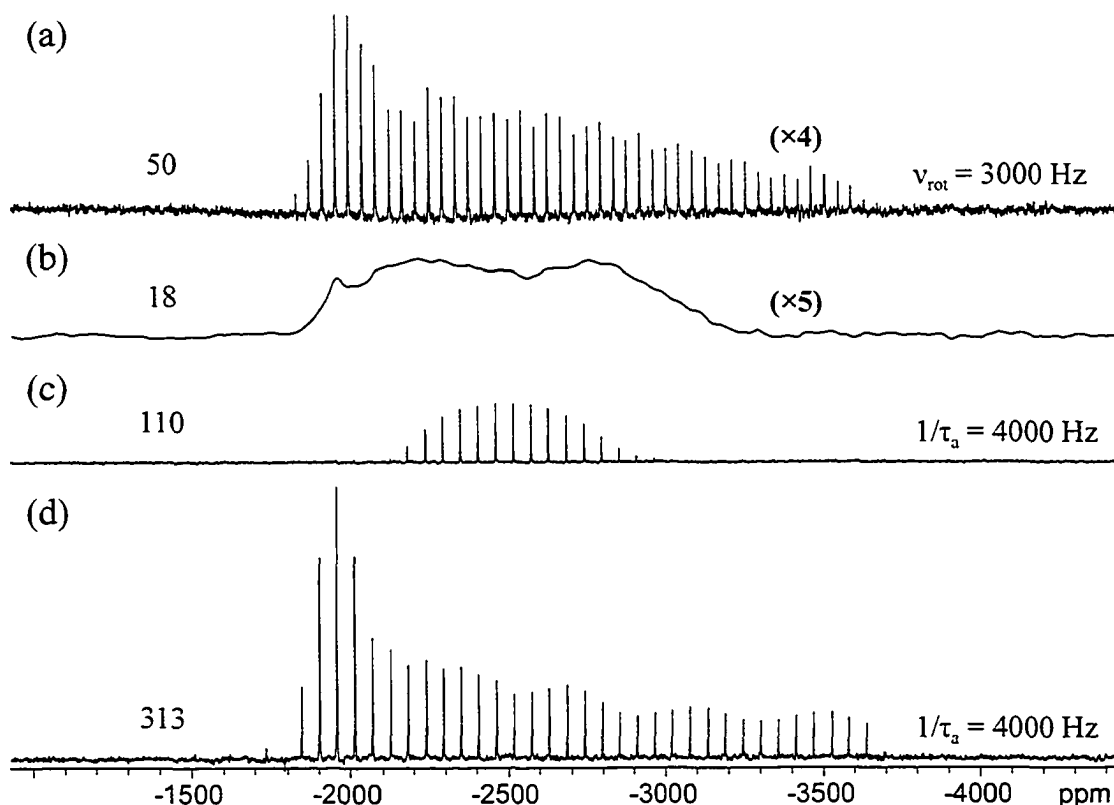


**Figure 5.4**  $^{199}\text{Hg}$  (a) CP/MAS at  $\nu_{\text{rot}} = 3000$  Hz, (b) CP/Hahn echo, (c) CP/CPMG ( $1/\tau_a = 4000$  Hz) and (d) piecewise wideline CP/CPMG ( $1/\tau_a = 4000$  Hz) NMR spectra of  $(\text{CH}_3\text{COO})_2\text{Hg}$ . 16 transients were recorded for the CP/MAS spectrum and CP/CPMG sub-spectra, while 160 transients were acquired for the CP/Hahn echo spectrum.

intervals over a wide frequency range. Possible methods of combining the data to produce the final wideline spectrum include (i) recording echo intensities over small intervals and plotting them as a function of frequency (the “point by point” method),<sup>[51, 52]</sup> and (ii) addition<sup>[53, 54]</sup> or (iii) skyline projection<sup>[8]</sup> of Fourier-transformed frequency-domain sub-spectra acquired over a range of evenly spaced offset frequencies. Each of the sub-spectra were acquired using  $^{199}\text{Hg}$  CP/CPMG NMR over transmitter increments of 28 kHz (top of Figure 5.5) and then co-added according to method (ii) (Figure 5.5b). For comparison, a skyline projection of the sub-spectra was also constructed (Figure

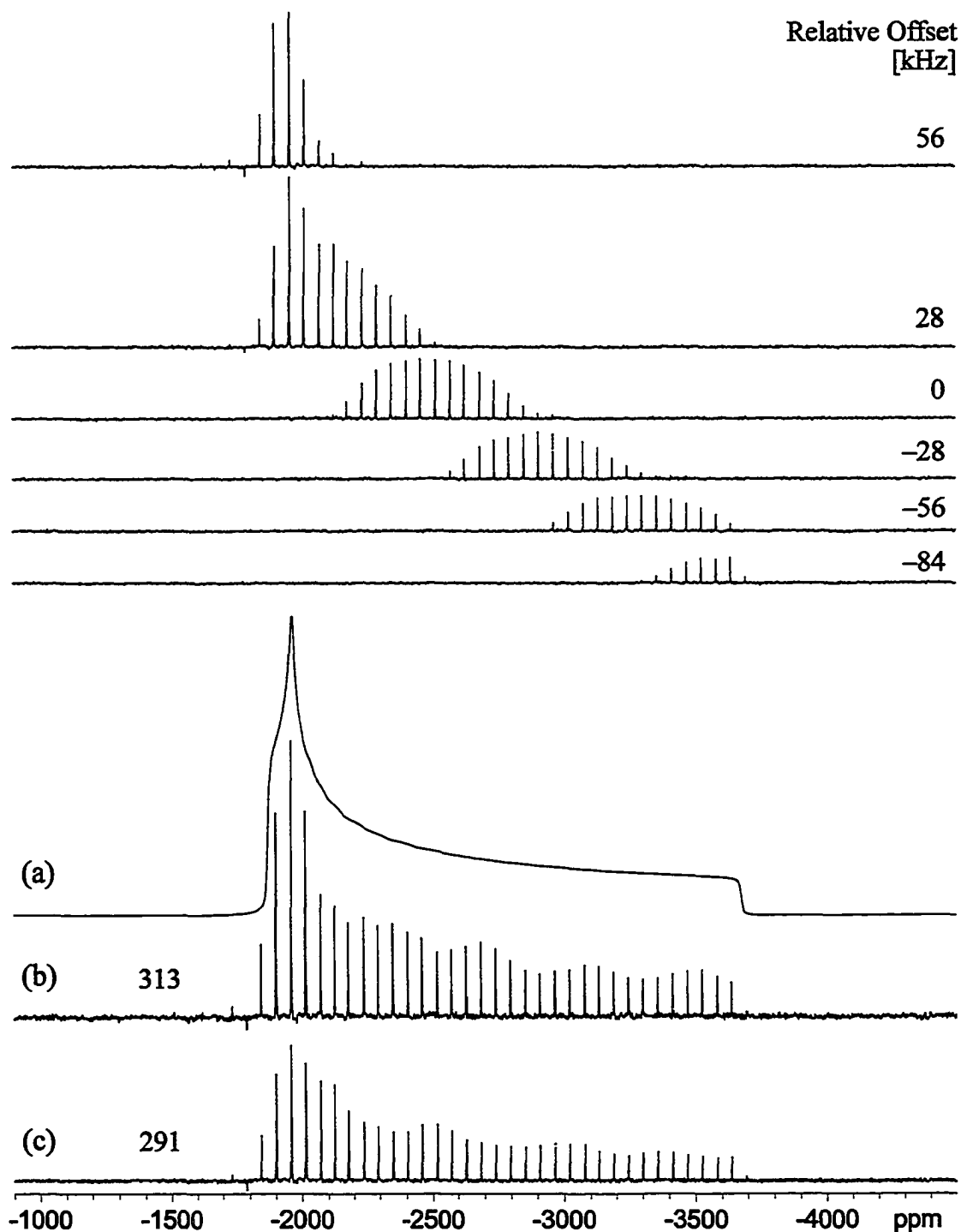


**Figure 5.5**  $^{199}\text{Hg}$  wideline CP/CPMG ( $1/\tau_a = 4000$  Hz) spectra of  $(\text{CH}_3\text{COO})_2\text{Hg}$  along with (a) analytical simulation of the spectral envelope. Sub-spectra (top of figure) were acquired by varying the transmitter frequency in 28 kHz steps, where 16 transients were acquired for each sub-spectrum. The  $^{199}\text{Hg}$  wideline CP/CPMG spectra were obtained by (b) addition, and (c) taking the skyline-projection of the individual segments in the frequency domain.



5.5c). There is better agreement between the co-added (Figure 5.5b) and idealized (Figure 5.5a) powder patterns; the intensity of the high-frequency discontinuity in Figure 5.5c is considerably diminished. Comparison of methods (ii) and (iii) was performed for all reported wideline spectra against patterns derived from simulations; method (iii) showed superior results only for the  $^{199}\text{Hg}$  wideline CPMG spectrum (*vide infra*). The slight “wobble” across the envelope of wideline spectra (both co-added and skyline) results from slight increases in intensity near the center of each pattern (the highest intensity is located at the center of excitation near the transmitter frequency). The spacing of the transmitter offsets and rf field strengths are chosen to minimize this wobble and maximize the uniform excitation of the entire pattern. Use of the CPMG sequence instead of a conventional spin echo sequence leads to a rapidly collected, high S/N (313) wideline static  $^{199}\text{Hg}$  NMR spectrum. While it is true that acquisition of the  $^{199}\text{Hg}$  wideline CP/CPMG spectrum (Figure 5.4d) took six times as long as the  $^{199}\text{Hg}$  CP/MAS spectrum to acquire (six sub-spectra were recorded), the former gives precise chemical shielding tensor information free from effects of incomplete excitation or variable ssb intensities. The corresponding CP/Hahn echo experiment would take much longer to acquire and would be restricted by poor S/N. Mercury CS parameters derived from simulation of the wideline CP/CPMG spectrum ( $\delta_{\text{iso}} = -2496$  ppm,  $\Omega = 1850$  ppm,  $\kappa = 0.87$ ) agree well with reported values<sup>[29]</sup> (according to Groombridge,  $\Omega$  ranges from 1781 ppm for a static sample to 1809 – 1845 ppm when spinning).<sup>[48]</sup>

$^{199}\text{Hg}$  NMR experiments without the application of cross-polarization were also conducted. All static  $^{199}\text{Hg}$  wideline CPMG ( $1/\tau_2 = 3$  kHz) NMR sub-spectra (three sub-

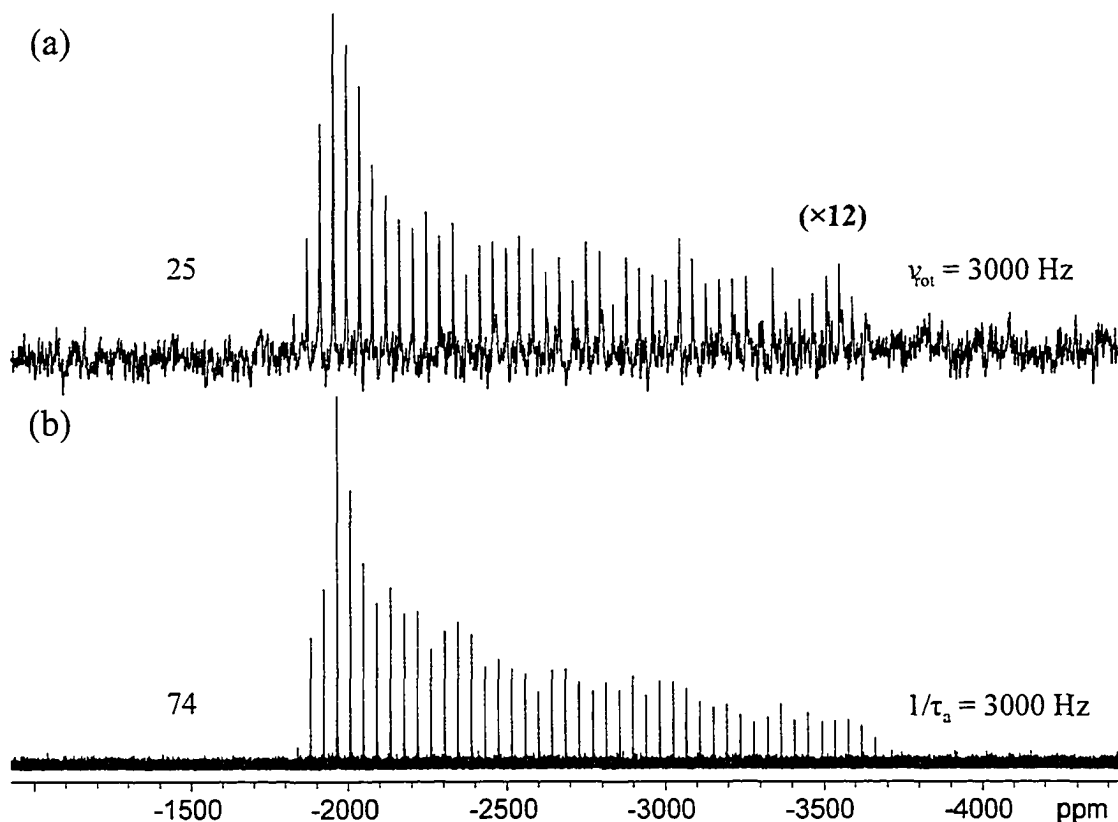


**Figure 5.6** Comparison of the  $^{199}\text{Hg}$  (a) MAS at  $\nu_{\text{rot}} = 3000$  Hz and (b) wideline CPMG ( $1/\tau_a = 3000$  Hz) spectra of  $(\text{CH}_3\text{COO})_2\text{Hg}$ ; 16 transients were acquired for the MAS spectrum and each of the three CPMG sub-spectra. The CPMG spectrum results from taking the skyline projection of the sub-spectra.

spectra acquired) and the  $^{199}\text{Hg}$  MAS ( $\nu_{\text{rot}} = 3$  kHz) spectrum were recorded with equal overall acquisition times (Figures 5.6a, 5.6b). The purpose of running these experiments is to demonstrate that the CPMG sequence is a viable pulse sequence for obtaining static powder patterns when CP conditions are poor or unavailable, and that an increased excitation bandwidth is attainable when directly exciting the observe nucleus.

Comparison of the two spectra in Figure 5.6, which have the same ssb and spikelet separation, demonstrates the large gains in S/N from employing the CPMG sequence.

Only three sub-spectra were required to reconstruct the entire static  $^{199}\text{Hg}$  CPMG spectrum, while comparable S/N in the MAS spectrum would require an increase in the

acquisition time by nearly an order of magnitude.

### 5.3.3 $^{207}\text{Pb}$ NMR

$^{207}\text{Pb}$  is an interesting NMR nucleus, due to the immense chemical shift range and large CSAs which result from the easily polarized lead valence orbitals.<sup>[45, 55, 56]</sup> Small changes in molecular structure and local symmetry about the  $^{207}\text{Pb}$  nucleus result in significant changes in the characteristics of  $^{207}\text{Pb}$  chemical shift tensors.<sup>[19]</sup> In fact, the changes are so sensitive to structural change that several lead-containing compounds are used as “NMR thermometers” for the calibration of temperature in NMR probes.<sup>[57, 58]</sup>  $^{207}\text{Pb}$  NMR is of great interest due to the number of technologically relevant materials containing lead,<sup>[59]</sup> for its application in studying lead speciation in waste disposal media,<sup>[34]</sup> and for recent involvement in the discovery of a spin-phonon Raman scattering mechanism contribution to spin-lattice relaxation in solids.<sup>[60]</sup> To our knowledge, solid-state  $^{207}\text{Pb}$  NMR spectra of  $(\text{CH}_3\text{COO})_2\text{Pb}\cdot 3\text{H}_2\text{O}$  have been reported twice before. Harbison and co-workers acquired the static  $^{207}\text{Pb}$  NMR spectrum and reported the CS tensor parameters  $\delta_{\text{iso}} = -1904$ ,  $\Omega = 1728$  ppm and  $\kappa = 0.62$ ,<sup>[43]</sup> while Irwin et al. determined that there is a single magnetically distinct Pb site with an isotropic chemical shift of  $\delta_{\text{iso}} = -1897$  ppm, as well as ssbs covering a breadth of 50 kHz at 4.7 T,<sup>[30]</sup> corresponding to  $\Omega \approx 1190$  ppm by  $^{207}\text{Pb}$  CP/MAS NMR.

A series of  $^{207}\text{Pb}$  NMR spectra acquired under various conditions are shown in Figure 5.7. There is a rapid drop off in CP efficiency with higher spinning speeds (even

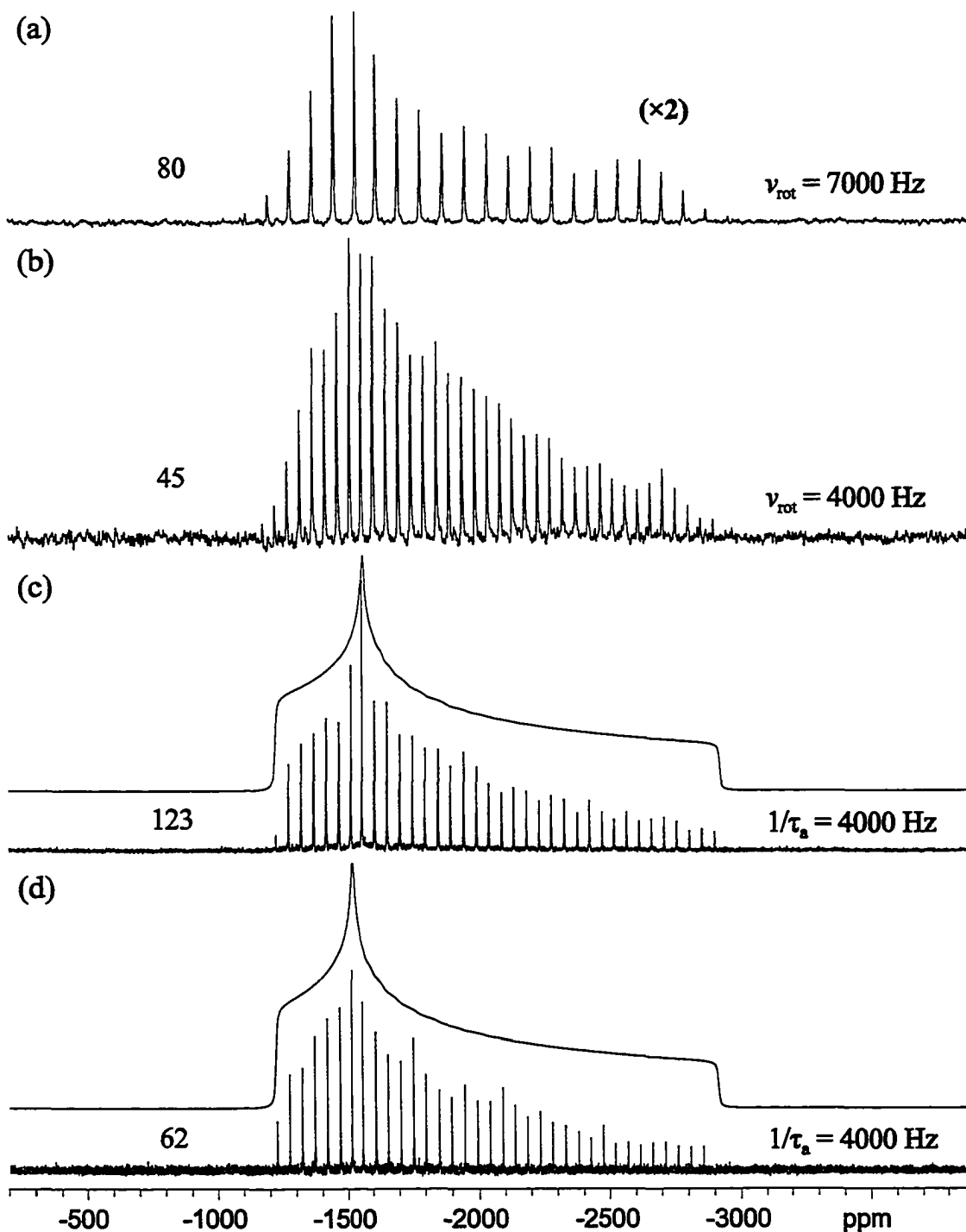


**Figure 5.7**  $^{207}\text{Pb}$  (a) MAS ( $\nu_{\text{rot}} = 7000$  Hz), (b) CP/MAS ( $\nu_{\text{rot}} = 4000$  Hz), (c) wideline CPMG and (d) wideline CP/CPMG ( $1/\tau_a = 4000$  Hz) NMR spectra of  $(\text{CH}_3\text{COO})_2\text{Pb}\cdot 3\text{H}_2\text{O}$ ; analytical simulations are shown above corresponding wideline spectra. 64 and 144 transients were acquired for each of the CPMG and CP/CPMG sub-spectra, respectively.

using variable amplitude CP pulse sequences), therefore, it was more efficient to acquire the  $^{207}\text{Pb}$  MAS spectrum at  $\nu_{\text{rot}} = 7$  kHz without CP. The poor CP efficiency is evidenced by the lower S/N of the CP/MAS spectrum ( $\nu_{\text{rot}} = 4$  kHz) compared to the MAS spectrum ( $\nu_{\text{rot}} = 7$  kHz), although the acquisition time of the CP/MAS spectrum was longer by a factor of 5 times (535 and 107 minutes, respectively). The static piecewise wideline  $^{207}\text{Pb}$  CPMG and CP/CPMG NMR spectra of  $(\text{CH}_3\text{COO})_2\text{Pb}\cdot 3\text{H}_2\text{O}$  were acquired with total acquisition times of 107 and 48 minutes, respectively (Figures 5.7c and 5.7d), and both wideline spectra display S/N superior to the CP/MAS spectrum. Fitting of the CPMG and CP/CPMG powder patterns (upper traces of Figures 5.7c and 5.7d) yields  $\delta_{\text{iso}} = -1898$  ppm,  $\Omega = 1693$  ppm,  $\kappa = 0.60$  and  $\delta_{\text{iso}} = -1881$  ppm,  $\Omega = 1690$  ppm,  $\kappa = 0.65$ , respectively, in agreement with CS tensor parameters reported by Harbison et al.<sup>[43]</sup> CS tensor parameters obtained from the  $^{207}\text{Pb}$  MAS NMR experiment are also in reasonable agreement with the parameters of Harbison et al. The CP/CPMG sequence is useful for samples such as  $(\text{CH}_3\text{COO})_2\text{Pb}\cdot 3\text{H}_2\text{O}$ , where spinning might alter the properties of the sample, and for samples which are difficult to spin, damaged by spinning, or undergo structural and/or phase changes as a result of small to moderate temperature variations. Furthermore, by acquiring spectra without mechanical spinning, artifacts due to mis-setting of the magic-angle will be absent.

### 5.3.4 $^{15}\text{N}$ NMR

$^{15}\text{N}$  NMR is of great interest for its applications in studying molecular structure and dynamics in a broad variety of nitrogen-containing systems. Hundreds of nitrogen

chemical shift tensors have been measured by standard  $^{15}\text{N}$  CP/MAS and static NMR experiments,<sup>[19]</sup> as well as studied by combined experimental and theoretical studies on important organic<sup>[61]</sup> and biological molecules.<sup>[62]</sup> The application of solid-state  $^{15}\text{N}$  is incredibly varied and ubiquitous: recent interesting applications include the study of polypeptides and proteins in membranes,<sup>[63]</sup> the use of  $^{15}\text{N}$ -labelled pyridine as a probe of mesoporous silica surfaces,<sup>[64]</sup> and natural abundance  $^{15}\text{N}$  NMR to study nitrogen sites in nylon-6.<sup>[65]</sup>

The  $^{15}\text{N}$  CP/MAS ( $\nu_{\text{rot}} = 5300$  Hz and 500 Hz), CP/Hahn echo and CP/CPMG spectra of the  $\text{NO}_3$  resonance of doubly 98%  $^{15}\text{N}$ -enriched ammonium nitrate, which is a solid-state NMR standard for  $^{15}\text{N}$  NMR,<sup>[35]</sup> are presented in Figure 5.8. Comparison of the spectra show results similar to those mentioned previously for  $^{113}\text{Cd}$ ,  $^{199}\text{Hg}$  and  $^{207}\text{Pb}$ . The static CP/CPMG spectrum (Figure 5.8d) yields comparable S/N to the slow-spinning CP/MAS spectrum (Figure 5.8b), while being much superior to the static CP/Hahn echo spectrum (Figure 5.8c), when equal acquisition times are employed (S/N = 171, 260 and 48, respectively). Due to the long spin-lattice relaxation times of the  $^{15}\text{N}$  nuclei in this molecule,  $^{15}\text{N}$  MAS NMR spectra without CP were not acquired. The  $\text{NH}_4$  resonance has a very narrow line-width (ca. 10 Hz) making it unsuitable for observation by CPMG type experiments due to the relatively long  $T_2^*$  (which when similar in magnitude to  $T_2$ , prevents the acquisition of echo trains). In fact, the small negative spikelets observed between the spikelets making up the  $\text{NO}_3$  resonance are found to arise from refocusing of the  $\text{NH}_4$  magnetization before complete dephasing in the transverse plane (i.e., at a time shorter than the ammonium  $^{15}\text{N}$   $T_2^*$ ). The spikelets interleaved between the nitrate

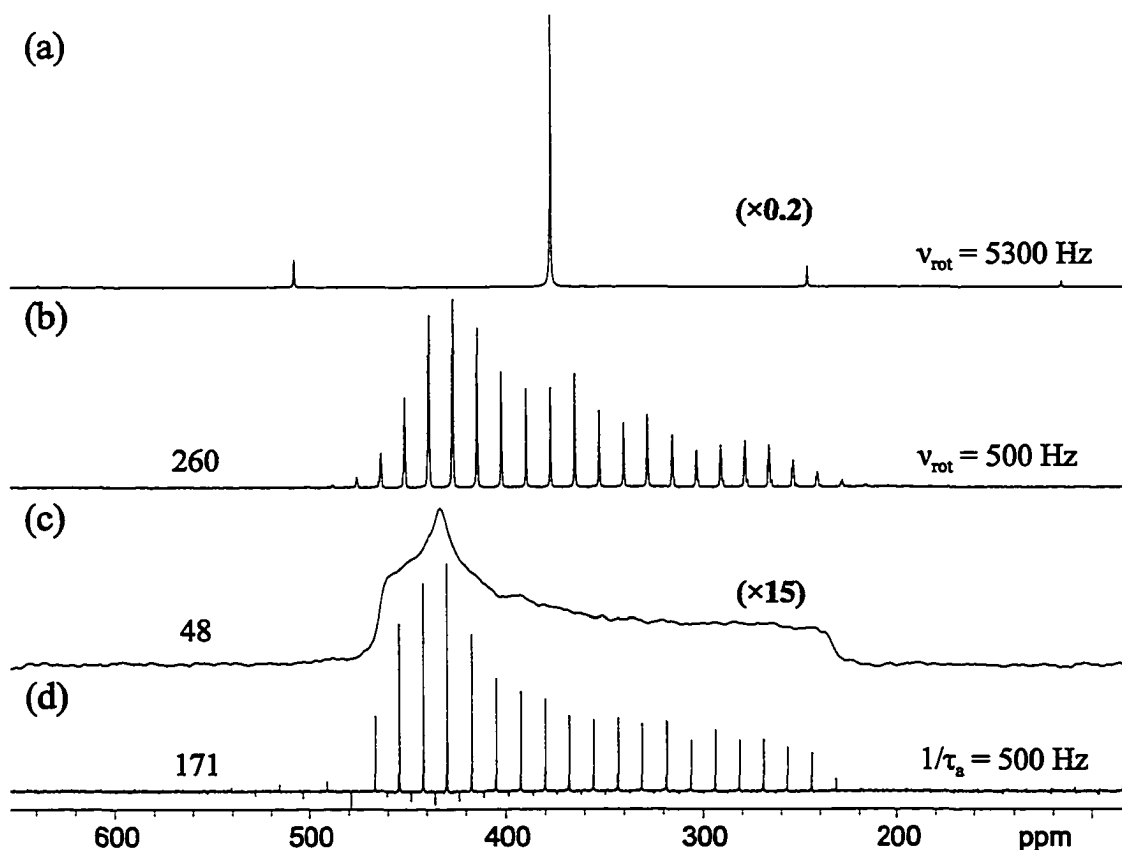


**Figure 5.8**  $^{15}\text{N}$  CP/MAS at (a)  $\nu_{\text{rot}} = 5300$  Hz and (b)  $\nu_{\text{rot}} = 500$  Hz, (c) CP/Hahn echo and (d) CP/CPMG ( $1/\tau_a = 500$  Hz) NMR spectra of the  $\text{NO}_3$  site in doubly 98%  $^{15}\text{N}$ -enriched  $\text{NH}_4\text{NO}_3$  recorded with a total of 16 transients in each case.

resonance can be removed by allowing enough time for the  $\text{NH}_4$  magnetization to fully decay, however, much of the intensity from the  $\text{NO}_3$  resonance is lost as well (not shown). The greatest disadvantage of employing CPMG type experiments lies in the inability to differentiate the isotropic shifts of multiple sites. However, if samples are singly labelled (often being the case), have only one site of interest or MAS experiments can be used to identify the isotropic shifts of multiple sites, the CP/CPMG pulse sequence can serve to acquire accurate  $^{15}\text{N}$  CS patterns, as evidenced by the parameters presented in Table 5.2. The ability to efficiently (i.e., comparable to CP/MAS) obtain a static  $^{15}\text{N}$  CP/CPMG powder pattern may prove useful for the study of  $^{15}\text{N}$ -labelled biological

compounds in oriented samples such as membranes.<sup>[66]</sup>

### 5.3.5 $^{109}\text{Ag}$ NMR

Silver has two NMR active nuclides,  $^{107}\text{Ag}$  and  $^{109}\text{Ag}$  (n.a. 51.82 % and 48.18 %, respectively), both of which have small magnetogyric ratios and long spin-lattice relaxation times.  $^{109}\text{Ag}$  is favoured, since it has a slightly larger  $\gamma$ ; however, the NMR frequencies are still so low that many  $^{109}\text{Ag}$  NMR experiments suffer from acoustic probe ringing and extremely lengthy experimental times. The first solid-state  $^{109}\text{Ag}$  NMR experiments were conducted on microcrystalline powders of silver halides and other simple materials,<sup>[67]</sup> since then, interesting materials containing silver such as glasses<sup>[68]</sup> have been investigated by NMR. Due to the aforementioned undesirable characteristics,  $^{109}\text{Ag}$  NMR is still largely avoided.

The first  $^{109}\text{Ag}$  CP/MAS NMR experiments were conducted on silver acetate and a variety of commercially available silver-containing compounds.<sup>[69]</sup> A suitable  $^{109}\text{Ag}$  CP/MAS standard could not be found at that time, so  $^{89}\text{Y}$  CP/MAS NMR of  $\text{Y}(\text{NO}_3)_3 \cdot 6\text{H}_2\text{O}$  was applied to set the initial conditions for  $^{109}\text{Ag}$ - $^1\text{H}$  Hartmann-Hahn matching due to the proximity of the  $^{89}\text{Y}$  Larmor frequency and favourable NMR properties.<sup>[70]</sup> More recently,  $\text{AgSO}_3\text{CH}_3$  was suggested as a set up sample for  $^{109}\text{Ag}$  CP/MAS experiments.<sup>[27]</sup> The  $^{109}\text{Ag}$  NMR powder pattern is about 4 kHz in breadth at 9.4 T and provides an ideal sample for testing of the CP/CPMG sequence. The  $^{109}\text{Ag}$  CP/MAS ( $\nu_{\text{rot}} = 500$  Hz), CP/Hahn echo and CP/CPMG NMR spectra of  $\text{AgSO}_3\text{CH}_3$  are shown in Figure 5.9. Similar to the  $\text{NH}_4\text{NO}_3$  example, the  $^{109}\text{Ag}$  CP/MAS (Figure 5.9a)



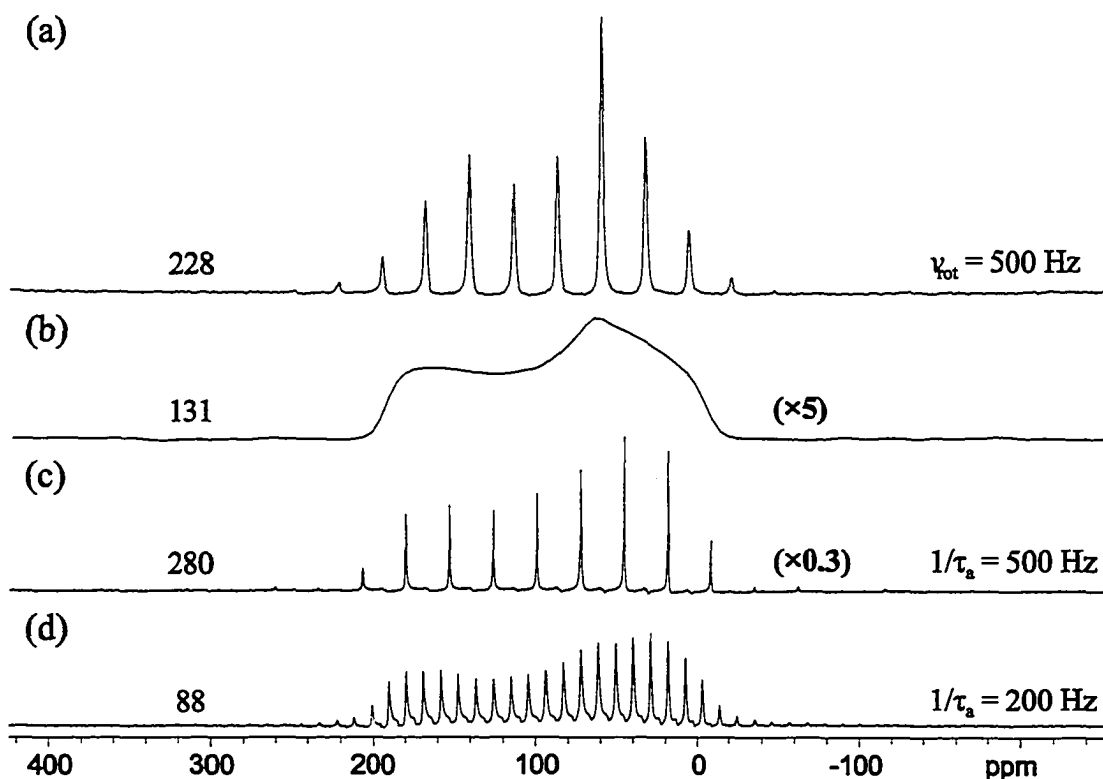


**Figure 5.9**  $^{109}\text{Ag}$  CP/MAS at (a)  $\nu_{\text{rot}} = 500$  Hz, (b) CP/Hahn echo and CP/CPMG with (c)  $1/\tau_a = 500$  Hz and (d)  $1/\tau_a = 200$  Hz NMR spectra of  $\text{AgSO}_3\text{CH}_3$ ; 480 transients were acquired for all spectra.

and CP/CPMG (Figure 5.9c) spectra show comparable S/N ratios (228 and 280, respectively), both being far superior to the CP/Hahn echo spectrum (Figure 5.9b). Extraction of a precise CSA tensor from either the CP/MAS or CP/CPMG spectra would be difficult, due to the relatively low resolution of these spectra. Acquisition of higher resolution spectra could prove difficult for the standard CP/MAS experiment, since stable spinning speeds of less than 500 Hz on standard NMR probes can be difficult to obtain – however, the needed resolution can easily be obtained using CPMG (Figure 5.9d). Attempts at recording spectra for  $\text{AgSO}_3\text{CH}_3$  without CP were unsuccessful due to the long  $^{109}\text{Ag}$  spin-lattice relaxation time.

## 5.4 Conclusions

The CPMG pulse sequence, in combination with CP and TPPM proton decoupling, has been successfully applied to acquire high S/N powder patterns of spin-1/2 nuclei exhibiting anisotropic chemical shielding patterns. Piecewise CPMG acquisition provides a rapid means of obtaining static NMR spectra of spin-1/2 nuclei with very broad patterns, which can be analysed to provide accurate chemical shielding tensor parameters unaffected by incomplete excitation or variations in ssb intensities. The manifold of spikelets from CPMG spectra closely resembles the static powder pattern, enabling increasingly accurate analysis of CSA in comparison to the Herzfeld-Berger analysis of MAS spectra (particularly for broad powder patterns). CPMG experiments are ideal for samples which are difficult or impossible to spin, undergo structural and/or phase changes from the stresses of spinning (notably due to temperature change), or even for oriented samples. In addition, signal enhancement of an order of magnitude or more can be attained using CPMG in comparison to conventional static spectra. This allows the acquisition of static spectra with equivalent and possibly better S/N compared to MAS spectra, depending on the spin-lattice and spin-spin relaxation times of the nucleus under observation. The CPMG pulse sequence is useful for samples with patterns that are homogeneously or inhomogeneously broadened (e.g., as demonstrated in this work and in the  $^{29}\text{Si}$  CPMG NMR spectra of Farnan et al.).<sup>[17]</sup> However, the CPMG sequence does suffer from serious drawbacks, in that it cannot resolve individual sites based upon their isotropic shifts unless they possess noticeably different CSA patterns or widely dispersed chemical shifts. CPMG also cannot be applied to acquire MAS spectra of spin-1/2 nuclei

at spinning speeds greater than 500 Hz, due to the distribution of signal intensity into sharp ssbs which increases  $T_2^*$  and decreases significantly (or nullifies) the number of times that the transverse magnetization can be refocused by the CPMG train of  $\pi$  pulses.

# Bibliography

- [1] M. E. Smith, *Annual Reports on NMR Spectroscopy* **2001**, 43, 121.
- [2] A. S. Lipton, J. A. Sears, P. D. Ellis, *J. Magn. Reson.* **2001**, 151, 48.
- [3] F. H. Larsen, H. J. Jakobsen, P. D. Ellis, N. C. Nielsen, *J. Phys. Chem. A* **1997**, 101, 8597.
- [4] H. Y. Carr, E. M. Purcell, *Physical Review* **1954**, 94, 630.
- [5] S. Meiboom, D. Gill, *Review of Scientific Instruments* **1958**, 29, 688.
- [6] R. Lefort, J. W. Wiench, M. Pruski, J. P. Amoureux, *J. Chem. Phys.* **2002**, 116, 2493.
- [7] A. S. Lipton, G. W. Buchko, J. A. Sears, M. A. Kennedy, P. D. Ellis, *J. Am. Chem. Soc.* **2001**, 123, 992.
- [8] A. S. Lipton, T. A. Wright, M. K. Bowman, D. L. Reger, P. D. Ellis, *J. Am. Chem. Soc.* **2002**, 124, 5850.
- [9] S. E. Shore, J. P. Ansermet, C. P. Slichter, J. H. Sinfelt, *Phys. Rev. Lett.* **1987**, 58, 953.
- [10] D. L. Bryce, M. Gee, R. E. Wasylshen, *J. Phys. Chem. A* **2001**, 105, 10413.
- [11] D. L. Bryce, R. E. Wasylshen, *Physical Chemistry Chemical Physics* **2002**, 4, 399.
- [12] I. Hung, R. W. Schurko, *Solid State Nuclear Magnetic Resonance* **2003**, 24, 78.
- [13] F. H. Larsen, H. J. Jakobsen, P. D. Ellis, N. C. Nielsen, *Mol. Phys.* **1998**, 95, 1185.
- [14] F. H. Larsen, A. S. Lipton, H. J. Jakobsen, N. C. Nielsen, P. D. Ellis, *J. Am. Chem. Soc.* **1999**, 121, 3783.

- [15] F. H. Larsen, N. C. Nielsen, *J. Phys. Chem. A* **1999**, *103*, 10825.
- [16] R. W. Schurko, I. Hung, C. M. Widdifield, *Chem. Phys. Lett.* **2003**, *379*, 1.
- [17] F. H. Larsen, I. Farnan, *Chem. Phys. Lett.* **2002**, *357*, 403.
- [18] R. K. Harris, A. Sebald, *Magnetic Resonance in Chemistry* **1987**, *25*, 1058.
- [19] T. M. Duncan, *A Compilation of Chemical Shift Anisotropies*, The Farragut Press, Chicago, **1990**.
- [20] S. E. Barrett, D. J. Durand, C. H. Pennington, C. P. Slichter, T. A. Friedmann, J. P. Rice, D. M. Ginsberg, *Physical Review B* **1990**, *41*, 6283.
- [21] J. S. Waugh, C. H. Wang, *Physical Review* **1967**, *162*, 209.
- [22] N. M. Szeverenyi, A. Bax, G. E. Maciel, *J. Magn. Reson.* **1985**, *61*, 440.
- [23] K. H. Lim, T. Nguyen, T. Mazur, D. E. Wemmer, A. Pines, *J. Magn. Reson.* **2002**, *157*, 160.
- [24] J. Z. Hu, R. A. Wind, *J. Magn. Reson.* **2003**, *163*, 149.
- [25] J. Salgado, S. L. Grage, L. H. Kondejewski, R. S. Hodges, R. N. McElhaney, A. S. Ulrich, *Journal of Biomolecular NMR* **2001**, *21*, 191.
- [26] A. E. Bennett, C. M. Rienstra, M. Auger, K. V. Lakshmi, R. G. Griffin, *J. Chem. Phys.* **1995**, *103*, 6951.
- [27] G. H. Penner, W. L. Li, *Solid State Nuclear Magnetic Resonance* **2003**, *23*, 168.
- [28] T. T. P. Cheung, L. E. Worthington, P. D. Murphy, B. C. Gerstein, *J. Magn. Reson.* **1980**, *41*, 158.
- [29] K. Eichele, S. Kroeker, G. Wu, R. E. Wasylshen, *Solid State Nuclear Magnetic Resonance* **1995**, *4*, 295.

- [30] A. D. Irwin, C. D. Chandler, R. Assink, M. J. Hampdensmith, *Inorganic Chemistry* **1994**, *33*, 1005.
- [31] R. G. Bryant, V. P. Chacko, M. C. Etter, *Inorganic Chemistry* **1984**, *23*, 3580.
- [32] R. S. Honkonen, F. D. Doty, P. D. Ellis, *J. Am. Chem. Soc.* **1983**, *105*, 4163.
- [33] J. M. Hook, P. A. W. Dean, L. C. M. van Gorkom, *Magnetic Resonance in Chemistry* **1995**, *33*, 77.
- [34] F. Fayon, I. Farnan, C. Bessada, J. Coutures, D. Massiot, J. P. Coutures, *J. Am. Chem. Soc.* **1997**, *119*, 6837.
- [35] S. Hayashi, K. Hayamizu, *Bulletin of the Chemical Society of Japan* **1991**, *64*, 688.
- [36] M. Witanowski, L. Stefaniak, G. A. Webb, *Annual Reports on NMR Spectroscopy* **1993**, *25*, 1.
- [37] K. Eichele, R. E. Wasylshen, WSOLIDS, v.1.17.28 - Software for simulations of solid state NMR powder patterns, Dalhousie University, Dalhousie, **2000**.
- [38] J. Herzfeld, A. E. Berger, *J. Chem. Phys.* **1980**, *73*, 6021.
- [39] M. F. Summers, *Coordination Chemistry Reviews* **1988**, *86*, 43.
- [40] J. E. Coleman, in *Metallobiochemistry, Pt D, Vol. 227*, **1993**, pp. 16.
- [41] J. Sola, P. Gonzalezduarte, J. Sanz, I. Casals, T. Alsina, I. Sobrados, A. Alvarezlarena, J. F. Piniella, X. Solans, *J. Am. Chem. Soc.* **1993**, *115*, 10018.
- [42] P. G. Mennitt, M. P. Shatlock, V. J. Bartuska, G. E. Maciel, *Journal of Physical Chemistry* **1981**, *85*, 2087.
- [43] Y. S. Kye, S. Connolly, B. Herreros, G. S. Harbison, *Main Group Metal Chemistry* **1999**, *22*, 373.

- [44] M. G. Gibby, R. G. Griffin, A. Pines, J. S. Waugh, *Chem. Phys. Lett.* **1972**, *17*, 80.
- [45] J. Mason, *Multinuclear NMR*, Plenum Press, New York, **1987**.
- [46] B. Wrackmeyer, R. Contreras, *Annual Reports on NMR Spectroscopy* **1992**, *24*, 267.
- [47] R. A. Santos, E. S. Gruff, S. A. Koch, G. S. Harbison, *J. Am. Chem. Soc.* **1991**, *113*, 469.
- [48] C. J. Groombridge, *Magnetic Resonance in Chemistry* **1993**, *31*, 380.
- [49] K. Schmidt-Rohr, H. W. Spiess, *Multidimensional Solid-State NMR of Polymers*, Academic Press, London, **1994**.
- [50] E. Fukushima, S. B. W. Roeder, *Experimental Pulse NMR: A Nuts and Bolts Approach*, Addison-Wesley Publishing Company, Inc., Reading, MA, **1981**.
- [51] P. D. Zhao, S. Prasad, J. Huang, J. J. Fitzgerald, J. S. Shore, *Journal of Physical Chemistry B* **1999**, *103*, 10617.
- [52] T. J. Bastow, M. E. Smith, *Solid State Nuclear Magnetic Resonance* **1992**, *1*, 165.
- [53] D. Massiot, I. Farnan, N. Gautier, D. Trumeau, A. Trokiner, J. P. Coutures, *Solid State Nuclear Magnetic Resonance* **1995**, *4*, 241.
- [54] A. Medek, V. Frydman, L. Frydman, *J. Phys. Chem. A* **1999**, *103*, 4830.
- [55] B. Wrackmeyer, K. Horchler, *Annual Reports on NMR Spectroscopy* **1990**, *22*, 249.
- [56] A. Nolle, *Zeitschrift Fur Naturforschung Section a-a Journal of Physical Sciences* **1977**, *32*, 964.
- [57] L. C. M. van Gorkom, J. M. Hook, M. B. Logan, J. V. Hanna, R. E. Wasylshen, *Magnetic Resonance in Chemistry* **1995**, *33*, 791.

- [58] A. Bielecki, D. P. Burum, *Journal of Magnetic Resonance, Series A* **1995**, *116*, 215.
- [59] C. Dybowski, G. Neue, *Prog. Nucl. Magn. Reson. Spectrosc.* **2002**, *41*, 153.
- [60] J. B. Grutzner, K. W. Stewart, R. E. Wasylshen, M. D. Lumsden, C. Dybowski, P. A. Beckmann, *J. Am. Chem. Soc.* **2001**, *123*, 7094.
- [61] R. Salzmann, M. Wojdelski, M. McMahon, R. H. Havlin, E. Oldfield, *J. Am. Chem. Soc.* **1998**, *120*, 1349.
- [62] J. Z. Hu, J. C. Facelli, D. W. Alderman, R. J. Pugmire, D. M. Grant, *J. Am. Chem. Soc.* **1998**, *120*, 9863.
- [63] S. Luca, H. Heise, M. Baldus, *Accounts of Chemical Research* **2003**, *36*, 858.
- [64] I. G. Shenderovich, G. Buntkowsky, A. Schreiber, E. Gedat, S. Sharif, J. Albrecht, N. S. Golubev, G. H. Findenegg, H. H. Limbach, *Journal of Physical Chemistry B* **2003**, *107*, 11924.
- [65] M. I. B. Tavares, C. M. G. de Souza, *Journal of Applied Polymer Science* **2003**, *90*, 3872.
- [66] F. M. Marassi, *Concepts in Magnetic Resonance* **2002**, *14*, 212.
- [67] H. Looser, D. Brinkmann, *J. Magn. Reson.* **1985**, *64*, 76.
- [68] K. K. Olsen, J. W. Zwanziger, *Solid State Nuclear Magnetic Resonance* **1995**, *5*, 123.
- [69] L. H. Merwin, A. Sebald, *J. Magn. Reson.* **1992**, *97*, 628.
- [70] L. H. Merwin, A. Sebald, *J. Magn. Reson.* **1990**, *88*, 167.



# Chapter 6

## Solid-State $^{25}\text{Mg}$ and $^{13}\text{C}$ NMR of Bis(cyclopentadienyl)magnesium

### 6.1 Introduction

Magnesium-25 has a low magnetogyric ratio ( $-1.63890 \times 10^7 \text{ rad T}^{-1} \text{ s}^{-1}$ ), low natural abundance (10.13%) and a moderately sized nuclear quadrupole moment (nuclear spin  $I = 5/2$ ,  $Q(^{25}\text{Mg}) = 2.2(3) \times 10^{-29} \text{ m}^2$ ).<sup>[1]</sup> Routine solid-state  $^{25}\text{Mg}$  NMR of biologically and industrially relevant samples is quite prohibitive, and generally avoided by NMR spectroscopists, because of the difficulties associated with acquiring NMR spectra of nuclei with low Larmor frequencies that may require expensive isotopic labelling. Such experiments are further confounded by the fact that half-integer quadrupolar nuclei such as  $^{25}\text{Mg}$  often have a broad central transition powder pattern affected by the second-order quadrupolar interaction. The general unreceptivity of  $^{25}\text{Mg}$  also makes experiments which resolve magnetically distinct nuclei, such as multiple-quantum magic-angle spinning (MQMAS),<sup>[2]</sup> very difficult to apply. Despite these difficulties,  $^{25}\text{Mg}$  NMR studies in the solid state have been reported on a variety of compounds, including a single crystal of magnesium,<sup>[3]</sup>  $\text{MgF}_2$ ,<sup>[4]</sup>  $\text{Mg}(\text{OH})_2$ ,<sup>[5]</sup>  $\text{Mg}(\text{OH})_2$  loaded into an ethylene-vinyl acetate copolymer,<sup>[6]</sup>  $\text{Mg}_2\text{SiO}_4$ ,<sup>[7,8]</sup>  $\text{MgTiO}_3$ ,<sup>[9]</sup>  $\text{MgCO}_3$ ,<sup>[10]</sup> Mg metal and  $\text{Mg}_{17}\text{Al}_{12}$  in Mg-Al alloys,<sup>[11]</sup>  $\text{MgB}_2$  superconductor,<sup>[12]</sup> silicate liquids,<sup>[13]</sup> and a series of glasses, minerals and inorganic materials.<sup>[14-17]</sup> However, many of the

aforementioned investigations were performed at low temperatures ( $< 5$  K), on single crystals, and/or in systems where the magnesium environment has a high degree of spherical symmetry (thereby reducing the line broadening effects of the second-order quadrupolar interaction). Where the above conditions did not hold true, long experiments requiring the collection of vast amounts of transients were usually performed via a spin echo ( $\pi/2 - \tau - \pi - \tau - \text{acq}$ ) type sequence which would yield spectra with relatively poor signal-to-noise. Recently, there have also been studies reported on  $^{25}\text{Mg}$  isotopically enriched inner-sphere  $\text{Mg}^{2+}$  binding complexes<sup>[18]</sup> and magnesium(II) adenosine 5'-triphosphate<sup>[19]</sup> employing  $^{25}\text{Mg}$  MQMAS, as well as studies on  $\text{Mg}(\text{OAc})_2 \cdot 4\text{H}_2\text{O}$ <sup>[20]</sup> and  $\text{Mg}(\text{VO}_3)_2$ <sup>[21]</sup> using the QCPMG (quadrupolar Carr-Purcell Meiboom-Gill) pulse sequence. To the best of our knowledge, no solid-state  $^{25}\text{Mg}$  NMR study on any organometallic compound has been reported. This may be attributed to the unusually low spherical symmetry of sites within which magnesium is positioned in organometallic complexes, and the correspondingly large values of  $C_Q(^{25}\text{Mg})$ . However, solution  $^{25}\text{Mg}$  NMR studies of organometallic compounds, including  $\text{Cp}_2\text{Mg}$ , have been conducted.<sup>[22]</sup>

Fortunately, the past decade has witnessed advances in instrumentation and methodology, allowing great strides towards the detection of insensitive half-integer quadrupolar nuclei. In particular, the development and application of the QCPMG<sup>[23]</sup> spin-echo pulse sequence has enabled significant sensitivity enhancements in NMR spectra of unresponsive half-integer quadrupolar nuclei with relatively large quadrupole interactions. The QCPMG pulse sequence exploits differences in  $T_2$  and  $T_2^*$  relaxation time constants by continually refocusing the dephased spin magnetization via a train of  $\pi$

pulses, effectively reacquiring the spin echo spectrum a multiple number of times within the same acquisition. The Fourier transformed spectra obtained from employing the QCPMG sequence are characterized by a manifold of echo “spikelets” with the same appearance as the corresponding spin echo powder pattern. In fact, a high signal-to-noise *static spectrum can be reconstructed by co-addition of the QCPMG train of echoes in the FID into a single echo and subsequent Fourier transformation of the FID.* In addition, special window functions made up of repetitive Lorentzian or Gaussian curves can be employed to apodize QCPMG FIDs,<sup>[24]</sup> improving the signal to noise ratio of the resulting frequency spectra. QCPMG has also been combined with magic angle spinning<sup>[25]</sup> and has found application in the study of inorganic<sup>[21]</sup> and biological<sup>[26]</sup> model compounds.

Herein the first solid-state <sup>25</sup>Mg NMR study of an organometallic compound, bis(cyclopentadienyl)magnesium, at natural abundance is reported. Cp<sub>2</sub>Mg has found application as a very pure source of magnesium for doping by metalorganic chemical vapor deposition (MOCVD) of GaN films, which are applied in blue light-emitting diodes (LEDs) and laser diodes (LDs), and have great potential uses in optoelectronics and high temperature electronic devices.<sup>[27]</sup> Magnesium-25 electric field gradient (EFG) and chemical shielding (CS) parameters are extracted from analysis of central transition spectra in order to correlate the NMR interaction tensors with the electronic environment at the metal center. Theoretical calculations compliment <sup>25</sup>Mg NMR experiments, giving insight into the orientation of the NMR interaction tensors with respect to the molecular frame and their correspondence with the molecular structure of Cp<sub>2</sub>Mg. Through a combination of theoretical calculations (RHF and B3LYP) and simulations of the effects

of carbon atom reorientation on  $^{13}\text{C}$  NMR powder patterns, the motion of the Cp rings in metallocenes is reasserted.

## 6.2 Experimental

### 6.2.1 Sample Preparation and Handling

$\text{Cp}_2\text{Mg}$  samples were purchased from Strem Chemicals, Inc. and used without further purification.  $\text{Cp}_2\text{Mg}$  was finely ground and packed into 4 mm and 5 mm outer diameter (o.d.) zirconia rotors for the acquisition of MAS and static QCPMG spectra, respectively. Due to the sensitivity of samples to air, sample preparation had to be performed inside a glovebox and rotors had to be sealed with specially made Teflon caps.

### 6.2.2 Solid-State NMR Spectroscopy

$^{25}\text{Mg}$  NMR spectra were acquired on a Varian Infinity+ NMR system with an Oxford 9.4 T ( $^1\text{H} = 400$  MHz) wide-bore magnet at a resonance frequency of  $\nu_0(^{25}\text{Mg}) = 24.46$  MHz. Tuning to this relatively low Larmor frequency, while at the same time maintaining a high forward-to-reflected power ratio, is made possible by use of a Varian/Chemagnetics Low Gamma Tuning Box installed on T3-HXY 4 mm and 5 mm triple-resonance wide-bore MAS NMR probes. An applied rf field of  $\nu_1 = 45.5$  kHz, a recycle delay of 2.5 s and central transition selective  $\pi/2$  and  $\pi$  pulses of 1.83  $\mu\text{s}$  and 3.66  $\mu\text{s}$ , respectively, were used throughout. The number of Meiboom-Gill loops was set so as to acquire the full  $T_2$  decay. For the static QCPMG spectrum, inter-pulse and inter-

acquisition delays  $\tau_1, \tau_2, \tau_3, \tau_4$  were set to 135  $\mu\text{s}$  in order to minimize the effects of acoustic ringing and pulse breakthrough. The acquisition period ( $\tau_a$ ) for each echo was adjusted to attain a spikelet separation ( $1/\tau_a$ ) of 2500 Hz in the frequency spectrum and 39584 transients were acquired. The  $^{25}\text{Mg}$  MAS QCPMG NMR spectrum was recorded at  $\nu_{\text{rot}} = 16000$  Hz with  $\tau_1, \tau_2, \tau_3, \tau_4$  set as 123.17  $\mu\text{s}$ , corresponding to two times the rotor period ( $\tau_r$ ) minus the  $\pi/2$  pulse width, and  $\tau_a$  was adjusted accordingly as in Reference [25] to attain  $1/\tau_a = 250$  Hz. A total of 108496 scans were acquired for the  $^{25}\text{Mg}$  MAS QCPMG spectrum. Magnesium-25 chemical shifts were referenced to a saturated aqueous solution of  $\text{MgCl}_2$  ( $\delta_{\text{iso}} = 0.0$  ppm).

Proton decoupled carbon-13 cross-polarization (CP) MAS NMR spectra were acquired on the same spectrometer indicated above with  $\nu_0(^{13}\text{C}) = 100.52$  MHz. Spectra were recorded at spinning frequencies of  $\nu_{\text{rot}} = 2000$  and 3500 Hz (requiring 440 and 88 transients), and referenced to adamantane as a secondary standard:  $^{13}\text{C}$  chemical shifts were set to the tetramethylsilane (TMS) reference scale ( $\delta_{\text{iso}} = 0.0$  ppm) by setting the high frequency peak of adamantane to  $\delta_{\text{iso}} = 38.57$  ppm. Pulse widths and applied rf fields of 5.5  $\mu\text{s}$  and 45.45 kHz, respectively, were typically applied.

### 6.2.3 Spectral Simulations

Extraction of  $^{25}\text{Mg}$  EFG and CS parameters was carried out by first performing analytical simulations on the envelope of the QCPMG spectra and then refining with numerical simulations. To perform analytical simulations, the WSOLIDS simulation package was utilized,<sup>[28]</sup> while numerical simulations were performed with the SIMPSON

simulation package.<sup>[29]</sup> SIMPSON simulations of all spectra were carried out by the *direct* method of powder averaging using the *zcw4180* crystal file provided with the package. The start and detect operators were set respectively to  $I_{1z}$  and  $I_{1c}$ , while experimental values were employed for all remaining parameters. The number of gamma angles was set to 1 and 20 for simulations of static and MAS QCPMG spectra, respectively. The experimental error for each measured parameter was determined by visual comparison of experimental spectra with simulations. The parameter of concern was varied bidirectionally starting from the best fit value and all other parameters were kept constant, until noticeable differences between the spectra were observed.

#### 6.2.4 Theoretical Calculations

Molecular coordinates from crystal structure data<sup>[30]</sup> of an isolated  $\text{Cp}_2\text{Mg}$  molecule (with optimized hydrogen positions) were employed for the calculation of  $^{25}\text{Mg}$  EFG and CS parameters on a dual-733 MHz Pentium III Dell Precision 420 workstation running Red Hat Linux 6.2. Computation of NMR interaction parameters employing a completely optimized gas-phase molecular structure were also undertaken (Appendix C, Tables C.3 and C.4). Calculations were performed with Gaussian 98<sup>[31]</sup> using the restricted Hartree-Fock (RHF) method and hybrid density functional theory with the B3LYP functional<sup>[32-34]</sup> in combination with basis sets provided with the package (6-31G\*\*, 6-311G\*\* and 6-311+G\*\*). Magnesium-25 quadrupole coupling constants were computed with the formula  $C_Q = eV_{33}Q/h \times 9.71736 \times 10^{21} \text{ V m}^{-2}$ ,<sup>[35]</sup> where  $Q(^{25}\text{Mg}) = 2.2 \times 10^{-29} \text{ m}^2$ ,<sup>[1]</sup>  $e = 1.602188 \times 10^{-19} \text{ C}$ ,  $h = 6.6260755 \times 10^{-34} \text{ J s}$ , and  $V_{33}$  is the largest

principal component of the electric field gradient tensor. Magnesium chemical shielding tensors were calculated using the GIAO (gauge-including atomic orbitals) method<sup>[36,37]</sup> and were referenced against the theoretical isotropic shielding ( $\delta_{\text{iso}} = 0.0$  ppm) of  $\text{Mg}(\text{H}_2\text{O})_6^{2+}$  computed with the corresponding methods and basis sets. In order to compare experimental chemical shifts and theoretical chemical shielding parameters, the latter were converted to the  $^{25}\text{Mg}$  chemical shift scale by subtracting the shielding of  $\text{Cp}_2\text{Mg}$  from that of  $\text{Mg}(\text{H}_2\text{O})_6^{2+}$ . Similarly,  $^{13}\text{C}$  CS tensors were referenced to the theoretical shielding ( $\delta_{\text{iso}} = 187.1$  ppm)<sup>[38]</sup> of CO as a secondary reference by subtracting the theoretical shielding data of  $\text{Cp}_2\text{Mg}$  from that of CO and then adding 187.1 ppm.

## 6.3 Results and Discussion

### 6.3.1 Solid-State $^{25}\text{Mg}$ NMR

The experimental  $^{25}\text{Mg}$  MAS QCPMG NMR spectrum of  $\text{Cp}_2\text{Mg}$  at spinning speed  $\nu_{\text{rot}} = 16$  kHz is shown in Figure 6.1a. A single second-order quadrupolar pattern is present at  $\delta_{\text{iso}} = -91$  ppm, which corresponds to the single asymmetric site in the reported crystal structure.<sup>[30]</sup> Spinning sideband powder patterns flank the isotropic centerband, and a low-intensity powder pattern corresponding to some impurity resulting from degradation of the sample is centered at  $-60$  ppm. Numerical (Figure 6.1b) and analytical (Figure 6.1c) simulations of the MAS QCPMG spectrum reveal a  $^{25}\text{Mg}$  quadrupole coupling constant of  $C_Q = 5.80$  MHz and an axially symmetric EFG tensor ( $\eta_Q = 0.01$ ). Inclusion of  $^{25}\text{Mg}$  chemical shielding anisotropy (*vide infra*) in the numerical simulations

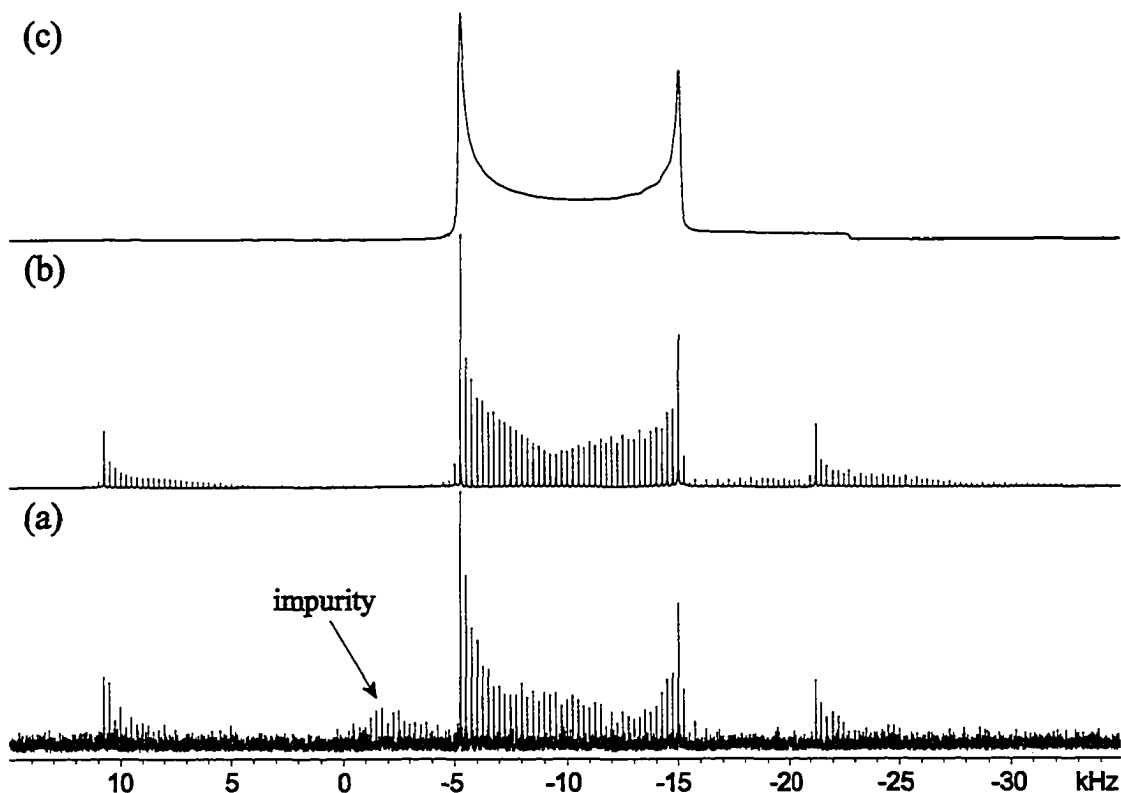


**Figure 6.1** (a) Experimental  $^{25}\text{Mg}$  MAS QCPMG NMR spectrum of  $\text{Cp}_2\text{Mg}$  and corresponding (b) SIMPSON numerical and (c) WSOLIDS analytical simulations.

did not present any noticeable differences in the spinning sideband intensities. The axial symmetry of the EFG tensor can likely be ascribed to the pseudo-axial symmetry of the  $\text{Cp}_2\text{Mg}$  molecule as well as the fact that the Cp rings undergo rapid five-fold rotation at ambient temperatures.<sup>[39]</sup> The relationship between the  $\text{Cp}_2\text{Mg}$  structure, ring dynamics and anisotropic NMR interaction tensors are further discussed below.

Superficially, the  $\text{Cp}_2\text{Mg}$  molecule appears to have a similar structure to the decamethylaluminocenium cation,  $\text{Cp}^*_2\text{Al}^+$ , which has  $D_{5d}$  symmetry with staggered  $\text{Cp}^*$  rings.<sup>[40]</sup> Close examination of the  $\text{Cp}_2\text{Mg}$  molecule reveals that it has  $C_i$  symmetry and that its Cp rings are further away from the central metal atom in comparison to  $\text{Cp}^*_2\text{Al}^+$  (i.e., the Cp ring centroid to metal distance in  $\text{Cp}^*_2\text{Al}^+$  is  $r(\text{Cp}_{\text{cent}}-\text{Al}) = 1.769 \text{ \AA}$  and in



$\text{Cp}_2\text{Mg}$  is  $r(\text{Cp}_{\text{cent}}-\text{Mg}) = 1.990 \text{ \AA}$ ). It has previously been shown that if  $V/2$  equal charges are positioned at the  $V$  vertices of a regular centrosymmetric polyhedron so that no two charges are related by a reflection operation through the center ( $S_0$ ) of the polyhedron, a null electric field gradient can be attained at  $S_0$ ;<sup>[41-43]</sup> this phenomenon has further been exemplified by a previous study on  $\text{Cp}^*_2\text{Al}^+$ .<sup>[40]</sup> The  $^{27}\text{Al}$  nuclear quadrupole coupling constant in  $\text{Cp}^*_2\text{Al}^+$  is very small, with  $C_Q(^{27}\text{Al}) = 0.86 \text{ MHz}$ , and is attributed to the fact that the aromatic Cp carbons are almost exactly located on ten of the twenty vertices of a dodecahedron with edge lengths equal to the C-C bond length and the aluminum positioned centro-symmetrically (Figure 6.2a). It might be expected that the  $C_Q(^{25}\text{Mg})$  in  $\text{Cp}_2\text{Mg}$  should also be small in magnitude, since the nuclear quadrupole moments of  $^{25}\text{Mg}$  and  $^{27}\text{Al}$  are comparable ( $Q(^{25}\text{Mg}) = 2.2 \times 10^{-29} \text{ m}^2$ ,  $Q(^{27}\text{Al}) = 1.409 \times 10^{-29} \text{ m}^2$ ); however, this is clearly not the case. If the  $\text{Cp}_2\text{Mg}$  molecule is superimposed upon the vertices of a

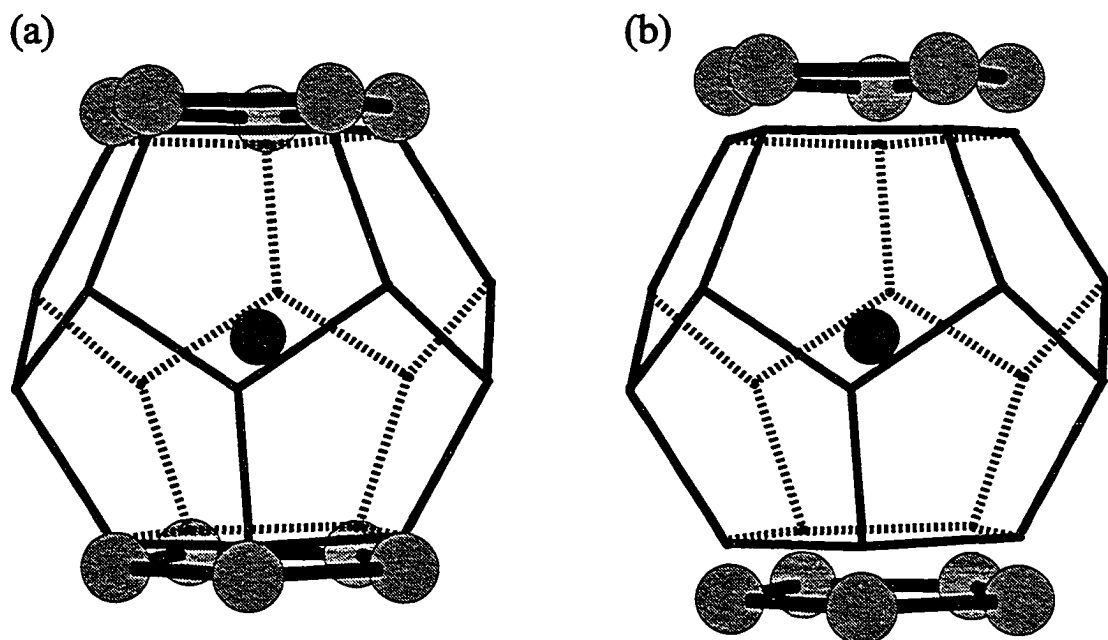


**Figure 6.2** Superposition of (a)  $\text{Cp}^*_2\text{Al}^+$  and (b)  $\text{Cp}_2\text{Mg}$  on centro-symmetric dodecahedra having edge lengths corresponding to their C-C bond lengths.

dodecahedron in a similar manner (Figure 6.2b), it is evident that a substantial electric field gradient will be present at the  $^{25}\text{Mg}$  nucleus, since the Cp carbon positions do not provide the high spherical symmetry of the dodecahedral charge arrangement. This observation serves to partially explain the large quadrupole coupling constant measured in  $\text{Cp}_2\text{Mg}$  (*vide infra*), despite the apparent similarity of its structure to that of  $\text{Cp}^*_2\text{Al}^+$ .

Numerical simulations of the static QCPMG spectrum (Figure 6.3a) performed with only the effects of the quadrupolar interaction (Figure 6.3b) provide a less than optimal fit. The presence of  $^{25}\text{Mg}$  chemical shielding anisotropy (CSA) is suspected; however, inclusion of CSA (ca. 40 ppm as predicted by theoretical calculations, *vide*

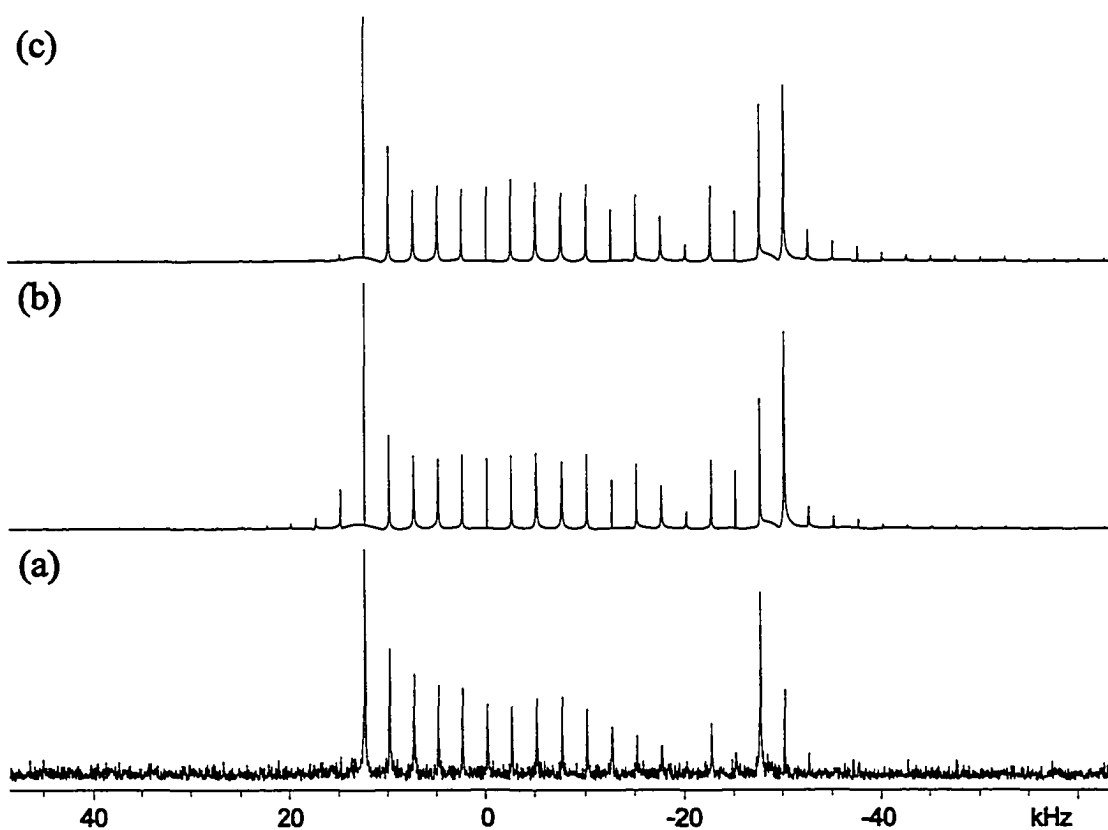


**Figure 6.3** (a) Experimental static  $^{25}\text{Mg}$  QCPMG NMR spectrum of  $\text{Cp}_2\text{Mg}$  along with numerical (SIMPSON) simulations (b) including and (c) excluding the effects of CSA.

*infra*) in simulations (Figure 6.3c) results in less than a 3% increase in the breadth of the static pattern. At the present time, only an upper bound of approximately 60 ppm can be estimated for the CSA. Some discrepancy between experimental and simulated spectra may also arise from difficulties in uniformly irradiating across the entire spectral breadth (ca. 50 kHz) with  $\nu_0(^{25}\text{Mg}) = 24.46$  MHz, a selective  $\pi/2$  pulse width of 1.83  $\mu\text{s}$  and  $\nu_1 = 45.5$  kHz. Interestingly, attempts at recording static  $^{25}\text{Mg}$  NMR spectra on a 11.7 T ( $\nu_0(^1\text{H}) = 500$  MHz) system employing a conventional spin echo pulse sequence did not yield an observable spectrum over a two day acquisition period, hence reasserting the advantage of employing the QCPMG pulse sequence for the study of insensitive quadrupolar nuclei.

### 6.3.2 Solid-State $^{13}\text{C}$ NMR

$^{13}\text{C}$  CP/MAS NMR spectra (Figure 6.4) obtained at different spinning frequencies ( $\nu_{\text{rot}} = 2000$  and 3500 Hz) attest to the presence of a single carbon site with  $\delta_{\text{iso}} = 108.6$  ppm. Magnetic equivalence of the cyclopentadienyl ring carbons is due to rapid ring rotation (*vide infra*). However, the peaks are relatively broad, with full width at half height (FWHH) between 300 to 400 Hz, which may arise from disorder in the Cp ring carbon positions or perhaps some type of motion in addition to the usual Cp ring rotation. In comparison,  $^{13}\text{C}$  CP/MAS NMR spectra of  $\text{Cp}^*_2\text{B}^+$  and  $\text{Cp}^*_2\text{Al}^+$  typically have peaks with FWHH ranging from 30 to 60 Hz.<sup>[40, 44]</sup> The presence of spinning sidebands about the isotropic peak is indicative of carbon chemical shielding anisotropy. Characterization

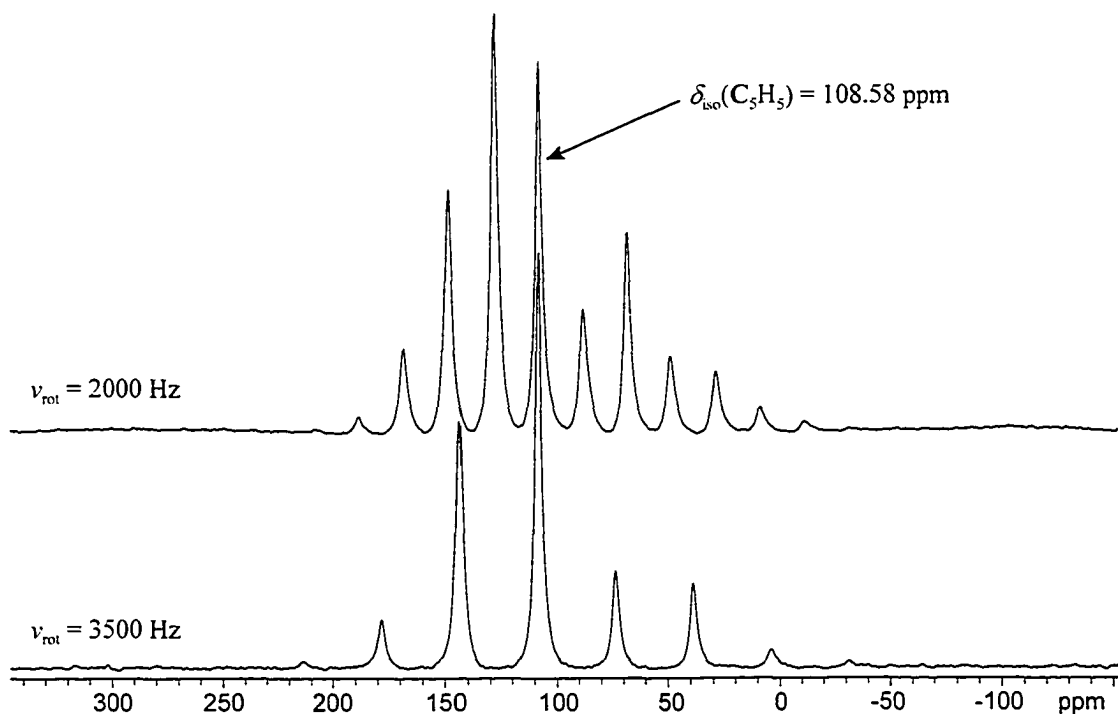


**Figure 6.4** Experimental  $^{13}\text{C}$  CP/MAS NMR spectra of  $\text{Cp}_2\text{Mg}$  at 9.4 T with spinning frequencies of 2000 and 3500 Hz.

of these sidebands by the method of Herzfeld and Berger<sup>[45, 46]</sup> yield a carbon chemical shift tensor with the principal components  $\delta_{11} = 149.9$ ,  $\delta_{22} = 144.9$  and  $\delta_{33} = 30.9$  ppm ( $\Omega = 119.0$  and  $\kappa = 0.9$ ); these are in close agreement with previously measured values by Wemmer and Pines.<sup>[47]</sup>

### 6.3.3 Theoretical Calculations

The agreement between experimental and theoretical  $^{25}\text{Mg}$  EFG tensors (Table 6.1) becomes better as larger basis sets are employed. Both the RHF and B3LYP methods underestimate the measured magnesium quadrupole coupling constant ( $C_Q = 5.80(5)$  MHz) and incorrectly predict the EFG tensor asymmetry ( $\eta_Q = 0.01(1)$ ). However, RHF calculations consistently afford better correlation with experimental  $^{25}\text{Mg}$

**Table 6.1**  
Experimental and Theoretical  $^{25}\text{Mg}$  Quadrupolar Parameters for  $\text{Cp}_2\text{Mg}$

Source	$V_{11}$ [a.u.]	$V_{22}$ [a.u.]	$V_{33}$ [a.u.]	$ C_Q $ [MHz]	$\eta_Q$
<b>Experimental<sup>[a]</sup></b>	-0.055540	-0.056662	0.112202	5.80(5)	0.01(1)
<b>RHF</b>					
6-31G**	-0.021606	-0.039154	0.060759	3.14	0.29
6-311G**	-0.038296	-0.060878	0.099174	5.13	0.23
6-311+G**	-0.038497	-0.060843	0.099339	5.14	0.22
<b>DFT(B3LYP)</b>					
6-31G**	0.006440	0.022402	-0.028842	1.49	0.55
6-311G**	-0.032586	-0.053497	0.086085	4.45	0.24
6-311+G**	-0.033383	-0.054027	0.087410	4.52	0.24

<sup>[a]</sup> The sign (+/-) and significant figures of experimental EFG tensor components ( $V_{11}$ ,  $V_{22}$  and  $V_{33}$ ) are set according to most proximate theoretical values for comparison.

$C_Q$ 's compared to B3LYP results, independent of the basis set employed. In particular, best agreement with experimental quadrupolar parameters is seen for the RHF calculation employing the 6-311+G\*\* basis set. There are several factors which may account for the discrepancy between experimental and theoretical EFG tensor parameters, including the model used for the calculation and the value of the  $^{25}\text{Mg}$  nuclear electric quadrupole moment. Perhaps most significant is that calculations were performed on an isolated  $\text{Cp}_2\text{Mg}$  molecule in the gas phase, and do not take into account long range electrostatic effects on the EFG tensor. In addition, calculations are conducted upon a static molecule, thereby eliminating the possibility that the experimental values of  $C_Q$  and  $\eta_Q$  are "average" EFG tensor parameters resulting from some sort of dynamic chemical exchange process. Finally, theoretical quadrupole coupling constants can vary by as much as 15% depending on the  $^{25}\text{Mg}$  quadrupole moment employed to calculate them; the generally accepted value ( $2.2 \times 10^{-29} \text{ m}^2$ ) measured by Lurio is employed in the present

work.<sup>[1]</sup>

All theoretical calculations, except the B3LYP/6-31G\*\* computation, generate similar magnesium EFG tensor orientations. In these cases,  $V_{33}$  is oriented close to the Cp ring centroid (i.e., in-plane center of the Cp ring) making a  $V_{33}$ -Mg-(Cp centroid) angle of ca.  $13^\circ$ , while  $V_{11}$  and  $V_{22}$  lie offset by a similar angle from a plane parallel to the Cp ring planes. The axial symmetry of the experimentally determined EFG tensor implies that  $V_{11}$  and  $V_{22}$  should be oriented in electronically similar environments, which is only possible in  $\text{Cp}_2\text{Mg}$  if they lie on a plane parallel to both Cp ring planes. However, the  $C_i$  symmetry of the  $\text{Cp}_2\text{Mg}$  molecule, coupled with the fact that there are differences in the Mg-C distances (i.e., the Cp rings are not positioned so that the carbon atoms are equidistant from the magnesium), suggests that  $V_{11}$  and  $V_{22}$  will be oriented in electronically distinct environments. Notably, one of the carbon atoms on each of the Cp rings is nearer to the magnesium atom (marked with an asterisk in Figure 6.5) by ca.  $0.017 - 0.038 \text{ \AA}$  compared to the other Cp carbons. Consequently, the major component of the EFG tensor ( $V_{33}$ ) tilts towards this carbon and,  $V_{11}$  and  $V_{22}$  are similarly offset in the same direction from the plane parallel to the Cp rings (Figure 6.5a). Thus, the absence of spherical symmetry in the  $\text{Cp}_2\text{Mg}$  molecule, which results from long Mg-Cp distances and  $C_i$  symmetry, accounts for the large values of  $C_Q(^{25}\text{Mg})$  measured by experiment and predicted by ab initio calculations. The experimental value of  $\eta_Q$  must derive from rotational or oscillatory motion of the Cp rings which serve to average the positions of  $V_{11}$  and  $V_{22}$  on a timescale which is fast compared to that of the experiment.

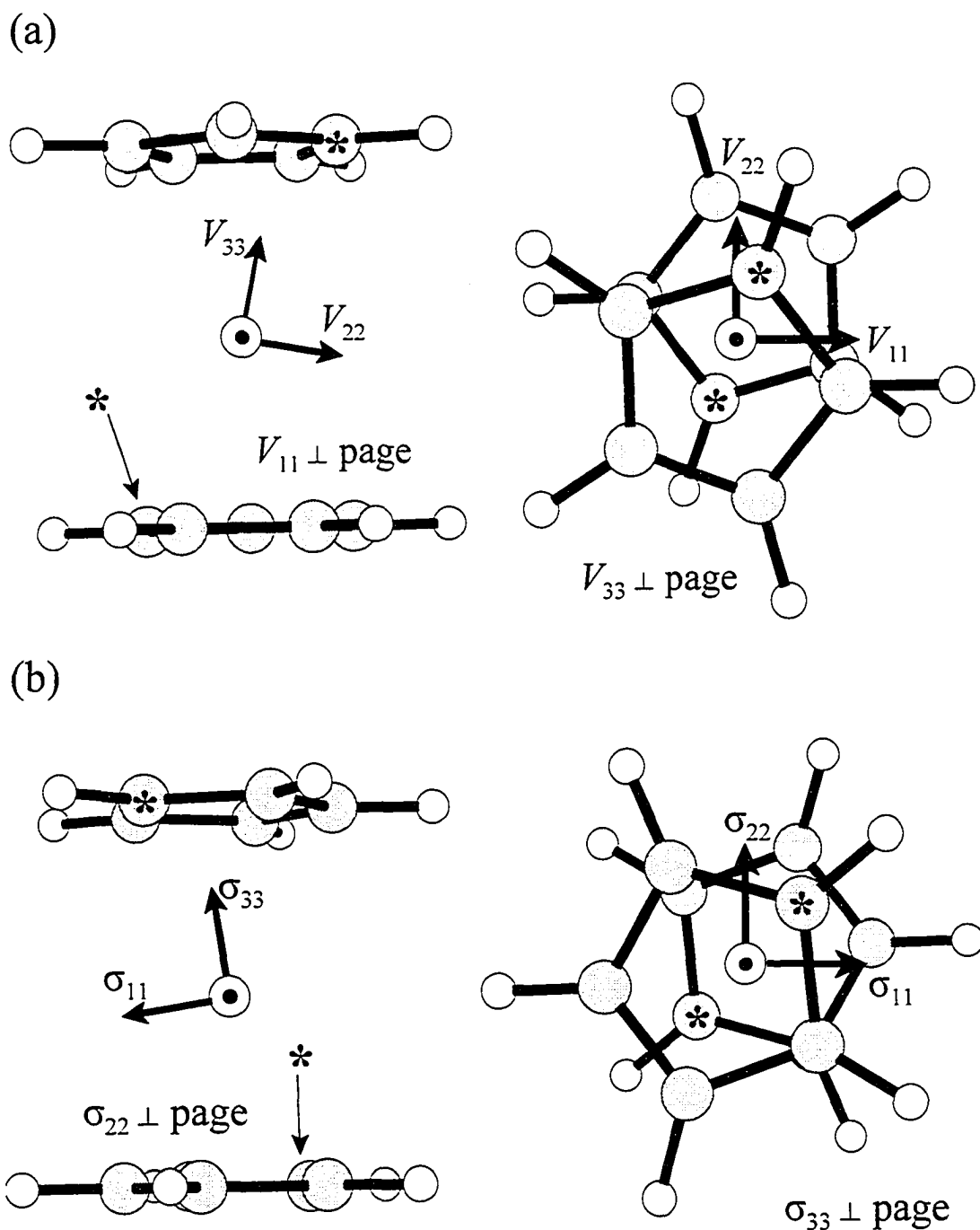


**Figure 6.5** Magnesium (a) EFG and (b) CS tensor orientations within the molecular frame from the calculation (RHF/6-311+G\*\*) yielding best agreement with experimental  $^{25}\text{Mg}$  EFG values. Asterisk marks the carbon closest to the magnesium nucleus.

RHF and B3LYP calculations (Table 6.2) predict a  $^{25}\text{Mg}$  chemical shift tensor span of  $\Omega \approx 40$  ppm with a skew of  $\kappa = 0.70 - 0.77$ . As discussed above, the magnesium CSA has a negligible effect on the appearance of the powder pattern relative to that of the quadrupolar interaction, thereby making experimental and theoretical comparison impossible with this set of data. Such a small CSA might only be measurable with the use of much higher magnetic fields where the effects of the quadrupolar and chemical shielding interactions are inversely and directly proportional to  $B_0$ , respectively, allowing for better differentiation of their contributions to the powder lineshape. The orientations of magnesium chemical shielding tensors are invariant for all theoretical calculations performed. In particular, the most shielded component,  $\sigma_{33}$ , is coincident with the largest component of the EFG tensor  $V_{33}$  and,  $\sigma_{11}$  and  $\sigma_{22}$  lie in the same plane as  $V_{11}$  and  $V_{22}$  making  $\sigma_{ii}$ -Mg- $V_{ii}$  angles of about  $35^\circ$ .

**Table 6.2**  
Theoretical Magnesium Chemical Shielding Tensors for  $\text{Cp}_2\text{Mg}$

Source	$\delta_{11}$ [ppm]	$\delta_{22}$ [ppm]	$\delta_{33}$ [ppm]	$\delta_{\text{iso}}$ [ppm]	$\Omega$ [ppm]	$\kappa$
<b>Experimental</b> <sup>[a]</sup>	—	—	—	-91(3)	—	—
<b>RHF</b>						
6-31G**	-73.28	-79.17	-114.48	-88.97	41.20	0.71
6-311G**	-77.29	-83.32	-118.37	-92.99	41.08	0.71
6-311+G**	-78.59	-84.65	-119.21	-94.15	40.62	0.70
<b>DFT(B3LYP)</b>						
6-31G**	-85.16	-90.99	-126.26	-100.80	41.10	0.72
6-311G**	-80.57	-85.96	-128.08	-98.20	47.51	0.77
6-311+G**	-81.71	-87.68	-127.49	-98.96	45.79	0.74

<sup>[a]</sup> Experimental chemical shift tensor parameters could not be determined. See Discussion section for details.



Theoretical calculations of  $^{13}\text{C}$  chemical shift tensors (Table 6.3) for  $\text{Cp}_2\text{Mg}$  present considerable discrepancies with experimentally measured values. In particular, the RHF method produces better agreement than the B3LYP method, yet both underestimate shielding of the  $\delta_{11}$  component and overestimate the shielding for  $\delta_{22}$  and  $\delta_{33}$ . The poor agreement is further evidenced by the significant differences between experimental and theoretical  $\Omega (= \delta_{11} - \delta_{33})$  and  $\kappa (= 3(\delta_{22} - \delta_{\text{iso}})/\Omega)$  values. In addition, greater deviation from experimental values is seen as larger basis sets are employed. However, all carbon CS tensors invariably have the most shielded component,  $\delta_{33}$ , aligned perpendicular to the plane of the Cp ring and the least shielded component,  $\delta_{11}$ , pointing towards the hydrogen atoms (Figure 6.6, inset).

**Table 6.3**  
Experimental and Theoretical Carbon Shielding Tensors for  $\text{Cp}_2\text{Mg}$

Source	$\delta_{11}$ [ppm]	$\delta_{22}$ [ppm]	$\delta_{33}$ [ppm]	$\delta_{\text{iso}}$ [ppm]	$\Omega$ [ppm]	$\kappa$
<b>Experimental</b>	149.92(6)	144.92(6)	30.88(6)	108.58(6)	119.04	0.92
RHF						
6-31G**	172.09	110.06	23.22	101.79	148.88	0.17
6-311G**	174.51	102.89	10.04	95.82	164.47	0.13
6-311+G**	176.69	105.01	10.98	97.56	165.71	0.13
DFT(B3LYP)						
6-31G**	169.40	102.38	9.04	93.61	160.36	0.16
6-311G**	170.27	96.69	-0.70	88.75	170.97	0.14
6-311+G**	171.39	97.90	-0.60	89.56	172.00	0.15

Much of the discrepancy between experimental and theoretical carbon chemical shift tensors can be attributed to rapid reorientation of the Cp rings about the molecular  $C_5$  axis. In order to support this claim, simulations of the  $^{13}\text{C}$  powder pattern resulting from exchange (through rotation) of the carbon positions at different rates were

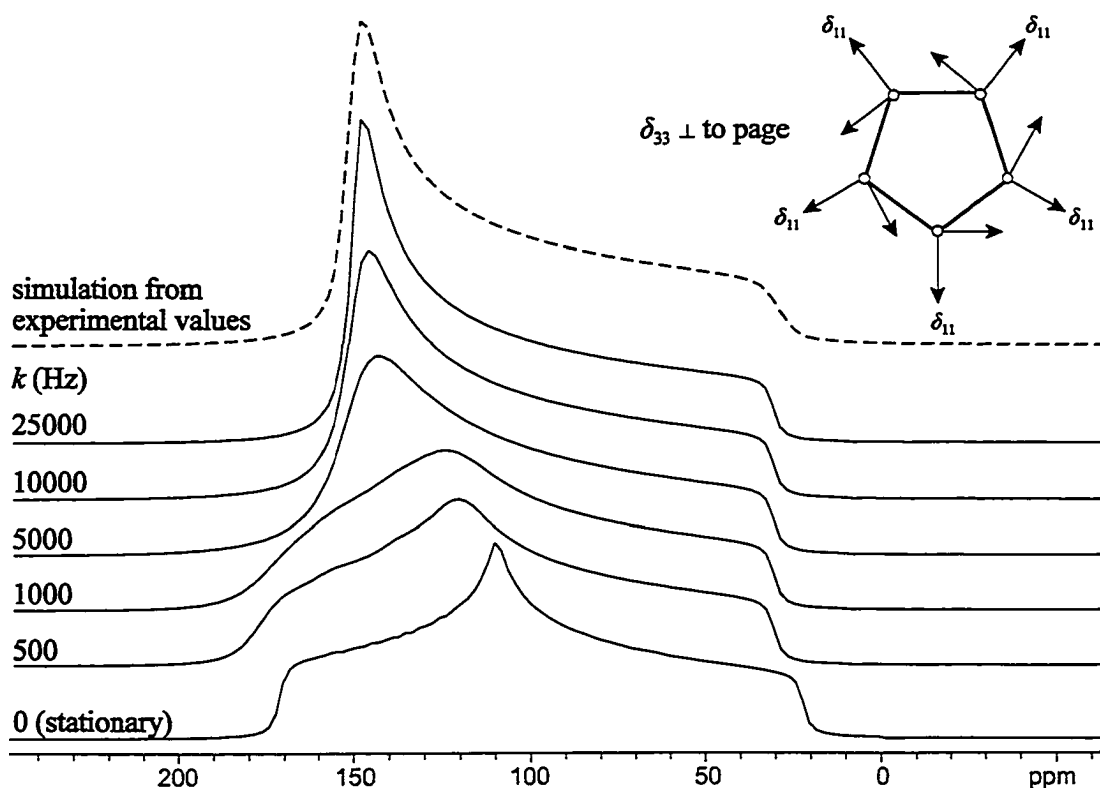


**Figure 6.6** Simulation of the  $^{13}\text{C}$  NMR powder pattern from a system undergoing 5-site chemical exchange (at different exchange rates). Dashed (---) spectrum is derived from experimentally obtained values. Inset:  $^{13}\text{C}$  chemical shift tensors from theoretical calculations.

performed (Figure 6.6). The exchange process consists of reorientation of the carbon CS tensors through the Euler angles  $\{(\theta, \varphi, \rho) \mid \theta = 0, 2\pi/5, 4\pi/5, 6\pi/5, 8\pi/5; \varphi = 0; \rho = 0\}$ . In effect,  $\delta_{33}$  is kept fixed parallel to the axis of rotation while  $\delta_{11}$  and  $\delta_{22}$  are rotated by  $72^\circ$  steps. Simulations were performed at various exchange rates ( $k = 500, 1000, 5000, 10000, 25000$  Hz) using  $^{13}\text{C}$  chemical shift values from the RHF/6-31G\*\* calculation, which gives best agreement with experimental values. At null and low exchange rates ( $k = 500, 1000$  Hz), theoretical tensor values give rise to a powder pattern where the discontinuities arising from  $\delta_{11}$ ,  $\delta_{22}$  and  $\delta_{33}$  are still readily discernible. At an exchange rate of  $k = 5000$  Hz, the  $\delta_{11}$  and  $\delta_{22}$  discontinuities begin to merge together forming an

increasingly axial CS tensor; as the exchange rate keeps on increasing, finally reaching  $k = 25000$  Hz, we are left with an axially symmetric powder pattern. However, the highest exchange rate simulation is noted as merely being a lower bound, for the rate of Cp ring rotation is likely much greater than this.<sup>[48]</sup> Analysis of this latter pattern yields a chemical shift tensor characterized by the values  $\delta_{\text{iso}} = 100$  ppm,  $\Omega = 120$  ppm and  $\kappa = 1$  ( $\delta_{11} = \delta_{22} = 140$  ppm,  $\delta_{33} = 20$  ppm), which are in good agreement with experimental data. Notably, if the isotropic shift is adjusted to match the experimental value, the resulting principal components of the chemical shift tensor become  $\delta_{11} = \delta_{22} = 149$  and  $\delta_{33} = 29$  ppm; matching experimental values almost exactly, as depicted in Figure 6.6. Therefore, we note that theoretical calculations are capable of providing very good agreement with experimental carbon chemical shielding tensors, but are less apt for the calculation of isotropic chemical shifts. Nevertheless, the theoretical isotropic chemical shift deviates from the measured value by only ca. 9 ppm.

## 6.4 Conclusion

Solid-state static and MAS  $^{25}\text{Mg}$  QCPMG NMR experiments were employed in the study of anisotropic NMR interactions in bis(cyclopentadienyl)magnesium. In particular, a large magnesium-25 quadrupole coupling constant was measured, which contrasts with what would be predicted from a simple survey of the molecular structure. Though being very similar in structure to  $\text{Cp}^*_2\text{Al}^+$ ,  $\text{Cp}_2\text{Mg}$  exhibits much longer Mg-(Cp centroid) distances and greater variation in Mg-C distances; these factors contribute to the vast difference in  $C_Q$  between  $\text{Cp}^*_2\text{Al}^+$  and  $\text{Cp}_2\text{Mg}$ . Attempts at extracting  $^{25}\text{Mg}$  CSA

parameters were hindered by the relatively minute effects on the  $\text{Cp}_2\text{Mg}$  powder pattern arising from magnesium shielding anisotropy. Theoretical calculations (RHF and B3LYP) performed correspond relatively well with experimentally measured values and allow us to rationalize the orientation of NMR interaction tensors with respect to the molecular symmetry. A comparison of experimental and theoretical  $^{13}\text{C}$  CSA data reveals discrepancies which are attributed to the exclusion of ring motion in theoretical calculations. Exchange simulations of static  $^{13}\text{C}$  NMR powder patterns were carried out to further support the previously accepted notion of Cp ring rotation. Discrepancies between experimental and theoretical  $^{25}\text{Mg}$  EFG tensor parameters are also very suggestive of rapid rotational or fluxional motion of the Cp rings in  $\text{Cp}_2\text{Mg}$ .

# Bibliography

- [1] A. Lurio, *Physical Review* **1962**, *126*, 1768.
- [2] A. Medek, J. S. Harwood, L. Frydman, *Journal of the American Chemical Society* **1995**, *117*, 12779.
- [3] P. D. Dougan, S. N. Sharma, D. L. Williams, *Canadian Journal of Physics* **1969**, *47*, 1047.
- [4] H. E. Bleich, A. G. Redfield, *Journal of Chemical Physics* **1977**, *67*, 5040.
- [5] T. J. Bastow, *Solid State Communications* **1991**, *77*, 547.
- [6] N. Pecoul, S. Bourbigot, B. Revel, *Macromolecular Symposia* **1997**, *119*, 309.
- [7] B. Derighetti, S. Hafner, H. Marxer, H. Rager, *Physics Letters A* **1978**, *66*, 150.
- [8] J. F. Stebbins, *American Mineralogist* **1996**, *81*, 1315.
- [9] D. Padro, A. P. Howes, M. E. Smith, R. Dupree, *Solid State Nuclear Magnetic Resonance* **2000**, *15*, 231.
- [10] T. J. Bastow, *Chemical Physics Letters* **2002**, *354*, 156.
- [11] T. J. Bastow, M. E. Smith, *Journal of Physics-Condensed Matter* **1995**, *7*, 4929.
- [12] M. Mali, J. Roos, A. Shengelaya, H. Keller, K. Conder, *Physical Review B* **2002**, *65*, art. no. 100518.
- [13] P. S. Fiske, J. F. Stebbins, *American Mineralogist* **1994**, *79*, 848.
- [14] R. Dupree, M. E. Smith, *Journal of the Chemical Society-Chemical Communications* **1988**, 1483.
- [15] K. J. D. MacKenzie, R. H. Meinhold, *American Mineralogist* **1994**, *79*, 250.

- [16] K. J. D. MacKenzie, C. M. Sheppard, C. McCammon, *Journal of the European Ceramic Society* **2000**, *20*, 1975.
- [17] S. Kroeker, P. S. Neuhoff, J. F. Stebbins, *Journal of Non-Crystalline Solids* **2001**, *293*, 440.
- [18] S. Sham, G. Wu, *Inorganic Chemistry* **2000**, *39*, 4.
- [19] C. V. Grant, V. Frydman, L. Frydman, *Journal of the American Chemical Society* **2000**, *122*, 11743.
- [20] A. S. Lipton, J. A. Sears, P. D. Ellis, *Journal of Magnetic Resonance* **2001**, *151*, 48.
- [21] F. H. Larsen, J. Skibsted, H. J. Jakobsen, N. C. Nielsen, *Journal of the American Chemical Society* **2000**, *122*, 7080.
- [22] R. Benn, H. Lehmkuhl, K. Mehler, A. Rufinska, *Angewandte Chemie-International Edition in English* **1984**, *23*, 534.
- [23] F. H. Larsen, H. J. Jakobsen, P. D. Ellis, N. C. Nielsen, *Journal of Physical Chemistry A* **1997**, *101*, 8597.
- [24] R. Lefort, J. W. Wiench, M. Pruski, J. P. Amoureux, *Journal of Chemical Physics* **2002**, *116*, 2493.
- [25] F. H. Larsen, H. J. Jakobsen, P. D. Ellis, N. C. Nielsen, *Journal of Magnetic Resonance* **1998**, *131*, 144.
- [26] A. S. Lipton, T. A. Wright, M. K. Bowman, D. L. Reger, P. D. Ellis, *Journal of the American Chemical Society* **2002**, *124*, 5850.
- [27] J. K. Sheu, Y. K. Su, G. C. Chi, B. J. Pong, C. Y. Chen, C. N. Huang, W. C. Chen, *Journal of Applied Physics* **1998**, *84*, 4590.

- [28] K. Eichele, R. E. Wasylishen, WSOLIDS, v.1.17.28 - Software for simulations of solid state NMR powder patterns, Dalhousie University, Dalhousie, **2000**.
- [29] M. Bak, J. T. Rasmussen, N. C. Nielsen, *Journal of Magnetic Resonance* **2000**, *147*, 296.
- [30] W. Bunder, E. Weiss, *Journal of Organometallic Chemistry* **1975**, *92*, 1.
- [31] M. J. Frisch, G. W. Trucks, H. B. Schlegel, G. E. Scuseria, M. A. Robb, J. R. Cheeseman, V. G. Zakrzewski, J. A. Montgomery Jr., R. E. Stratmann, J. C. Burant, S. Dapprich, J. M. Millam, A. D. Daniels, K. N. Kudin, M. C. Strain, O. Farkas, J. Tomasi, V. Barone, M. Cossi, R. Cammi, B. Mennucci, C. Pomelli, C. Adamo, S. Clifford, J. Ochterski, G. A. Petersson, P. Y. Ayala, Q. Cui, K. Morokuma, D. K. Malick, A. D. Rabuck, K. Raghavachari, J. B. Foresman, J. Cioslowski, J. V. Ortiz, A. G. Baboul, B. B. Stefanov, G. Liu, A. Liashenko, P. Piskorz, I. Komaromi, R. Gomperts, R. L. Martin, D. J. Fox, T. Keith, M. A. Al-Laham, C. Y. Peng, A. Nanayakkara, M. Challacombe, P. M. W. Gill, B. Johnson, W. Chen, M. W. Wong, J. L. Andres, C. Gonzalez, M. Head-Gordon, E. S. Replogle, J. A. Pople, Gaussian 98, Revision A. 9. Gaussian, Inc., Pittsburgh, PA, **1998**.
- [32] A. D. Becke, *Physical Review A* **1988**, *38*, 3098.
- [33] A. D. Becke, *Journal of Chemical Physics* **1993**, *98*, 5648.
- [34] C. Lee, W. Yang, R. G. Parr, *Physical Review B* **1988**, *37*, 785.
- [35] S. Coriani, C. Hattig, P. Jorgensen, A. Rizzo, K. Ruud, *Journal of Chemical Physics* **1998**, *109*, 7176.
- [36] R. Ditchfield, *Molecular Physics* **1974**, *27*, 789.

- [37] K. Wolinski, J. F. Hinton, P. Pulay, *Journal of the American Chemical Society* **1990**, *112*, 8251.
- [38] A. K. Jameson, C. J. Jameson, *Chemical Physics Letters* **1987**, *134*, 461.
- [39] E. A. C. Lucken, *Nuclear Quadrupole Coupling Constants*, Academic Press, New York, **1969**.
- [40] R. W. Schurko, I. Hung, C. L. B. Macdonald, A. H. Cowley, *Journal of the American Chemical Society*, doi: 10.1021/ja020394p.
- [41] O. Knop, *Acta Crystallographica Section A* **1976**, *32*, 147.
- [42] O. Knop, E. M. Palmer, R. W. Robinson, *Acta Crystallographica Section A* **1975**, *31*, 19.
- [43] J. W. Akitt, W. S. McDonald, *Journal of Magnetic Resonance* **1984**, *58*, 401.
- [44] R. W. Schurko, I. Hung, S. Schauff, C. L. B. Macdonald, A. H. Cowley, *Journal of Physical Chemistry A* **2002**, *106*, 10096.
- [45] M. M. Maricq, J. S. Waugh, *Journal of Chemical Physics* **1979**, *70*, 3300.
- [46] J. Herzfeld, A. E. Berger, *Journal of Chemical Physics* **1980**, *73*, 6021.
- [47] D. E. Wemmer, A. Pines, *Journal of the American Chemical Society* **1981**, *103*, 34.
- [48] A. M. Orendt, J. C. Facelli, Y. J. Jiang, D. M. Grant, *Journal of Physical Chemistry A* **1998**, *102*, 7692.



# Chapter 7

## Solid-State $^{91}\text{Zr}$ NMR of Bis(cyclopentadienyl)dichloro Zirconium(IV)

### 7.1 Introduction

There are relatively few examples of solid-state  $^{91}\text{Zr}$  NMR in the literature due to the fact that  $^{91}\text{Zr}$  is a half-integer quadrupolar nucleus with a moderately-sized nuclear quadrupole moment (nuclear spin  $I = 5/2$ ,  $Q(^{91}\text{Zr}) = -1.76(3) \times 10^{-29} \text{ m}^2$ ),<sup>[11]</sup> and is relatively unreceptive due to its low natural abundance (11.23%) and low magnetogyric ratio ( $-2.49750 \times 10^7 \text{ rad T}^{-1} \text{ s}^{-1}$ ). Solid-state  $^{91}\text{Zr}$  NMR studies have previously been conducted on a number of zirconium-containing inorganic materials and metallic alloys, including Zr-Nb-Fe Laves phase compounds,<sup>[2]</sup> zircon ( $\text{ZrSiO}_4$ ),<sup>[3]</sup> zirconium oxide ceramics,<sup>[4, 5]</sup> synthetic zirconium oxide materials,<sup>[6]</sup> sodium zirconate ( $\text{Na}_2\text{ZrO}_3$ ),<sup>[7]</sup> crystalline  $\text{Na}_2\text{O-ZrO}_2\text{-SiO}_2$  materials,<sup>[8]</sup> and aluminum-zirconium inter-metallic alloys.<sup>[9]</sup> To the best of our knowledge, there are no reported solid-state  $^{91}\text{Zr}$  NMR studies on organometallic zirconium complexes, although a number of different organometallic complexes have been studied in detail by solution  $^{91}\text{Zr}$  NMR<sup>[10-12]</sup> and ab initio calculations.<sup>[11]</sup>

The majority of the aforementioned solid-state  $^{91}\text{Zr}$  NMR studies have utilized Hahn spin-echo pulse sequences of the form  $\{\pi/2 - \tau - \pi - \tau - \text{acq}\}$ .<sup>[13]</sup> Spin-echo sequences are required in most cases to observe the quickly decaying signal of a half-

integer quadrupolar nucleus, since Bloch decay acquisition is limited by both the dead time of the coil in the NMR probe and acoustic ringing at low Larmor frequencies. Due to both the broadening of solid-state NMR powder patterns by the second-order quadrupolar interaction and the general unreceptivity of  $^{91}\text{Zr}$ , many of these spectra require the acquisition of hundreds of thousands of transients in order to obtain a reasonable signal-to-noise (S/N) ratio. Furthermore, if the  $^{91}\text{Zr}$  quadrupolar interaction is large, the breadth of the  $^{91}\text{Zr}$  spectrum exceeds the excitation bandwidth at standard magnetic field strengths (i.e., 9.4 T to 14.1 T); thus, in some cases it is necessary to collect spectra that are greater than 50 kHz wide in stepwise manner (in frequency offset increments), which is a very time-consuming process.<sup>[14, 15]</sup> In addition, many of the spectra acquired by stepped-echo techniques lack the definition (i.e., S/N and spectral resolution) required to obtain accurate chemical shielding and quadrupolar parameters from spectral analysis.

There has recently been much progress in the observation of unreceptive low-gamma half-integer quadrupolar nuclei due to the availability of higher magnetic fields, stable low-temperature double-resonance NMR probes and the development of special spin-echo pulse sequences.<sup>[16, 17]</sup> In particular, a multi-pulse spin-echo technique for quadrupolar nuclei, known as the “quadrupolar Carr-Purcell Meiboom-Gill” (QCPMG) pulse sequence,<sup>[18]</sup> has found application in the study of dilute, insensitive quadrupolar nuclei in inorganic materials<sup>[19]</sup> and biologically relevant samples.<sup>[20, 21]</sup> QCPMG has also been modified for magic-angle spinning (MAS) and multiple-quantum magic-angle spinning (MQMAS) to study receptive half-integer quadrupolar nuclei with large

quadrupolar interactions.<sup>[22, 23]</sup> In addition, the QCPMG pulse sequence has recently been combined with the preparatory rotor-assisted polarization transfer (RAPT)<sup>[24]</sup> and amplitude-modulated double frequency sweep (AM-DFS)<sup>[25]</sup> pulse sequences for overall signal enhancements of an order of magnitude or more.<sup>[26]</sup>

The first solid-state  $^{91}\text{Zr}$  NMR study of an organometallic zirconium(IV) complex using Hahn echo, QCPMG and modified QCPMG pulse sequences is presented. The compound under investigation is bis(cyclopentadienyl)dichloro zirconium(IV) ( $\text{Cp}_2\text{ZrCl}_2$ ), which is an important precursor in the design of zirconium-containing metallocene catalysts.<sup>[27]</sup> Acquisition of static and MAS  $^{91}\text{Zr}$  QCPMG NMR spectra of  $\text{Cp}_2\text{ZrCl}_2$  packed in a zirconium-oxide NMR rotor shows that there is some degree of background signal from the rotor, but it can easily be distinguished from the  $\text{Cp}_2\text{ZrCl}_2$  signal. It is demonstrated that  $\text{ZrO}_2$  rotors are suitable for  $^{91}\text{Zr}$  MAS NMR experiments on compounds with small to moderate quadrupole coupling constants such as  $\text{Cp}_2\text{ZrCl}_2$ , and that Zr-free sample containers are a necessity for Zr compounds with larger quadrupolar interactions. The central-transition  $^{91}\text{Zr}$  NMR spectra, which are influenced by anisotropic chemical shielding and second-order quadrupolar effects, can be used to probe the electronic environment about the zirconium atom. The first anisotropic zirconium chemical shielding tensor is determined from simulation of experimental  $^{91}\text{Zr}$  static spectra acquired at two different field strengths. Significant gains in signal can be obtained in the  $^{91}\text{Zr}$  NMR spectra of  $\text{Cp}_2\text{ZrCl}_2$  by using preparatory DFS or RAPT sequences, followed by the QCPMG sequence. Our work demonstrates that it is possible to rapidly and efficiently acquire solid-state  $^{91}\text{Zr}$  NMR spectra of zirconium-containing

organometallic and inorganic materials using QCPMG methods, regardless of the magnitude of the quadrupolar interaction. These techniques hold promise for the investigation of catalytic mechanisms in solid zirconium-containing systems, in addition to a wide array of technologically important materials. We also present various theoretical calculations of NMR interaction tensors, for the purpose of examining the orientations of the NMR interaction tensors within the molecular frame and correlating the anisotropic NMR interactions to the molecular structure.

## 7.2 Experimental

$\text{Cp}_2\text{ZrCl}_2$  was purchased from Strem Chemicals, Inc. and used without further purification.

### 7.2.1 Solid-State NMR Spectroscopy

Zirconium-91 NMR spectra were acquired on a Varian Infinity Plus NMR spectrometer with an Oxford 9.4 T ( $\nu_0(^1\text{H}) = 400$  MHz) wide-bore magnet operating at  $\nu_0(^{91}\text{Zr}) = 37.16$  MHz. Samples were finely powdered and packed under a nitrogen atmosphere into a 4 mm outer diameter (o.d.) zirconia rotor for MAS experiments, and into both a 5 mm o.d. zirconia rotor and a 5 mm o.d. Teflon tube for static experiments. All  $^{91}\text{Zr}$  experiments employed a central transition selective  $\pi/2$  pulse width of 1.17  $\mu\text{s}$ , rf field ( $\nu_1$ ) of 71.4 kHz and recycle delay of 0.75 s. Static QCPMG spectra of  $\text{Cp}_2\text{ZrCl}_2$  packed in a Teflon tube were recorded using inter-pulse and inter-acquisition delays  $\tau_1 =$

$\tau_2 = \tau_3 = \tau_4 = 45 \mu\text{s}$  in order to minimize the effects of probe ringing. The acquisition period ( $\tau_a$ ) for each echo was adjusted to attain a spikelet separation ( $1/\tau_a$ ) of 1905 Hz in the frequency spectrum and the number of Meiboom-Gill (MG) loops was set so as to acquire the complete transverse decay of the FID. Where applicable, a converging DFS pulse was employed starting at  $\nu_s = 2 \text{ MHz}$  and finishing at  $\nu_f = 185 \text{ kHz}$  over a period of 800  $\mu\text{s}$ , which corresponds to a sweep rate ( $\lambda$ ) of ca.  $2.3 \text{ GHz s}^{-1}$  and an adiabaticity parameter ( $A = \nu_1^2/\lambda$ ) of 2.25.<sup>[28]</sup> The static QCPMG sub-spectra of  $\text{Cp}_2\text{ZrCl}_2$  in a 5 mm o.d. zirconia rotor as well a rotor containing an adamantane/KBr mixture (i.e., to measure  $^{91}\text{Zr}$  background from the rotor) were acquired in a stepwise fashion using 50 kHz irradiation frequency offsets (integer multiple of  $1/\tau_a$ ) until no signal could be detected upon further increase or decrease of the transmitter frequency. Uniform excitation over a “rectangular” spectral region was accomplished by determining the effective excitation bandwidth for given rf fields and pulse widths from an individual sub-spectrum and then setting the appropriate transmitter offset step size.<sup>[29-31]</sup> For each sub-spectrum, 3200 transients were collected with  $1/\tau_a = 2000 \text{ Hz}$  and  $\tau_1 = \tau_2 = \tau_3 = \tau_4 = 35 \mu\text{s}$ . Central transition selective pulse widths mentioned herein are non-selective pulse widths which have been scaled by the factor  $(I + 1/2)^{-1}$ . Zirconium-91 chemical shifts were referenced to a concentrated solution of  $\text{Cp}_2\text{ZrCl}_2$  in  $\text{CH}_2\text{Cl}_2$  ( $\delta_{\text{iso}} = 0 \text{ ppm}$ ).

All MAS experiments were synchronized with the rotor period by setting  $\tau_1$  equal to the inverse of the rotor spinning frequency,  $\nu_{\text{rot}}$ , or a multiple thereof. Since all MAS experiments were performed at  $\nu_{\text{rot}} = 15 \text{ kHz}$ , all  $\tau_1$  were set to either 66.67  $\mu\text{s}$  or 133.34  $\mu\text{s}$ ; MAS Hahn echo experiments employed  $\tau_1 = 133.34 \mu\text{s}$  and  $\tau_2 = 70.84 \mu\text{s}$ . For the

$^{91}\text{Zr}$  MAS QCPMG spectrum, 14642 transients were acquired with 40 MG loops,  $\tau_a = 2$  ms and  $\tau_1 = \tau_2 = 66.67 \mu\text{s}$ , while  $\tau_3$  and  $\tau_4$  were set to  $65.5 \mu\text{s}$  according to the equation  $2N\tau_r = \tau_a + \tau_3 + \tau_4 + \tau_\pi$ , where  $N$  is an integer,  $\tau_r$  is the rotor period,  $\tau_3 = \tau_4$ , and  $\tau_\pi$  is the duration of the selective  $\pi$  pulse.<sup>[22]</sup> The recently reported RAPT sequence for spin 5/2 nuclei was employed,<sup>[32]</sup> where two consecutive RAPT sequences are involved: the former utilized a X- $\bar{X}$  unit of  $2.02 \mu\text{s}$  repeated 37 times and the latter a X- $\bar{X}$  unit of  $2.4 \mu\text{s}$  repeated 48 times, a subsequent delay of  $1.5 \mu\text{s}$  was instilled before the  $\pi/2$  pulse.

For the comparison of RAPT and DFS enhanced spectra with conventional spectra, a total of 8000 transients were collected for all non-spinning  $^{91}\text{Zr}$  NMR spectra and MAS spin-echo spectra, while 800 scans were collected for MAS QCPMG type experiments. The same parameters (including those for DFS and RAPT) were employed for spectra in this section as those mentioned above, except  $\tau_a$  was set to  $512 \mu\text{s}$  and 1 ms for static and MAS QCPMG spectra, respectively. For further background information on the combination of DFS and RAPT sequences with QCPMG pulse trains, refer to Reference [26] for further experimental details and a review of the literature.

In addition, a static Hahn echo spectrum of  $\text{Cp}_2\text{ZrCl}_2$  packed into a 4 mm o.d. Teflon tube was acquired on a Bruker DRX-500 NMR spectrometer (usually dedicated to solution NMR) with an 11.74 T ( $\nu_0(^1\text{H}) = 500 \text{ MHz}$ ) standard bore magnet operating at  $\nu_0(^{91}\text{Zr}) = 46.5 \text{ MHz}$  to aid in the extraction of  $^{91}\text{Zr}$  chemical shielding tensor parameters. A standard-bore double-resonance HX NMR probe with a Helmholtz coil was used for all experiments on the DRX-500. For experiments conducted at  $B_0 = 11.74 \text{ T}$ , a  $\pi/2$  pulse width of  $6 \mu\text{s}$ , rf field  $\nu_1 = 13.9 \text{ kHz}$  and spectral width of 100 kHz were employed with  $\tau_1$

and  $\tau_2$  set to 150  $\mu\text{s}$  and 40  $\mu\text{s}$ , respectively.

## 7.2.2 Spectral Simulations

Analytical simulations of  $^{91}\text{Zr}$  static and MAS NMR spectra were generated with the WSOLIDS software package.<sup>[33]</sup> Further refinement of these parameters was obtained via numerical simulations for QCPMG spectra with the SIMPSON software package.<sup>[34]</sup> SIMPSON simulations were accomplished by the *direct* method of powder averaging using 20 gamma angles and the *zcw4180* crystal file provided with the package. The start and detect operators were set to  $I_{1z}$  and  $I_{1c}$ , respectively, while all other parameters, including the inter-pulse acquisition period ( $1/\tau_a$ ), central transition selective pulse widths and inter-pulse delays were set equal to those employed experimentally. Simulated spectra were saved in ASCII format as free induction decay (FID) files without any mathematical manipulation and converted to files readable by the NUTS (Acorn NMR) software for further processing. Best-fit spectra were obtained by comparison of root mean square difference spectra and error bounds were determined through bidirectional variation of the NMR parameters.

Conventions used for the specification of electric field gradient (EFG) and chemical shift parameters differ between the WSOLIDS and SIMPSON simulation programs, and the reader is alerted to these differences. Whereas WSOLIDS uses the right-handed EFG and chemical shift tensors given by ( $|V_{zz}| \geq |V_{yy}| \geq |V_{xx}|$ ;  $C_Q = eV_{zz}Q/h$ ;  $\eta_Q = (V_{xx} - V_{yy})/V_{zz}$ ) and ( $\delta_{11} \geq \delta_{22} \geq \delta_{33}$ ;  $\Omega = \delta_{11} - \delta_{33}$ ;  $\kappa = 3(\delta_{22} - \delta_{iso})/\Omega$ ), respectively, the conventions employed in SIMPSON differ ( $|V_{zz}| \geq |V_{xx}| \geq |V_{yy}|$ ;  $C_Q = eV_{zz}Q/h$ ;  $\eta_Q = (V_{yy} -$

$V_{xx})/V_{zz}; |\delta_{zz} - \delta_{iso}| \geq |\delta_{xx} - \delta_{iso}| \geq |\delta_{yy} - \delta_{iso}|; \delta = \delta_{zz} - \delta_{iso}; \kappa = (\delta_{yy} - \delta_{xx})/\delta$ . In cases where the chemical shift and EFG tensors do not coincide, Euler angles are implemented to describe their relative orientation. One must be cautious in selecting Euler angles appropriate to the convention implemented within the simulation software. The WSOLIDS conventions are followed in the present work. Namely, the Euler angles  $\alpha$ ,  $\beta$  and  $\gamma$  are employed for unitary transformations in the order  $\mathbf{R}_z(\gamma)\mathbf{R}_y(\beta)\mathbf{R}_x(\alpha)$ ,<sup>[35, 36]</sup> where  $\mathbf{R}_i(\theta)$  performs a counter-clockwise (positive) rotation about the positive  $i$ -axis by angle  $\theta$ , producing a new rotation axis  $i'$ , such that a coordinate system initially coincident with the EFG principal axis system (PAS) ends up coincident with the chemical shift PAS after the transformation (i.e., an active transformation).

### 7.2.3 Theoretical calculations

Calculations of EFG and chemical shielding (CS) tensors were performed using Gaussian 98<sup>[37]</sup> on a Dell Precision 420 workstation with two 733 MHz Pentium III processors running Red Hat Linux 6.2. Molecular coordinates of  $\text{Cp}_2\text{ZrCl}_2$  used in calculations were obtained from crystal structure data resolved by X-ray diffraction.<sup>[38]</sup> Calculations of NMR interaction tensors of the fully optimized gas-phase geometry were also performed (see section C.5 of Appendix C), and poorer agreement with experimental data was obtained. Computations were carried out using restricted Hartree-Fock (RHF) and hybrid density functional theory (DFT) with the B3LYP functional.<sup>[39-41]</sup> The 6-31G\*\* and 6-311G\*\* basis sets were used for all nuclei except zirconium, for which expanded all-electron basis sets were applied [3F (33333/333/33), 3F (43222/422/33), 3F



(43333/433/43), 5F (33333/333/33), 5F(43222/422/33) and 5F (43333/433/43), designated respectively as 3F1, 3F2, 3F3, 5F1, 5F2 and 5F3].<sup>[42]</sup> Zirconium 3F and 5F basis sets differ in the occupation of valence orbitals: 3F and 5F represent the  $KLM4s^24p^64d^25s^2$  and  $KLM4s^24p^64d^35s^1$  ground state configurations, respectively. Chemical shielding tensors were calculated using the gauge-including atomic orbital (GIAO) method<sup>[43, 44]</sup> without taking relativistic effects into account. Calculated shielding data was referenced by setting the theoretical isotropic chemical shielding of  $Cp_2ZrCl_2$  to  $\delta_{iso} = 0.0$  ppm.

## 7.3 Results and Discussion

### 7.3.1 Solid-State $^{91}Zr$ NMR

Comparison of  $^{91}Zr$  DFS/Hahn echo and DFS/QCPMG NMR spectra of  $Cp_2ZrCl_2$  (Figure 7.1) in a stationary Teflon sample tube reveals that the QCPMG powder pattern is split into “spikelets” and possesses a significant signal enhancement. The acquisition times of the  $^{91}Zr$  DFS/Hahn echo (Figure 7.1a) and DFS/QCPMG NMR (Figures 7.1b, 7.1c) spectra were approximately 1925 and 197 minutes, respectively. The integrated intensity of a QCPMG spectrum can be compared to that of a standard spin echo spectrum by co-adding the echoes in the time domain and then performing a Fourier transform (Figure 7.1b) followed by powder pattern integration. Alternatively, one may also compare the signal to noise between the “spikelet” form of the QCPMG spectrum (Figure 7.1c) and the conventional Hahn echo spectrum, though variability in the

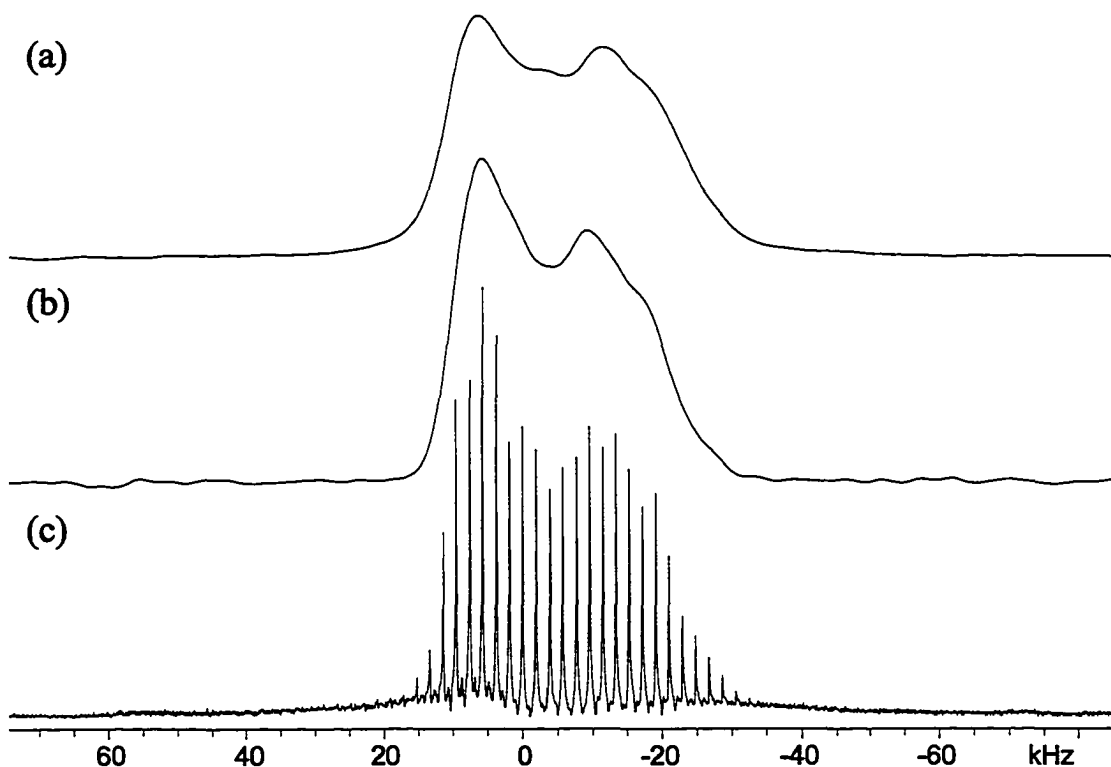


**Figure 7.1**  $^{91}\text{Zr}$  static NMR spectra of  $\text{Cp}_2\text{ZrCl}_2$  at 9.4 T: (a) DFS/Hahn echo spectrum (1925 minute acquisition time), (b) DFS/QCPMG spectrum, from Fourier transformation of co-added spin echoes and (c) DFS/QCPMG spectrum, from Fourier transformation of complete echo train (197 minute acquisition time).

properties of echo and QCPMG spectra make accurate numerical comparisons dubious.

The co-added echo spectrum has an integrated intensity of 1.1 compared to the normalized intensity of the echo spectrum (which is set to 1.0), and a higher signal-to-noise, despite the fact that 10 times less scans are acquired in the DFS/QCPMG experiment. The S/N gain in the spectrum obtained using the QCPMG pulse sequence originates from localization of all the intensity under sharp spikelets which arises from the repetitive collection of *numerous* spin echoes within a single experiment and subsequent Fourier transformation. The extent to which spin echoes can be acquired depends on the  $T_2$  relaxation time constant specific to the nuclei in the sample. The

magnitude of S/N enhancement also depends upon the spacing of spin echoes in the time domain, and consequently, the separation of the spikelets ( $1/\tau_a$ ) in the frequency domain after Fourier transformation of the FID. It is necessary to adjust  $1/\tau_a$  properly to attain the optimum signal intensity and S/N enhancement while retaining sufficient resolution to extract the desired NMR parameters. Comparison of the spectra in Figure 7.1 demonstrates that NMR parameters extractable from the conventional Hahn echo experiment could also be obtained from the envelope of a closely spaced QCPMG spectrum.

Static  $^{91}\text{Zr}$  QCPMG NMR experiments on  $\text{Cp}_2\text{ZrCl}_2$  in a standard 5 mm o.d. NMR rotor reveal a powder pattern similar to what is acquired for the sample in a Teflon tube. However, the spectrum is not as well-defined and displays portions of another broad powder pattern flanking the expected pattern. This additional powder pattern, which is characteristic of a very large quadrupolar coupling constant, arises from  $^{91}\text{Zr}$  nuclei in the rotor. A stepped-echo experiment (see section 7.2.1 for details) combined with QCPMG (Figure 7.2) was employed to record the full breadth of the  $^{91}\text{Zr}$  NMR powder pattern.<sup>[45]</sup> The individually acquired segments were Fourier transformed and summed together to produce the full powder pattern (see Appendix B, Figure B.6 for a comparison with the wideline spectrum resulting from a skyline projection of the individual pieces).

A comparison of the  $^{91}\text{Zr}$  QCPMG NMR spectra of  $\text{Cp}_2\text{ZrCl}_2$  in the  $\text{ZrO}_2$  rotor and in the Teflon sample tube, as well as a  $\text{ZrO}_2$  rotor containing an adamantane/KBr mixture is shown in Figure 7.3. Clearly, the background interference from the  $^{91}\text{Zr}$  nuclei in the rotor is substantial enough to warrant the use of a zirconium-free sample container or

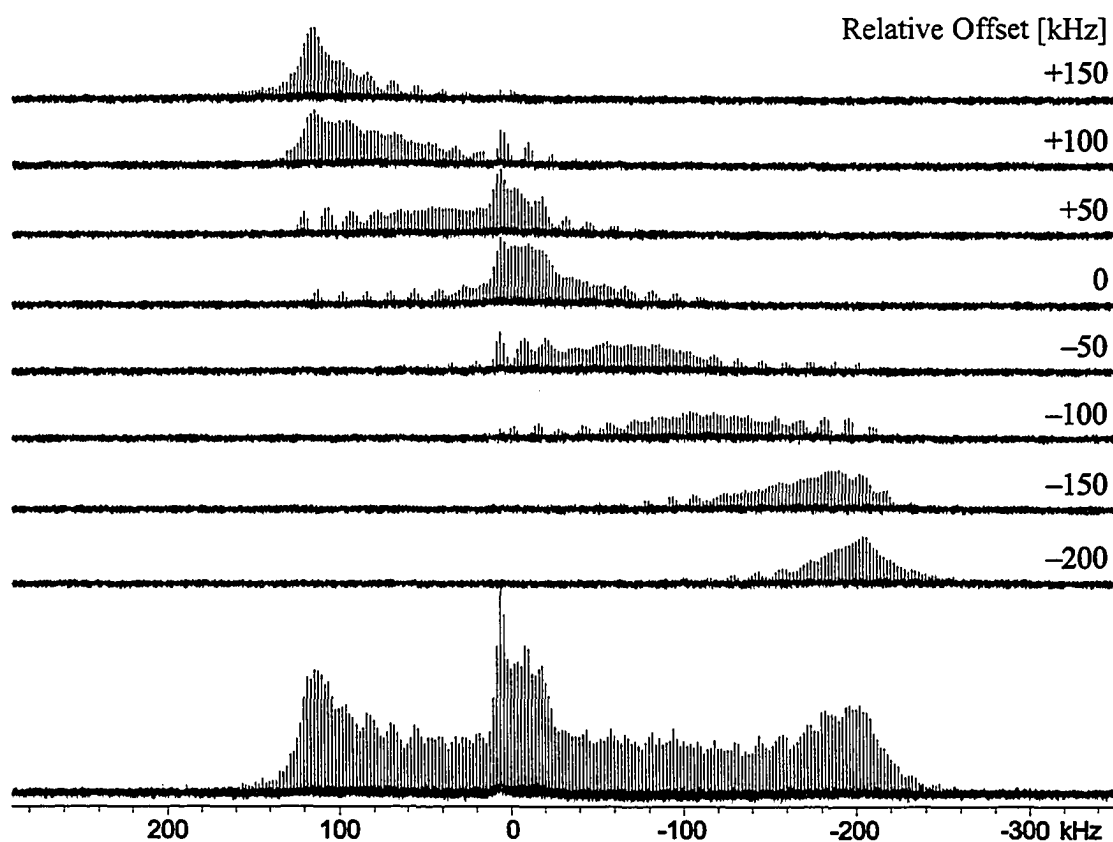


**Figure 7.2** Piecewise acquisition of the static  $^{91}\text{Zr}$  QCPMG NMR spectrum of  $\text{Cp}_2\text{ZrCl}_2$  packed inside a 5 mm o.d.  $\text{ZrO}_2$  rotor. Irradiation frequencies are offset by 50 kHz steps in order to acquire the complete powder pattern.

rotor for static NMR experiments, since accurate simulation of the  $^{91}\text{Zr}$  powder pattern is complicated by the presence of the broad underlying powder pattern. A simulation of  $^{91}\text{Zr}$  NMR powder patterns corresponding to a mixture of tetragonal and orthorhombic phases of zirconia (in an approximate 7:10 ratio) roughly approximates the shape of the rotor powder pattern. Simulations of the individual  $^{91}\text{Zr}$  NMR powder patterns for the tetragonal and orthorhombic phases are based on data for disordered zirconium oxide materials previously reported by Bastow and coworkers,<sup>141</sup> and neglect any effects of chemical shielding anisotropy.

It is of interest to determine whether  $\text{ZrO}_2$  rotors can be used for  $^{91}\text{Zr}$  MAS NMR

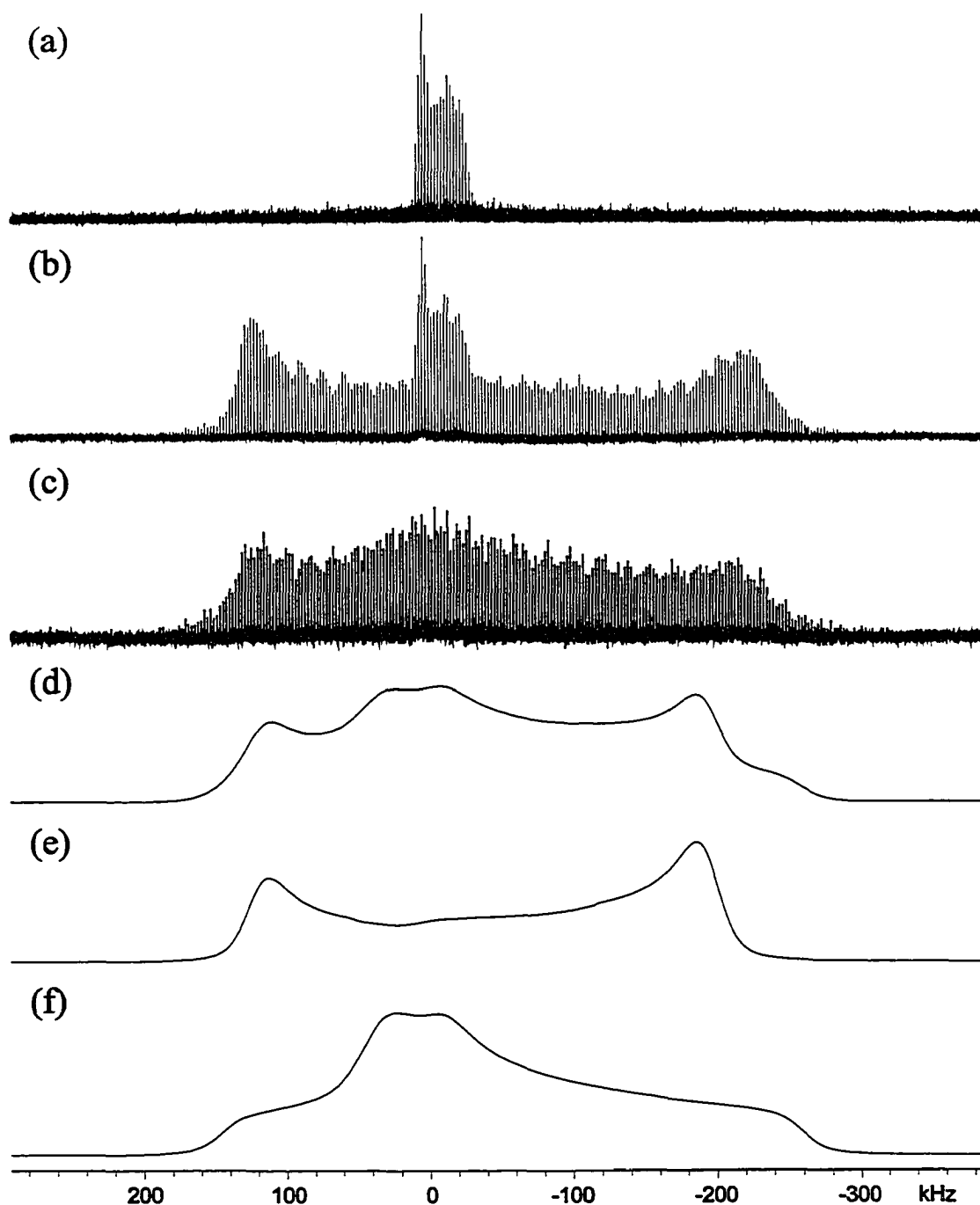


**Figure 7.3** Static  $^{91}\text{Zr}$  QCPMG NMR spectra of  $\text{Cp}_2\text{ZrCl}_2$  packed inside (a) a 5 mm o.d. Teflon tube and (b) a 5 mm o.d.  $\text{ZrO}_2$  rotor, and (c)  $^{91}\text{Zr}$  QCPMG spectrum of a  $\text{ZrO}_2$  rotor filled with adamantane and KBr (this latter sample is to get a measurement of the  $^{91}\text{Zr}$  NMR spectrum arising solely from the rotor). Simulated static  $^{91}\text{Zr}$  NMR powder patterns for (d) a 7:10 mixture of tetragonal and orthorhombic phases of zirconia, along with the sub-spectra for (e) the tetragonal phase ( $C_Q = 19.4$  MHz,  $\eta_Q = 0.0$ ,  $\delta_{\text{iso}} = 200$  ppm) and (f) the orthorhombic phase of zirconia ( $C_Q = 16.5$  MHz,  $\eta_Q = 0.85$ ,  $\delta_{\text{iso}} = 300$  ppm).

experiments, since they are the most reliable and readily available ceramic rotors currently used. An experimental  $^{91}\text{Zr}$  MAS RAPT/QCPMG NMR spectrum acquired at  $\nu_{\text{rot}} = 15$  kHz (Figure 7.4a), displays a single second-order quadrupolar pattern at  $\delta_{\text{iso}} = 25$  ppm. The difference in isotropic shifts between powdered  $\text{Cp}_2\text{ZrCl}_2$  and the same sample dissolved in  $\text{CH}_2\text{Cl}_2$  (i.e.,  $\delta_{\text{iso}} = 0.0$  ppm) can be attributed to solvent effects and/or crystal packing. The SIMPSON and MAS envelope simulations (Figures 7.4b, 7.4c) yield  $C_Q = 6.35$  MHz and  $\eta_Q = 0.3$ , which is comparable to some of the relatively smaller  $C_Q(^{91}\text{Zr})$ 's measured previously by Hartmann and Scheler in various zirconates.<sup>[15]</sup> There are actually two distinct  $\text{Cp}_2\text{ZrCl}_2$  molecules in the unit cell with magnetically non-equivalent  $^{91}\text{Zr}$  nuclei,<sup>[38]</sup> however, their structures are alike and values of  $C_Q$ ,  $\eta_Q$  and  $\delta_{\text{iso}}$  are expected to be very similar. This is evidenced by the apparent observation of a single type of  $^{91}\text{Zr}$  environment, as well as ab initio calculations of  $^{91}\text{Zr}$  NMR interaction tensors (see section C.4 of Appendix C and discussion of ab initio data below). The QCPMG pulse sequence gives rise to spectra in the form of spikelets which are offset from the irradiation frequency by  $1/\tau_a$ ; therefore, differentiation of nonequivalent sites by chemical shift is not possible unless gross differences (i.e., fairly distinct overlapping powder patterns) can be observed. Numerical simulations of the  $^{91}\text{Zr}$  MAS QCPMG NMR spectrum of the  $\text{ZrO}_2$  rotor were also conducted (not shown), revealing a complicated powder pattern composed of overlapping isotropic and spinning sidebands. The intensity of this spectrum is very low due to the comparatively large value of  $C_Q(^{91}\text{Zr})$  in  $\text{ZrO}_2$  and does not significantly interfere with the spectrum of  $\text{Cp}_2\text{ZrCl}_2$ . Nonetheless, a small influence on the  $^{91}\text{Zr}$  MAS QCPMG NMR spectrum of  $\text{Cp}_2\text{ZrCl}_2$  is observed, being specially pronounced in regions

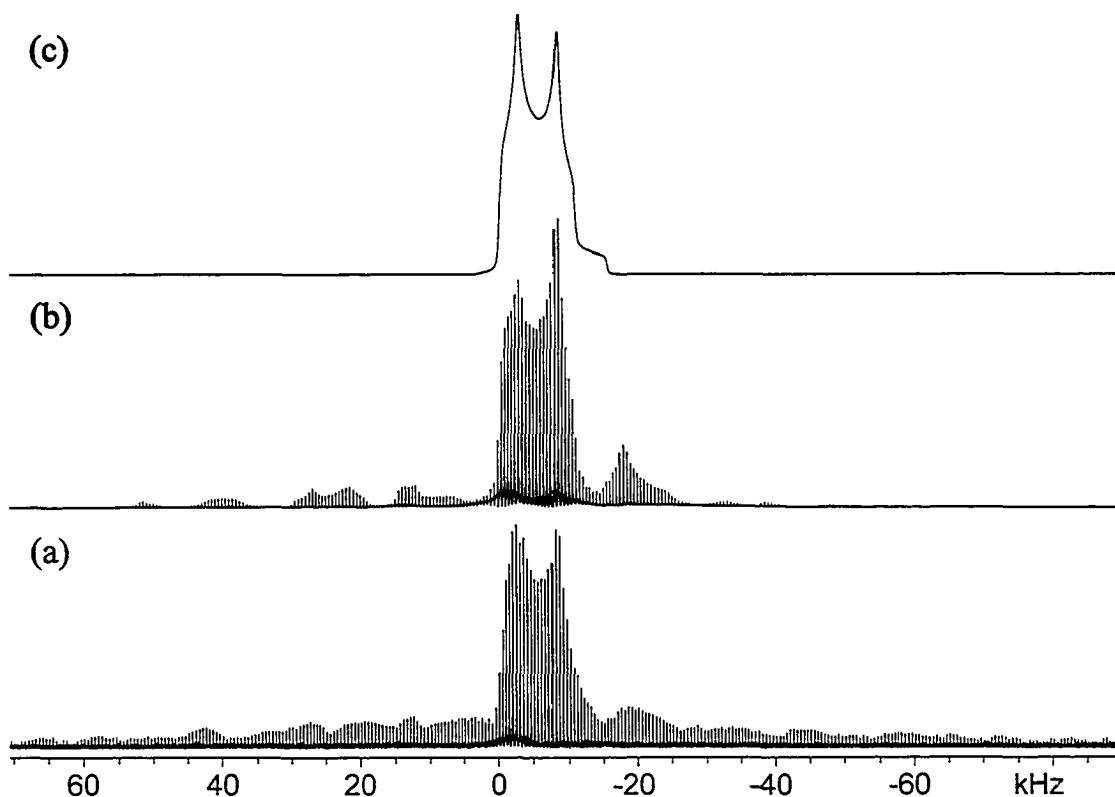


**Figure 7.4** (a) Experimental  $^{91}\text{Zr}$  MAS RAPT/QCPMG NMR spectrum of  $\text{Cp}_2\text{ZrCl}_2$  along with (b) numerical and (c) analytical simulations at 9.4 T.

between the spinning sidebands where “extra intensity” can be seen (Figure 7.4a).

Simulation of the  $\text{Cp}_2\text{ZrCl}_2$  static  $^{91}\text{Zr}$  NMR powder patterns acquired at magnetic fields of 9.4 T (Figure 7.5a, bottom trace) and 11.74 T (Figure 7.5b, bottom trace) reveal the presence of zirconium chemical shielding anisotropy (CSA). Spectral simulations employing only quadrupolar parameters and the isotropic chemical shift (obtained from analysis of MAS QCPMG NMR spectra), excluding the effects of CSA (Figure 7.5, top traces) yield patterns which do not match the appearance of experimentally recorded spectra. Simulations including CSA (Figure 7.5, middle traces) point to a non-axial zirconium chemical shielding tensor with the parameters  $\delta_{\text{iso}} = 25$  ppm,  $\Omega = 475$  ppm, and  $\kappa = -0.55$ , corresponding to the principal components  $\delta_{11} = 306$  ppm,  $\delta_{22} = -62$  ppm and

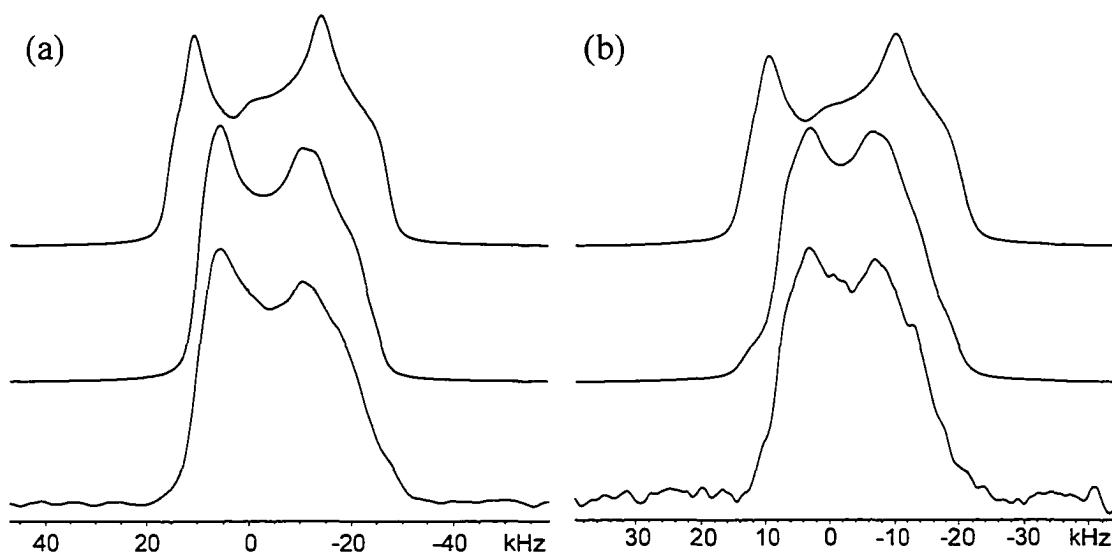


**Figure 7.5** Experimental (bottom trace)  $^{91}\text{Zr}$  static NMR spectra of  $\text{Cp}_2\text{ZrCl}_2$  along with simulations including (middle trace) and excluding (top trace) the effects of CSA at magnetic fields (a)  $B_0 = 9.4$  T and (b)  $B_0 = 11.74$  T.

$\delta_{33} = -169$  ppm. CSA parameters corresponding to spectra acquired at a lower field ( $B_0 = 9.4$  T) are taken as the primary values for discussion (Table 7.1) due to the higher S/N in these spectra resulting from larger sample volume and higher rf field. To the best of our knowledge, this is the only report of zirconium chemical shielding anisotropy to date. Due to the presence of relatively large quadrupole couplings in many zirconium compounds, it is often not possible to establish the presence of chemical shielding anisotropy without the use of two or more vastly different magnetic fields, unless its effects are quite pronounced. Even in the case presented here, the contribution of the second-order quadrupolar interaction to the overall breadth of the  $^{91}\text{Zr}$  powder pattern of  $\text{Cp}_2\text{ZrCl}_2$  is considerably larger than that of the chemical shielding anisotropy and a high degree of accuracy cannot be attained in the extraction of Zr CSA.

Simulations of the experimental static spectra reveal that the zirconium CS and EFG tensors are non-coincident – it is well known that the relative orientation of the CS



and EFG tensors have dramatic effects on the appearance of solid-state NMR powder patterns of half-integer quadrupolar nuclei.<sup>[46-48]</sup> For  $\text{Cp}_2\text{ZrCl}_2$ , the Euler angles describing the orientation of the CS tensor with respect to the EFG tensor are  $\alpha = 26^\circ$ ,  $\beta = 92^\circ$  and  $\gamma = 10^\circ$ . The relationships between these Euler angles and the orientation of the CS and EFG tensors with respect to the molecular frame are discussed later on.

**Table 7.1**  
Experimental  $^{91}\text{Zr}$  Chemical Shielding and Quadrupolar Parameters

Parameter	$\text{Cp}_2\text{ZrCl}_2$		$\text{ZrO}_2$ Rotor
Magnetic Field, $B_0$ [T]	9.4	11.74	9.4
$C_Q$ [MHz]	6.35(10)	6.35(10)	19.9(6)
$\eta_Q$	0.3(1)	0.3(1)	0.04(2)
$\delta_{\text{iso}}$ [ppm]	25	40	60(30)
$\Omega$ [ppm]	475	430	—
$\kappa$	-0.55	-0.50	—
$\delta_{11}$ [ppm]	306	291	—
$\delta_{22}$ [ppm]	-62	-32	—
$\delta_{33}$ [ppm]	-169	-139	—
$\alpha$ [ $^\circ$ ]	26	31	—
$\beta$ [ $^\circ$ ]	92	89	—
$\gamma$ [ $^\circ$ ]	10	11	—

### 7.3.2 Comparing Signal Enhancement Pulse Techniques

The use of amplitude-modulated double frequency sweeps (DFS) for signal enhancement of the central transition by population inversion (e.g., of the  $\pm 1/2$  and  $\pm 3/2$  levels of spin  $3/2$  nuclei) has been known for approximately a decade.<sup>[28, 49]</sup> In particular, it has been found that setting an adequate DFS rate and finishing frequency ( $\nu_f$ ) are of paramount importance for sweeps to be effective. An adiabaticity parameter,  $A$ , is often

quoted in order to characterize the efficiency of the DFS population inversion.<sup>[25]</sup>

Another scheme for signal enhancement of the central transition is rotor assisted population transfer (RAPT), which takes advantage of polarization transfer during sample spinning, has also been developed.<sup>[24, 50]</sup> The RAPT pulse sequence saturates all the nuclear spin levels of the same sign yielding a theoretical signal enhancement of  $I + \frac{1}{2}$ , where  $I$  is the nuclear spin. Both techniques mentioned above have recently been combined with QCPMG to yield an even greater enhancement in overall signal;<sup>[26]</sup> their performance is briefly examined below for the case of  $\text{Cp}_2\text{ZrCl}_2$ .

Static  $^{91}\text{Zr}$  Hahn echo, DFS/Hahn echo, QCPMG and DFS/QCPMG NMR spectra are shown in Figure 7.6a. The QCPMG pulse sequence alone increases the signal intensity by a factor of 9.1 compared to the conventional Hahn echo experiment (normalized integrated intensity of 1.0). The DFS preparation sequence yields enhancements of 2.7 and 2.9 in integrated intensity for echo and QCPMG experiments, respectively. Overall, the DFS/QCPMG sequence provides an enhancement of 26.7 with respect to the Hahn echo experiment. The theoretical signal enhancement achievable by DFS is  $2I$ , which for the case of  $^{91}\text{Zr}$  ( $I = 5/2$ ) should be 5. However, due to the distribution of crystallite orientations in powder samples which results in varying magnitudes of  $C_Q$ , only an enhancement of ca. 3 is expected.<sup>[51]</sup>

$^{91}\text{Zr}$  MAS NMR spectra are shown in Figure 7.6b. It is important to note that MAS QCPMG experiments were recorded with 10 times fewer transients than their echo counterparts, yet comparison of Hahn echo and QCPMG spectra shows that the latter possesses three times greater S/N! Both the RAPT and DFS preparatory sequences give a

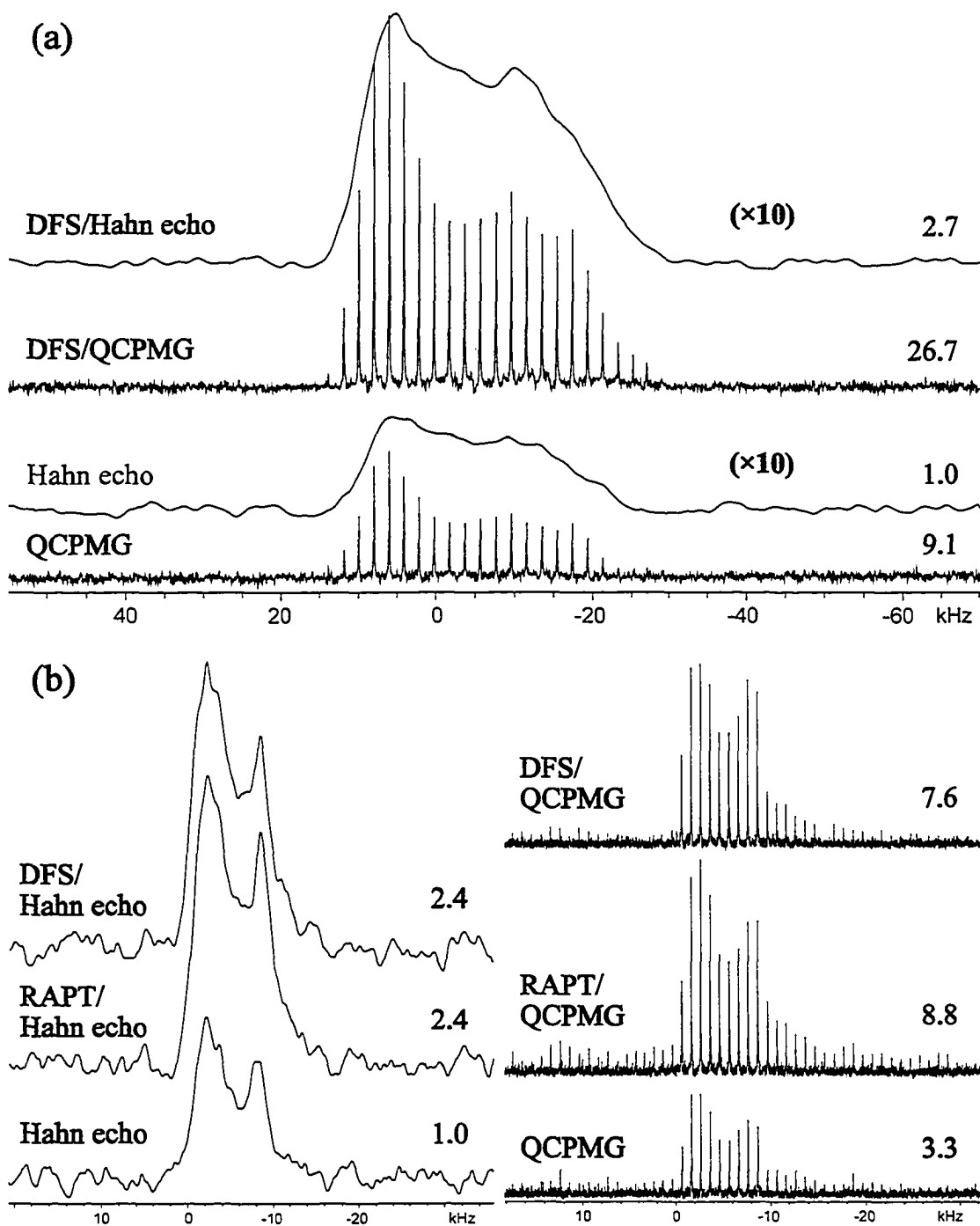


**Figure 7.6** (a) Static  $^{91}\text{Zr}$  Hahn echo and DFS/Hahn echo NMR spectra of  $\text{Cp}_2\text{ZrCl}_2$  and corresponding QCPMG experiments (same number of transients recorded in each case). The vertical scales of echo spectra are augmented by a factor of 10. (b)  $^{91}\text{Zr}$  MAS Hahn echo, RAPT/Hahn echo, DFS/Hahn echo and corresponding QCPMG NMR spectra of  $\text{Cp}_2\text{ZrCl}_2$ . MAS QCPMG experiments were acquired with 10 times less scans than their spin-echo counterparts. Integrated intensities with respect to the static and MAS  $^{91}\text{Zr}$  Hahn echo experiments are located to the right of each spectrum.

signal enhancement of 2.4 compared to the Hahn echo experiment, while enhancements of 2.7 and 2.3 are observed respectively for corresponding QCPMG experiments. The poor S/N and severe distortions seen in MAS spectra are caused by the  $^{91}\text{Zr}$  NMR signal of the rotor, which also accounts for the large number of spikelets on the baseline surrounding the powder pattern of MAS QCPMG experiments. The combination of DFS or RAPT with QCPMG leads to spectra with considerably higher S/N (or integrated intensity in the case of co-added echoes), meaning greatly reduced experimental times.

### 7.3.3 Theoretical Calculations

Experimental and theoretical zirconium chemical shielding tensors are shown in Table 7.2, where theoretical shielding values have been converted to chemical shifts as described in the section 7.2.3. Agreement between experimental and theoretical shielding tensors improve as larger zirconium basis sets (3F1 – 3F3 and 5F1 – 5F3) are employed. Changing the basis set on all of the other atoms results in significant changes in the zirconium CS tensors for many of the calculations, except those using the 3F3 and 5F3 Zr basis sets. In particular, relatively accurate calculations of the span ( $\Omega = 475$  ppm) and asymmetry parameter ( $\kappa = -0.55$ ) of the zirconium chemical shielding tensor only occur for calculations employing zirconium F3 basis sets, with 5F3 consistently giving the best agreement with experiment. Compared to RHF, most B3LYP calculations yield higher values of  $\Omega$  and  $\kappa$ , and consistently afford much better agreement with experimental data.

**Table 7.2**  
Calculated Zirconium Chemical Shielding Tensors for Cp<sub>2</sub>ZrCl<sub>2</sub>

Source	$\delta_{11}$ [ppm]	$\delta_{22}$ [ppm]	$\delta_{33}$ [ppm]	$\delta_{iso}$ [ppm]	$\Omega$ [ppm]	$\kappa$
<b>Experimental</b>						
B <sub>0</sub> = 9.4 T	306	-62	-169	25	475	-0.55
B <sub>0</sub> = 11.74 T	291	-32	-139	40	430	-0.50
<b>RHF/6-31G**</b>						
3F (33333/333/33)	30.9	25.7	-56.6	0.0	87.5	0.88
3F (43222/422/33)	27.9	20.5	-48.4	0.0	76.3	0.80
3F (43333/433/43)	166.3	-33.6	-132.8	0.0	299.1	-0.34
5F (33333/333/33)	61.5	9.1	-70.5	0.0	132.0	0.21
5F (43222/422/33)	49.3	11.8	-61.0	0.0	110.3	0.32
5F (43333/433/43)	201.5	-51.1	-150.4	0.0	351.9	-0.44
<b>RHF/6-311G**</b>						
3F (33333/333/33)	38.3	8.8	-47.0	0.0	85.3	0.31
3F (43222/422/33)	32.8	8.2	-41.1	0.0	73.9	0.34
3F (43333/433/43)	160.0	-31.8	-128.2	0.0	288.2	-0.33
5F (33333/333/33)	20.6	20.1	-40.7	0.0	61.3	0.98
5F (43222/422/33)	26.7	16.2	-42.9	0.0	69.6	0.70
5F (43333/433/43)	204.4	-42.6	-161.8	0.0	366.1	-0.35
<b>DFT(B3LYP)/6-31G**</b>						
3F (33333/333/33)	94.9	2.1	-97.1	0.0	192.0	0.03
3F (43222/422/33)	81.0	5.3	-86.3	0.0	167.2	0.10
3F (43333/433/43)	236.6	-58.3	-178.3	0.0	414.9	-0.42
5F (33333/333/33)	120.2	-13.5	-106.8	0.0	227.0	-0.18
5F (43222/422/33)	105.9	-9.8	-96.2	0.0	202.1	-0.15
5F (43333/433/43)	263.3	-74.5	-188.9	0.0	452.2	-0.49
<b>DFT(B3LYP)/6-311G**</b>						
3F (33333/333/33)	34.5	9.0	-43.4	0.0	77.9	0.35
3F (43222/422/33)	35.1	7.1	-42.1	0.0	77.2	0.28
3F (43333/433/43)	213.1	-63.2	-149.9	0.0	363.0	-0.52
5F (33333/333/33)	59.1	-2.7	-56.4	0.0	115.5	-0.07
5F (43222/422/33)	63.8	-5.4	-58.3	0.0	122.1	-0.13
5F (43333/433/43)	246.2	-69.7	-176.5	0.0	422.8	-0.50

**Table 7.3**  
Theoretical Zirconium Quadrupolar Parameters in Cp<sub>2</sub>ZrCl<sub>2</sub>

Source	$V_{11}$ [a.u.]	$V_{22}$ [a.u.]	$V_{33}$ [a.u.]	$ C_Q $ [MHz]	$\eta_Q$
<b>Experimental<sup>[a]</sup></b>	0.0537	0.0998	-0.1536	6.35(10)	0.3(1)
RHF/6-31G**					
3F (33333/333/33)	0.1223	0.2480	-0.3703	15.31	0.34
3F (43222/422/33)	0.0996	0.2312	-0.3308	13.68	0.40
3F (43333/433/43)	0.0695	0.1129	-0.1824	7.54	0.24
5F (33333/333/33)	0.1266	0.2171	-0.3437	14.21	0.26
5F (43222/422/33)	0.1012	0.1989	-0.3001	12.41	0.33
5F (43333/433/43)	0.0494	0.1015	-0.1509	6.24	0.34
RHF/6-311G**					
3F (33333/333/33)	0.2205	0.4953	-0.7158	29.60	0.38
3F (43222/422/33)	0.1917	0.4223	-0.6140	25.39	0.38
3F (43333/433/43)	0.0954	0.1824	-0.2778	11.49	0.31
5F (33333/333/33)	0.2080	0.4091	-0.6181	25.52	0.33
5F (43222/422/33)	0.1741	0.3292	-0.5033	20.81	0.31
5F (43333/433/43)	0.0634	0.1056	-0.1690	6.99	0.25
DFT(B3LYP)/6-31G**					
3F (33333/333/33)	0.1593	0.2995	-0.4588	18.97	0.31
3F (43222/422/33)	0.1375	0.2827	-0.4201	17.37	0.35
3F (43333/433/43)	0.1130	0.1597	-0.2726	11.27	0.17
5F (33333/333/33)	0.1624	0.2639	-0.4263	17.63	0.24
5F (43222/422/33)	0.1382	0.2448	-0.3829	15.84	0.28
5F (43333/433/43)	0.0936	0.1395	-0.2331	9.64	0.20
DFT(B3LYP)/6-311G**					
3F (33333/333/33)	0.2987	0.6140	-0.9127	37.74	0.35
3F (43222/422/33)	0.2725	0.5378	-0.8103	33.51	0.33
3F (43333/433/43)	0.1764	0.3042	-0.4806	19.87	0.27
5F (33333/333/33)	0.2849	0.5181	-0.8030	33.21	0.29
5F (43222/422/33)	0.2531	0.4341	-0.6872	28.42	0.26
5F (43333/433/43)	0.1458	0.2122	-0.3580	14.81	0.19

<sup>[a]</sup> The sign (+/-) and significant figures of experimental EFG tensor components ( $V_{11}$ ,  $V_{22}$  and  $V_{33}$ ) are set according to most proximate theoretical values for comparison.

Theoretical  $^{91}\text{Zr}$  EFG tensors in  $\text{Cp}_2\text{ZrCl}_2$  are presented in Table 7.3. In stark contrast to the calculated chemical shielding tensors, the majority of calculations overestimate the magnitude of the quadrupolar coupling constant (as do the EFG tensor calculations of Buhl et al.),<sup>[11]</sup> though better agreement with experimental data is seen for the EFG tensor asymmetry parameter  $\eta_Q = 0.3$ . In particular, upon employing larger basis sets (3F3 and 5F3) on zirconium, correlation between theoretical and experimental ( $C_Q = 6.35$  MHz) zirconium quadrupole coupling constants improve, whereas values for  $\eta_Q$  stay in close agreement for all cases. The opposite is seen when a larger basis set (6-311G\*\*) is used for Cl, C and H atoms:  $C_Q$  values are larger and further away from the experimental compared to values calculated with the smaller basis set (6-31G\*\*). Notably, calculations employing zirconium F3 basis sets invariably result in better correlation with experimental values regardless of the method employed, in agreement with observations gathered from the calculation of zirconium chemical shielding. In the case of  $\text{Cp}_2\text{ZrCl}_2$ , the zirconium 5F3 basis set gives best results and RHF calculations are superior for predicting zirconium EFG parameters.

Experimental powder pattern simulations yield a  $^{91}\text{Zr}$  CS tensor asymmetry parameter  $\kappa = -0.55$  indicating that  $\sigma_{22}$  and  $\sigma_{33}$  are relatively similar in magnitude compared to  $\sigma_{11}$ , which is in good agreement with theory. Thus,  $\sigma_{11}$  should be oriented towards a distinct electronic environment compared to  $\sigma_{22}$  and  $\sigma_{33}$ . Ab initio calculations (B3LYP/{6-31G\*\*(Cl, C, H)|5F3(Zr)}) resulting in best agreement with experimental data predict a zirconium CS tensor (Figure 7.7a) where:  $\sigma_{11}$  is oriented perpendicular to the plane formed by zirconium and the two chlorine atoms (hereafter referred to as the Cl-

Zr-Cl plane),  $\sigma_{22}$  approximately bisects the Cl-Zr-Cl angle, and  $\sigma_{33}$  lies in the Cl-Zr-Cl plane making a  $\sigma_{33}$ -Zr-Cl angle of about  $37^\circ$  with the nearest chlorine atom. With the exception of RHF calculations using basis sets {6-31G\*\*|3F2}, {6-311G\*\*|3F1} and {6-311G\*\*|3F2}, all remaining calculations (RHF and B3LYP) yield the  $^{91}\text{Zr}$  CS tensor orientation described above.

Experimental powder pattern simulations reveal a nearly axial  $^{91}\text{Zr}$  EFG tensor ( $\eta_Q = 0.3$ ) indicating that  $V_{11}$  and  $V_{22}$  are similar in magnitude; accordingly,  $V_{11}$  and  $V_{22}$  must be oriented in directions of similar electronic environments (i.e., similar electric field gradients). Although most theoretical values of the  $^{91}\text{Zr}$  nuclear quadrupole coupling constant are not in agreement with the experimental  $C_Q$  of 6.35 MHz, all calculations

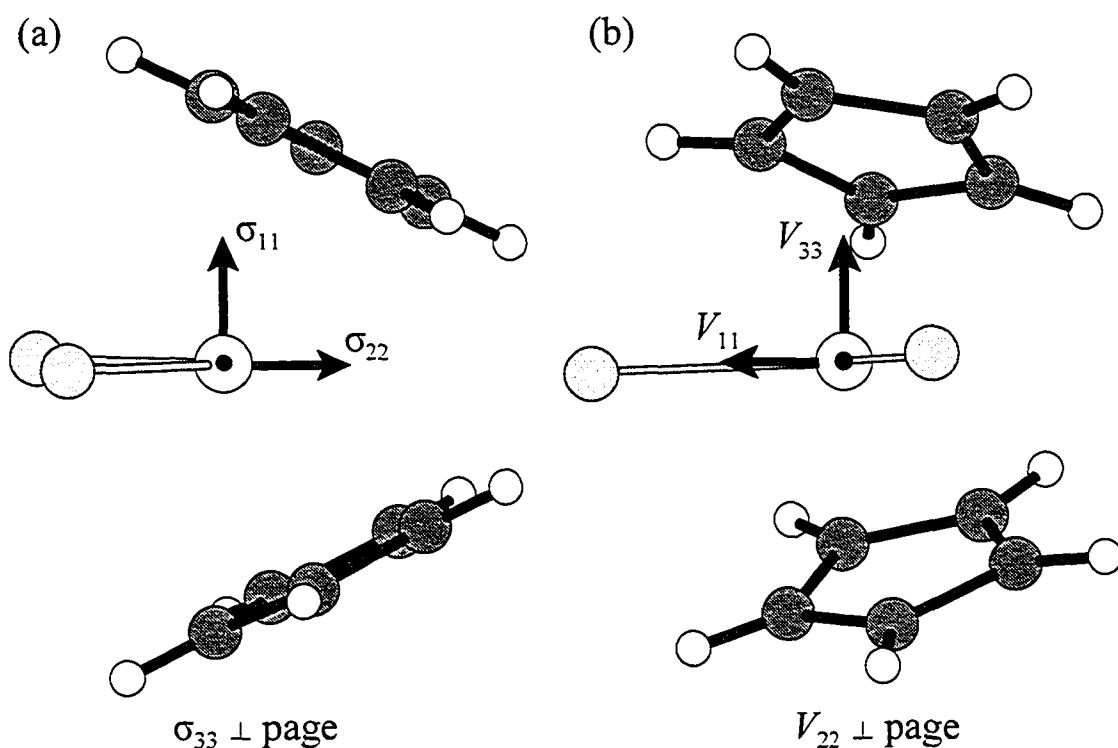


**Figure 7.7** (a) Relative orientation of the zirconium CS tensor with respect to the theoretical  $^{91}\text{Zr}$  EFG tensor obtained using experimentally measured Euler angles. (b)  $^{91}\text{Zr}$  EFG tensor orientation within the molecular frame from calculations yielding best agreement with experimental values.



yield very similar zirconium EFG tensor orientations.  $^{91}\text{Zr}$  EFG tensors are calculated to have  $V_{33}$  oriented approximately perpendicular to the Cl-Zr-Cl plane. For the calculation which results in best agreement between theoretical and experimental EFG tensor parameters (RHF/{6-31G\*\*(Cl,C,H)|5F3(Zr)}),  $V_{11}$  and  $V_{22}$  lie approximately in the Cl-Zr-Cl plane (Cl-Zr-Cl angle:  $97^\circ$ ) making  $V_{ii}$ -Zr-Cl angles with nearest chlorine atoms of approximately  $13^\circ$  and  $19^\circ$ , respectively. All other calculations orient the zirconium EFG tensor in a similar fashion differing only in the  $V_{11}$ -Zr-Cl (range:  $13^\circ$  to  $-45^\circ$ ) and  $V_{22}$ -Zr-Cl (range:  $19^\circ$  to  $-39^\circ$ ) angles. Following the conventions set out earlier, the  $^{91}\text{Zr}$  EFG tensor is taken as the reference frame in order to deduce the orientation of the experimental CS tensor. The experimental zirconium CS tensor defined by Euler angles  $\alpha = 26^\circ$ ,  $\beta = 92^\circ$  and  $\gamma = 10^\circ$  (Figure 7.7b) directs  $\sigma_{11}$ ,  $\sigma_{22}$  and  $\sigma_{33}$  in the same general directions as in the theoretically determined CS tensor, displaying only very slight deviations (Euler angles determined from theoretical calculations:  $\alpha = 24.55^\circ$ ,  $\beta = 96.25^\circ$  and  $\gamma = 0.43^\circ$ ). The remarkable agreement between the theoretical and experimental Euler angles ascertains the reliability of the CS and EFG tensor orientations determined herein. However, in order to unambiguously determine the orientation of the NMR interaction tensors with respect to the molecular frame,  $^{91}\text{Zr}$  single-crystal NMR experiments on  $\text{Cp}_2\text{ZrCl}_2$  would have to be performed. Much difficulty remains in producing accurate theoretical EFG parameters, which can be remedied in part by employing extended all-electron basis sets as seen for calculations with the 3F3 and 5F3 Zr basis sets. However, much work still remains in determining the optimal method and basis sets most suitable for calculation of  $^{91}\text{Zr}$  NMR properties.

## 7.4 Conclusion

The use of recently developed signal-enhancement schemes, such as DFS/QCPMG, RAPT/QCPMG and piecewise wideline QCPMG, for the acquisition of  $^{91}\text{Zr}$  NMR spectra permits the study of an organometallic system with a moderate quadrupolar interaction,  $\text{Cp}_2\text{ZrCl}_2$ , as well as an inorganic material with a large quadrupolar interaction, a ceramic zirconium oxide NMR rotor. Experiments on samples contained within ceramic zirconium oxide rotors (the most common type of NMR rotor material available) indicate that static NMR experiments should be conducted with sample containers comprised of other materials due to the background  $^{91}\text{Zr}$  rotor signal. On the other hand, MAS NMR experiments, which can only be conducted on samples with small to moderate values of  $C_Q(^{91}\text{Zr})$ , are still feasible (background interference is minimal if the central transition signal is narrow enough to perform MAS NMR experiments). The performance of the RAPT/ and DFS/QCPMG pulse sequences on  $^{91}\text{Zr}$  nuclei demonstrate that a signal enhancement of an order of magnitude or more compared to the conventional spin-echo can be attained, which can greatly facilitate the study of Zr-containing inorganic and organometallic compounds. Such techniques will be invaluable for the investigation of Zr-containing compounds important in heterogeneous and homogeneous catalysis, as well as countless other materials containing unresponsive non-integer quadrupolar nuclei.

The anisotropic zirconium chemical shielding and quadrupolar interactions in  $\text{Cp}_2\text{ZrCl}_2$  have been characterized by  $^{91}\text{Zr}$  solid-state NMR experiments and quantum mechanical calculations of NMR interaction tensors. Analytical and numerical lineshape

simulations reveal the first reported experimental evidence for  $^{91}\text{Zr}$  chemical shielding anisotropy. Theoretical zirconium chemical shielding and electric field gradient tensors from RHF and hybrid DFT (B3LYP) calculations are in reasonable agreement with experimental values, with best agreement between theory and experiment arising for calculations which use large basis sets (3F3 and 5F3) for zirconium and a relatively small basis set (6-31G\*\*) on all other atoms. Experimental  $^{91}\text{Zr}$  CS and EFG tensor orientations are elucidated from theoretical calculations and found to relate consistently with experimentally obtained data on relative tensor orientations. Further experimental determinations of NMR interaction tensors and corresponding ab initio calculations are clearly necessary to determine which theoretical methods and basis sets are appropriate for conducting calculations on zirconium-containing organometallic complexes.

# Bibliography

- [1] V. Kello, P. Pyykko, A. J. Sadlej, P. Schwerdtfeger, J. Thyssen, *Chemical Physics Letters* **2000**, *318*, 222.
- [2] Y. Yamada, K. Ohira, *Journal of the Physical Society of Japan* **1983**, *52*, 3646.
- [3] T. J. Bastow, *Journal of Physics-Condensed Matter* **1990**, *2*, 6327.
- [4] J. J. Fitzgerald, S. S. Han, S. F. Dec, M. F. Davis, C. E. Bronnimann, G. E. Maciel, *NIST Special Publication* **1991**, *804*, 173.
- [5] S. F. Dec, M. F. Davis, G. E. Maciel, C. E. Bronnimann, J. J. Fitzgerald, S. S. Han, *Inorganic Chemistry* **1993**, *32*, 955.
- [6] J. S. Hartman, F. P. Koffyberg, J. A. Ripmeester, *Journal of Magnetic Resonance* **1991**, *91*, 400.
- [7] T. J. Bastow, M. E. Hobday, M. E. Smith, H. J. Whitfield, *Solid State Nuclear Magnetic Resonance* **1994**, *3*, 49.
- [8] T. J. Bastow, M. E. Hobday, M. E. Smith, H. J. Whitfield, *Solid State Nuclear Magnetic Resonance* **1996**, *5*, 293.
- [9] T. J. Bastow, C. T. Forwood, M. A. Gibson, M. E. Smith, *Physical Review B: Condensed Matter and Materials Physics* **1998**, *58*, 2988.
- [10] R. Benn, A. Rufinska, *Journal of Organometallic Chemistry* **1984**, *273*, C51.
- [11] M. Buhl, G. Hopp, W. von Philipsborn, S. Beck, M. H. Prosenc, U. Rief, H. H. Brintzinger, *Organometallics* **1996**, *15*, 778.
- [12] C. Janiak, K. C. H. Lange, U. Versteeg, D. Lentz, P. H. M. Budzelaar, *Chemische*

*Berichte-Recueil* **1996**, *129*, 1517.

[13] A. C. Kunwar, G. L. Turner, E. Oldfield, *Journal of Magnetic Resonance* **1986**, *69*, 124.

[14] T. J. Bastow, M. E. Smith, S. N. Stuart, *Chemical Physics Letters* **1992**, *191*, 125.

[15] P. Hartmann, G. Scheler, *Zeitschrift Fur Naturforschung Section A-A Journal of Physical Sciences* **1995**, *50*, 90.

[16] A. S. Lipton, J. A. Sears, P. D. Ellis, *Journal of Magnetic Resonance* **2001**, *151*, 48.

[17] M. E. Smith, in *Annual Reports on NMR Spectroscopy, Vol. 43*, **2001**, pp. 121.

[18] F. H. Larsen, H. J. Jakobsen, P. D. Ellis, N. C. Nielsen, *Journal of Physical Chemistry A* **1997**, *101*, 8597.

[19] F. H. Larsen, J. Skibsted, H. J. Jakobsen, N. C. Nielsen, *Journal of the American Chemical Society* **2000**, *122*, 7080.

[20] F. H. Larsen, A. S. Lipton, H. J. Jakobsen, N. C. Nielsen, P. D. Ellis, *Journal of the American Chemical Society* **1999**, *121*, 3783.

[21] A. S. Lipton, G. W. Buchko, J. A. Sears, M. A. Kennedy, P. D. Ellis, *Journal of the American Chemical Society* **2001**, *123*, 992.

[22] F. H. Larsen, H. J. Jakobsen, P. D. Ellis, N. C. Nielsen, *Journal of Magnetic Resonance* **1998**, *131*, 144.

[23] F. H. Larsen, N. C. Nielsen, *Journal of Physical Chemistry A* **1999**, *103*, 10825.

[24] Z. Yao, H. T. Kwak, D. Sakellariou, L. Emsley, P. J. Grandinetti, *Chemical Physics Letters* **2000**, *327*, 85.

[25] A. P. M. Kentgens, R. Verhagen, *Chemical Physics Letters* **1999**, *300*, 435.

- [26] R. W. Schurko, I. Hung, C. M. Widdifield, *Chemical Physics Letters* **2003**, 379, 1.
- [27] S. Mortara, D. Fregonese, S. Bresadola, R. Boaretto, S. Sostero, *Journal of Polymer Science Part a-Polymer Chemistry* **2001**, 39, 4243.
- [28] E. Van Veenendaal, B. H. Meier, A. P. M. Kentgens, *Molecular Physics* **1998**, 93, 195.
- [29] A. Medek, V. Frydman, L. Frydman, *Journal of Physical Chemistry A* **1999**, 103, 4830.
- [30] P. L. Bryant, L. G. Butler, A. P. Reyes, P. Kuhns, *Solid State Nuclear Magnetic Resonance* **2000**, 16, 63.
- [31] R. W. Schurko, S. Wi, L. Frydman, *Journal of Physical Chemistry A* **2002**, 106, 51.
- [32] P. K. Madhu, K. J. Pike, R. Dupree, M. H. Levitt, M. E. Smith, *Chemical Physics Letters* **2003**, 367, 150.
- [33] K. Eichele, R. E. Wasylshen, WSOLIDS, v.1.17.28 - Software for simulations of solid state NMR powder patterns, Dalhousie University, Dalhousie, **2000**.
- [34] M. Bak, J. T. Rasmussen, N. C. Nielsen, *Journal of Magnetic Resonance* **2000**, 147, 296.
- [35] M. Mehring, *Principles of High Resolution NMR in Solids*, Springer-Verlag, New York, **1983**.
- [36] R. N. Zare, *Angular Momentum: Understanding Spatial Aspects in Chemistry and Physics*, John Wiley & Sons, Inc., Toronto, **1988**.
- [37] M. J. Frisch, G. W. Trucks, H. B. Schlegel, G. E. Scuseria, M. A. Robb, J. R. Cheeseman, V. G. Zakrzewski, J. Montgomery, J. A., R. E. Stratmann, J. C. Burant, S.

Dapprich, J. M. Millam, A. D. Daniels, K. N. Kudin, M. C. Strain, O. Farkas, J. Tomasi, V. Barone, M. Cossi, R. Cammi, B. Mennucci, C. Pomelli, C. Adamo, S. Clifford, J. Ochterski, G. A. Petersson, P. Y. Ayala, Q. Cui, K. Morokuma, D. K. Malick, A. D. Rabuck, K. Raghavachari, J. B. Foresman, J. Cioslowski, J. V. Ortiz, A. G. Baboul, B. B. Stefanov, G. Liu, A. Liashenko, P. Piskorz, I. Komaromi, R. Gomperts, R. L. Martin, D. J. Fox, T. Keith, M. A. Al-Laham, C. Y. Peng, A. Nanayakkara, M. Challacombe, P. M. W. Gill, B. Johnson, W. Chen, M. W. Wong, J. L. Andres, C. Gonzalez, M. Head-Gordon, E. S. Replogle, J. A. Pople, Gaussian 98, Revision A.9. Gaussian, Inc., Pittsburgh, PA, **1998**.

[38] T. Repo, M. Klinga, L. Mutikainen, Y. Su, M. Leskela, M. Polamo, *Acta Chemica Scandinavica* **1996**, *50*, 1116.

[39] A. D. Becke, *Physical Review A* **1988**, *38*, 3098.

[40] A. D. Becke, *Journal of Chemical Physics* **1993**, *98*, 5648.

[41] C. Lee, W. Yang, R. G. Parr, *Physical Review B* **1988**, *37*, 785.

[42] S. Huzinaga (Ed.), Elsevier, New York, **1984**.

[43] R. Ditchfield, *Molecular Physics* **1974**, *27*, 789.

[44] K. Wolinski, J. F. Hinton, P. Pulay, *Journal of the American Chemical Society* **1990**, *112*, 8251.

[45] A. S. Lipton, T. A. Wright, M. K. Bowman, D. L. Reger, P. D. Ellis, *Journal of the American Chemical Society* **2002**, *124*, 5850.

[46] J. F. Baugher, P. C. Taylor, T. Oja, P. J. Bray, *Journal of Chemical Physics* **1969**, *50*, 4914.

- [47] W. P. Power, R. E. Wasylshen, S. Mooibroek, B. A. Pettitt, W. Danchura, *Journal of Physical Chemistry* **1990**, *94*, 591.
- [48] J. T. Cheng, J. C. Edwards, P. D. Ellis, *Journal of Physical Chemistry* **1990**, *94*, 553.
- [49] J. Haase, M. S. Conradi, *Chemical Physics Letters* **1993**, *209*, 287.
- [50] P. K. Madhu, A. Goldbourn, L. Frydman, S. Vega, *Chemical Physics Letters* **1999**, *307*, 41.
- [51] D. Iuga, H. Schafer, R. Verhagen, A. P. M. Kentgens, *Journal of Magnetic Resonance* **2000**, *147*, 192.



# Chapter 8

## Ongoing Research: Towards the Study of Zirconocenes Immobilized on Solid Support Materials via Solid-State $^{91}\text{Zr}$ NMR

### 8.1 Introduction

Group 4 metallocenes comprise one of the largest and most versatile class of olefin polymerization catalysts available today; this can largely be attributed to the favorable electronic properties of the metal centers. For group 4 metallocenes, it is generally accepted that the active catalytic species is a coordinatively unsaturated cationic system with  $d^0$  configuration (i.e., oxidation state IV). This characteristic is believed to be of paramount importance in polymerization processes because it prevents stabilization of metal–olefin adducts caused by back-bonding from the metal to the  $\pi^*$  orbital of the olefin.<sup>[1]</sup> In particular, zirconium metallocenes (zirconocenes) have probably attracted the most research interest due to their practical properties, which include stability at conventional polymerization temperatures and cost of materials.<sup>[2]</sup>

Much work on zirconocene derivatives has focused around the development of new polymeric materials and the understanding of polymer-chain initiation, growth and termination mechanisms at the reactive site. The study of polymerization mechanisms is of special interest due to the generally elusive nature of these processes. Though much information has been gathered about the mechanistic and chemical details of catalytic species taking part in polymerization, much also remains to be examined in a detailed and

definitive manner. For example, methylalumoxane (MAO) has long been used as a cocatalyst for zirconocene derivatives, however, its full cocatalytic role as well as its active structure are still largely unknown. Similarly, intermediate species of the type  $\text{Cp}_2\text{Zr}(\text{R})(\text{olefin})^+$  are generally assumed to form during the polymerization process, but they have never been directly observed.<sup>[2]</sup> The nature of catalyst species after termination of catalytic activity also remains to be explored.

The study of zirconocene derivatives in the condensed phase is especially desirable because this is the state in which they often occur in industrial applications (i.e., as heterogeneous catalysts, solid byproducts in homogeneous catalysis, etc.). A technique which has been used extensively for the study of zirconocenes in the solution and solid phases is nuclear magnetic resonance (NMR) spectroscopy. The power of NMR spectroscopy as a characterization technique is derived from the sensitivity of interactions it can investigate (e.g., chemical shielding, dipolar coupling, etc.) to molecular structure and dynamics. Furthermore, by employing NMR spectroscopy on solid samples, one is provided with the ability to examine the anisotropy of nuclear interactions which afford detailed angular information about the electronic and bonding environment of nuclei. Solid-state  $^{13}\text{C}$  NMR is a very informative probe of carbon molecular environments and is used ubiquitously for the characterization of chemical compounds. However, for the case of zirconocenes (and metallocenes in general),  $^{13}\text{C}$  NMR only allows detailed characterization of the carbocycles and other peripheral ligands. The electronic environment and chemistry of the central metal atom, which tends to govern the reactivity of zirconocene catalysts, can be examined directly via  $^{91}\text{Zr}$  NMR.

Recent advances in NMR spectroscopy have allowed for the investigation of numerous compounds in the solid state. Notably, the significant signal to noise (S/N) enhancement attainable using the quadrupolar Carr-Purcell Meiboom-Gill (QCPMG) pulse sequence<sup>[3]</sup> has allowed the study of insensitive quadrupolar nuclei such as  $^{91}\text{Zr}$ , particularly in combination with wideline techniques,<sup>[4,5]</sup> since zirconium compounds can often exhibit large quadrupolar interactions ( $C_Q \approx 10 - 20$  MHz) which result in patterns that are hundreds of kilohertz in breadth. A more thorough explanation of the QCPMG pulse sequence and its applications can be found elsewhere.<sup>[6]</sup>

There are relatively few NMR studies of zirconium compounds in the condensed phase owing to the relatively low sensitivity of  $^{91}\text{Zr}$ , which is a quadrupolar nucleus with spin  $I = 5/2$ , a moderate quadrupole moment ( $Q(^{91}\text{Zr}) = -1.76(3) \times 10^{-29} \text{ m}^2$ ),<sup>[7]</sup> low natural abundance (11.23%) and a relatively low magnetogyric ratio ( $-2.49750 \times 10^7 \text{ rad T}^{-1} \text{ s}^{-1}$ ). Therefore, it is of importance to initially characterize model zirconocene species in order to gain a fundamental understanding of the correlation between measured NMR parameters and molecular properties.

Following the successful characterization of  $\text{Cp}_2\text{ZrCl}_2$ , the study of zirconocene derivatives which could serve as model compounds for heterogeneous catalysts, i.e., zirconocenes immobilized on surface materials through chemisorption or physisorption, was undertaken. Due to the sensitivity of the quadrupolar interaction towards the overall electronic environment around nuclei, the use of solid-state  $^{91}\text{Zr}$  MAS NMR for the characterization of immobilized zirconocenes should prove fruitful in understanding the mechanistic details of polymerization processes. Herein, we report a comprehensive

solid-state  $^{91}\text{Zr}$  NMR study of various ring-bridged, ring-substituted and unsubstituted zirconocene species, which serve as catalyst precursors or starting materials for the preparation of heterogeneous catalysts, including  $\text{Cp}^*\text{ZrCl}_2$  **1**,  $\text{Cp}_2\text{ZrBr}_2$  **2**,  $(\text{C}_5\text{Me}_3\text{H}_2)_2\text{ZrBr}_2$  **3**,  $(\text{Me}_3\text{Si}-\text{C}_5\text{H}_4)_2\text{ZrBr}_2$  **4**,  $\text{O}(\text{Me}_2\text{SiC}_5\text{H}_4)_2\text{ZrBr}_2$  **5**,  $(\text{O}(\text{Me}_2\text{Si})_2\text{C}_5\text{H}_3)_2\text{ZrBr}_2$  **6**,  $(\text{Me}_2\text{ClSi}-\text{C}_5\text{H}_4)\text{ZrCl}_3$  **7**, and  $\text{Cp}_2\text{ZrMe}_2$  **8** (Figure 8.1). This is the first solid-state  $^{91}\text{Zr}$  NMR study of organometallic compounds **1** – **8**. Buhl and co-workers (BvPB) have performed a similar study on compounds **1**, **2**, **4** and **8** and other compounds analogous to **5** and **6** using solution  $^{91}\text{Zr}$  NMR and ab initio calculations,<sup>[8]</sup>

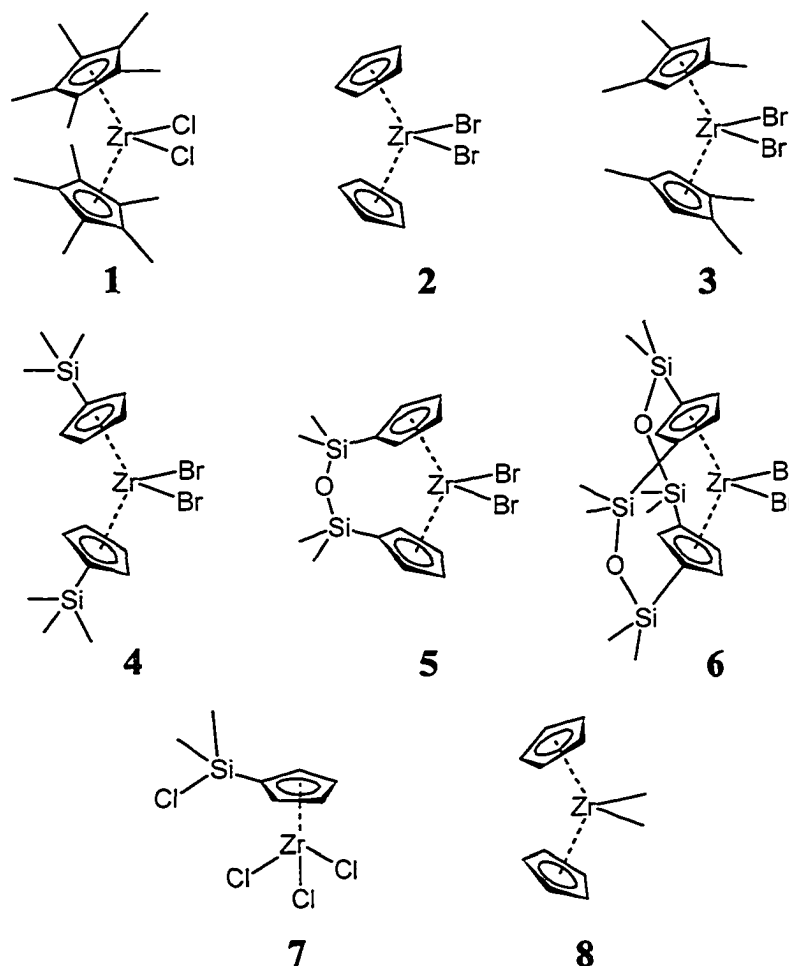


**Figure 8.1** Schematic representation of compounds **1** – **8**.

therefore, we will often refer to their work in comparison with the results presented here.

## 8.2 Experimental

### 8.2.1 Samples

Samples of  $\text{Cp}^*_2\text{ZrCl}_2$  **1** and  $\text{Cp}_2\text{ZrMe}_2$  **8** were purchased from Strem Chemicals, Inc. and used without further purification. The samples of  $\text{Cp}_2\text{ZrBr}_2$  **2**,  $(\text{C}_5\text{Me}_3\text{H}_2)_2\text{ZrBr}_2$  **3**,  $(\text{Me}_3\text{Si}-\text{C}_5\text{H}_4)_2\text{ZrBr}_2$  **4**,  $\text{O}(\text{Me}_2\text{SiC}_5\text{H}_4)_2\text{ZrBr}_2$  **5**, and  $(\text{O}(\text{Me}_2\text{Si})_2\text{C}_5\text{H}_3)_2\text{ZrBr}_2$  **6** were kindly provided by M. Mensch and P. A. Deck (Virginia Polytechnic Institute and State University). The sample of  $(\text{Me}_2\text{ClSi}-\text{C}_5\text{H}_4)\text{ZrCl}_3$  **7** was provided by K. Yu and C. W. Jones (Georgia Institute of Technology).

### 8.2.2 Solid-State NMR Spectroscopy

NMR experiments were performed on a Varian Infinity+ NMR console with an Oxford 9.4 T wide bore magnet as described elsewhere.<sup>[5]</sup> The Larmor (or resonance) frequency for  $^{91}\text{Zr}$  at the applied magnetic field is 37.2 MHz. Typical pulse widths of ca. 2.0  $\mu\text{s}$  with radio frequency fields of 40 kHz were employed along with an interval of 0.7 s between acquisitions. Where necessary, the QCPMG pulse sequence<sup>[3]</sup> was employed with or without wide-line techniques.  $^{91}\text{Zr}$  MAS NMR spectra were typically acquired at spinning frequencies ( $\nu_{\text{rot}}$ ) of 10000 – 15000 Hz. In all cases,  $\text{ZrO}_2$  rotors were employed for acquisition of MAS spectra and Teflon sample tubes were used for non-spinning experiments. Zirconium chemical shifts were referenced to a concentrated

solution of  $\text{Cp}_2\text{ZrCl}_2$  ( $\delta_{\text{iso}} = 0.0$  ppm) in dichloromethane ( $\text{CH}_2\text{Cl}_2$ ).

### 8.2.3 Spectral Simulations

Analytical and numerical simulations of NMR spectra were performed as described previously<sup>[5]</sup> with the WSOLIDS<sup>[9]</sup> and SIMPSON<sup>[10]</sup> packages. The convention used herein for specification of electric field gradient tensors is:  $|V_{33}| \geq |V_{22}| \geq |V_{11}|$ ;  $C_Q = eQV_{33}/h$ ;  $\eta_Q = (V_{11} - V_{22})/V_{33}$ .

### 8.2.4 Theoretical Calculations

Calculations of EFG tensors were performed using Gaussian 03<sup>[11]</sup> employing molecular coordinates for isolated molecules resolved by X-ray diffraction.<sup>[8, 12, 13]</sup> Computations were carried out using the restricted Hartree-Fock (RHF), as well as hybrid (B3LYP, B3P86) and pure (BLYP, BP86) density functional theory methods with an all-electron basis set on zirconium ((17s13p9d)<sup>[14, 15]</sup> contracted to [12s9p5d], including two sets of diffuse p functions<sup>[16]</sup> with  $\alpha_p = 0.11323$  and  $0.04108$ , and one diffuse d function with  $\alpha_d = 0.0382$ )<sup>[8]</sup> and bromine ((13s10p1d) contracted to [4s3p1d]),<sup>[17]</sup> and the 6-31G\*\* basis set on all other atoms. Quadrupole coupling constants ( $C_Q$ ) were converted from atomic units (a.u.) to Hz by multiplying the largest component of the EFG tensor,  $V_{33}$ , by  $eQ/h \times 9.71736 \times 10^{21} \text{ V m}^{-2}$ , where  $Q(^{91}\text{Zr}) = -1.76(3) \times 10^{-29} \text{ m}^2$ ,<sup>[17]</sup> and  $e = 1.602188 \times 10^{-19} \text{ C}$ .

## 8.3 Results and Discussion

### 8.3.1 Solid-State NMR

The central-transition  $^{91}\text{Zr}$  MAS NMR spectra of **1**–**6**, which are influenced by second-order quadrupolar effects, are shown in Figure 8.2. It can readily be seen that solid-state  $^{91}\text{Zr}$  NMR can serve as a powerful tool for the identification of zirconocene derivatives. Variations in the ring substitution and overall symmetry of the molecule have an obvious influence on the lineshape of the spectra. The  $^{91}\text{Zr}$  EFG parameters derived from simulation of these spectra are compiled in Table 8.1. The isotropic chemical shifts for **1** – **8** are in good agreement with values measured by Buhl and co-workers using solution  $^{91}\text{Zr}$  NMR.<sup>[8]</sup>

**Table 8.1**  
Experimental  $^{91}\text{Zr}$  EFG Parameters

Compound	$\delta_{\text{iso}}$ [ppm]	$ C_Q $ [MHz]	$\eta_Q$
$\text{Cp}_2\text{ZrCl}_2$ <sup>[a]</sup>	25(10)	6.35(10)	0.3(1)
$\text{Cp}^*_2\text{ZrCl}_2$ <b>1</b>	208(2)	2.6(1)	0.22(10)
$\text{Cp}_2\text{ZrBr}_2$ <b>2</b> <sup>[b]</sup>	127(10)	2.4(2)	0.4(2)
$(\text{C}_5\text{Me}_3\text{H}_2)_2\text{ZrBr}_2$ <b>3</b>	260(30)	5.5(2)	0.97(3)
$(\text{Me}_3\text{Si}-\text{C}_3\text{H}_4)_2\text{ZrBr}_2$ <b>4</b>	154(5)	4.7(1)	0.88(4)
$\text{O}(\text{Me}_2\text{SiC}_5\text{H}_4)_2\text{ZrBr}_2$ <b>5</b>	143(3)	2.5(1)	0.68(7)
$\text{O}(\text{Me}_2\text{Si})_2\text{C}_5\text{H}_3)_2\text{ZrBr}_2$ <b>6</b>	163(7)	3.9(2)	0.25(9)
$(\text{Me}_2\text{ClSi}-\text{C}_3\text{H}_4)\text{ZrCl}_3$ <b>7</b>	0(100)	14.8(10)	0.9(1)
$\text{Cp}_2\text{ZrMe}_2$ <b>8</b>	500(60)	22.7(5)	0.14(4)

<sup>[a]</sup> Reference [5]. <sup>[b]</sup> Estimated parameters from overlapping sites (see text for details).

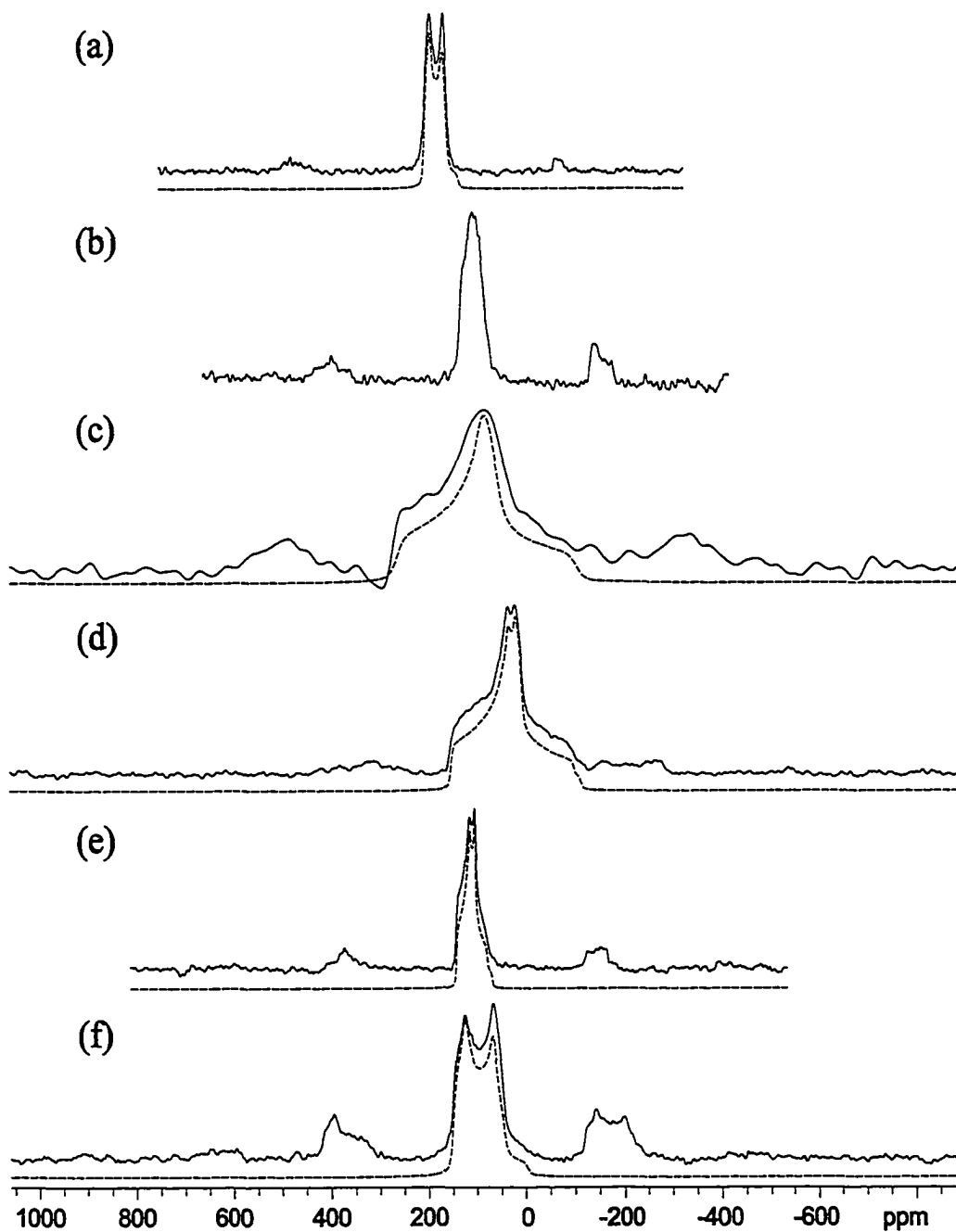


**Figure 8.2**  $^{91}\text{Zr}$  MAS NMR spectra of (a) **1** at  $\nu_{\text{rot}} = 10000$  Hz, (b) **2** at  $\nu_{\text{rot}} = 10000$  Hz, (c) **3** at  $\nu_{\text{rot}} = 15500$  Hz, (d) **4** at  $\nu_{\text{rot}} = 11000$  Hz, (e) **5** at  $\nu_{\text{rot}} = 10000$  Hz, and (f) **6** at  $\nu_{\text{rot}} = 10000$  Hz. Corresponding analytical simulations are drawn as dashed lines (---).



The spectrum of **1** (Figure 8.2a) is characterized by a  $^{91}\text{Zr}$  quadrupole coupling constant that is smaller than the value measured for  $\text{Cp}_2\text{ZrCl}_2$  by a factor of ca. 2.4 (Table 8.1). Examination of the crystal structures for these two compounds ( $\text{Cp}_2\text{ZrCl}_2$ :  $r(\text{Zr}-\text{Cl}) = 2.446 \text{ \AA}$ ,  $r(\text{Zr}-\text{Cp centroid}) = 2.198 \text{ \AA}$ ,  $\angle(\text{Cp}-\text{Zr}-\text{Cp}) = 129.29^\circ$ ;<sup>[12]</sup> **1**:  $r(\text{Zr}-\text{Cl}) = 2.462 \text{ \AA}$ ,  $r(\text{Zr}-\text{Cp}^* \text{ centroid}) = 2.262 \text{ \AA}$ ,  $\angle(\text{Cp}^*-\text{Zr}-\text{Cp}^*) = 130.88^\circ$ )<sup>[18]</sup> reveals a lengthening in the average  $\text{Zr}-\text{Cl}$  and  $\text{Zr}-\text{Cp}'$  distances of **1** in comparison to  $\text{Cp}_2\text{ZrCl}_2$ . The longer  $\text{Zr}-\text{Cp}^*$  distance in **1** is likely caused by steric bulk effects, which is evident from distortion of  $\text{Cp}^*$  ring planarity in the direction opposite to the Cl atoms. A decrease in  $C_Q$  with lengthening of the metal- $\text{Cp}'$  distance is consistent with observations made from variable-temperature experiments on linear sodocenes<sup>[19]</sup> and  $\text{CpK}$ .<sup>[20]</sup> BvPB have also shown using ab initio calculations that the lower  $C_Q$  in **1** is caused largely by the electronic effects of the highly basic  $\text{Cp}^*$  ligand.<sup>[8]</sup> However, since the magnitude of EFG components scale as  $1/r^3$ , the increased  $r(\text{Zr}-\text{Cl})$  distance in **1** likely contributes to the reduction in  $C_Q$ .

The  $^{91}\text{Zr}$  MAS NMR spectrum of **2** (Figure 8.2b) appears to show the overlap of signals from two distinct zirconium species. The observation of more than one zirconium site is in agreement with the existence of two molecules in the asymmetric unit of the crystal structure<sup>[8]</sup> (interestingly, the two crystallographic sites for the isomorphous compound  $\text{Cp}_2\text{ZrCl}_2$  were indistinguishable by solid-state  $^{91}\text{Zr}$  NMR spectroscopy). Unfortunately, the chemical shift dispersion at the applied magnetic field strength ( $B_0 = 9.4 \text{ T}$ ) is insufficient to resolve the inequivalent sites of **2** even with a high-resolution

solid-state NMR technique, such as triple-quantum (3Q) multiple-quantum (MQ) MAS<sup>[21, 22]</sup> (Appendix B, Figure B.7). Nevertheless, by considering the approximate width of the pattern, it is possible to make rough estimates of the maximum  $C_Q$ , as well as the  $\delta_{\text{iso}}$  and  $\eta_Q$  for **2** (Table 8.1). Application of higher magnetic fields should aid in resolving the overlapping patterns of **2**, since line broadening due to the second order quadrupolar interaction and chemical shift dispersion are inversely and directly proportional to  $B_0$ , respectively.

The  $^{91}\text{Zr}$  MAS NMR spectrum of **3** is shown in Figure 8.2c. In comparison with **2**, a dramatic change in the EFG parameters is observed from partial substitution of the Cp rings (Table 8.1):  $C_Q$  more than doubles and  $\eta_Q$  shows a complete deviation from axial symmetry. These observations are intriguing in light of the fact that complete methylation of  $\text{Cp}_2\text{ZrCl}_2$  (resulting in compound **1**) causes a decrease in  $C_Q$ , instead of an increase. The X-ray crystal structure of **3** has not been reported, therefore, correlations between measured NMR parameters and the structural differences between **2** and **3** cannot be made. However, the increase in  $C_Q$  can likely be attributed to structural distortions of the spherical molecular symmetry of **3**, which have a strong effect on the EFG and overshadow the inductive effects caused by methylation of the Cp ring. This is consistent with the theoretical examination by Buhl and co-workers of the  $C_Q$  dependence on the deviation of the normal to the Cp plane from the Zr–Cp centroid vector.<sup>[8]</sup>

The  $^{91}\text{Zr}$  MAS NMR spectra of **4** – **6** are shown in Figures 8.2d, 8.2e, and 8.2f, respectively. Compounds **4** – **6** comprise a set of structures which can be regarded as isolated molecular models of surface anchored species, i.e., representations of the

zirconium environment in immobilized zirconocene derivatives. The conformation of **4** reflects a zirconocene prior to adsorption and **5** and **6** are models of surface-bound species. Surprisingly, if the model employed is accurate, in going from isolated to adsorbed species (i.e., **4** – **5/6**), there will be a decrease in the magnitude of the quadrupolar interaction. The molecules of **4** – **6** only display slight differences in the local Zr structure (i.e.,  $r(\text{Zr}-\text{Br})$ ,  $r(\text{Zr}-\text{Cp}$  centroid and  $\Delta(\text{Cp}-\text{Zr}-\text{Cp})$ ), which do not seem to account for the observed changes in  $C_Q$  and  $\eta_Q$ . Nevertheless, the differences between **4**, **5** and **6** can be distinguished using  $^{91}\text{Zr}$  MAS NMR. These results provide strong support for the possibility of observing and characterizing surface anchored zirconocene moieties, since (i) large changes in the substitution and conformation of the Cp' rings, such as for **4** – **6**, do not cause a massive increase in the Zr EFG so as to make acquisition of NMR spectra intractable, and (ii)  $^{91}\text{Zr}$  NMR spectra show incredible sensitivity to changes in coordination and molecular geometry.

“Piano-stool” complexes or half-sandwich metallocenes are often employed as surface-adsorbed catalysts. Therefore, a representative example,  $(\text{Me}_2\text{ClSi}-\text{C}_5\text{H}_4)\text{ZrCl}_3$  **7**, was examined. The static  $^{91}\text{Zr}$  wideline QCPMG spectrum of **7** (Figure 8.3) shows a pattern with an unusually large breadth of ca. 300 kHz. This is consistent with a decrease in the overall spherical symmetry of the molecule compared to the bis-Cp' complexes and is manifested as an increase in magnitude of the quadrupolar interaction. This type of compound (see Appendix B, Figure B.8 for another example) is not a good candidate for investigation of surface immobilized species; the spectrum of **7** required approximately five hours to record. Upon adsorption, the mass percentage of Zr as well as the overall

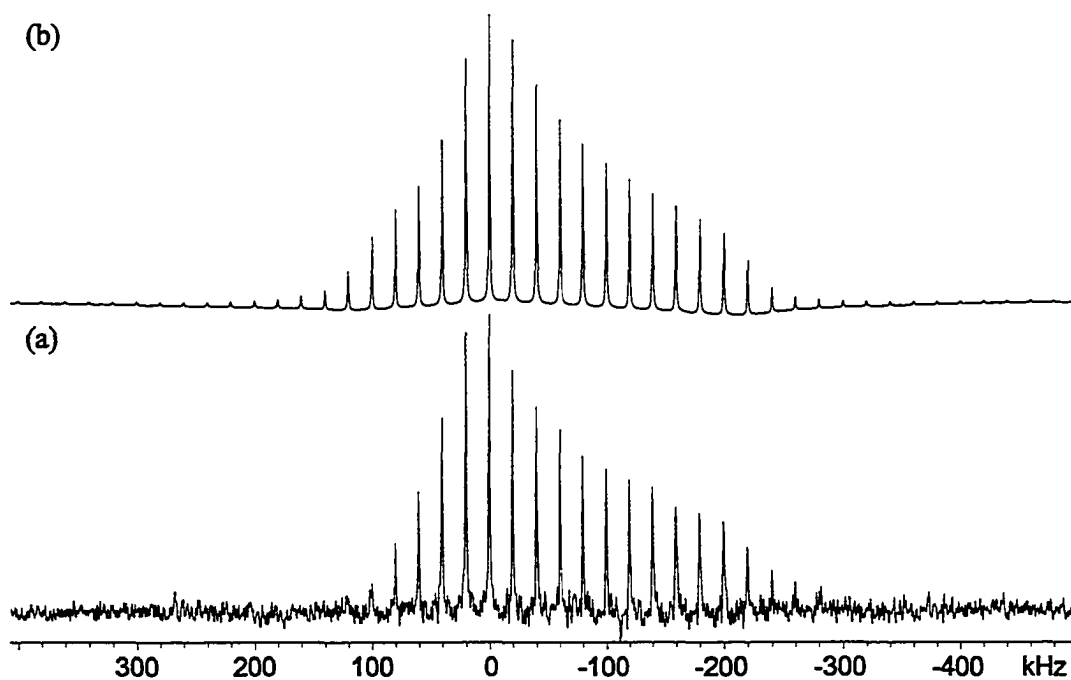


**Figure 8.3** (a) Experimental and (b) calculated static  $^{91}\text{Zr}$  wide-line QCPMG NMR spectra of **7**.

symmetry of the molecule are expected to decrease, consequently, the time necessary to acquire spectra of reasonable S/N would be greatly increased. However, **7** serves as a model/reference compound for comparison with the structure of zirconocene species which result as “piano-stool” compounds when anchored onto surface materials. With the use of isotopic enrichment and/or high magnetic fields, it may be possible to detect such species under dilute conditions.

Since catalytically active zirconocenes are generally presumed to have the form  $[\text{Cp}'_2\text{ZrMe}]^+$ , the closest neutral analog to this,  $\text{Cp}_2\text{ZrMe}_2$  **8**, has also been investigated. The static  $^{91}\text{Zr}$  wide-line QCPMG NMR spectrum of **8** (Figure 8.4) exhibits a 500 kHz wide powder pattern, which yields the largest  $C_Q(^{91}\text{Zr})$  observed so far in the solid state (Table 8.1); this is in agreement with the measurement by BvPB of a large line-width

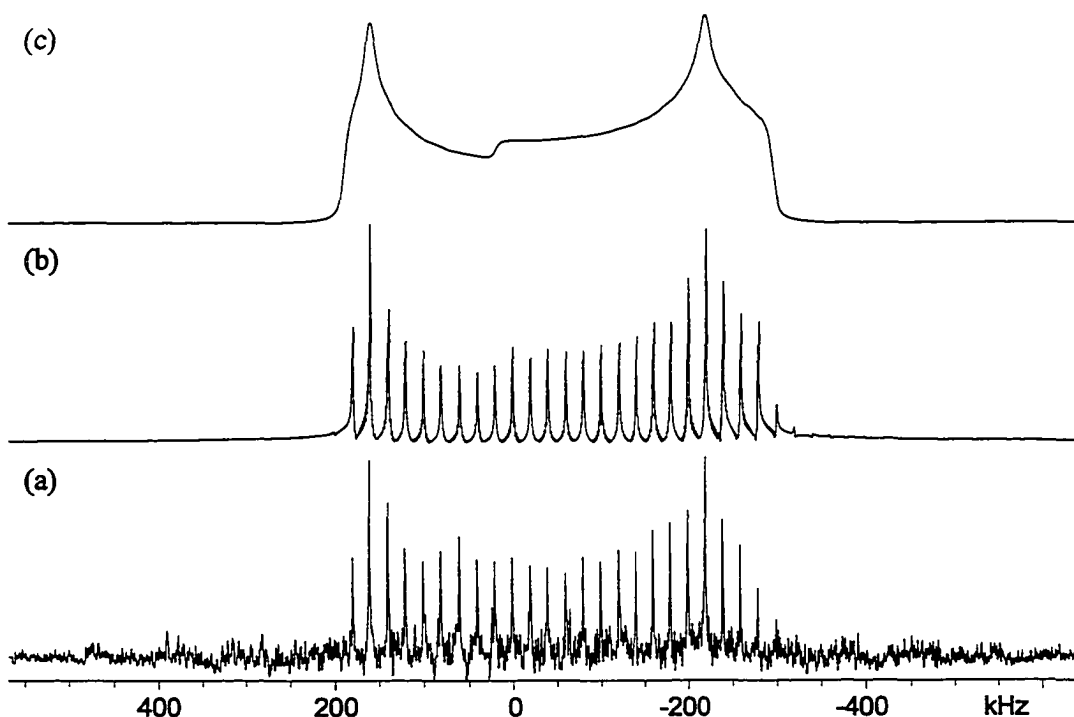


**Figure 8.4** (a) Static  $^{91}\text{Zr}$  wide-line QCPMG NMR spectrum of **8**. (b) Numerical and (c) analytical simulations of (a).

(2530 Hz at 300 K) in solution. Examination of the crystal structure of **8** ( $r(\text{Zr-X}) = 2.277 \text{ \AA}$ ,  $r(\text{Zr-Cp centroid}) = 2.231 \text{ \AA}$ ,  $\angle(\text{Cp-Zr-Cp}) = 132.54^\circ$ )<sup>[13]</sup> does not unearth a plausible cause for the immense difference in  $C_Q$  between **8** and the structurally analogous compounds **2** and  $\text{Cp}_2\text{ZrCl}_2$ . However, the large  $C_Q$  of **8** agrees qualitatively with theoretical results obtained by BvPB,<sup>[8]</sup> namely, that the  $C_Q$  should be relatively similar for **2** and  $\text{Cp}_2\text{ZrCl}_2$ , and larger by a factor of ca. 3 for **8**. A possible explanation for the large contrast in the  $C_Q$ 's measured for **8** and  $\text{Cp}_2\text{ZrCl}_2$  is provided below in section 8.3.2.

Solid-state  $^{91}\text{Zr}$  NMR experiments have been conducted on zirconocene species anchored onto silica, including  $(\text{Me}_2\text{BrSi-C}_5\text{H}_4)\text{Zr}(\text{Cp})\text{Br}_2/\text{SiO}_2$ ,  $((\text{Me}_2\text{BrSi})_2\text{-C}_5\text{H}_3)\text{Zr}(\text{Cp})\text{Br}_2/\text{SiO}_2$ , and  $(\text{Me}_2\text{BrSi-C}_5\text{H}_4)_2\text{ZrBr}_2/\text{SiO}_2$ . Unfortunately,

attempts at observing a  $^{91}\text{Zr}$  NMR signal were unsuccessful, which gives rise to suspicion regarding the actual structure of immobilized species. The nature of compounds under study and their method(s) of preparation was also questioned, due to the fact that no signal could be observed. Furthermore, as a representative example, the  $^{13}\text{C}$  CP/MAS NMR spectra of  $(\text{Me}_2\text{BrSi}-\text{C}_5\text{H}_4)_2\text{ZrBr}_2/\text{SiO}_2$  revealed a major resonance at ca. 51 ppm and a minor resonance at ca. 0 ppm and a broadened distribution of small peaks from 97 – 137 ppm (Figure 8.5). The resonance at 51 ppm likely corresponds to residual  $\text{CH}_2\text{Cl}_2$  which was used in the reflux procedure and washing of the metallocene-treated samples. There may be a resonance within the 97 – 137 ppm range corresponding to Cp'

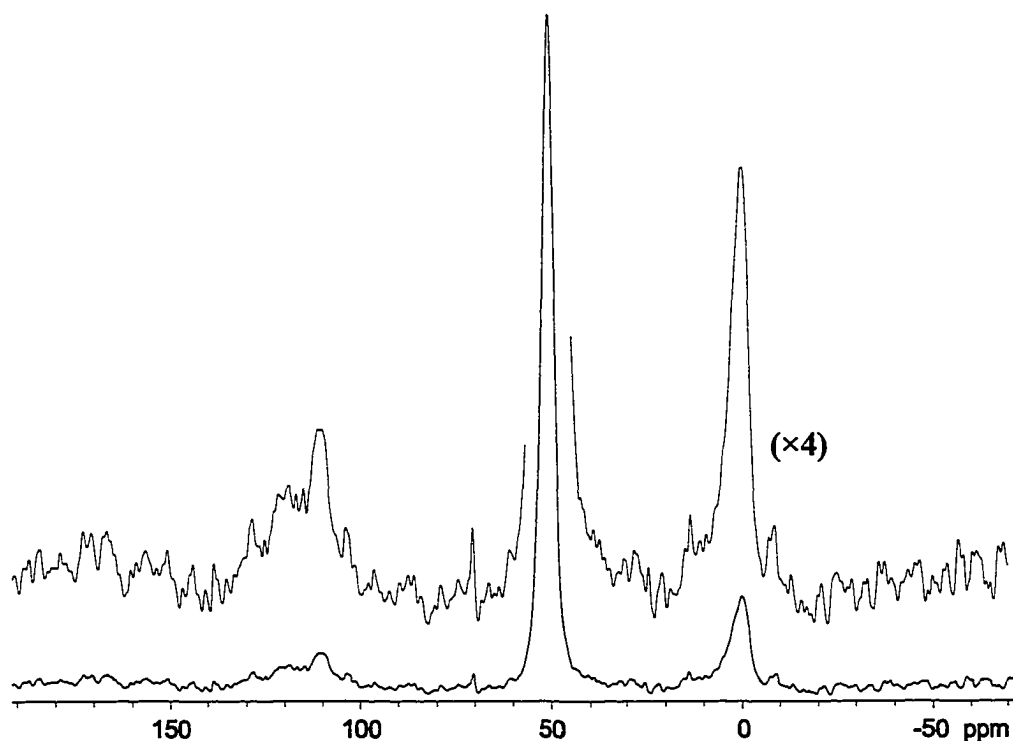


**Figure 8.5**  $^{13}\text{C}$  CP/MAS NMR spectrum of  $(\text{Me}_2\text{BrSi}-\text{C}_5\text{H}_4)_2\text{ZrBr}_2/\text{SiO}_2$  at  $\nu_{\text{rot}} = 6000$  Hz.

ring carbon nuclei, and the resonance at 0 ppm may correspond to the methyl groups of the Me<sub>2</sub>BrSi- moiety. There are some ambiguities regarding the sample preparation, and a number of resonances corresponding to unidentified species. Unfortunately, an unloaded support material was not provided for examination and comparison. Estimates of metallocene retention on the surface materials are on the order of  $\leq 1$  mol%, which would severely hamper the detection of a <sup>91</sup>Zr signal.

According to our investigations, acquisition of <sup>91</sup>Zr NMR spectra for zirconocene derivatives adsorbed onto support materials is feasible. The brominated zirconocene species seem to be the best candidates, due to their low C<sub>Q</sub> values and high sensitivity to structural changes. However, samples with high loading levels and precise preparation protocols must be examined; while such samples may not be practical in actual applications, great insight into the structure and conformation of metallocene species in heterogeneous catalyst systems could be obtained.

### 8.3.2 Theoretical Calculations

The results of quantum mechanical calculations of the <sup>91</sup>Zr EFG tensor parameters for Cp<sub>2</sub>ZrMe<sub>2</sub> **8** and the distinct crystallographic sites of Cp<sub>2</sub>ZrCl<sub>2</sub> and Cp<sub>2</sub>ZrBr<sub>2</sub> **2** are shown in Table 8.2. One of the crystallographic sites of **2** consists of two sets of half-occupied carbon sites for one of the Cp rings (which arises from five-fold rotation), therefore, three sets of calculations are shown for **2**. Qualitative trends in theoretical C<sub>Q</sub>'s for the three compounds are in agreement with experimental values and results obtained by BvPB,<sup>[8]</sup> hence only salient features of the calculations will be discussed here.

**Table 8.2**  
Experimental and Theoretical  $^{91}\text{Zr}$  EFG Parameters

Source	$V_{11}$ [a.u.]	$V_{22}$ [a.u.]	$V_{33}$ [a.u.]	$ C_Q $ [MHz]	$\eta_Q$
<b>Cp<sub>2</sub>ZrCl<sub>2</sub>, site 1</b>					
<b>Experimental<sup>[a]</sup></b>	0.0537	0.0998	-0.1536	6.35(10)	0.3(1)
RHF	0.1136	0.1746	-0.2882	11.92	0.21
BLYP	0.0681	0.1441	-0.2122	8.78	0.36
BP86	0.8799	0.1489	-0.2369	9.80	0.26
B3LYP	0.0862	0.1433	-0.2295	9.49	0.25
B3P86	0.1003	0.1481	-0.2484	10.27	0.19
<b>Cp<sub>2</sub>ZrCl<sub>2</sub>, site 2</b>					
<b>Experimental</b>	0.0537	0.0998	-0.1536	6.35(10)	0.3(1)
RHF	0.1069	0.1876	-0.2945	12.18	0.27
BLYP	0.0763	0.1391	-0.2154	8.91	0.29
BP86	0.0969	0.1453	-0.2423	10.02	0.20
B3P86	0.0939	0.1400	-0.2339	9.67	0.20
B3LYP	0.1074	0.1468	-0.2542	10.51	0.16
<b>Cp<sub>2</sub>ZrBr<sub>2</sub>, site 1</b>					
<b>Experimental</b>	-0.1741	-0.0406	0.0580	2.4(2)	0.4(2)
RHF	-0.0428	-0.1101	0.1529	6.32	0.44
BLYP	-0.0102	-0.1732	0.1833	7.58	0.89
BP86	-0.0180	-0.1526	0.1706	7.05	0.79
B3LYP	-0.0174	-0.1612	0.1787	7.39	0.80
B3P86	-0.0230	-0.1463	0.1693	7.00	0.73
<b>Cp<sub>2</sub>ZrBr<sub>2</sub>, site 2, conformation 1</b>					
<b>Experimental</b>	-0.1741	-0.0406	0.0580	2.4(2)	0.4(2)
RHF	-0.0034	-0.1864	0.1898	7.85	0.96
BLYP	-0.0108	-0.2340	0.2448	10.12	0.91
BP86	-0.0008	-0.2116	0.2124	8.78	0.99
B3LYP	-0.0117	-0.2250	0.2367	9.79	0.90
B3P86	-0.0038	-0.2083	0.2121	8.77	0.96



Table 8.2 (cont.)

Source	$V_{11}$ [a.u.]	$V_{22}$ [a.u.]	$V_{33}$ [a.u.]	$ C_Q $ [MHz]	$\eta_Q$
Cp <sub>2</sub> ZrBr <sub>2</sub> , site 2, conformation 2					
<b>Experimental</b>	-0.1741	-0.0406	0.0580	2.4(2)	0.4(2)
RHF	-0.0458	-0.1142	0.1160	4.80	0.59
BLYP	-0.0092	-0.1890	0.1982	8.20	0.91
BP86	-0.0142	-0.1645	0.1787	7.39	0.84
B3LYP	-0.0169	-0.1757	0.1927	7.97	0.82
B3P86	-0.0207	-0.1574	0.1781	7.37	0.77
Cp <sub>2</sub> ZrMe <sub>2</sub>					
<b>Experimental</b>	0.2360	0.3129	-0.5489	22.7(5)	0.14(4)
RHF	0.3250	0.5849	-0.9099	37.63	0.29
BLYP	0.2190	0.5762	-0.7952	32.88	0.45
BP86	0.2230	0.5927	-0.8157	33.73	0.45
B3LYP	0.2493	0.5774	-0.8267	34.19	0.40
B3P86	0.2517	0.5880	-0.8397	34.73	0.40

<sup>[a]</sup> The sign (+/-) and significant figures of experimental EFG tensor components ( $V_{11}$ ,  $V_{22}$  and  $V_{33}$ ) are set according to most proximate theoretical values for comparison.

Calculations for both sites of Cp<sub>2</sub>ZrCl<sub>2</sub> yield very similar  $C_Q$  and  $\eta_Q$  values (differences of less than 3%), whereas much larger differences are observed for the distinct sites of **2**. This agrees with the experimental observation of different Zr sites for **2**, but not for Cp<sub>2</sub>ZrCl<sub>2</sub>, in corresponding <sup>91</sup>Zr MAS NMR spectra. Remarkably, there is a larger difference in theoretical  $C_Q$  values between the two Cp conformations of site **2** for **2** than between the two crystallographic sites. The two conformations appear to differ only by rotation of one of the Cp rings about the five-fold molecular axis by an angle of ca. 30°. A closer inspection of the crystal structure reveals a 2.3° difference in the tilt angle  $\theta$  (as defined by BvPB) between the two Cp ring conformations as well.<sup>[8]</sup> In the theoretical study by BvPB of geometry effects on the EFG in Cp<sub>2</sub>ZrCl<sub>2</sub>, an increase in the magnitude of  $V_{33}$  from 0.2903 to 0.7915 atomic units from a change in  $\theta$  of 7.5° was

observed, which translates into an increase in  $C_Q$  by a factor of 2.7. If a similar correlation is assumed, the difference in EFG parameters between the different ring conformations of **2** would be justified.

The calculated  $^{91}\text{Zr}$  EFG tensor orientations of **8** and  $\text{Cp}_2\text{ZrCl}_2$  are shown in Figures 8.6a and 8.6b, respectively. All calculations resulted in the tensor orientations shown: with  $V_{11}$  and  $V_{22}$  lying approximately parallel to the X-Zr-X (X = Me, Cl) plane and  $V_{33}$  pointing towards the Cp rings forming an angle with the X-Zr-X plane of  $88.4^\circ$  and  $90.3^\circ$  for X = Me and Cl, respectively. However, the  $V_{11}$  and  $V_{22}$  components of **8**

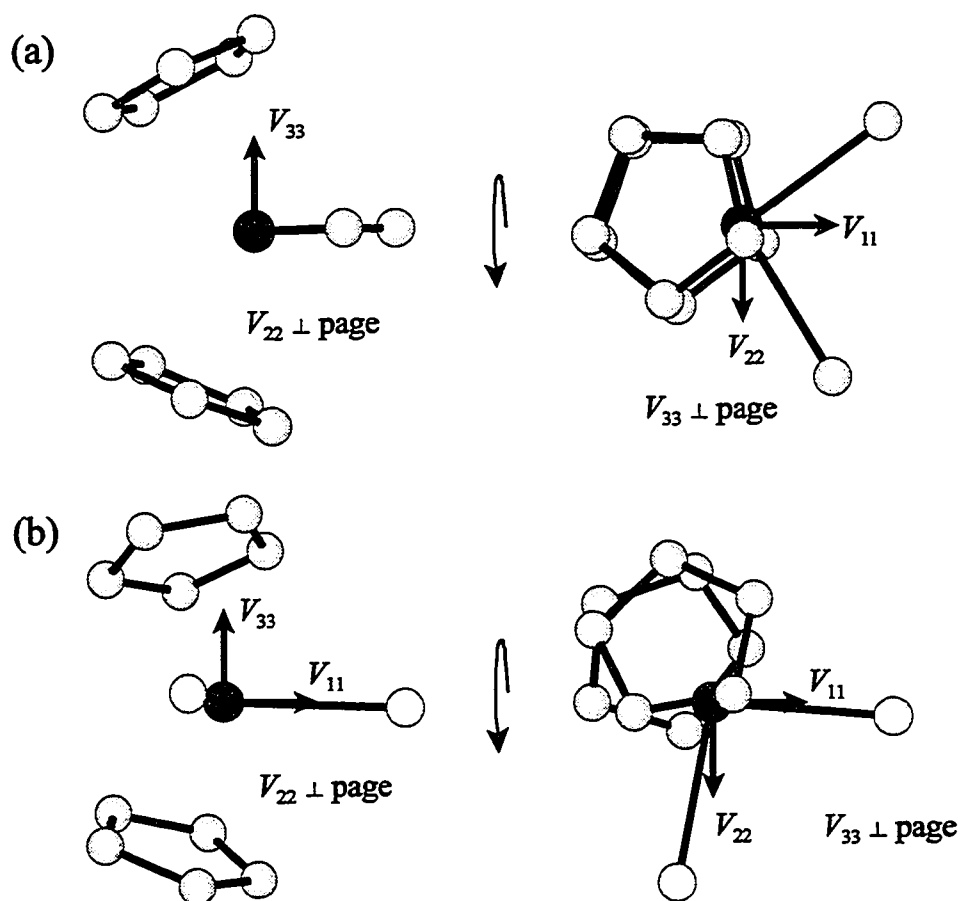


**Figure 8.6** Theoretical  $^{91}\text{Zr}$  EFG orientations viewed from the top and sides of (a) **8** and (b)  $\text{Cp}_2\text{ZrCl}_2$ .

and  $\text{Cp}_2\text{ZrCl}_2$  show slight deviations: for **8**,  $V_{11}$  is approximately bisecting the Me-Zr-Me angle, whereas  $V_{11}$  and  $V_{22}$  are aligned towards the two Zr-Cl bonds in  $\text{Cp}_2\text{ZrCl}_2$ . These orientations are in line with experimental values of  $\eta_Q$ , which indicate near-axial EFG tensors. This corresponds to  $V_{33}$  being the unique component and its alignment towards an electronic environment distinct from  $V_{11}$  and  $V_{22}$ .

At a glance, **8** and  $\text{Cp}_2\text{ZrCl}_2$  appear to be similar in many respects and a cause for the large difference in their  $C_Q$ 's is not readily apparent. The most significant difference in the molecular structures of **8** and  $\text{Cp}_2\text{ZrCl}_2$  appear in the X-Zr-X planes ( $r(\text{Zr-Cl}) = 2.446\text{\AA}$ ,  $r(\text{Zr-Me}) = 2.277\text{\AA}$ ), which in both cases lie orthogonal to  $V_{33}$  and are therefore not likely to have a considerable effect on the magnitude of  $C_Q$ . Instead, the electronic characteristics of the ligands appear as the only plausible explanation for the variation in  $C_Q$ : the theoretical calculations shown above consistently yield a higher anionic character for the Cp carbon atoms of **8** (Figure 8.7). This can be attributed to the absence of  $\pi$ -donation from the methyl groups to Zr, which is anticipated to play a major role in the Zr-Cl bonding of  $\text{Cp}_2\text{ZrCl}_2$ . As  $\pi$ -donation increases the electron density at the metal also increases and the allocation of negative charge on the Cp rings decreases. The lower  $C_Q$  in  $\text{Cp}_2\text{ZrCl}_2$  presumably arises due to a decrease in the charge difference between the Cp rings and Zr, which leads to a decrease in the electric field gradient along  $V_{33}$ . In addition, an increase in the spherical symmetry around Zr might be expected due to the increased electron density caused by  $\pi$ -donation. Evidence for the  $\pi$  interaction discussed above stems from examination of molecular orbitals taking part in Zr-Cl  $\pi$ -bonding obtained through quantum mechanical calculations (Appendix B, Figure B.9).

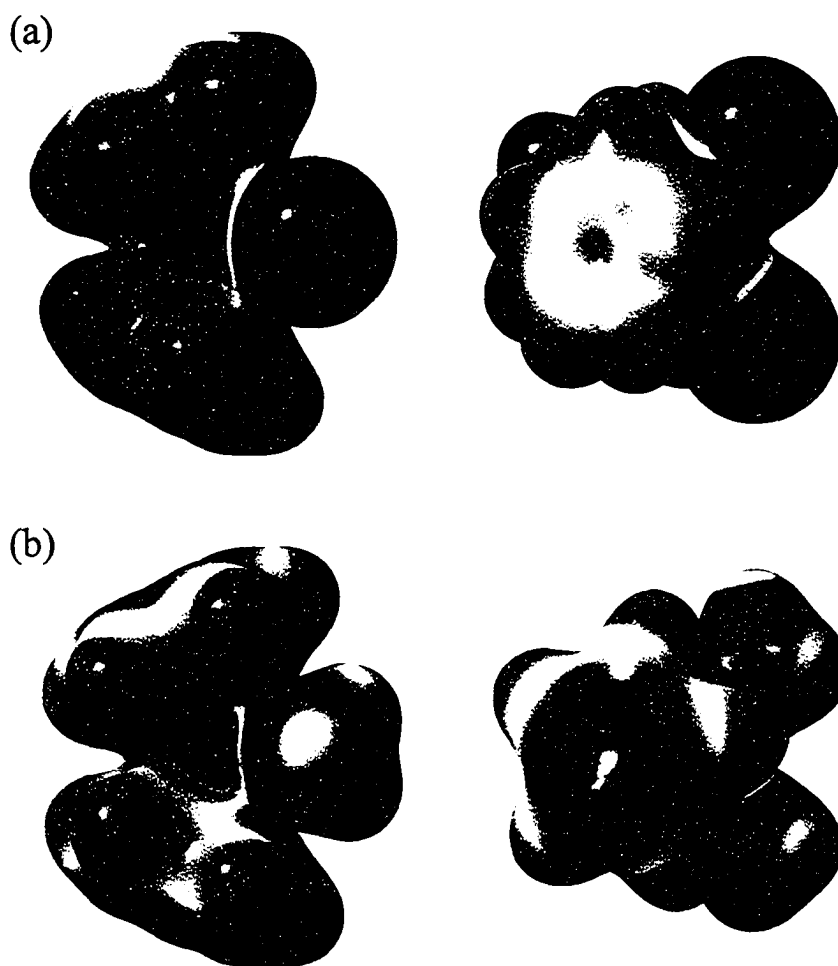


**Figure 8.7** Side and top views of the electrostatic potential mapped onto the total electron density of (a)  $\text{Cp}_2\text{ZrCl}_2$  and (b)  $\text{Cp}_2\text{ZrMe}_2$ . Regions of highest positive and negative charge are denoted by the blue and red colored areas, respectively.

### 8.3 Conclusion

The use of solid-state  $^{91}\text{Zr}$  NMR and quantum mechanical calculations has allowed for the examination of the  $^{91}\text{Zr}$  quadrupolar interaction in various ring-bridged, ring-substituted and unsubstituted zirconocene species. Notably, the previously

facilitates the acquisition of broad static patterns that span hundreds of kilohertz (e.g., spectra of **7** and **8**), which would require prohibitively long acquisition times using conventional spin echo sequences. Analytical and numerical lineshape simulations reveal variations in the  $C_Q(^{91}\text{Zr})$  of compounds **1** – **8**, which in many cases can be attributed to geometrical distortions or electronic effects. For instance, an increase in  $C_Q$  by a factor of 3.5 from substitution of the Cl ligands in  $\text{Cp}_2\text{ZrCl}_2$  with methyl groups is explained on the basis of the presence and absence of  $\pi$ -donation to Zr, respectively. Theoretical  $^{91}\text{Zr}$  electric field gradient tensors are in qualitative agreement with experimental values, in accordance with previous work by Buhl and co-workers; hence, experimental EFG tensor orientations are elucidated from theoretical calculations and found to relate consistently with experimentally obtained data.

The purpose of studying compounds **4** – **6** was to mimic the structural conformation of zirconocene species before (**4**) and after (**5** and **6**) adsorption to surface materials. The  $^{91}\text{Zr}$  MAS NMR spectra of **2** – **6** provide results which strongly encourage the study of more industrially relevant systems: (i) drastic changes in ring substitution, such as the incorporation of methyl groups (**3**) or siloxane bridges (**5** and **6**) do not create structural distortions severe enough to prohibit the efficient acquisition of NMR spectra, while (ii) even small differences in the local Zr structure of these compounds (ascertained by comparison of X-ray crystal structures) can readily be distinguished with  $^{91}\text{Zr}$  MAS NMR. In the event that ligands directly bound to Zr are replaced during the anchoring process, a significant increase in the breadth of the NMR pattern is expected (cf. spectra of **2**,  $\text{Cp}_2\text{ZrCl}_2$  and **8**). Acquisition of  $^{91}\text{Zr}$  NMR spectra for these systems might prove

challenging due to the dilution of the  $^{91}\text{Zr}$  nuclei and the distribution of the signal intensity over a large spectral region. However, the development and use of other signal enhancement techniques which involve the application of higher magnetic fields, lower temperatures, isotopic labelling, spin polarization pulse sequences, etc. should be very advantageous. Compounds **1** – **6** remain to be completely characterized using static  $^{91}\text{Zr}$  NMR and theoretical calculations, which is anticipated to provide a greater understanding of these systems through examination of the zirconium anisotropic chemical shielding interaction.

It is the continuing goal of our research to find suitable candidates which will allow the investigation of surface-adsorbed metallocene catalysts and their participation in olefin polymerization processes. Adsorption of the zirconocene species onto support materials (e.g.,  $\text{SiO}_2$ ,  $\text{Al}_2\text{O}_3$ ,  $\text{MgCl}_2$ ) is expected to greatly increase the difficulty of using solid-state  $^{91}\text{Zr}$  NMR, due to great losses in S/N arising from two main factors: (i) the potential alteration of zirconocene structure due to chemisorption or physisorption, which will lower the symmetry around the metal site and greatly increase  $C_Q$  and the breadth of the pattern; and/or (ii) the dilution of zirconocene species from loading onto a support material, which reduces the number of  $^{91}\text{Zr}$  nuclear spins which are available for detection in the NMR experiment. The ideal candidate for modelling immobilized zirconocenes should (i) possess a pattern which suffers relatively little broadening from second-order quadrupolar effects, and (ii) be possible to load in high quantities onto support materials. Brominated zirconocenes have been shown to fulfill the first condition, while the second condition remains to be explored. If there is a large dilution factor resulting from a low

mol % of metallocenes, it is worth considering the use of  $^{91}\text{Zr}$  isotopic enrichment, since heavy NMR active isotopes are becoming more routinely available for purchase from commercial and government isotope laboratories.

# Bibliography

- [1] N. J. Long, *Metallocenes: An introduction to sandwich complexes*, Blackwell Science, Malden, **1998**.
- [2] C. Janiak, in *Metallocenes: Synthesis, Reactivity, Applications. Vol. 2* (Eds.: A. Togni, R. L. Halterman), Wiley-VCH Verlag GmbH, Weinheim, **1998**, pp. 547.
- [3] F. H. Larsen, H. J. Jakobsen, P. D. Ellis, N. C. Nielsen, *Journal of Physical Chemistry A* **1997**, *101*, 8597.
- [4] A. S. Lipton, T. A. Wright, M. K. Bowman, D. L. Reger, P. D. Ellis, *Journal of the American Chemical Society* **2002**, *124*, 5850.
- [5] I. Hung, R. W. Schurko, *Journal of Physical Chemistry B* **2004**, *108*, 9060.
- [6] I. Hung, A. J. Rossini, R. W. Schurko, *Journal of Physical Chemistry A* **2004**, *108*, 7112.
- [7] V. Kello, P. Pyykko, A. J. Sadlej, P. Schwerdtfeger, J. Thyssen, *Chemical Physics Letters* **2000**, *318*, 222.
- [8] M. Buhl, G. Hopp, W. vonPhilipsborn, S. Beck, M. H. Prosenc, U. Rief, H. H. Brintzinger, *Organometallics* **1996**, *15*, 778.
- [9] K. Eichele, R. E. Wasylshen, WSOLIDS, 1.17.28. Dalhousie University, Halifax, Nova Scotia, **2000**.
- [10] M. Bak, J. T. Rasmussen, N. C. Nielsen, *Journal of Magnetic Resonance* **2000**, *147*, 296.
- [11] M. J. Frisch, G. W. Trucks, H. B. Schlegel, G. E. Scuseria, M. A. Robb, J. R.



Cheeseman, J. Montgomery, J. A., T. Vreven, K. N. Kudin, J. C. Burant, J. M. Millam, S. S. Iyengar, J. Tomasi, V. Barone, B. Mennucci, M. Cossi, G. Scalmani, N. Rega, G. A. Petersson, H. Nakatsuji, M. Hada, M. Ehara, K. Toyota, R. Fukuda, J. Hasegawa, M. Ishida, T. Nakajima, Y. Honda, O. Kitao, H. Nakai, M. Klene, X. Li, J. E. Knox, H. P. Hratchian, J. B. Cross, C. Adamo, J. Jaramillo, R. Gomperts, R. E. Stratmann, O. Yazyev, A. J. Austin, R. Cammi, C. Pomelli, J. W. Ochterski, P. Y. Ayala, K. Morokuma, G. A. Voth, P. Salvador, J. J. Dannenberg, V. G. Zakrzewski, S. Dapprich, A. D. Daniels, M. C. Strain, O. Farkas, D. K. Malick, A. D. Rabuck, K. Raghavachari, J. B. Foresman, J. V. Ortiz, Q. Cui, A. G. Baboul, S. Clifford, J. Cioslowski, B. B. Stefanov, G. Liu, A. Liashenko, P. Piskorz, I. Komaromi, R. L. Martin, D. J. Fox, T. Keith, M. A. Al-Laham, C. Y. Peng, A. Nanayakkara, M. Challacombe, P. M. W. Gill, B. Johnson, H. Chen, M. W. Wong, C. Gonzalez, J. A. Pople, Gaussian 03, Revision B.03. Gaussian, Inc., Pittsburgh, PA, 2003.

[12] T. Repo, M. Klinga, L. Mutikainen, Y. Su, M. Leskela, M. Polamo, *Acta Chemica Scandinavica* **1996**, *50*, 1116.

[13] W. E. Hunter, D. C. Hrcir, R. V. Bynum, R. A. Penttila, J. L. Atwood, *Organometallics* **1983**, *2*, 750.

[14] H. Horn, *unpublished data*.

[15] A. Schafer, H. Horn, R. Ahlrichs, *Journal of Chemical Physics* **1992**, *97*, 2571.

[16] S. P. Walch, C. W. Bauschlicher, C. J. Nelin, *Journal of Chemical Physics* **1983**, *79*, 3600.

[17] S. Huzinaga (Ed.), *Gaussian Basis Sets for Molecular Calculations*, Elsevier, New

York, **1984**.

[18] U. Bohme, B. Rittmeister, *Private Communication* **1998**.

[19] M. J. Willans, R. W. Schurko, *Journal of Physical Chemistry B* **2003**, *107*, 5144.

[20] C. M. Widdifield, R. W. Schurko, *Journal of Physical Chemistry B* **2005**,  
*submitted*.

[21] A. Medek, L. Frydman, *Journal of the Brazilian Chemical Society* **1999**, *10*, 263.

[22] A. Medek, J. S. Harwood, L. Frydman, *Journal of the American Chemical Society*  
**1995**, *117*, 12779.

[23] J. W. Lauher, R. Hoffmann, *Journal of the American Chemical Society* **1976**, *98*,  
1729.

## Chapter 9

### Future Work: Solid-State NMR Study of Surface-Adsorbed Metallocenes

We believe that the stage is set for investigation of immobilized zirconocenes and that much information will be made available through future solid-state NMR studies of the many catalyst systems used industrially for olefin polymerization. Preliminary studies of immobilized zirconocenes have pointed out limitations in current surface adsorption techniques: the average mole percent of zirconium anchored onto surface materials is ca. 1 %. It is unlikely that solid-state  $^{91}\text{Zr}$  NMR studies of systems with these extremely low Zr mass percentages will be presently possible by conventional means. However, there remain numerous possibilities which can aid the study of these dilute insensitive nuclei, including:

(i) The application of higher magnetic fields, such as those available in national facilities like the National Ultra-high Field NMR Facility for Solids (Ottawa, Ontario) and the National High Magnetic Field Laboratory (Tallahassee, Florida), would provide a substantial enhancement in signal. Since the S/N ratio of NMR experiments is proportional to  $B_0^2$  ( $B_0$  = applied field) and the broadening due to the quadrupolar interaction is inversely proportional to  $B_0$ , a higher signal intensity over a narrower frequency range would be observed for the NMR spectra of quadrupolar nuclei. Furthermore, the chemical shielding interaction is directly proportional to  $B_0$  leading to much better resolution due to enhanced chemical shift dispersion.

(ii) Improved probe designs which are more sensitive and can reduce the significant amount of noise due to “probe ringing” at low operation frequencies, as well as special probes for the acquisition of NMR spectra at cryogenic temperatures. A substantial increase in the S/N can be achieved at low temperatures from the increased differences in population, which are governed by the Boltzmann distribution, between the nuclear spin states.

(iii) Design of new pulse sequences which will provide greater enhancements in signal intensity and resolution. With the advent of technological enhancements and the discovery of new phenomena in “spin space,” the possibilities for pulse sequence development are endless.

Solid-state NMR of catalysts is by no means restricted to the study of zirconocenes. With the aid of signal enhancement techniques, the study of systems with less sensitive nuclei is also envisioned. As an example, the first solid-state  $^{47/49}\text{Ti}$  MAS NMR spectrum of an organometallic complex,  $\text{CpTiCl}_3$  (Figure 9.1), is presented herein; the DFS/Hahn echo and DFS/QCPMG pulse sequences detailed in chapter 4 were employed. Notably, the spectrum in Figure 9.1b has a S/N which is greater by a factor of 24 compared to Figure 9.1a. Accounting for the differences in the experimental times of the spectra, the experiment time of the DFS/Hahn echo spectrum would have to be lengthened by a factor of ca. 37.5 to attain the same S/N as in Figure 9.1b.

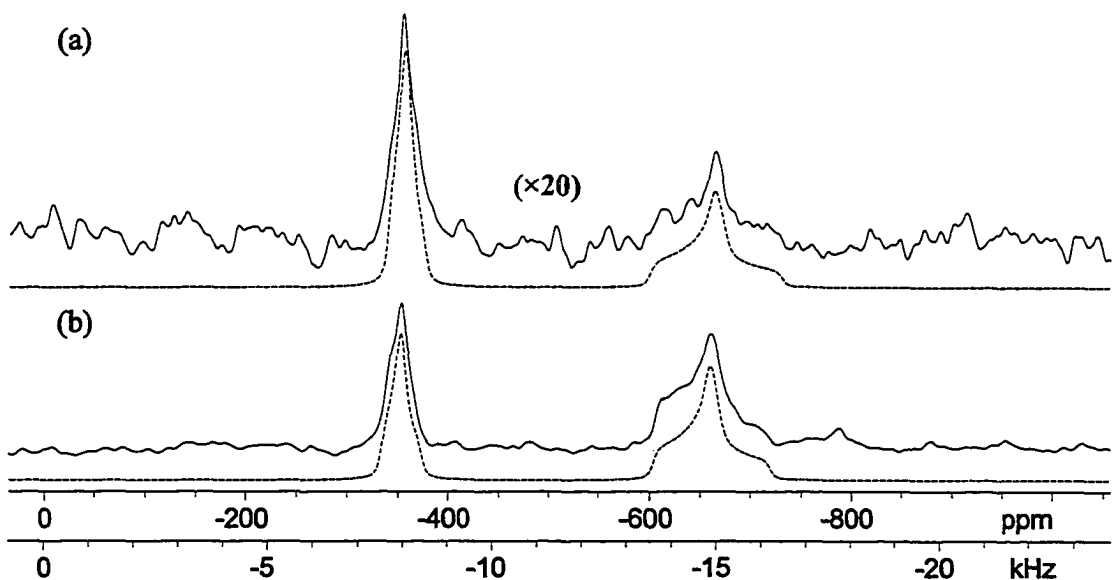


**Figure 9.1** Solid-state  $^{47/49}\text{Ti}$  MAS NMR spectra of  $\text{CpTiCl}_3$ , at a spectrometer frequency of 22.5 MHz and  $\nu_{\text{rot}} = 10000$  Hz, acquired using the (a) DFS/Hahn echo and (b) DFS/QCPMG pulse sequences. The spectrum in (b) is the result of Fourier transformation of the sum of all echoes in the time domain QCPMG fid. The vertical scale of (a) has been expanded by a factor of 20. Simulation of the  $^{47}\text{Ti}$  and  $^{49}\text{Ti}$  patterns in spectra (a) and (b) are shown as dashed lines (- - -), and are characterized by the quadrupolar parameters [ $^{47}\text{Ti}$ :  $\delta_{\text{iso}} = -600$  ppm,  $C_Q = 1.90$  MHz,  $\eta_Q = 1.0$ ;  $^{49}\text{Ti}$ :  $\delta_{\text{iso}} = -340$  ppm,  $C_Q = 1.65$  MHz,  $\eta_Q = 1.0$ .].

Incredible advances in the field of solid-state NMR have taken place over the last few decades and as researchers continue to push the frontiers of NMR, the complete characterization of any NMR active nucleus in the periodic table seems to be within grasp.

# Appendix A – Synthesis and X-ray Crystallography

## A.1.1 Preparation of $[\text{Cp}^*_2\text{Al}][\text{AlCl}_4]$

Pentamethylcyclopentadiene ( $\text{Cp}^*\text{H}$ ) was synthesized according to a published procedure.<sup>[1]</sup> Aluminum(III) chloride and all other reagents were obtained from the Aldrich Chemical Company and were used as received. Diethyl ether, hexanes, and toluene were dried over sodium with benzophenone and  $\text{CH}_2\text{Cl}_2$  was dried over  $\text{CaH}_2$ . All solvents were distilled and degassed immediately prior to use. All reagents were handled in argon-filled glove-boxes (Vacuum Atmospheres or MBraun) and reactions were performed using standard inert-atmosphere techniques. Melting points were recorded in sealed capillaries on an Electrothermal apparatus and are uncorrected. Solution NMR spectra were recorded on a General Electric QE-300 Fourier transform spectrometer with spectrometer frequencies of 300.19 MHz for  $^1\text{H}$ , 75.48 MHz for  $^{13}\text{C}$  and 78.31 MHz for  $^{27}\text{Al}$ . Solution NMR samples were either run immediately after removal from the glove box or flame-sealed in 5 mm NMR tubes. All solution chemical shifts are reported in ppm relative to an external standard (TMS for  $^1\text{H}$  and  $^{13}\text{C}$ ,  $[\text{Al}(\text{D}_2\text{O})_6]^{3+}$  for  $^{27}\text{Al}$ ). Low resolution mass spectra (CI,  $\text{CH}_4$ ) were obtained on a Finnigan MAT TSQ 700 instrument. High resolution mass spectra (CI,  $\text{CH}_4$ ) were obtained on a VG ZAB-VE sector instrument. " $\text{Cp}^*_2\text{AlCl}$ " was prepared by a slight variation of the reported method.<sup>[2]</sup>

A suspension of  $\text{Al}_2\text{Cl}_6$  (0.40 g, 1.50 mmol) in  $\text{CH}_2\text{Cl}_2$  (40 mL) was added to a

stirred pale yellow solution of “Cp\*<sub>2</sub>AlCl” (1.00 g, 3.00 mmol) in CH<sub>2</sub>Cl<sub>2</sub> (40 mL) at –78 °C. After warming to room temperature, the resulting amber solution was allowed to stir for 14 hours. The solution was concentrated to a volume of 10 mL and cooled to –20 °C to afford a crop of colourless block-shaped crystals (1.3 g, 92.8 %). mp 123 – 124 °C (decomp). LRMS: 464 (Cp\*<sub>2</sub>Al<sub>2</sub>Cl<sub>4</sub>, 3%), 429 (Cp\*<sub>2</sub>Al<sub>2</sub>Cl<sub>3</sub>, 60%), 329 (Cp\*Al<sub>2</sub>Cl<sub>4</sub>, 7%), 297 (Cp\*<sub>2</sub>Al, 20%), 197 (Cp\*AlCl, 100%), 137 (Cp\*H<sub>2</sub>, 55%). HRMS: calcd for C<sub>20</sub>H<sub>30</sub>Al<sub>2</sub>Cl<sub>4</sub>, 464.0732; found, 464.0743; HRMS: calcd for C<sub>20</sub>H<sub>30</sub>Al 297.2163; found, 297.2166. <sup>1</sup>H NMR (300.19 MHz, CD<sub>2</sub>Cl<sub>2</sub>): d 2.187 (s, C<sub>5</sub>Me<sub>5</sub>). <sup>27</sup>Al NMR (78.31 MHz, CD<sub>2</sub>Cl<sub>2</sub>): *d* -102.92 (s, (h<sup>5</sup>-C<sub>5</sub>Me<sub>5</sub>)<sub>2</sub>Al<sup>+</sup>), *d* 115.215 (s, AlCl<sub>4</sub><sup>-</sup>).

### A.1.2 Preparation of Cp\*<sub>2</sub>BMe

A solution of MeLi in Et<sub>2</sub>O (4.6 mL of a 1.4 M solution, 6.4 mmol) was added to a solution of (C<sub>5</sub>Me<sub>5</sub>)<sub>2</sub>BCl (2.03 g, 6.4 mmol) in Et<sub>2</sub>O at –40 °C. The pale yellow mixture was stirred overnight. Volatiles were removed *in vacuo* and the resulting white powder was extracted with consecutive portions of hexane and dried under vacuum. Colorless crystals were obtained by sublimation of the remaining white residue at 45 °C and 0.04 Torr. Yield: 75%. mp 57 – 58 °C. CI HRMS: calcd for C<sub>21</sub>H<sub>33</sub>B, 296.2675; found, 296.2687. NMR (C<sub>6</sub>D<sub>6</sub>): <sup>1</sup>H: δ 0.389 (s, BMe), δ 1.595 (s, C<sub>5</sub>Me<sub>5</sub>). <sup>13</sup>C {<sup>1</sup>H}: δ 13.442 (s, C<sub>5</sub>Me<sub>5</sub>), δ 124.440 (s, C<sub>5</sub>Me<sub>5</sub>). <sup>11</sup>B: δ 85.625.

## A.2.1 X-ray Crystallography Procedures for [Cp\*<sub>2</sub>Al][AlCl<sub>4</sub>] and Cp\*<sub>2</sub>BMe

**Table A.1**  
Crystal data and structure refinement for [Cp\*<sub>2</sub>Al][AlCl<sub>4</sub>] and Cp\*<sub>2</sub>BMe

Empirical formula	C <sub>20</sub> H <sub>30</sub> Al <sub>2</sub> Cl <sub>4</sub>	C <sub>21</sub> H <sub>33</sub> B
Formula weight [g mol <sup>-1</sup> ]	466.20	296.28
Temperature [°C]	-120	-120
Wavelength [Å]	0.71069	0.71073
Crystal system	Triclinic	Orthorhombic
Space group	<i>P</i> $\bar{1}$	<i>P</i> 2 <sub>1</sub> 2 <sub>1</sub> 2 <sub>1</sub>
Unit cell dimensions:		
a [Å]	7.7548(1)	7.5688(15)
b [Å]	17.3747(3)	17.863(4)
c [Å]	18.0806(4)	27.857(6)
α [°]	85.7100(7)	90.
β [°]	83.6011(8)	90.
γ [°]	84.7879(7)	90.
Volume [Å <sup>3</sup> ]	2405.79(7)	3766.4(13)
Z, Calculated density [g cm <sup>-3</sup> ]	4, 1.287	8, 1.045
Absorption coefficient [mm <sup>-1</sup> ]	0.568	0.057
F(000)	976	1312
Crystal size [mm]	0.4 x 0.4 x 0.3	0.4 x 0.4 x 0.2
q range for data collection [°]	2.99 to 25.06	2.92 to 27.48
Index ranges	-9 ≤ h ≤ 9 -18 ≤ k ≤ 20 -21 ≤ l ≤ 20	-9 ≤ h ≤ 9 -23 ≤ k ≤ 23 -36 ≤ l ≤ 35
Reflections collected	32448	7702
Independent reflections	8499 [R <sub>(int)</sub> = 0.0411]	7702 [R <sub>(int)</sub> = 0.0600]
Refinement method	Full-matrix least-squares on F <sup>2</sup>	Full-matrix least-squares on F <sup>2</sup>
Data / restraints / parameters	8499 / 0 / 489	7702 / 0 / 419
Goodness-of-fit on F <sup>2</sup>	1.021	1.017
Final R indices [I > 2σ(I)]	R <sub>1</sub> = 0.0465, wR <sub>2</sub> = 0.1097	R <sub>1</sub> = 0.0696, wR <sub>2</sub> = 0.1416
R indices (all data)	R <sub>1</sub> = 0.0703, wR <sub>2</sub> = 0.1219	R <sub>1</sub> = 0.1413, wR <sub>2</sub> = 0.1783
Largest diff. peak and hole [e Å <sup>-3</sup> ]	0.971 and -0.754	0.189 and -0.255



The crystals of  $[\text{Cp}^*_2\text{Al}][\text{AlCl}_4]$  and  $\text{Cp}^*_2\text{BMe}$  were covered in perfluoro(poly)ether, mounted on a goniometer head and rapidly placed into the  $-120\text{ }^\circ\text{C}$  stream of dry nitrogen of an Oxford Cryostream low temperature device. The data were collected on a Nonius Kappa CCD diffractometer using a graphite monochromator with MoK $\alpha$  radiation ( $\lambda = 0.71073\text{ \AA}$ ). A total of 280 frames of data were collected using  $\omega$ -scans with a scan range of  $1.9^\circ$  and a counting time of 38 seconds per frame for  $[\text{Cp}^*_2\text{Al}][\text{AlCl}_4]$ , while for  $\text{Cp}^*_2\text{BMe}$ , a total of 103 frames of data were collected using  $\omega$ -scans with a scan range of  $1^\circ$  and a counting time of 20 seconds per frame. A summary of the collection, solution and refinement data are presented in Table A.1. Data reduction was performed using DENZO-SMN.<sup>[3]</sup> The structures of  $[\text{Cp}^*_2\text{Al}][\text{AlCl}_4]$  and  $\text{Cp}^*_2\text{BMe}$  were solved by direct methods using SIR92<sup>[4]</sup> and SIR97,<sup>[5]</sup> respectively, and refined by full-matrix least-squares on  $F^2$  with anisotropic displacement parameters for the non-H atoms using SHELXL-93.<sup>[6]</sup> Hydrogen atoms were placed in geometrically calculated positions and were refined using a riding model and a general isotropic thermal parameter. For  $\text{Cp}^*_2\text{BMe}$ , no correction for secondary extinction effects was necessary. Neutral atom scattering factors and values used to calculate the linear absorption coefficient were obtained from the International Tables for X-ray Crystallography (1992).<sup>[7]</sup> All figures were generated using SHELXTL/PC.<sup>[8]</sup>

### A.2.2 X-ray Crystallography Procedures for $\text{Cp}_2\text{Be}$ , $\text{Cp}^*_2\text{Be}$ and $(\text{C}_5\text{Me}_4\text{H})_2\text{Be}$

Crystalline samples of each of the beryllocenes ( $\text{Cp}_2\text{Be}$  1,  $\text{Cp}^*_2\text{Be}$  2 and

(C<sub>5</sub>Me<sub>4</sub>H)<sub>2</sub>Be 3) were obtained by cooling saturated pentane solutions of the compounds to -30 °C. In a glove box containing a dry N<sub>2</sub> atmosphere, the data crystals were selected and mounted in thin-walled glass capillaries, which were subsequently flame-sealed. The sealed capillaries were affixed to brass specimen pins using epoxy. A Kryo-Flex low temperature device was used for low temperature experiments. Note that the same crystal of Cp<sub>2</sub>Be was used to collect data at both 20 °C and -100 °C. The data were collected on a Bruker APEX CCD diffractometer using a graphite monochromator with MoK<sub>α</sub> radiation ( $\lambda = 0.71069 \text{ \AA}$ ). A hemisphere of data was collected using a counting time of 30 seconds per frame. Details of crystal data, data collection and structure refinement are listed in Table A.2. Data reduction was performed using the SAINT software<sup>[9]</sup> and the data were corrected for Lorentz, polarization and absorption effects using the SAINT and SADABS programs. The structures were solved by direct methods using SIR97<sup>[10]</sup> and refined by full-matrix least-squares on F<sup>2</sup> with anisotropic displacement parameters for the non-H atoms using SHELXL-97.<sup>[11]</sup> Neutral atom scattering factors and values used to calculate the linear absorption coefficient are from the International Tables for X-ray Crystallography (1992).<sup>[7]</sup> Hydrogen atoms were placed in calculated positions and were assigned coupled isotropic temperature factors using an appropriate riding model.<sup>[12]</sup> CCDC-234475 to 234478 contain the supplementary crystallographic data for this paper. These data can be obtained free of charge via [www.ccdc.cam.ac.uk/conts/retrieving.html](http://www.ccdc.cam.ac.uk/conts/retrieving.html) (or from the Cambridge Crystallographic Data Centre, 12 Union Road, Cambridge CB2 1EZ, UK; fax:(44)1223-336-033; or e-mail: [deposit@ccdc.cam.ac.uk](mailto:deposit@ccdc.cam.ac.uk)).

**Table A.2**  
Summary of X-ray crystallographic data for 1, 2, and 3.

Compound Number	1	1	2	3
Empirical formula	C <sub>10</sub> H <sub>10</sub> Be	C <sub>10</sub> H <sub>10</sub> Be	C <sub>20</sub> H <sub>30</sub> Be	C <sub>18</sub> H <sub>26</sub> Be
Formula weight [g mol <sup>-1</sup> ]	139.19	139.19	279.45	251.40
Temperature [°C]	20	-100	-120	-100
Wavelength [Å]	0.71069	0.71069	0.71069	0.71069
Crystal system	Monoclinic	Monoclinic	Monoclinic	Orthorhombic
Space group	<i>P2<sub>1</sub>/n</i> <sup>[a]</sup>	<i>P2<sub>1</sub>/c</i>	<i>C2/c</i>	<i>Pnma</i>
Unit cell dimensions:				
a [Å]	5.8901(6)	5.9255(6)	15.1014(13)	12.9448(10)
b [Å]	7.6768(9)	7.4919(10)	12.2367(10)	15.7223(13)
c [Å]	9.3233(14)	10.5501(14)	9.5512(8)	7.6583(6)
α [°]	90.	90.	90.	90.
β [°]	92.297(11)	121.345(8)	95.020(2)	90.
γ [°]	90.	90.	90.	90.
Volume [Å <sup>3</sup> ]	421.23(9)	400.00(9)	1758.2(3)	1558.6(2)
Z	2	2	4	4
Calculated density [g cm <sup>-3</sup> ]	1.097	1.156	1.056	1.071
Absorption coefficient [mm <sup>-1</sup> ]	0.059	0.063	0.057	0.058
F(000)	148	148	616	552
Crystal size [mm]	0.50 x 0.30 x 0.30	0.50 x 0.30 x 0.30	0.70 x 0.50 x 0.30	0.60 x 0.50 x 0.30
q range for data collection [°]	3.44 to 27.56	3.54 to 27.49	2.15 to 27.55	2.59 to 24.98
Index ranges:	-7 ≤ h ≤ 7 -9 ≤ k ≤ 9 -11 ≤ l ≤ 12	-7 ≤ h ≤ 7 -9 ≤ k ≤ 9 -13 ≤ l ≤ 13	-19 ≤ h ≤ 19 -15 ≤ k ≤ 15 -12 ≤ l ≤ 12	-15 ≤ h ≤ 15 -18 ≤ k ≤ 18 -9 ≤ l ≤ 9
Reflections collected	3964	3273	8454	9848
Independent reflections	976 [R(int) = 0.0351]	904 [R(int) = 0.0354]	2035 [R(int) = 0.0274]	1406 [R(int) = 0.0525]
Completeness to q [%]	99.9	98.2	100.0	98.8
Absorption correction	None	None	None	None
Refinement method		Full matrix least squares on F <sup>2</sup>		

Data / restraints / parameters	976 / 0 / 56	904 / 0 / 57	2035 / 0 / 97	1406 / 0 / 105
Goodness-of-fit on $F^2$	1.007	1.447	1.019	1.244
Final R indices [ $I > 2\sigma(I)$ ]	$R_1 = 0.0803$ , $wR_2 = 0.2583$	$R_1 = 0.1052$ , $wR_2 = 0.2219$	$R_1 = 0.0582$ , $wR_2 = 0.1559$	$R_1 = 0.0872$ , $wR_2 = 0.1928$
R indices (all data)	$R_1 = 0.1477$ , $wR_2 = 0.3188$	$R_1 = 0.1105$ , $wR_2 = 0.2240$	$R_1 = 0.0863$ , $wR_2 = 0.1759$	$R_1 = 0.0983$ , $wR_2 = 0.1980$
Largest diff. peak and hole [ $e \text{ \AA}^{-3}$ ]	0.237 and -0.113	0.248 and -0.277	0.183 and -0.151	0.310 and -0.216
Extinction Coefficient	0.13(6)	0.07(2)		

<sup>[a]</sup> The  $P2_1/n$  unit cell of  $\text{Cp}_2\text{Be}$  at 20 °C corresponds to a  $P2_1/c$  cell with unit cell parameters:  $a = 5.8901(6) \text{ \AA}$ ,  $b = 7.6768(9) \text{ \AA}$ ,  $c = 10.8266(12) \text{ \AA}$ ,  $\beta = 120.63(1)^\circ$ .

### A.3.1 X-ray crystal structure of $[\text{Cp}^*_2\text{Al}][\text{AlCl}_4]$

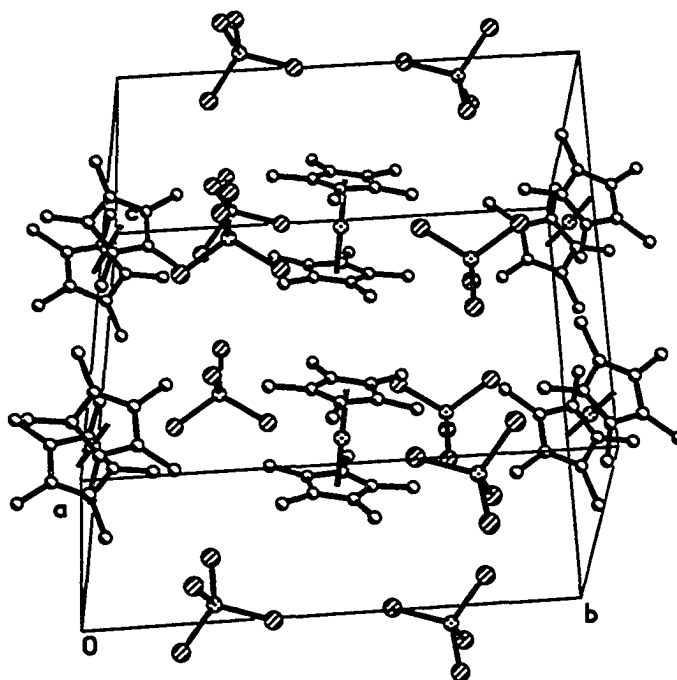
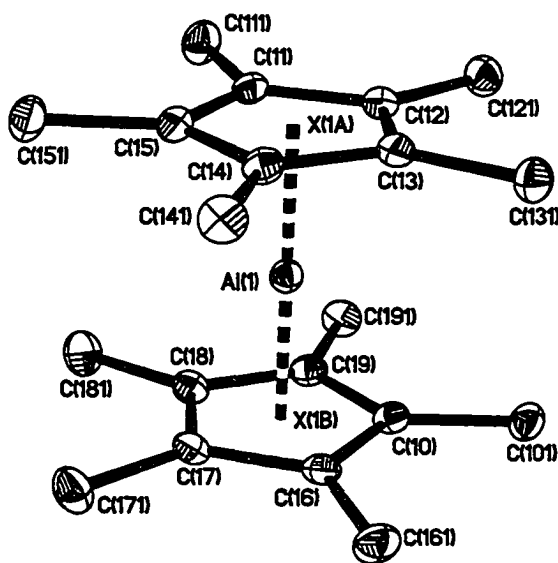


Figure A.1 The unit cell for  $[\text{Cp}^*_2\text{Al}][\text{AlCl}_4]$ .

The unit cell for the X-ray crystal structure of  $[\text{Cp}^*_2\text{Al}][\text{AlCl}_4]$  is depicted in Figure A.1, with the summary of pertinent X-ray data given in Table A.1. The salt  $[\text{Cp}^*_2\text{Al}][\text{AlCl}_4]$  crystallizes in the space group  $P\bar{1}$  and features four asymmetric units per unit cell. There are two crystallographically non-equivalent  $\text{Cp}^*_2\text{Al}^+$  cations in the unit cell. However the structures of both cations are very similar and each cation possesses almost perfect  $D_{5d}$  symmetry due to the staggering of the  $\text{Cp}^*$  rings. The structure of one such cation, which is virtually identical to those found in other decamethylaluminumocenium salts,<sup>[2, 13-16]</sup> is shown in Figure A.2. The tetrachloroaluminate anions are only slightly distorted from ideal tetrahedral symmetry and there are no unusually short contacts between the chlorine atoms of the tetrachloroaluminate anions and the decamethylaluminumocenium cations.



**Figure A.2** Structure of the  $[\text{Cp}^*_2\text{Al}]^+$  cation with  $D_{5d}$  symmetry. Hydrogen atoms are omitted for clarity.

### A.3.2 X-ray Crystallography of $\text{Cp}_2\text{Be}$ , $\text{Cp}^*_2\text{Be}$ and $(\text{C}_5\text{Me}_4\text{H})_2\text{Be}$

Representative crystals from the samples subsequently used for the NMR experiments were subjected to X-ray crystallographic analysis to confirm the structural features of the materials. Figure A.3a shows one molecule from each of the low-temperature (either  $-100\text{ }^\circ\text{C}$  or  $-120\text{ }^\circ\text{C}$ ) crystal structures of **1**, **2** and **3**; the metrical parameters and the geometries of the refined structures agree with those reported previously (Table A.2). Crystallographic data for the same crystal of **1** was also collected at  $20\text{ }^\circ\text{C}$  and refined. As illustrated in Figure A.3b, the model for the higher temperature structure exhibits significantly larger thermal ellipsoids than that of the lower temperature structure. In addition, whereas the structure at  $-100\text{ }^\circ\text{C}$  is best described as having

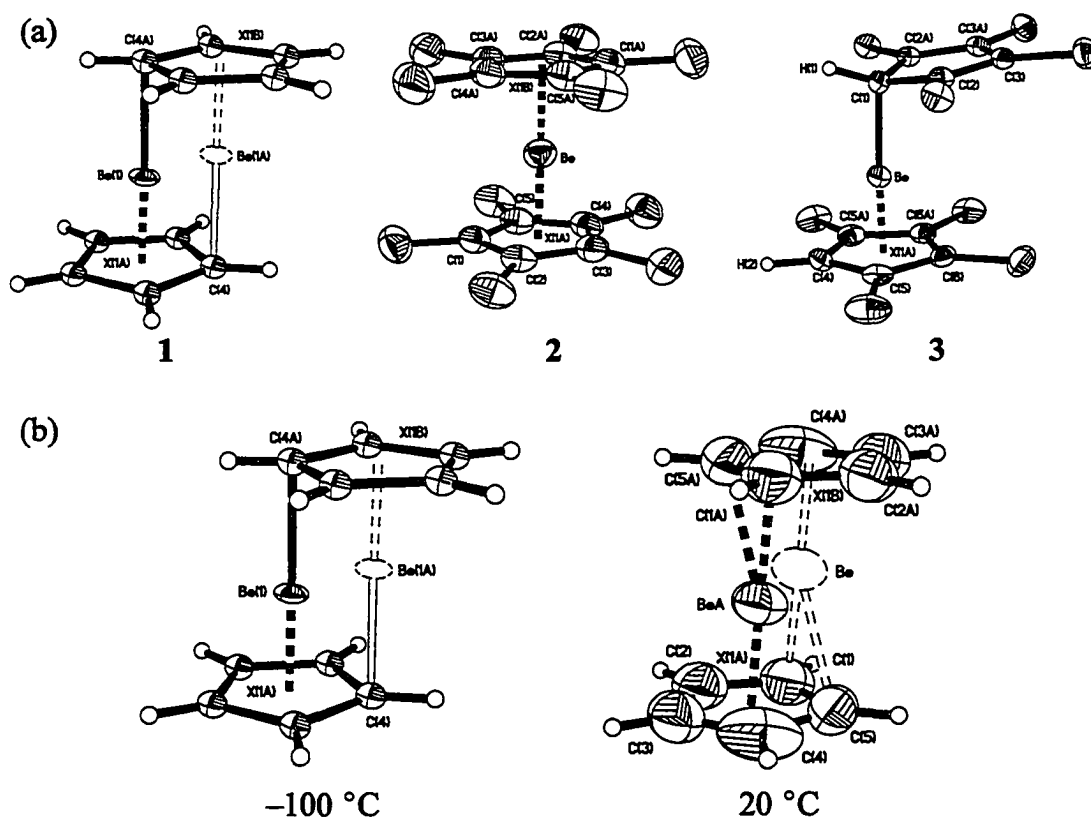


**Figure A.3** (a) Molecules of **1** – **3** from their respective crystal structures; (b) molecular structure of **1** at  $-100\text{ }^\circ\text{C}$  and  $20\text{ }^\circ\text{C}$ .

$\eta^5, \eta^1$ -coordination, the model at 20 °C is better described as exhibiting an  $\eta^5, \eta^2$  arrangement of the Cp rings. Furthermore, the inversion-related positions of the Be atoms are significantly closer together at 20 °C (0.828 Å) than at low temperature (1.230 Å) and there is less “slippage” of the two Cp rings at higher temperature. These related structural features are consequences of the increased inter-ring separation at higher temperature (3.406 Å at 20 °C vs. 3.346 Å at –100 °C) that is accommodated by the increase of the crystallographic *c* axis (from 10.550(2) Å to 10.827(2) Å using the  $P2_1/c$  space group for each unit cell). While the structural features observed by the X-ray diffraction “snapshots” are consistent with significantly greater disorder in the structure of Cp<sub>2</sub>Be at 20 °C than at –100 °C, the NMR experiments described herein provide more detailed information about the nature of the motion in the solid state.

# Bibliography

- [1] V. Quindt, D. Saurenz, O. Schmitt, M. Schar, T. Dezember, G. Wolmershauser, H. Sitzmann, **1999**, 579, 376.
- [2] C. T. Burns, P. J. Shapiro, P. H. M. Budzelaar, R. Willett, A. Vij, **2000**, 19, 3361.
- [3] Z. Otwinowski, W. Minor, in *Methods in Enzymology: Macromolecular Crystallography, part A, Vol. 276* (Eds.: C. W. Carter, Jr., R. M. Sweets), Academic Press, New York, **1997**, pp. 307.
- [4] A. Altomare, G. Cascarano, C. Giacovazzo, A. Guagliardi, **1993**, 26, 343.
- [5] A. Altomare, M. C. Burla, M. Camalli, G. Cascarano, C. Giacovazzo, A. Guagliardi, A. G. G. Moliterni, G. Polidori, R. Spagna, SIR97. A program for crystal structure solution., **1997**.
- [6] G. M. Sheldrick, SHELXL93. Program for the Refinement of Crystal Structures, University of Gottingen, Germany, **1993**.
- [7] in *International Tables for X-ray Crystallography, Vol. C* (Ed.: A. J. C. Wilson), Kluwer Academic Press, Boston, **1992**, p. Tables 4.2.6.8 and 6.1.1.4.
- [8] G. M. Sheldrick, SHELXTL/PC (v.5.03). Siemens Analytical X-ray Instruments, Madison, Wisconsin, USA, **1994**.
- [9] SAINT, Bruker AXS, Inc., Madison, WI, **2001**.
- [10] A. Altomare, M. C. Burla, M. Camalli, B. Carrozzini, G. L. Cascarano, C. Giacovazzo, A. Guagliardi, A. G. G. Moliterni, G. Polidori, R. Rizzi, *J. Appl. Cryst.* **1999**, 32, 115.



- [11] G. M. Sheldrick, SHELXL97, Program for the Refinement of Crystal Structures, University of Gottingen, Germany, **1997**.
- [12] G. M. Sheldrick, SHELXTL/PC, Version 6.10, Bruker AXS, Inc., Madison, WI, **1994**.
- [13] C. Dohmeier, H. Schnockel, C. Robl, U. Schneider, R. Ahlrichs, **1993**, *32*, 1655.
- [14] C. Uffing, A. Ecker, E. Baum, H. Schnockel, *Z. Anorg. Allg. Chem.* **1999**, *625*, 1354.
- [15] C. Dohmeier, E. Baum, A. Ecker, R. Koppe, H. Schnockel, **1996**, *15*, 4702.
- [16] C. T. Burns, D. S. Stelck, P. J. Shapiro, A. Vij, K. Kunz, G. Kehr, T. Concolino, A. L. Rheingold, **1999**, *18*, 5432.

# Appendix B – Additional Figures

## B.1 Supplementary Figures for Chapter 3

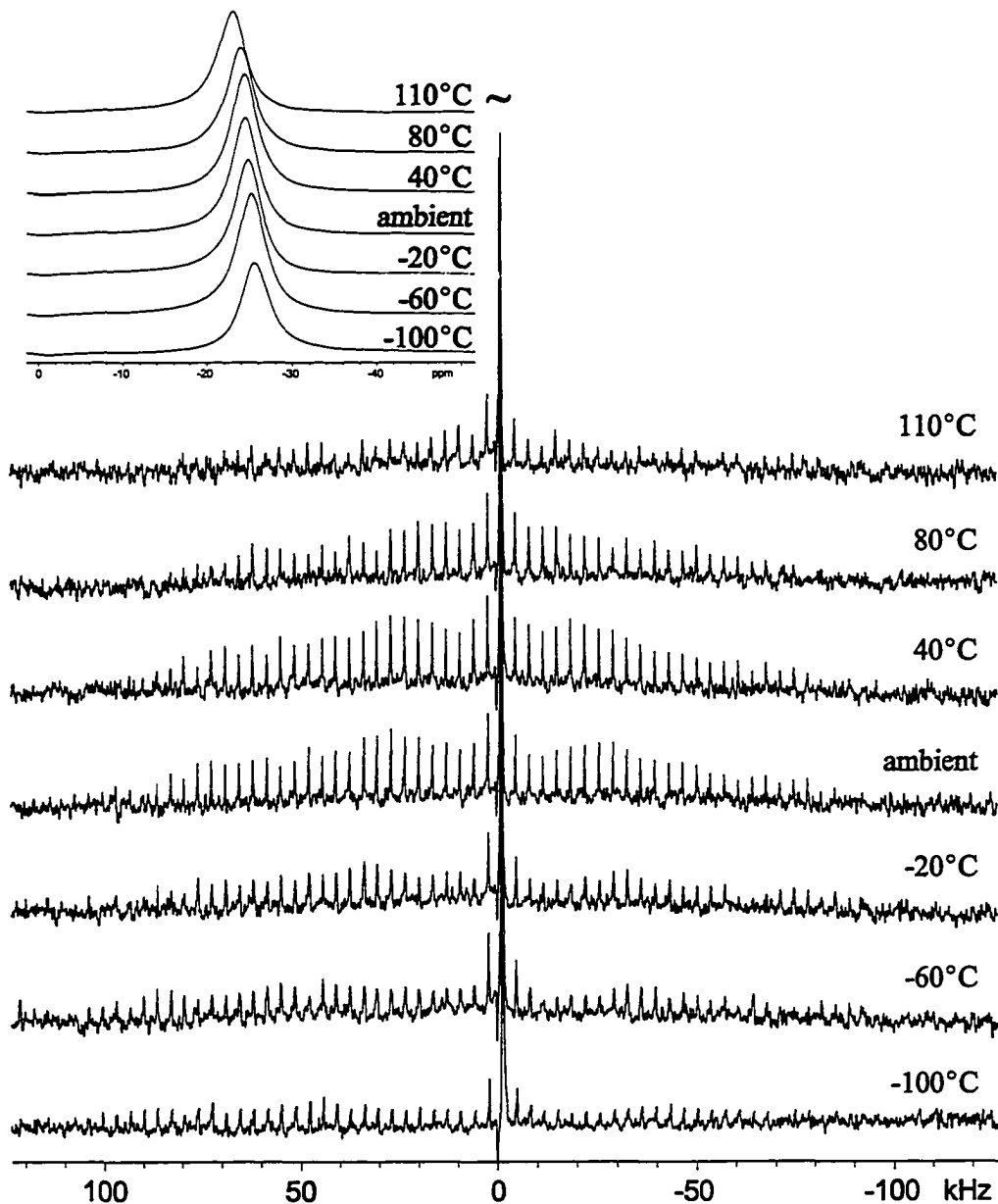


**Figure B.1** Inset shows an expansion of the central transition, which demonstrates a change in the isotropic shift from  $-23.1$  ppm to  $-25.7$  ppm as the temperature is decreased through the temperature range shown. It is also interesting to note that the  $C_Q(^9\text{Be})$  appears to increase with decrease in temperature, as shown by the increase in area covered by spinning sidebands.

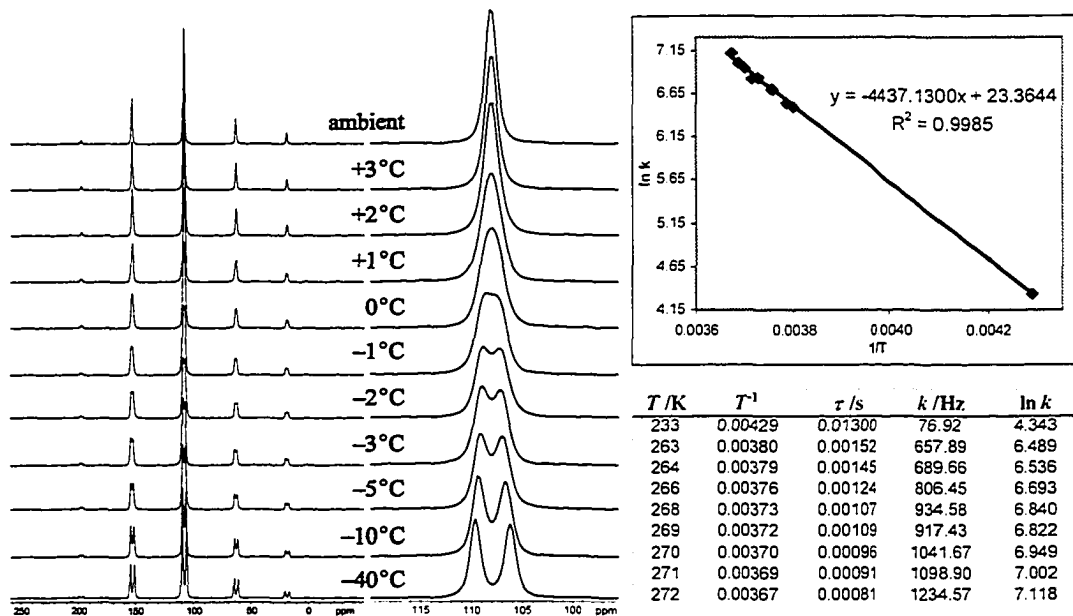


**Figure B.2** Analysis of  $^{13}\text{C}$  VT CP/MAS NMR spectra of  $\text{Cp}_2\text{Be}$ . The activation energy was calculated to be  $36.9 \text{ kJ mol}^{-1}$  for the chemical exchange process giving rise to the observed spectra.

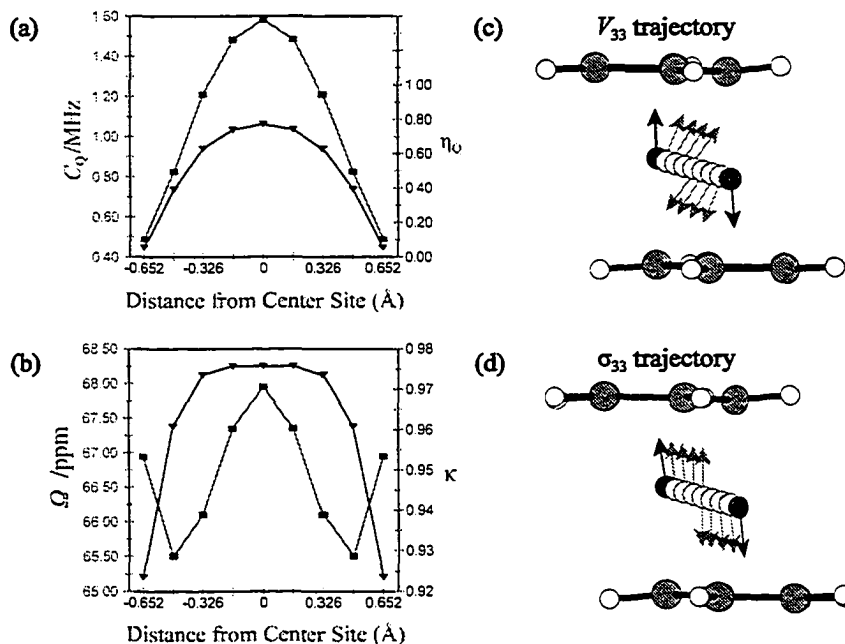


**Figure B.3** Trajectories of the largest principal components,  $V_{33}$  and  $\sigma_{33}$ , of the theoretical  $^9\text{Be}$  (c) EFG and (d) CS tensors of **1** at different positions along the 'inversion.' Accompanying are plots of (a)  $C_Q$  ( $\blacksquare$ ) and  $\eta_Q$  ( $\blacktriangledown$ ), and (b)  $\Omega$  ( $\blacksquare$ ) and  $\kappa$  ( $\blacktriangledown$ ), at each of the positions where  $^9\text{Be}$   $V_{33}$  and  $\sigma_{33}$  vectors are shown.

## B.2 Supplementary Figures for Chapter 5

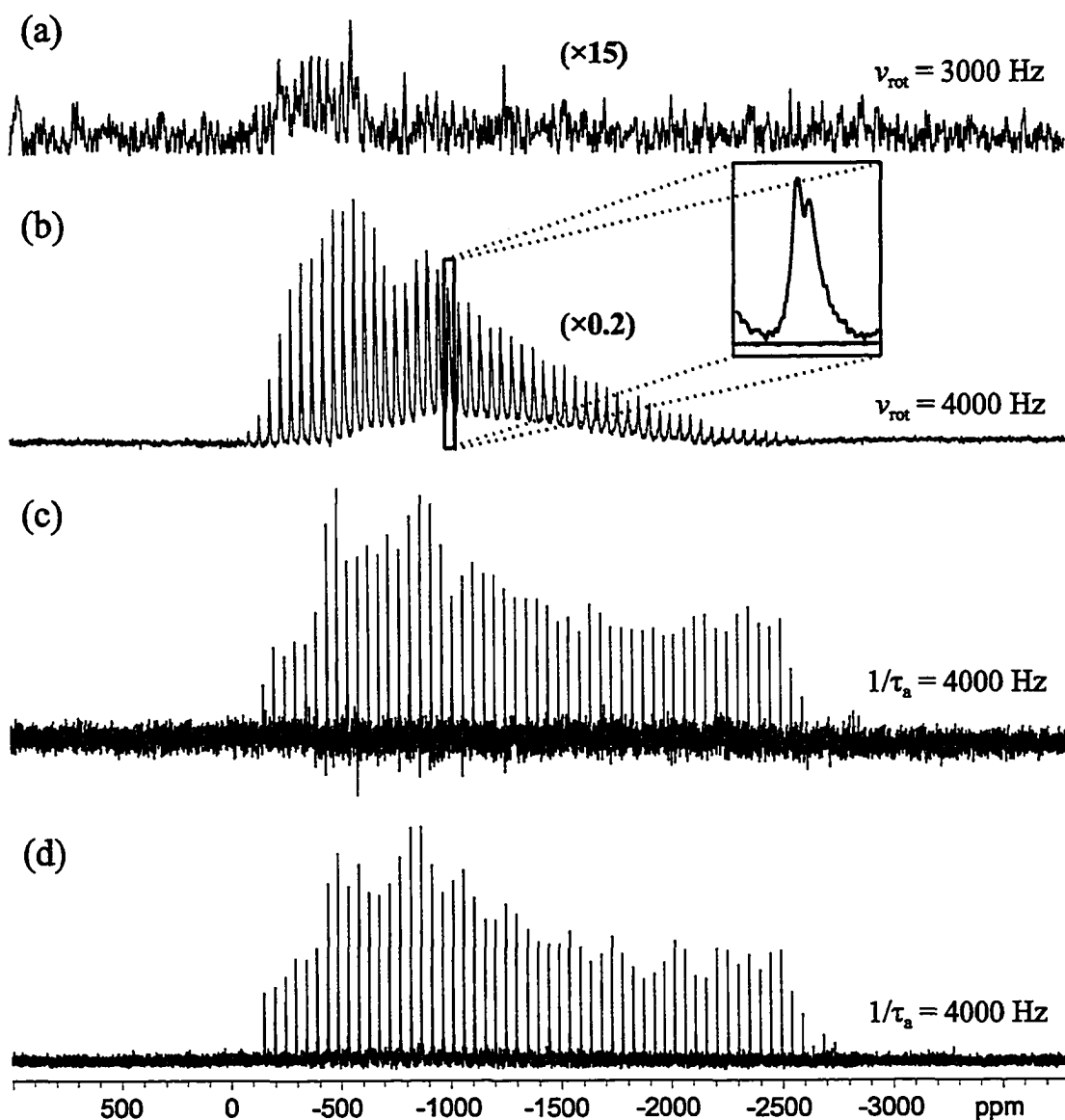


**Figure B.4**  $^{207}\text{Pb}$  (a) MAS, (b) CP/MAS, (c) wideline CPMG and (d) wideline CP/CPMG NMR spectra of a  $(\text{CH}_3\text{COO})_2\text{Pb}\cdot 3\text{H}_2\text{O}$  sample before recrystallization; sample is believed to have undergone dehydration and phase transformation. Notably, the optimal CP conditions for the hydrated and dehydrated compounds were markedly different. 64 and 16 transients were acquired for each of the CPMG and CP/CPMG sub-spectra, respectively.

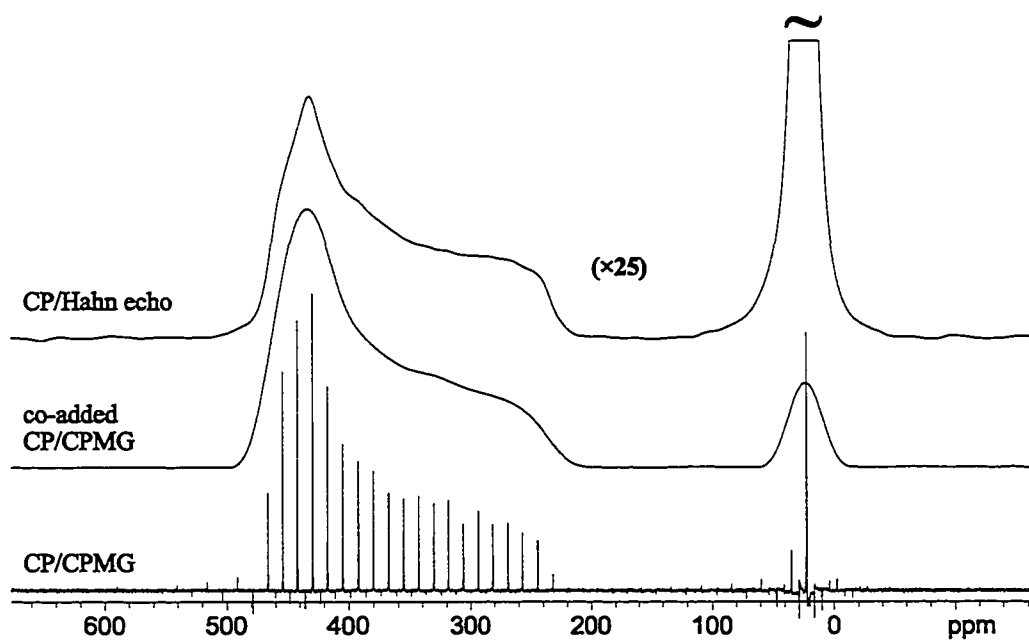


**Figure B.5** Comparison of the  $^{15}\text{N}$  CP/Hahn echo and CP/CPMG NMR spectra of  $^{15}\text{N}$   $\text{NH}_4^+\text{NO}_3$  (98% enriched in  $^{15}\text{N}$ ). The co-added CP/CPMG spectrum results from adding up the train of echoes in the time-domain and subsequent Fourier transformation. For comparison, the vertical scale of the CP/Hahn echo spectrum has been scaled up by a factor of 25 times.

### B.3 Supplementary Figures for Chapter 7

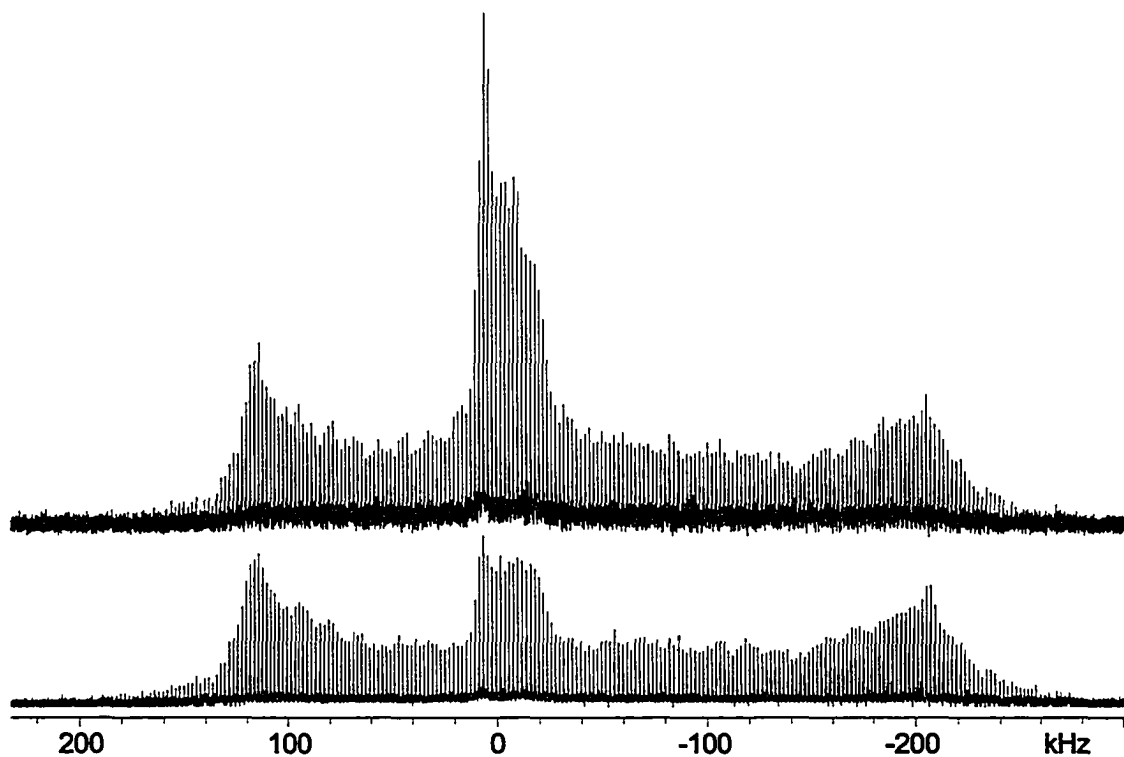


**Figure B.6**  $^{91}\text{Zr}$  wideline QCPMG spectrum of  $\text{Cp}_2\text{ZrCl}_2$  in a  $\text{ZrO}_2$  NMR rotor. Comparison of taking the skyline projection (bottom trace) and adding (top trace) of the individually acquired spectral pieces.

## B.4 Supplementary Figures for Chapter 8

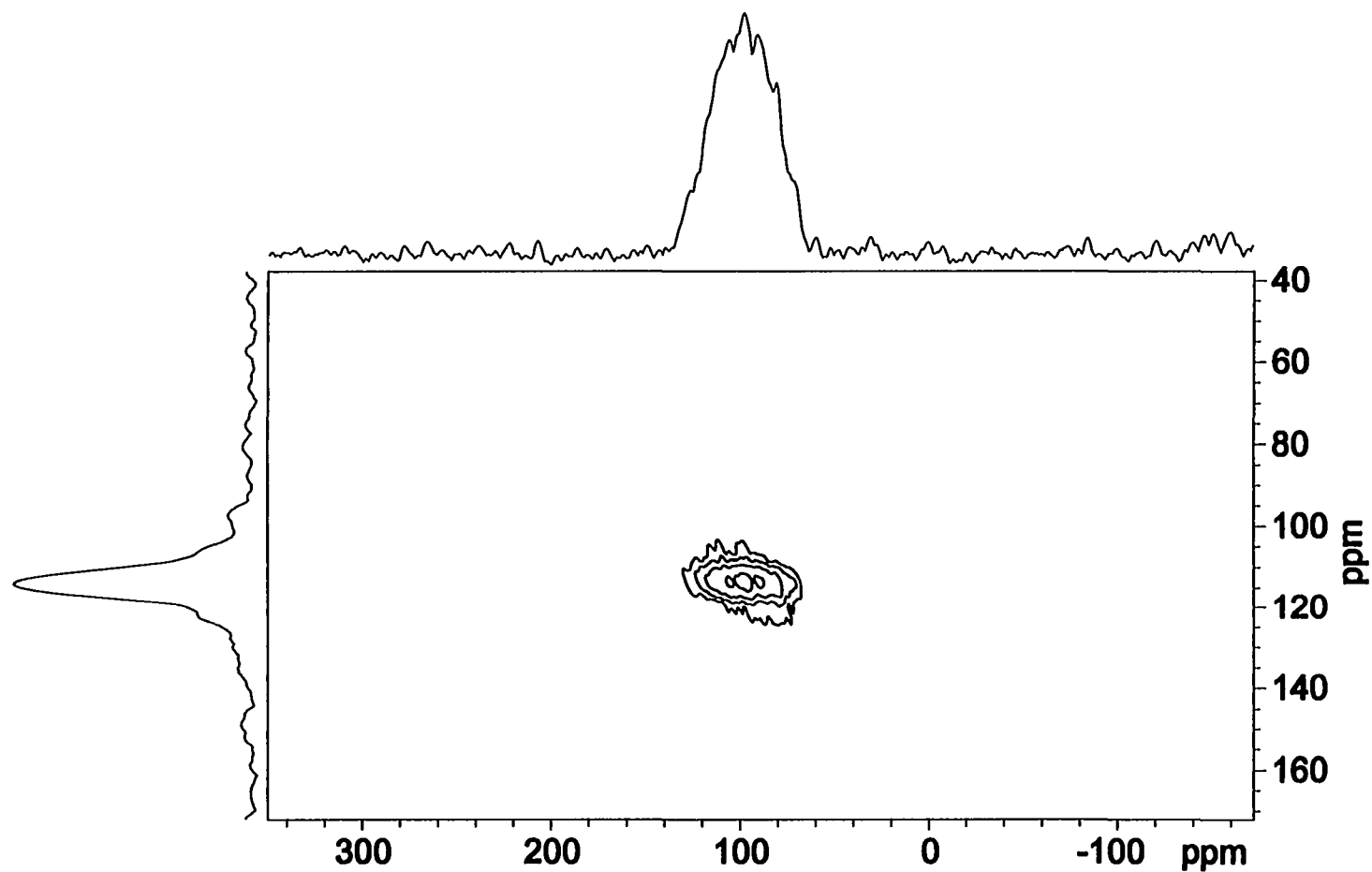


**Figure B.7**  $^{91}\text{Zr}$  triple-quantum multiple-quantum MAS NMR spectrum of  $\text{Cp}_2\text{ZrBr}_2$  at  $\nu_{\text{rot}} = 10000$  Hz. The isotropic projection is shown on the left and the anisotropic projection on top.

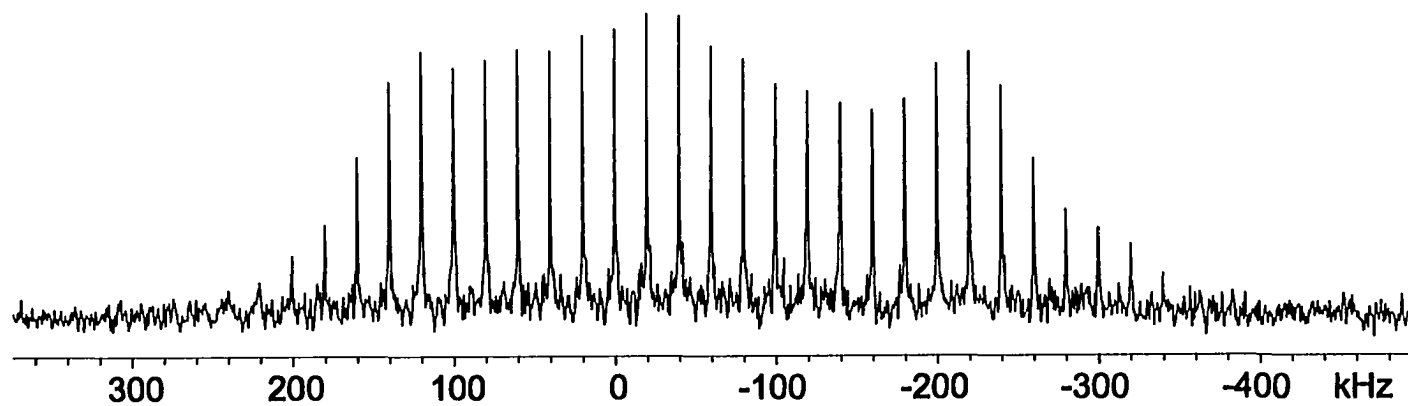


**Figure B.8** Static  $^{91}\text{Zr}$  wideline QCPMG NMR spectrum of  $\text{CpZrCl}_3$ . The pattern seems to result from the overlap of more than one zirconium site.



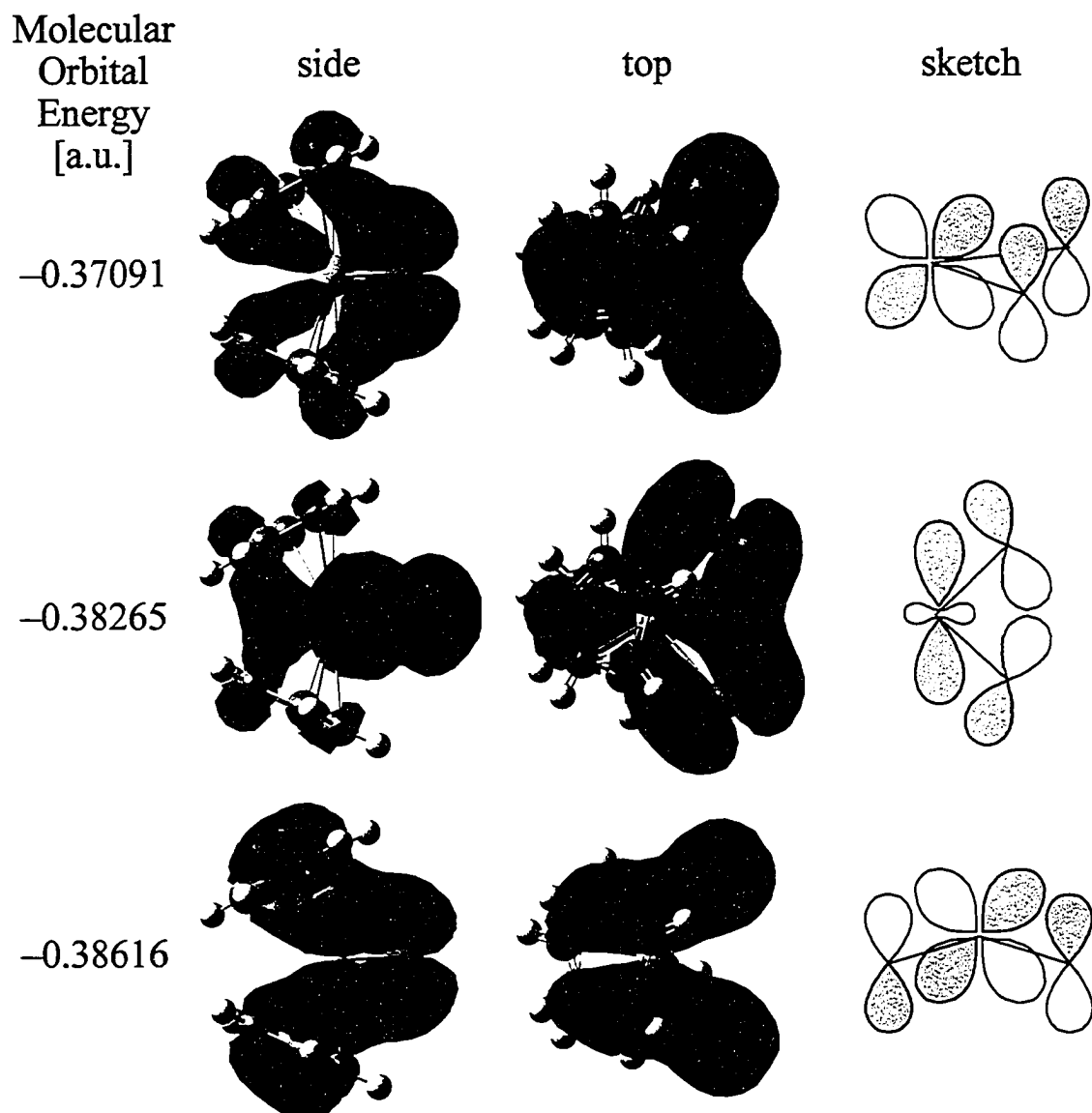


**Figure B.9** Side and top views of molecular orbitals taking part in  $\pi$ -donation between the Zr and Cl atoms obtained from the calculation using the B3LYP method and basis sets mentioned in chapter 8. The molecular orbital energies are given in the left-most column, while simplified sketches are presented on the right for easier visualization of the orbitals involved.

# Appendix C – Supplementary Calculations and SCF Energies

## C.1 SCF Energies from Calculations for Cp<sub>2</sub>Mg Presented in Chapter 6

**Table C.1**

SCF energies of calculations performed on the X-ray crystal structure (optimized hydrogen positions) of Cp<sub>2</sub>Mg

Source	SCF Energy [a.u.]
RHF	
6-31G**	-584.100775838
6-311G**	-584.179043477
6-311+G**	-584.182646980
DFT(B3LYP)	
6-31G**	-587.168385983
6-311G**	-587.266076058
6-311+G**	-587.269561809
MP2	
6-31G**	-584.100775966
6-311G**	-584.179043603

**Table C.2**

SCF energies of calculations performed on the optimized gas-phase structure of Cp<sub>2</sub>Mg

Source	SCF Energy [a.u.]
RHF	
6-31G**	-584.126054892
6-311G**	-584.203153920
6-311+G**	-584.206861984
DFT(B3LYP)	
6-31G**	-587.198355513
6-311G**	-587.293833297
6-311+G**	-587.297449814

## C.2 Supplementary Calculations for Cp<sub>2</sub>Mg

**Table C.3**  
Theoretical <sup>25</sup>Mg Quadrupolar Parameters in Cp<sub>2</sub>Mg<sup>[a]</sup>

Source	$V_{11}$ [a.u.]	$V_{22}$ [a.u.]	$V_{33}$ [a.u.]	$ C_Q $ [MHz]	$\eta_Q$
<b>Experimental</b>	-0.055540	-0.056662	0.112202	5.80(5)	0.01(1)
RHF					
6-31G**	-0.022621	-0.022643	0.045264	2.34	0.00
6-311G**	-0.043765	-0.044533	0.088298	4.56	0.01
6-311+G**	-0.044003	-0.044776	0.088779	4.59	0.01
DFT(B3LYP)					
6-31G**	0.005213	0.006372	-0.011584	0.60	0.10
6-311G**	-0.038435	-0.038794	0.077229	3.99	0.00
6-311+G**	-0.039104	-0.039404	0.078507	4.06	0.00
MP2					
6-31G**	-0.021606	-0.039153	0.060759	3.14	0.29
6-311G**	-0.038296	-0.060878	0.099174	5.13	0.23

<sup>[a]</sup> Calculations performed with optimized gas-phase geometry of Cp<sub>2</sub>Mg; crystal structure geometry with optimized hydrogen positions was utilized for MP2 calculations.

**Table C.4**  
Calculated Magnesium Chemical Shielding Tensors in Cp<sub>2</sub>Mg<sup>[a]</sup>

Source	$\delta_{11}$ [ppm]	$\delta_{22}$ [ppm]	$\delta_{33}$ [ppm]	$\delta_{iso}$ [ppm]	$\Omega$ [ppm]	$\kappa$
<b>Experimental</b>	—	—	—	-91(3)	—	—
RHF						
6-31G**	-78.19	-78.20	-112.42	-89.60	34.23	1.00
6-311G**	-82.42	-82.67	-116.52	-93.87	34.10	0.99
6-311+G**	-83.61	-83.87	-117.28	-94.92	33.66	0.98
DFT(B3LYP)						
6-31G**	-83.17	-83.50	-123.46	-96.71	40.29	0.98
6-311G**	-78.91	-78.99	-125.37	-94.43	46.46	1.00
6-311+G**	-79.25	-79.92	-124.44	-94.54	45.19	0.97
MP2 <sup>[b]</sup>						
6-31G**	-92.53	-98.42	-133.73	-108.23	41.20	0.71

<sup>[a]</sup> Calculations performed with optimized gas-phase geometry of Cp<sub>2</sub>Mg; crystal structure geometry with optimized hydrogen positions was utilized for MP2 calculations.

### C.3 SCF Energies from Calculations for $\text{Cp}_2\text{ZrCl}_2$ Presented in Chapter 7

**Table C.5**  
SCF Energies for Calculations on the Isolated Solid-State Geometry of  $\text{Cp}_2\text{ZrCl}_2$

Source	SCF Energy [a.u.]
RHF/6-31G**	
3F (33333/333/33)	-4829.59122261
3F (43222/422/33)	-4838.45016399
3F (43333/433/43)	-4839.58280686
5F (33333/333/33)	-4829.56952374
5F (43222/422/33)	-4838.42548391
5F (43333/433/43)	-4839.57353448
RHF/6-311G**	
3F (33333/333/33)	-4829.73417357
3F (43222/422/33)	-4838.59079284
3F (43333/433/43)	-4839.71406917
5F (33333/333/33)	-4829.71460489
5F (43222/422/33)	-4838.56812497
5F (43333/433/43)	-4839.70553729
DFT(B3LYP)/6-31G**	
3F (33333/333/33)	-4835.60965145
3F (43222/422/33)	-4844.46561275
3F (43333/433/43)	-4845.61980320
5F (33333/333/33)	-4835.58877298
5F (43222/422/33)	-4844.44148874
5F (43333/433/43)	-4845.61041911
DFT(B3LYP)/6-311G**	
3F (33333/333/33)	-4835.79434830
3F (43222/422/33)	-4844.64887080
3F (43333/433/43)	-4845.79173780
5F (33333/333/33)	-4835.77498359
5F (43222/422/33)	-4844.62623986
5F (43333/433/43)	-4845.78259404

## C.4 Calculations Comparing the Two Inequivalent Crystallographic Sites of $\text{Cp}_2\text{ZrCl}_2$

**Table C.6**

Ab Initio SCF Energies for Calculations on Both Crystallographic Sites of  $\text{Cp}_2\text{ZrCl}_2$

Source	SCF Energy [a.u.]
RHF/6-31G** 5F (43333/433/43)	
Site 1	-4839.58131184
Site 2	-4839.57353568

**Table C.7**

Theoretical  $^{91}\text{Zr}$  Quadrupolar Parameters for Both Crystal Sites of  $\text{Cp}_2\text{ZrCl}_2$

Source	$V_{11}$ [a.u.]	$V_{22}$ [a.u.]	$V_{33}$ [a.u.]	$ C_Q $ [MHz]	$\eta_Q$
<b>Experimental</b>	0.0537	0.0998	-0.1536	6.35(10)	0.3(1)
RHF/6-31G** 5F (43333/433/43)					
Site 1	0.0508	0.0933	-0.1442	5.96	0.29
Site 2	0.0494	0.1014	-0.1509	6.24	0.34

**Table C.8**

Ab Initio Zirconium Chemical Shielding Tensors for Both Crystal Sites of  $\text{Cp}_2\text{ZrCl}_2$

Source	$\delta_{11}$ [ppm]	$\delta_{22}$ [ppm]	$\delta_{33}$ [ppm]	$\delta_{\text{iso}}$ [ppm]	$\Omega$ [ppm]	$\kappa$
<b>Experimental</b>	306	-62	-169	25	475	-0.55
RHF/6-31G** 5F (43333/433/43)						
Site 1	204.8	-27.2	-131.9	15.2	336.62	-0.38
Site 2	201.5	-51.1	-150.4	0.0	351.91	-0.44

## C.5 Calculations for a Geometry Optimized Molecule of $\text{Cp}_2\text{ZrCl}_2$

**Table C.9**  
SCF Energies for Calculations on Geometry Optimized Isolated Gas-Phase Molecule of  $\text{Cp}_2\text{ZrCl}_2$

Source	SCF Energy [a.u.]
RHF/6-31G**/5F (43333/433/43)	-4839.72148505
DFT(B3LYP)/6-31G**/5F (43333/433/43)	-4845.77680539

**Table C.10**  
Theoretical  $^{91}\text{Zr}$  Quadrupolar Parameters in Geometry Optimized  $\text{Cp}_2\text{ZrCl}_2$

Source	$V_{11}$ [a.u.]	$V_{22}$ [a.u.]	$V_{33}$ [a.u.]	$ C_Q $ [MHz]	$\eta_Q$
<b>Experimental</b>	—	—	—	6.35(10)	0.3(1)
RHF/6-31G**/5F (43333/433/43)	-0.0047	-0.0802	0.0849	3.51	0.89
DFT(B3LYP)/6-31G**/5F (43333/433/43)	0.0662	0.1619	-0.2281	9.43	0.42

**Table C.11**  
Zirconium Chemical Shielding Tensors in Geometry Optimized  $\text{Cp}_2\text{ZrCl}_2$

Source	$\delta_{11}$ [ppm]	$\delta_{22}$ [ppm]	$\delta_{33}$ [ppm]	$\delta_{\text{iso}}$ [ppm]	$\Omega$ [ppm]	$\kappa$
<b>Experimental</b>	306	-62	-169	25	475	-0.55
RHF/6-31G**/5F (43333/433/43)	178.4	-49.2	-129.2	0.0	307.61	-0.48
DFT(B3LYP)/6-31G**/5F (43333/433/43)	256.8	-83.8	-173.0	0.0	429.83	-0.59

## **Vita Auctoris**

Ivan Hung was born on August 10th, 1979 in Acarigua, Portuguesa, Venezuela, and still currently retains his Venezuelan citizenship. He graduated from Mountain View High School, California, USA in 1996. From there he went on to the University of Windsor, Ontario, Canada where he obtained a Bachelor of Science (B.Sc.) degree in Chemistry in 2000. He is currently a candidate for the Philosophiae Doctor (Ph.D.) in Chemistry at the University of Windsor and hopes to graduate in the Spring of 2005.